FOUNDRY MICROFABRICATION OF DEFORMABLE
MIRRORS FOR ADAPTIVE OPTICS

DISSERTATION

William D. Cowan, Major, USAF

AFIT/DS/ENG/98-07
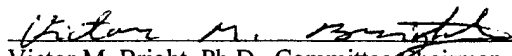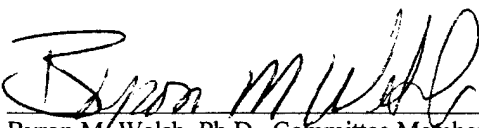
19980629 031

Foundry Microfabrication of Deformable Mirrors for Adaptive Optics

William D. Cowan, MSEE, BSEE
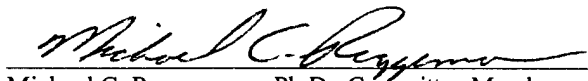Major, USAF

Approved:

_____
Victor M. Bright, Ph.D., Committee Chairman
AFIT Department of Electrical and Computer Engineering
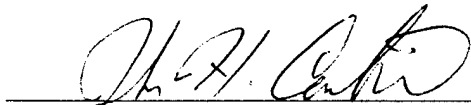
_____22 May 98_____
Date

_____
Byron M. Welsh, Ph.D., Committee Member
AFIT Department of Electrical and Computer Engineering
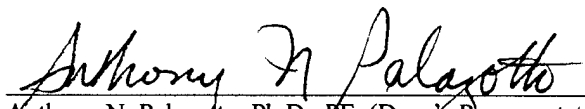
_____22 May 98_____
Date

_____
Michael C. Roggemann, Ph.D., Committee Member
AFIT Department of Engineering Physics

_____22 May 98_____
Date
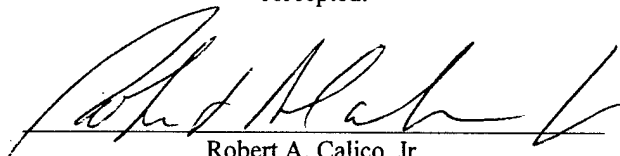
_____
John H. Comtois, Ph.D., Major, USAF, Committee Member
Air Force Research Laboratory

_____22 May 98_____
Date

_____
Anthony N. Palazotto, Ph.D., PE, (Dean's Representative)
AFIT Department of Aeronautics and Astronautics

_____26 May 98_____
Date

Accepted:

_____
Robert A. Calico, Jr.
Dean, Graduate School of Engineering

FOUNDRY MICROFABRICATION OF DEFORMABLE MIRRORS
FOR ADAPTIVE OPTICS

DISSERTATION

Presented to the Faculty of the Graduate School of Engineering
of the Air Force Institute of Technology
Air Education and Training Command
In Partial Fulfillment of the Requirements for the Degree of
Doctor of Philosophy

William D. Cowan, MSEE, BSEE

Major, USAF

24 April 1998

Table of Contents

Table of Contents (cont.)

Table of Contents (cont.)

Acknowledgments

Without the love, support, and understanding of my wife Sue and children, Charolette age 11, and Bill age 9, this dissertation research effort would have been neither possible nor worth pursuing. Despite my absences from home, both physically and mentally, my heart was always with you. Probably not many families count fast-food picnics in the laboratory, evenings spent watching interferometric microscope video tapes, or Saturday scanning electron microscope sessions with Dad as "quality time", but I'm grateful that you always do. Thanks also to longtime friends Greg, Jane, and Arden Zeman who extended their family fun to include my family, while I had my nose buried in a computer screen or microscope.

I am thankful to have had a research advisor and committee chairman, Dr. Victor Bright, who encouraged a broad study of MEMS technology and devices, taking advantage of publication opportunities, and interaction with other researchers in the MEMS field. Having a number of publications to draw from certainly made writing this document easier. The breadth of my AFIT MEMS experience, from mirrors to motors, will I'm sure serve the Air Force well in my future endeavors. The vision, expertise, and constructive comments of committee members, Dr. Mike Roggemann and Dr. Byron Welsh, were instrumental in helping me bring MEMS deformable mirrors to the attention of the adaptive optics community. Committee member, Major John Comtois, Ph.D., provided a wealth of ideas, funding support, and most importantly accomplished much of the ground work necessary to do MEMS research at AFIT when he was here. Dean's Representative Dr. Anthony Palazotto provided some valuable insight into solving some MEMS materials problems which currently plague many MEMS researchers.

I am indebted to Dr. Max Lee, for his assistance in making measurements on the adaptive optics test bench. Max's willingness to match my long hours in the laboratory with his own greatly contributed to the successful demonstration of MEMS deformable mirrors in a test bed adaptive optics system.

I owe another debt of gratitude to Mr. Jeff Brown, who arranged the long term loan of an interferometric microscope for AFIT MEMS research. I found this piece of equipment to be by far the

iv

List of Figures

List of Figures (cont.)

List of Figures (cont.)

List of Tables

Abstract

Microelectromechanical Systems (or MEMS) is a rapidly emerging field of research in which batch fabrication processes, similar to those of the integrated circuit industry, are used to construct miniature devices with moving parts. MEMS devices are particularly well suited to optical applications, where microscopic deflections can produce macroscopic results. Although existing MEMS foundry processes have not been optimized for optical applications, the use of foundry microfabrication offers a substantial cost advantage for prototype system development through low volume production. In this dissertation research effort, foundry MEMS processes are used to fabricate low-cost deformable mirror systems (MEM-DMs) for adaptive optics. The challenges and design trades associated with fabrication of continuous and segmented deformable mirrors in foundry processes are examined in detail. The importance of controlling micromirror surface figure is experimentally demonstrated, and post-foundry metallization techniques are shown to improve the optical performance of foundry fabricated piston micromirror arrays. Beam steering and optical aberration correction experiments, with and without using a lenslet array to improve optical characteristics, conclusively demonstrate the potential of low-cost MEM-DMs. The prototype MEM-DM systems are approximately $1/500^{th}$ the cost of conventionally manufactured deformable mirrors. Optical experiment results show good agreement with theory. The development of an innovative direct digital control scheme further reduces adaptive optic system cost by eliminating the digital to analog converter typically required for each controlled element. In addition to the MEM-DMs demonstrated, other MEMS devices are shown. Two dimensional arrays of thermally actuated piston micromirrors are designed and tested. The thermally actuated devices offer greater deflections for operation at longer optical wavelengths. A variety of tilting and beam steering mirrors are demonstrated, including two-axes steering mirrors which are self-assembled using metal stress cantilevers. Other MEMS devices examined include pressure gauges, test structures, electrostatic scratch drive actuated rotors, and a new type of electrostatic cantilever motor with lateral motion output.

Foundry Microfabrication of Deformable Mirrors for Adaptive Optics

1. Introduction

Microelectromechanical systems (MEMS) is a rapidly emerging technology that employs batch fabrication processes similar to those of the integrated circuit industry to fabricate electromechanical parts. Like the early history of the laser, MEMS is a technology searching for applications. A number of MEMS component level devices such as automotive airbag accelerometers, inkjet nozzles, and pressure sensors, have found commercial success. Systems comprised of large numbers of identical components such as projection displays have also been demonstrated. The use of MEMS techniques to fabricate deformable mirrors for adaptive optics represents a nearly ideal match of technology and application. Optical system apertures are readily scaled to MEMS dimensions. The small motion ranges of MEMS are well suited to optical phase modulation. Likewise, the mass that must be moved is only that of the reflecting surface. The conventionally manufactured deformable mirrors currently in use are large, heavy, and power hungry. Perhaps most importantly, current deformable mirrors are very expensive. Using MEMS fabrication techniques the cost of deformable mirrors for adaptive optics can potentially be reduced by a factor of 1000. This dissertation demonstrates the potential of MEMS deformable mirrors for adaptive optics, through the development, testing, and successful demonstration of prototype systems fabricated in low-cost foundry processes.

The problem statement and justification for the foundry microfabrication approach are detailed in Section 1.1. Section 1.2 provides a brief background and identifies adaptive optics applications. Requirements for atmospheric adaptive optics are examined in Section 1.3. Section 1.4 summarizes the research accomplished and Section 1.5 provides the organization of this dissertation.

1.1 Problem Statement and Approach

The realization of astronomical adaptive optic systems to correct for aberrations induced by atmospheric turbulence has lead researchers to consider many other applications. Unfortunately, many of these new applications are made impractical only by the size, weight, power dissipation, and high cost of adaptive optics components, specifically the deformable mirror. This dissertation addresses the problem of reducing deformable mirror size, weight, power consumption, and cost by employing MEMS technology. Microfabrication yields a two part cost savings. First, is the reduced manufacturing cost per unit. Second, but more significant, is the elimination of characterization testing of each mirror or actuator element comprising the deformable mirror. Microfabrication is ideally suited to the manufacture of parts with identical characteristics.

The approach pursued in this research effort was to employ available surface micromachining foundry processes for low cost fabrication of prototype deformable mirror systems. Like any integrated circuit, the ultimate production cost of a microfabricated deformable mirror is primarily the process development cost divided by the number of units produced (or more importantly, sold). Until a large market is identified, the expense of process development does not make microfabrication particularly attractive. Foundries spread the processing cost among a larger number of applications and make prototype microfabricated systems feasible. In addition, the low cost and quick turnaround of foundry processes allows rapid design iteration, and parallel design approaches.

1.2 Background

Adaptive optics has a long history. The earliest use of adaptive optics is often attributed to Archimede's [1]. In 211 BC Archimede's soldiers defending Syracuse used polished shields (or some other reflecting surfaces) to direct sunlight onto the ships of the approaching Roman fleet. The combined intensity was apparently enough to burn the attacking ships. Most certainly this first deformable mirror system was large, crude, and expensive; but effective. Much later, Sir Isaac Newton foresaw no solution to the

limitations of atmospheric turbulence on astronomy. In 1953, Horace Babcock proposed the use of a deformable mirror driven by a wavefront sensor to compensate for atmospheric turbulence [2]. It is only in the past 10 years that technology has enabled practical adaptive optics systems. The first compensated astronomical telescope images were obtained by military researchers at the Starfire Optical Range while working in secret. A short time later civilian researchers in France demonstrated an adaptive optical system [3]. Adaptive optics has been compared to Galileo's invention of the telescope in importance to the astronomy community.

It is not surprising that military researchers in the big budget "Reagan defense buildup years" were among the first to develop adaptive optics systems. As with any endeavor dependent on technology development, adaptive optics systems have historically been costly. In the introduction of his 1991 book, Tyson makes the following statements [1]. *"Adaptive optics is growing; it is changing. It is expensive"*. This dissertation research effort challenges the latter sentence in the quote above. By employing microfabrication techniques to fabricate deformable mirrors, the cost of this critical adaptive optic component can be greatly reduced. As deformable mirror cost decreases, the number of practical applications increases. For many applications, a low-cost deformable mirror may be the enabling technology, even if the performance specifications of the microfabricated part are not as good as a much more expensive conventional deformable mirror. The small size, weight, and power dissipation of a microfabricated part are also critical for airborne or space-borne adaptive optics applications.

Potential atmospheric adaptive optics applications include astronomy, (or more generally space object imaging), beaming of laser power to satellites, and laser communications systems. Phase conjugate adaptive optics can also be applied to a number of other problems. Medical applications are one area of interest [4]. Endoscopic surgeons must view tissues through bodily fluids that aberrate and degrade image quality. Opthamologists and optometrists imaging the retina are confronted with aberrations in the eye lens, cornea, and the turbulent ocular fluids of the eye. In both endoscopic and eye laser surgeries precise delivery of laser power is also affected by these aberrations. Other potential uses of adaptive optics include laser machining, direct write (maskless) photolithography, holographic data storage, optical microscopy

systems, and laser ranging systems. With sufficiently low cost deformable mirrors, consumer electro-optical applications become feasible [5]. Optical pickups for compact disks, adaptive optical systems for amateur telescopes, optical communication systems and replacements for photographic or video lenses are just a few potential consumer applications. Undoubtedly the list of potential adaptive optics applications will continue to grow as component costs decrease.

1.3 Deformable Mirror Requirements

Desired adaptive optical system performance and the nature of the aberrations corrected define the requirements for deformable mirrors. Design goals for the microfabricated deformable mirror systems developed in this research were derived from the requirements for atmospheric aberration correction. Atmospheric aberration correction has been extensively studied, and the large body of work scales directly to the microfabricated deformable mirror case. Design goals for the prototype systems were tempered by the constraints of foundry fabrication processes, and practical laboratory testing. Thus, the devices produced and demonstrated may be more applicable to other, less demanding, aberration correction applications. This section briefly examines deformable mirror requirements for atmospheric aberration correction, and notes some of the constraints imposed on the prototype systems.

1.3.1 Modulation Requirements for Optical Aberration Correction

The critical difference between micromirror arrays for projection display or printing applications, and microfabricated deformable mirrors is the type of optical modulation. The optical modulation required by different applications can in general be described as amplitude-only or phase-only. The type of motion of the micromirror surface determines its light modulation characteristics. Piston or up-down mirror motion performs phase modulation by changing the optical path length. Amplitude modulation is accomplished by a tip-tilt mirror motion which redirects the peak intensity of the reflected light. Projection display devices, printing mechanisms, and optical switching networks require primarily amplitude modulation, or

redirection of the incident light source. Adaptive optical systems typically employ amplitude modulation

for image stabilization or tracking, and phase modulation to compensate for higher order aberrations.
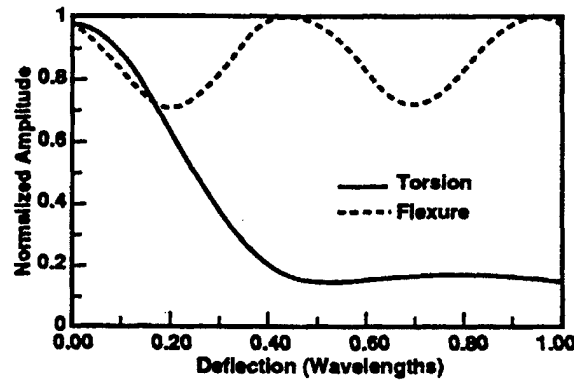
(a) Amplitude response
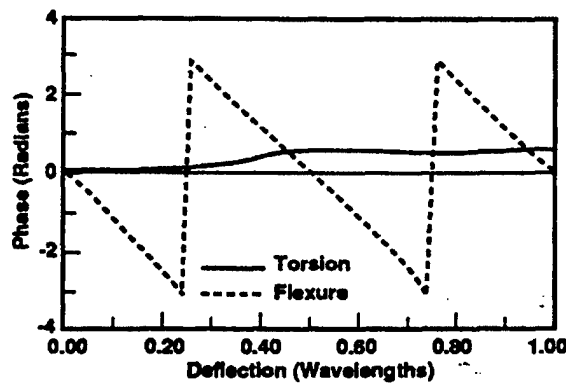
(b) Phase response

Figure 1-1. Micromirror optical modulation characteristics [6].

Figure 1-1 compares the optical modulation characteristics of two different types of micromirror

arrays [6]. The amplitude and phase modulation for theoretical arrays of symmetric torsion mirrors and

piston only elements with the same 80% active area are plotted as a function of mirror deflection in units of

wavelength. The torsion mirror array exhibits almost 80% amplitude modulation with virtually no phase

modulation. The piston-only (flexure supported) array provides 4π radians of phase shift for one

wavelength (2π radians) of deflection. The 25% amplitude modulation of the piston array is due to

constructive and destructive interference of light reflecting off the active mirror elements and the inactive

background. Cantilever micromirror devices exhibit optical modulation characteristics somewhere between torsion and piston devices [6]. Continuous facesheet mirrors can be considered as the limiting case of a piston only array, i.e. a phase only light modulator. As individual piston elements and the inactive region between elements become infinitesimally small, the piston element array becomes a continuous facesheet mirror.
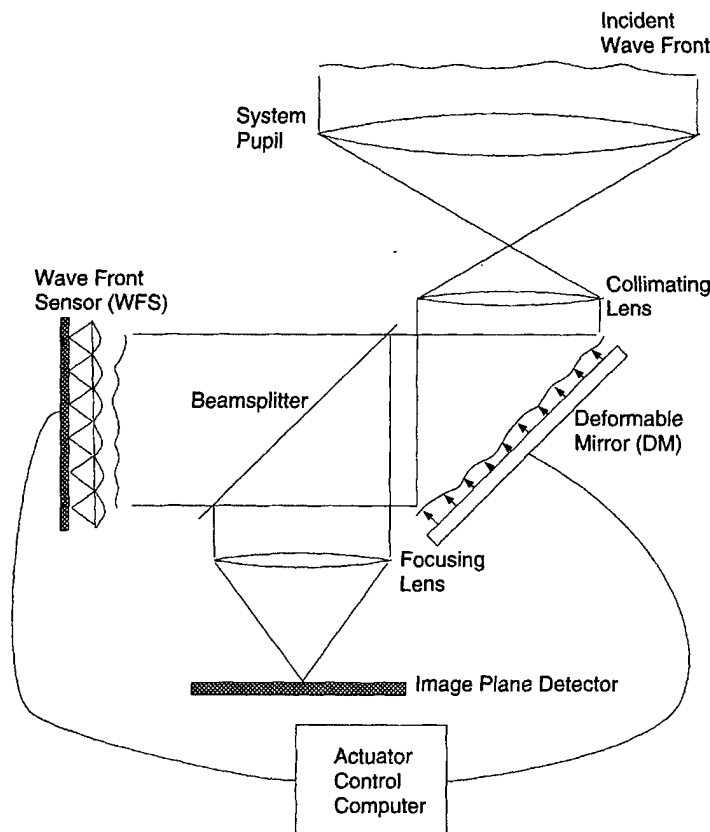
Figure 1-2. Simplified adaptive optic system [9].

1.3.2   System Requirements for Optical Aberration Correction

Overall system performance goals drive the design of micromachined deformable mirrors for adaptive optical systems. Previous work characterizing the contribution of particular deformable mirror designs to overall system performance is directly applicable to the microfabricated deformable mirror case [1,7,8]. The generic adaptive optic system of Figure 1-2 serves as a context for micromachined deformable mirrors [9]. This simplified diagram shows how the deformable mirror is coupled optically and electrically to

other system components for closed loop adaptive optics. The optical beam reflects off the deformable mirror on its way to the wavefront sensor. The wavefront sensor detects the phase perturbation of the incoming signal. Control electronics compute the required phase conjugation signals and translate those signals into mirror drive signals. The total uncorrected phase error of this system is given by

$$\sigma_{Total}^2 = \sigma_{Noise}^2 + \sigma_{Sampling}^2 + \sigma_{Fitting}^2 + \sigma_{Control}^2 \quad \left(\text{rad}^2\right)$$ (1-1)

where σ_{Noise}^2 is the detector noise of the wavefront sensor, $\sigma_{Sampling}^2$ is the uncorrectable distortion of the sampling process (which is generally small compared to other terms), $\sigma_{Control}^2$ is the control loop time delay error, and $\sigma_{Fitting}^2$ is the fitting error of the deformable mirror [1,10]. For atmospheric turbulence with a Kolmogorov spectrum, the deformable mirror's direct error term $\sigma_{Fitting}^2$ is given by

$$\sigma_{Fitting}^2 = \kappa_f \left(\frac{d}{r_o}\right)^{5/3} \quad \left(\text{rad}^2\right)$$ (1-2)

where d is the interactuator spacing in the system aperture, r_o is a measure of the atmospheric distortion, and κ_f is a fitting parameter [11]. The fitting parameter is a complicated function of deformable mirror influence functions, actuator geometry, coupling, and mirror-wavefront registration [7]. Computed values of κ_f range widely, from 1.32 for a square array of piston only segments [10], to 0.23 for axial actuators which impart a Gaussian shape to a continuous mirror surface [1]. The interactuator spacing, d, is usually computed as the average over the aperture area to account for nonuniform spacing in all directions,

$$d = \frac{D}{\sqrt{\frac{4N_a}{\pi}}} \, ,$$ (1-3)

where D is the aperture diameter, and N_a is the number of actuators [1]. Substituting Equation (1-3) into Equation (1-2) shows that the fitting error is proportional to $N_a^{-5/6}$, thus the more actuators or mirror segments, the lower the fitting error term. Two other approximations are useful in relating deformable mirror requirements to the atmospheric turbulence problem. The first relates the commonly used imaging performance metric Strehl ratio to the fitting error. Strehl ratio is defined as the ratio of the on-axis

1-7

intensity of an aberrated (or aberration corrected) optical beam to the on-axis intensity of an unaberrated (or diffraction limited) beam. If considering only the spatial effects of the deformable mirror, the Strehl ratio and fitting error are approximately related by, $S = \exp{(\sigma^2_{Fitting})}$ [1]. The atmospheric coherence length is given as $r_0 = 1.68(C_n^2 z k^2)^{-3/5}$ [1]. Substituting these approximations and Equation (1-3) into Equation (1-2) and solving for the number of actuators required yields,

$$N_a = \left[\frac{\kappa_f}{2.9} \frac{k^2 z C_n^2 D^{5/3}}{\ln(1/S)} \right]^{6/5}, \qquad (1\text{-}4)$$

where k is the wavenumber $(2\pi/\lambda)$, z is the altitude or propagating distance, and C_n^2 is the refractive index structure constant [1]. Values for C_n^2 are by no means constant, but together with z define the aberrating environment.

In addition to the direct contribution of the fitting error term to overall system error, the deformable mirror design also impacts both the noise σ^2_{Noise}, and control $\sigma^2_{Control}$, error terms. For a given control loop bandwidth, reduced deformable mirror reflectivity decreases the signal-to-noise ratio of the wavefront sensor thereby increasing the noise error. Likewise, for a given wavefront sensor signal-to-noise ratio, poor deformable mirror reflectivity requires reduction of the control loop bandwidth to allow longer sensor integration time, increasing the control error term. The system control loop bandwidth also defines the maximum operating frequency required for individual corrector elements. For atmospheric aberations current wavefront sensors limit the control loop bandwidth to about 1 kHz. As might be expected intuitively, continuous face sheet mirrors with axially operated actuators have been shown to be among the most efficient deformable mirror geometries [8].

The required stroke for actuators driving a continuous facesheet mirror is defined by the range of wavefront error across the system aperture. The required phase excursion for atmospheric adaptive optics is approximately [1],

$$(\Delta\phi)_{\max} = 0.57 k \sqrt{z C_n^2 D^{5/3}} . \qquad (1\text{-}5)$$

Equation (1-5) again shows the dependence of a deformable mirror requirement on operating wavelength, system aperture, and the nature of the atmospheric turbulence. For segmented deformable mirrors the stroke of each element need only be plus or minus $\lambda/2$ for narrowband operation [12].

One example computation, based on moderate atmospheric turbulence, near infrared operation (λ=1.0 μm), a 1 meter diameter telescope aperture, and a corrected Strehl ratio of 0.2, results in a requirement for 400 actuators with a 2 μm stroke for a continuous facesheet deformable mirror [13]. The 400 actuator (mirror) requirement is no problem for microfabricated devices, but packaging, wire bonding, and testing such a system is expensive in both labor and test equipment. The required 2 μm stroke is difficult to obtain in foundry fabricated electrostatic devices. Rather than allow these particular application driven requirements to impede research progress, prototype deformable mirror systems were designed to exploit the capabilities of the foundry processes and test equipment. The lessons learned are applicable to larger systems meeting the requirements for atmospheric aberration correction in large apertures. The successful prototype systems might serve well for atmospheric aberration correction if only a few requirements are changed. For example, a 128 element square piston micromirror array used for aberration correction in an amateur telescope system with 12 inch (30.5 cm) aperture, and poor seeing (r_0=5 cm), yields a fitting error of 0.385, corresponding to a corrected Strehl ratio of ~0.68. This same example system might be used for tactical ground to satellite laser communication. Likewise, the prototype deformable mirror systems produced in this research may be useful for some of the other applications mentioned for which the requirements are not as well defined. Reduced actuator spacing and the corresponding increase in image resolution represents the key performance advantage possible with micromachined deformable mirrors. Other advantages include reduced system size, weight, power consumption, and cost. These non-performance factors become substantially more important for adaptive optic systems that are not ground based, and for systems employing multiple deformable mirrors.

1.4 Research Accomplished

A number of practical foundry microfabricated deformable mirror systems have been designed, fabricated, tested, and demonstrated in an adaptive optics testbed as part of this research effort. Successful designs include high yield electrostatic piston micromirror arrays with fill factors of over 70% in the MUMPs foundry process, and 95% in the SUMMiT foundry process. Microfabricated continuous facesheet designs were also produced in both processes. Use of a refractive lenslet array to improve the fill-factor of a segmented MEMS deformable mirror was experimentally demonstrated for aberration correction and beam steering applications. An analytical model was developed to explain the behavior of the hybrid lenslet/MEM-DM correcting element.

A new type of piston micromirror (or actuator) employing direct digital deflection control was devised and tested. This new type of phase modulating element further reduces adaptive optics system cost by eliminating digital-to-analog converters in the deformable mirror control system. The simplified control circuitry of the digital deflection scheme also paves the way for a fully integrated deformable mirror system on a chip.

Micromirror surface figure was extensively studied. Metal stress induced mirror curvature was modeled using commercially available MEMS computer aided design software. The impact of stress-induced mirror curvature and print-through topography on the optical performance of micromirror arrays was experimentally verified. Post-foundry metallization techniques were developed to preserve and even improve the flatness of micromirror elements.

The first two-dimensional thermally actuated piston micromirror arrays were designed and tested. Prior to this work, pure piston motion had not been demonstrated with thermal devices. Electro-thermal models were developed to analyze device behavior. MEMS computer aided design tool developers have subsequently used one of the author's thermal piston micromirror designs to test and demonstrate new analysis software [14].

In addition to microfabricated deformable mirrors, a number of other MEMS devices were developed. Beam tracking or steering mirrors for image stabilization are an important part of many

adaptive optics systems. Several tip-tilt mirror systems using novel methods to lift the steering mirror off the substrate were designed to demonstrate the capability of MEMS for this function. Other devices of general MEMS interest include vacuum gauges, test structures, switches, and mechanical drive systems.

Much of the research contained in this dissertation has already been published in the technical literature. The scholarly publications to which the author has contributed are listed in Table 1-1, for reference.

Table 1-1. List of Technical Publications by the Author

M. C. Roggemann, V. M. Bright, B. M. Welsh, S. R. Hick, P. C. Roberts, W. D. Cowan, and J. H. Comtois, "Use of micro-electro-mechanical deformable mirrors to control aberrations in optical systems: theoretical and experimental results," *Opt. Eng.*, **36**(5), 1326-1338, (May 1997).

M. C. Roggemann, V. M. Bright, B. M. Welsh, S. R. Hick, P. C. Roberts, W. D. Cowan, and J. H. Comtois, "Experimental demonstration of using micro-electro-mechanical deformable mirrors to control optical aberrations," in *Adaptive Optics and Applications, Proc. SPIE,* **3126**, 174-184, (July 1997).

W. D. Cowan, V. M. Bright, A. A. Elvin, and D. A. Koester, "Modeling of stress-induced curvature in surface-micromachined devices," in *Microlithography and Metrology in Micromachining III, Proc. SPIE* **3225**, 56-67, (September 1997).

W. D. Cowan and V. M. Bright, "Thermally actuated piston micromirror arrays," in *Optical Scanning Systems: Design and Applications, Proc. SPIE* **3131**, 260-271, (July 1997).

W. D. Cowan, V. M. Bright, and G. C. Dalton II, "Measuring the frequency response of surface-micromachined resonators," in *Microelectronic Structures and MEMS for Optical Processing III, Proc. SPIE* **3225**, 32-43, (September 1997).

W. D. Cowan and V. M. Bright, "Vertical thermal actuators for micro-opto-electro-mechanical systems," in *Optical Scanning Systems: Design and Applications, Proc. SPIE* **3131**, 260-271 (July 1997).

J. Butler, V. M. Bright, and W. D. Cowan, "SPICE modeling of polysilicon thermal actuators," in *Micromachined Devices and Components, Proc. SPIE* **3224**, 284-293, (September 1997).

W. D. Cowan, V. M. Bright, M. K. Lee, J. H. Comtois, and M. A. Michalicek, "Design and testing of polysilicon surface-micromachined piston micromirror arrays," to be published in *Spatial Light Modulators, Proc. SPIE* **3292** (1998).

W. D. Cowan, V. M. Bright, M. K. Lee, and B. M. Welsh, "Evaluation of microfabricated deformable mirror systems", to be published in *Adaptive Optical System Technologies, Proc. SPIE* **3353** (1998).

M. C. Roggemann, V. M. Bright, B. M. Welsh, W. D. Cowan, and M. Lee, "Micro-electro-mechanical deformable mirrors for aberration control in optical systems", submitted to *Quantum Optics and Electronics*, December, 1997. Currently in review.

M. K. Lee, W. D. Cowan, B. M. Welsh, V. M. Bright, and M. C. Roggemann, "Aberration correction results using a segmented micro-electro-mechanical deformable mirror and refractive lenslet array", to be published in *Optics Letters*, 15 April 1998.

W. D. Cowan, M. K. Lee, B. M. Welsh, V. M. Bright, and M. C. Roggemann, "Optical phase modulation using a refractive lenslet array and micro-electro-mechanical deformable mirror", submitted to *Optical Engineering* in January 1998. Currently in review.

J. T. Butler, V. M. Bright, and W. D. Cowan, "Average power control and positioning of polysilicon thermal actuators", submitted to *Sensors and Actuators* in September 1997. Currently in review.

V. M. Bright, J. T. Butler, W. D. Cowan, D. M. Burns, and J. R. Reid, "Automated assembly of micro-electro-mechanical systems", submitted for publication in *The International Journal of Advanced Manufacturing Systems* (special issue on Micro/Miniature Manufacturing).

J. H. Comtois, M. A. Michalicek, N. Clark, and W. D. Cowan, "MOEMS for adaptive optics", abstract submitted for IEEE/LEOS Summer Topical Meeting on Optical MEMS, 20-22 July 1998, Monterrey, California.

C. Ghaddar, J. von Kuijk, J. Gilbert, W. D. Cowan, J. T Butler, and V. M. Bright, "Simulation and design of electro-thermally actuated MEMS devices, a case study: the AFIT piston micromirror", abstract submitted for the Winter Annual Meeting of ASME, November 15-20, 1998, Anaheim Convention Center & Hilton, Anaheim, California.

1.5 Dissertation Organization

The remainder of this dissertation is organized into 9 chapters. Chapter 2 provides a review of micromirror fabrication technology, including a general description of MEMS fabrication techniques, and detailed descriptions of the surface micromachining foundry processes. The planarization of MEMS devices, which significantly impacts microfabricated deformable mirror design, is examined in detail. Selected micromirror designs illustrate different mirror types and fabrication techniques. The mirror designs presented in Chapter 2 are representative of the state-of-the-art when this research began. Chapter 3 covers

electrostatic piston micromirror array design and testing, starting with the basic operating principle, and concluding with experimental optical aberration correction results. Development of the digital deflection micromirror is also included in Chapter 3. Chapter 4 is a detailed study of micromirror surface figure. The use of refractive lenslets to improve the optical fill-factor of a MEMS deformable mirror is presented in Chapter 5, including the analytical model and experimental aberration correction and beam steering results. Development of thermal piston micromirror arrays is described in Chapter 6. Beam steering or tracking mirrors designed and tested by the author are described in Chapter 7. Microfabricated continuous facesheet mirror designs fabricated in two foundry processes are presented in Chapter 8. Evaluation of these designs illustrates the limitations of the existing foundry processes. Chapter 9 briefly describes other MEMS designed by the author that are of general interest. Conclusions and recommendations for future research are offered in Chapter 10.

References

1   R. K. Tyson, *Principles of Adaptive Optics*, San Diego: Academic Press, 1991.

2   H. W. Babcock, "The possibility of compensating astronomical seeing", *Pub. Astron. Soc. Pac.*, 65(386), pp. 229-236, October 1953.

3   G. Rousset and others, "First diffraction limited astronomical images with adaptive optics", *Astron. And Astrophys.*, vol. 230, pp. 29-32, 1990.

4   R. L. Clark, Adaptive optics: aims for earthly applications", *Photonics Spectra*, pp. 100-106, April 1997.

5   G. Vdovin, S. Middlehoek, and P. Sarro, "Technology and applications of micromachined silicon adaptive mirrors", *Opt. Eng.*, vol. 36, no. 5, pp. 1382-1390, May 1997.

6   L. J. Hornbeck, "Deformable-mirror spatial light modulators", *SPIE Critical Review Series*, vol. 1150, pp. 86-102, August 1989.

7   R. K. Tyson, "Theoretical studies of system performance and adaptive optics design parameters", *SPIE Adaptive Optics and Optical Structures*, vol. 1271, pp. 51-62, 1990.

8   M. A. Ealey and J. A. Wellman, "Deformable mirrors: design fundamentals, key performance specifications, and parametric trades", *SPIE Active and Adaptive Optical Components*, vol. 1543, pp. 36-51, 1991.

9   M. C. Roggeman and B. Welsh, *Imaging Through Turbulence*, Boca Raton: CRC Press, 1996.

10   D. C. Johnston, "Increasing the corrected field of view of an adaptive optical telescope", *Ph.D. Dissertation*, Air Force Institute of Technology, Wright-Patterson AFB, OH, AFIT/DS/ENG/92-06, December 1992.

11   R. Hudgin, "Wave-front compensation error due to finite corrector-element size", *J. Opt. Soc. Am.,* vol. 67, no. 3, pp. 393-395, March 1977.

12   B. Hulburd and D. Sandler, "Segmented mirrors for atmospheric compensation", *Opt. Eng.*, vol. 29, no. 10, pp. 1186-1190, October 1990.

13   R. Mali, T. G. Bifano, N. Vandelli, and M. Horenstein, "Development of microelectromechanical deformable mirrors for phase modulation of light", *Opt. Eng.*, vol. 36, no. 2, pp. 542-548, February 1997.

14   MEMCAD, Microcosm Technologies Inc., Cambridge, MA 02142

2. Micromirror Fabrication Technology

2.1 Chapter Overview

This chapter briefly reviews micromirror fabrication technology. The more common fabrication processes used to construct micro-electro-mechanical systems are divided into three categories; surface micro-machining, bulk micromachining, and special purpose techniques. The two surface micromachining processes extensively used to fabricate devices for this research are detailed in Section 2.2. Bulk micromachining techniques are described in Section 2.3.   Some special purpose micromachining techniques are described in Section 2.4. Perhaps the most important problem to be addressed in the fabrication of micromirror systems is that of making optically flat mirror surfaces. Section 2.5 reviews planarization approaches and the applicability of each technique to micromirror fabrication. In Section 2.6 selected micromirror designs illustrating different mirror types and fabrication techniques are presented.

2.2 Surface Micromachining

In surface micromachining the substrate, typically a silicon wafer, serves as the foundation on which structural and sacrificial material layers are selectively deposited to fabricate electro-mechanical structures. Currently, surface micromachining is the most readily available fabrication process from outside vendors. The two surface micromachining foundry processes used to fabricate devices for this research are presented in the following subsections.

2.2.1 Multi-User MEMS Processes (MUMPs)

The DARPA sponsored Multi-User MEMS Processes (MUMPs) developed by Microelectronics Center of North Carolina (MCNC) represents a typical polysilicon surface micromachining process [1]. Most of the devices presented in this dissertation were fabricated in the MUMPs. The starting substrate for MUMPs is a low resistivity (0.5 Ω-cm) n-doped silicon wafer with <100> crystal orientation. Before addition of any

surface layers, the wafer surface is heavily doped with phosphorus (using POCl$_3$) in a standard diffusion furnace. The primary purpose of the highly doped surface is to prevent charge buildup during operation of electrostatic devices. Phosphorus is also an n-type dopant so no junction is formed but the heavy doping ($\approx 10^{22}$ atoms/cm^3) is sufficient to affect some silicon etchants. The first surface layer is a low pressure chemical vapor deposition (LPCVD) of silicon nitride nominally 600 nm thick. Silicon nitride is a dielectric material which is very tough mechanically and chemically. Immediately following the nitride deposition, a 0.5 μm thick polysilicon layer (Poly0) is deposited. The Poly0 is primarily a wiring layer and is not intended to be released. The Poly0 layer is patterned using standard photolithography techniques and Reactive Ion Etching (RIE). Over the patterned Poly0 layer a 2.0 μm thick layer of phosphosilicate glass (Oxide1) is deposited by LPCVD. Two different photolithographic steps are applied to the Oxide1 layer. First, a DIMPLE mask is used to define and etch 0.75 μm deep holes in the oxide. The dimples serve the necessary function of holding fully released polysilicon structures off the substrate to mitigate stiction effects. Dimples also provide a stop mechanism for fully deflected parallel-plate electrostatic devices, holding the upper electrode of a vertical actuator 0.25 μm above the bottom electrode. A second photolithographic step provides anchor holes (ANCHOR1) through the Oxide1 layer for attaching Poly1 structures to either the nitride or Poly0 layers. After removing the photoresist for the ANCHOR1 patterning, the entire wafer surface is blanketed with a 2.0 μm thick structural polysilicon layer (Poly1). The Poly1 layer is photolithograpically patterned and excess material removed by RIE. Following the patterning of Poly1, the wafer is blanketed with a second sacrificial oxide layer (Oxide2), nominally 0.75 μm thick. Two photolithographic steps and separate etches also define holes in the Oxide2 layer. Vias between the two mechanical layers Poly1 and Poly2 are defined by the P1P2Via etch. Anchoring of Poly2 structures to the nitride or Poly0 layers is accomplished using the ANCHOR2 etch which is sufficient to cut through the combined 2.75 μm thickness of Oxide1 and Oxide2. A second mechanical polysilicon layer (Poly2) 1.5 μm thick is deposited and patterned in the same manner as the Poly1 layer. A high temperature (1050 °C) anneal relieves stress and drives phosphorus from the oxide layers into the polysilicon to

increase conductivity. An eighth mask defines a 0.5 µm thick gold metallization with ≈100 nm chrome adhesion layer. Metal can be reliably deposited only on top of the Poly2 layer.

Through the metallization step, the MUMPs fabrication sequence is remarkably similar to standard integrated circuit fabrication with the notable exceptions of layer thicknesses and high temperature anneals. A release etch which removes the sacrificial oxide layers freeing the mechanical polysilicon layers makes this a MEMS process. MUMPs devices are normally shipped before the release etch covered with a protective layer of photoresist. Typical release etches consist of a 2-4 minute bath in room temperature hydrofluoric (49%) acid followed by rinses in deionized water, and 2-propanol. The 2-propanol rinse displaces water and its low surface tension prevents stiction problems.

Because MCNC does not enforce "design rules", MUMPs devices are limited only by the process technology and creativity of the designer. The key concepts to fully exploiting the MUMPs process are recognition of the deposition conformality and an understanding of reactive ion etching. Previous AFIT researchers developed several techniques which expand the design space of MUMPs considerably [2]. Among these techniques are bossing, stacked polysilicon layers, use of Poly1 formers, low resistance wiring, and a means of breaching the silicon nitride layer.

The RIEs used in the MUMPs process are material specific. Overetches are employed to prevent "stringers" - literally strings of material left in the bottom corners of etched features. Typical MUMPs overetches are 100% for Poly1, 50% for Oxide2, and 175% for Poly2. A releasable polysilicon layer nominally 3.5 µm thick is achieved by exposing an area of Poly1 with P1P2Via, which is then covered by Poly2. The resulting thick polysilicon layer can then be patterned with the 175% Poly2 overetch. An even thicker plate structure may be formed by selectively trapping the 0.75 µm Oxide2 layer between the Poly1 and Poly2 layers. If completely sealed by a ring of P1P2Via, the "trapped glass" is not exposed to the release etch.

Bossing or corrugation selectively strengthens (or weakens) a feature in the polysilicon structural layers. Low resistance wiring employs a stacked structure of Poly0, anchored Poly2, and metal. Where the increased resistance of a short Poly0 segment is tolerable, wiring crossovers are possible. Breaching

the nitride layer provides electrical contact to the substrate. An ANCHOR1 region which is not covered by Poly1 exposes the nitride layer to two RIEs. The ANCHOR1 etch partially cuts the nitride and the 100% Poly1 removal overetch completes the cut. The substrate can be used as a common bottom electrode for electrostatic devices or as a common electrical connection.

2.2.2 Sandia Ultra-planar Multi-level MEMS Technology (SUMMiT)

The Sandia Ultra-planar Multi-level MEMS Technology (SUMMiT) polysilicon surface micromachining process developed by Sandia National Laboratory is similar in many respects to MUMPs. The critical difference is the addition of a chemical mechanical polishing (CMP) step just prior to deposition of the final polysilicon layer [3,4,5].

Sandia's SUMMiT process begins with 6 inch n-doped silicon (100-cut) wafers with a starting resistivity of 2-20 Ω-cm. An oxide layer 0.6 μm thick and a 0.8 μm silicon nitride layer form the electrical isolation layer. The non-releasable polysilicon (MMPOLY0) layer is 0.3 μm thick and is used like the MUMPs Poly0 layer for address electrodes, ground planes, and wiring. The first sacrificial oxide layer (SACOX1) is 2 μm thick. Unless intentionally separated by the thin sacrificial oxide (SACOX2, 0.5 μm thick) the first releasable polysilicon layer (MMPOLY1, 1.0 μm thick) and second releasable polysilicon layer (MMPOLY2, 1.5 μm thick) form a single polysilicon layer that is 2.5 μm thick. The combined MMPOLY1 and MMPOLY2 structural layer is comparable to the MUMPs Poly1 layer. Prior to deposition of the final structural layer, wafers in the SUMMiT process are planarized by chemical mechanical polishing (CMP). A third sacrificial oxide layer (SACOX3) approximately 5.6 μm thick is deposited, then polished back to a final thickness of 1.5 to 2 μm above the highest polysilicon structures. At this point in the process SUMMiT wafers are nominally as flat as the CMP process will produce. After patterning the planarized SACOX3, the final polysilicon structural layer (MMPOLY3, 2.0 μm thick) is deposited. Print-through of all the underlying topography can be eliminated by the polishing process. The only perturbations required in a MMPOLY3 micromirror surface are release etch access holes and attachments to the underlying actuator structure or substrate. Because the sacrificial oxide used in the SUMMiT process is very hard (resistant to etching), an etch hole spacing of 25 μm is recommended. No metal is

offered in the SUMMiT process, so provisions for post foundry metallization must be considered during device design. Design and testing of SUMMiT segmented and continuous facesheet micromirrors are presented in Chapters 4 and 8, respectively.

2.2.3 Actuation Mechanisms

Presently the only actuation mechanisms available for MEMS designers using foundry fabrication processes are electrostatic and thermal. Specialized processes employing magnetic, piezo-electric and magneto-strictive materials, and shape memory alloys have been developed [6, 7], but are unlikely to be available in commercial foundry processes in the near term.

The general characteristics of electrostatic and thermal actuators are complementary. Electrostatic actuators rely on Coulombic attraction, a relatively weak force, proportional to magnitude of the charge difference between two conductors and inversely proportional to the square of the distance between them. Thermal actuators harness the much stronger atomic forces of thermal expansion. Power dissipation of electrostatic actuators is negligible. Thermal actuator designs which employ ohmic heating dissipate significant power. The maximum operating frequency of electrostatic devices is limited by the mechanical structure. The ability of the device structure to dissipate heat limits the maximum operating frequency of thermally actuated devices. Electrostatic and thermal actuator designs with horizontal (parallel to wafer surface) or vertical (perpendicular to wafer surface) motion are readily fabricated in foundry processes. Because optical applications typically require high speed and low force, most micromirror systems employ electrostatic actuation.

2.3 Bulk Micromachining

Unlike surface micromachining processes which evolved from standard integrated circuit fabrication techniques, bulk micromachining processes were specifically developed for MEMS. The most common structural material for bulk micromachining is single crystal silicon. The anisotropic structure of the silicon crystal causes some etchants to exhibit an orientation dependent etch rate. Anisotropic etching is the workhorse of bulk micromachining processes.

Single crystal silicon has a diamond lattice structure which belongs to the cubic crystal family [8]. Miller indices provide a convenient means of identifying crystal planes. The most studied anisotropic silicon etchants involve the low order index (<100>,<110>, and <111>) crystal planes. Generally the <111> crystal planes exhibit the slowest etch rate while the <100> and <110> etch fastest. It is the selectivity of etch rates in differing crystal directions that makes bulk micromachining of silicon useful as a MEMS process. While not precisely understood, silicon's etch orientation dependence is a function of the areal density of atoms, the energy required to remove atoms from the etch plane, and geometric screening effects due to the three dimensional crystal structure.

Popular anisotropic silicon etchants include potassium hydroxide (KOH), ethylene diamine pyrocatechol (EDP), and tetramethyl ammonium hydroxide (TMAH). Each of these etchants (and others that have been studied) has its advantages and disadvantages. Etch selectivity is expressed as a ratio of desired etching to undesired etching. In addition to the etch selectivity of silicon crystal planes, the selectivity over masking materials and metallizations must be considered. There is no "ideal" anisotropic etchant for all bulk micromachining applications. Some characteristics of the etchants listed above are discussed below.

KOH preferentially etches <100> and <110> silicon crystal planes over <111> crystal planes with a selectivity of up to 500:1. But the selectivity of KOH for SiO_2 is less than 500 so masking for long etches typically requires a silicon nitride layer. Etch rates for 20% KOH at 100 °C are 233 μm/hr for <100> silicon and 1.1 μm/hr for silicon dioxide [8]. EDP exhibits a silicon selectivity of 10,000 over SiO_2 but is less selective to crystal orientation (about 50:1). It is also much slower: type-S EDP etches <100> silicon at 36 μm/hr at 100 °C [8]. EDP is compatible with some metals including gold but attacks aluminum. TMAH is comparable to EDP in selectivity over oxide and nitride layers with a slightly higher <100> silicon etch rate of up to 50 μm/hr at 80 °C [9]. Controlling TMAH etch solution pH by adding dissolved silicon or acid yields improved selectivity over aluminum metallizations and reduces hillock formation (uneven etching) [9, 10].

2.4 Special Purpose Micromachining Techniques

Many special purpose micromachining techniques have been developed for particular applications. The techniques discussed below were selected for inclusion based on their relevance to micromirror devices presented in subsequent sections.

Because metal plating rates are typically much greater than other film deposition methods, plating methods make fabrication of tall (up to 100s of microns) structures practical. The LIGA label derived from the German "LIthographie Galvanoformung und Abformung" is frequently applied to these plating processes. In the LIGA process synchrotron x-ray radiation is used to expose thick resist layers applied to a plating base. Removal of the exposed resist forms a plating mold. Similar "LIGA-like" processes use thicker than normal UV sensitive photoresists to avoid the need for an x-ray source, but still use plating to deposit the structural material [11,12].

Bonding techniques permit the fabrication of more complex MEMS by increasing the number of available machined layers. The principle approaches are silicon fusion bonding, anodic bonding, and eutectic bonding. Low temperature glasses, proprietary frits, and polymers are also commonly used but will not be discussed here.

Silicon fusion bonding begins with the mating of two highly polished and thoroughly clean wafer surfaces. Once mated, Van der Waals forces hold the workpeices in place. Through subsequent application of heat and pressure the mating surfaces are fused together with no visible interface. The high temperature (≈ 1000 °C) of fusion bonding precludes its use if metals or active devices are present.

Anodic bonding provides a means of joining silicon to sodium-rich glass. Silicon wafers can also be joined via a thin intermediate glass layer. The exact bond mechanism is not well understood but yields bonds which exceed the individual material strengths. The anodic bonding process is straightforward. After mating the glass and silicon surfaces, the assembly is heated to 350-450 °C to mobilize the sodium ions. Application of a 400-1000 Volt DC bias across the interface induces an electrostatic pressure of several atmospheres. When the monitored current across the interface drops to about 10% of its starting

value bonding is complete. The high electrostatic pressure makes anodic bonding more tolerant of imperfect interface planarity than fusion bonding.

Reactive metals can also be used for bonding [8]. Gold is commonly used for eutectic bonding of silicon. A 97.1% Au, 2.85% Si eutectic system forms at 363 °C. When sandwiched between silicon or polysilicon structures and heated to the eutectic temperature, gold layers 0.7 to 1.0 μm thick form a bond with shear strengths of about 0.39 GPa, and tensile strengths of 5.5 GPa [13, 14]. Presence of native silicon oxide can inhibit eutectic bonding. Two methods of handling the native oxide problem are commonly employed. Either the native oxide is removed by a short etch in buffered hydrofluoric acid, or the formation of native oxide is prevented by coating both mating surfaces with a layer of gold. The presence of a thin ($\approx$100 nm) chromium adhesion layer does not inhibit formation of the eutectic bond. Its apparent compatibility with MUMPs surface micromachined die suggests investigation of Au/Si eutectic bonding as a means of fabricating more complex MEMS from foundry fabricated parts.

For bulk micromachined structures not requiring the crystallographic selectivity afforded by anisotropic etchants, isotropic silicon etchants can be considered. Two simple isotropic etchants are considered here. The acidic etch system of hydrofluoric, nitric, and acetic acids ($HF:HNO_3:CH_3COOH$) is an isotropic silicon etchant with characteristics dependent on the mixture ratio. Doping selectivity is obtained with a 1:3:8 volume ratio respectively, which exhibits selectivity of 150:1 for highly doped (p^+ or $n^+ > 5 \times 10^{18}$ cm^{-3}) silicon over low doped silicon ($<10^{17}$ cm^{-3}), with an etch rate of up to 200 μm/hr. A 1:2:1 mixture yields etch rates of up to 250 μm/hr with no doping selectivity. As might be expected from the presence of HF, the selectivity over oxide is not especially good. SiO_2 etches at about 2 μm/hr so gold or nitride masks are required for long etches.[8]

Xenon difluoride is a gas phase isotropic silicon etchant recently "rediscovered" by the MEMS community. Originally synthesized in 1962 [15], XeF_2 was shown useful for silicon etching by IBM researchers in 1978 [16]. IBM reported an etch rate linearly dependent on $P(XeF_2)$ of 0.7 μm/minute for $P(XeF_2) < 1.4$mT, with "no observable etching of SiO_2, Si_3N_4, and or SiC." Recent MEMS researchers have demonstrated the potential of XeF_2 for bulk micromachining applications by etching at pressures up to

2500 mT [17,18]. XeF_2 offers the one-two punch of high etch rate and exceptional selectivity for silicon over other common microfabrication materials. Etch rates of over 20 μm/minute for square etch windows up to 4 mm on a side have been reported. XeF_2 selectivity exceeds 1000:1 for silicon dioxide, photoresists such as OCG825 and AZ5214, polyimides, aluminum, copper, gold, titanium-nickel alloy, and acrylic.

2.5 Planarization of MEMS Mirrors

The key requirement for microfabrication of deformable mirrors is the ability to deposit the nominally flat facesheet (either segmented or continuous) on an array of actuators. With this application in mind, the following section examines several approaches to planarization through review of recent technical literature. None of the planarization references are targeted specifically at micromirror fabrication. The industry drives for planarization technology are improved photolithography, and fabrication of special semiconductor device geometries such as isolation trenches. The complexity and equipment required for the different planarization techniques presented varies widely, as does the performance. Because planarization techniques offer semiconductor manufacturers a competitive edge in fabrication of denser integrated circuits and special devices, details are often omitted from the technical literature. The following sections begin with a discussion of common terms and definitions and a relationship of those terms to the intended micromirror device application. The planarization approaches examined are categorized as: chemical-mechanical polishing, spin-on films, deposition and etch back, and sacrificial wafer bonding. Application of each type of approach to the intended application is discussed.

2.5.1 Planarization Basics

The principle industry driver of planarization research is photolithography. The resolution of conventional photolithographic systems is determined by the numerical aperture (*NA*) and wavelength (λ) of the exposure system. The resolvable line width and depth of focus are estimated by the Raleigh equations [19]

$$LW = k_1 \lambda \,/\, NA$$
$$DOF = k_2 \lambda \,/\, (NA)^2$$

(2-1)

The empirical factors k_1 and k_2 depend on the resist system and type of features being imaged. For this discussion we will use the values of $k_1=0.7$ and $k_2=0.6$; cited as reasonable for a multilayer resist system with no feature dependence and a tolerable exposure variation of $\pm 10\%$. For a system with NA=0.5, computed values for LW and DOF are listed in Table 2-1 for three exposure wavelengths [19].

Table 2-1. Computed Values for LW and DOF for Different Wavelengths [19].

λ (nm)	LW(μm)	DOF(μm)
360 (*i*-line)	0.50	0.88
248	0.35	0.59
193	0.25	0.46

The practical microlithographic DOF is defined as the total defocus allowable for a desired tolerance on the minimum feature size. Device topography, resist thickness, wafer flatness, focus errors, and tilt errors all reduce the practical DOF. Thus we can see how photolithographic requirements, as device geometries decrease, are driving the semiconductor industry toward planarization techniques which are also consistent with the fabrication of high quality optical micro-mirrors.

The commonly used figure-of-merit for film planarization processes is Degree Of Planarization (DOP). Distinction is made between local planarization (smoothing of a feature < 10 μm) and global planarization (non-planarity over distances > 10 μm). Local DOP is defined as $DOP_{LOC} = 1 - h_f / h_o$, where h_f is the height of the planarized feature above the surrounding film thickness and h_o is the height of the feature before planarization. Figure 2-1 (a) shows how the local DOP decreases from a maximum of nearly 100% for narrow lines to 0% for features of width w_{lim}, called the planarization limit. Figure 2-1(b) indicates how the DOP decreases with increasing feature height. As shown in Figure 2-1(c) the DOP decreases with feature density until at the spacing limit s_{lim} the DOP equals the DOP of an isolated line. Good mirror surfaces require both local (smoothness) and global (flatness) planarity. In some cases it may be possible to use the actuation mechanism to improve global planarity (flatten) a deformable micromirror, but local planarity (or topography) can not be corrected.

For the baseline MUMPs process we can consider two cases depending on whether the process is modified to include planarization prior to deposition of the Poly2 layer, or after complete processing. If

planarized prior to the Oxide2 etch and Poly2 deposition, the maximum feature step height is 4.75 μm (Poly0 + Oxide1 + Poly1). After complete MUMPs processing, the maximum feature step height is about 7 μm (Poly0 + Oxide1 + Poly1 + Oxide2 + Poly2). Actual mirror/actuator designs are unlikely to have such extreme topographies so this represents a worst case scenario. Assuming a desired post planarization step height of $\lambda/4$ for HeNe wavelength (0.632 μm /4 = 0.158 μm) we can see that across the mirror surface a DOP=1-0.158/7= 0.98 is required. A minimum step height actuator design in Poly1 might only have a step of about 2 μm yielding a required DOP=1-0.158/2= 0.92. In either case, the degree of planarization required is quite high. Typical MUMPs electrostatic actuator array structures display both large (electrode plate) and small (flexures) features. Thus the topological factors affecting the DOP achievable with film processes are a significant concern.
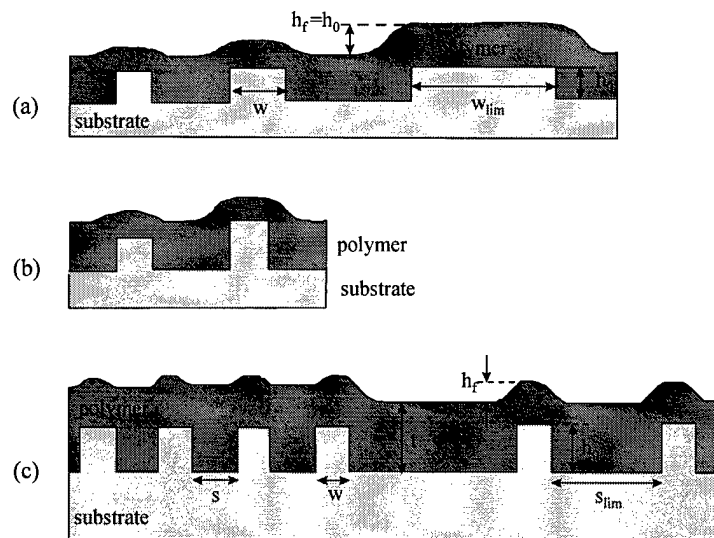
Figure 2-1. Planarization. Influence of topography on planarization performance (a) and (b). Terms for degree of planarization definition (c). [after 23]

2.5.2 Chemical-Mechanical Polishing

For decades chemical-mechanical polishing (CMP) has been used for optical finishing of glass and silicon surfaces. Planarization of interlevel dielectric layers with tungsten and/or polysilicon electrical feedthroughs was pioneered by IBM and has been used for VLSI fabrication since the mid 1980s. Driven

by the global planarization requirements of sub micron photolithography, CMP is predicted by some to be the fastest growing segment in the semiconductor industry. The global flatness achieved by CMP can be up to two orders of magnitude greater than other approaches [19,20].

The superior performance of CMP is costly. The complex chemical-mechanical process is not well understood and detailed theoretical models do not exist. Specific applications require trial and error to optimize polishing parameters using statistical methods. Precise process control requirements make the equipment expensive. For the most part, only large organizations have been able to develop viable CMP processes and have kept their developments proprietary.

In CMP a rotating wafer is pressed against a polishing pad wetted with a chemical slurry. For oxide removal the slurry consists of silica particles in water. The slurry chemically modifies the oxide layer and the mechanical polishing action carries reacted particles away. Recent DoD funded university research provides a CMP performance benchmark applicable to the micromirror fabrication planarization problem posed [21]. After polishing a 2 inch wafer blanketed with a SiO_2 layer, the global planarity in the middle of the wafer is ± 10 nm. This corresponds to a mirror flatness of about $\lambda/30$; a very good mirror indeed. Similar performance is cited for planarization of patterned wafers. The oxide removal rate of the process is reportedly reproducible enough to complete the polishing of patterned wafers with 200 nm step heights in a single attempt. Optimization of the CMP process for equal polysilicon and oxide selectivity permits fabrication of a flat sacrificial oxide surface with exposed polysilicon attachment posts. Results for this two material system in a trench refill application exhibit excellent planarity [22]. Sandia National Laboratory researchers have developed surface micromachining processes employing CMP to increase the number of structural layers possible, and to facilitate integration of MEMS devices with CMOS electronics [3-5].

CMP can clearly meet mirror flatness requirements but does have one significant drawback. Fabrication of a continuous facesheet on a planarized sacrificial oxide limits access of the release etch. Releasing actuator structures for large arrays might be difficult due to the long distances and large volume of oxide that must be etched away. Improving etch access requires either holes in the mirror surface or

through the substrate. Holes in the mirror surface are undesirable. Holes through the substrate require front to backside alignment and very deep etching.

2.5.3 Spin-on Films

Spin coating is the most common means of applying thin films (usually photoresist) to circular wafers. The planarization effects of spin coating are easily observed but difficult to model because the planarization obtained is a function not only of the coating material but the surface topography. The large number of analytical and empirical models developed to describe the planarizing effects of spin coated materials indicates that a single "one size fits all" model does not exist. After a brief review of spin-on theory a recently developed empirical model is used to characterize the expected planarizing performance of spin coating a MUMPs die.

In spin coating, a film material/solvent mixture is applied to the substrate which is mounted on a rotating chuck. The substrate is spun at speeds up to several thousand revolutions per minute evenly spreading the film by centrifugal force. The principal factors determining film thickness are the rotation speed and film material properties. A common model is the power law equation

$$t = a\Omega^{-b} \qquad\qquad (2\text{-}2)$$

where t is the film thickness, Ω is the spin speed, and a and b are empirically determined spin coating constants [23]. Table 2 lists the "a" and "b" constants for some common film materials. Other factors such as rotational acceleration, static vs. dynamic dispense, spreading cycle, and spin time are less important and are usually adjusted empirically to optimize the uniformity of the coating [24]. For any spin-on film material, the film thickness and underlying feature/space widths are the dominating factors in the DOP achieved. As film thickness tends towards infinity, the planarized step height (h_f) tends toward zero (DOP=100).

The planarization performance of different film materials is a complicated function of material parameters best determined empirically. A recent empirical model relates DOP to the three most important

topographic parameters, feature width w, feature height h_O, film thickness t, and a planarization constant K specific to the film solution [23]:

$$DOP = 1 - \frac{\sqrt{T^2 + w^2} - T}{w}, \qquad (2\text{-}3)$$

where $T=Kt/h_O$. The empirically determined constant K represents the combined influence of all the physical parameters of the planarizing solution including: viscosity, surface tension, film shrinkage, and solvent evaporation rate. Once determined, the K value can be used to calculate the DOP for other film thicknesses (obtained by adjusting the spin speed or multiple applications) and feature widths. Measured profile data was used to derive the constants for the materials listed in Table 2-2.

Table 2-2. Polymer Spin and Planarization Model Constants (after [23])

Polymer	Constant 'a'	Constant 'b'	Thickness t (μm)	h_0 (μm)	Constant 'K' (μm)	Measured w_{lim} (μm)
HPR 204	113.4	0.543	1.0	0.5	2.63	50
SOG 204	3.5	0.492	0.37	0.5	6.05	50
PMMA-496K	19.8	0.403	1.0	0.5	2.21	20-30
Polyimide 2555	3773	0.729	1.6	1.0	2.18	20-30
PPQ-IP200	187.4	0.520	1.5	0.5	0.13	7
PIQ13	205.9	0.556	1.5	0.5	0.92	20-30

Using this data and the empirical model of Eq.(2-3) we can estimate the DOP for a MUMPs mirror/actuator structure using spin-on films. Choosing a 5 μm thickness (assuming this layer thickness is possible with multiple applications) of spin-on glass (SOG 204) for its high K value and large w_{lim}, and letting the maximum feature width equal w_{lim} and $h_O=2$ μm, the estimated DOP is approximately 25%. As this estimate represents a best case scenario, it shows that spin coating alone will not provide the planarization required for a reasonably good mirror surface. Possible exceptions to the preceeding statement include thick (5 μm) layers of epoxy or PBCB material mentioned in [23] but not characterized.

Baking can dramatically improve planarization performance of spin coated polymer films. Almost complete planarization ($h_f=0.05$ μm) of isolated 25 μm lines has been reported for polymer films

baked for 90 minutes at 150-200°C [25]. Though baking may cause the polymer material to decompose this may not have the same ramifications for planarizing a MEMS die as it does for other IC processing. In the MEMS mirror case the planarizing material is sacrificial and the only concern is that it be easily removed after deposition of a mirror surface.

2.5.4 Deposit and Etch Back

For planarization of large step heights perhaps the most common method is deposition and etch back of a thick layer of planarizing material. For the most part, planarization occurs during the deposition process and the etch back transfers the planarity to the desired level. Thus, the benefit of increased planarizing film thickness is obtained while not retaining that thickness. While deposition methods vary, reactive ion etching (RIE) provides the greatest flexibility for the etch-back process. The methods presented below represent recent works which illustrate the possibilities and performance of deposit and etch-back approaches. Though most of the work referenced extensively presents RIE chemistry and parameter optimization, the RIE discussion here will be limited.

For applications such as trench isolation, capacitor formation, topside substrate contacts and high performance transistors, deep substrate etches (up to 4 μm) are often filled with thick polysilicon layers then etched back. The polysilicon deposition process typically leaves a small dimple in the polysilicon surface which can be planarized using a spin-on glass (SOG) film [26]. By adjusting the chemistry of the RIE so that the etch rates of the SOG and polysilicon are equal, the planarity of the SOG layer is transferred to the substrate level. Results for this approach are remarkably good even for high aspect ratio structures. For 1 μm wide trenches 4 μm deep the *DOP* obtained by polysilicon filling, SOG, and RIE etch back was approximately 94% (1-0.25/4).

More frequently, organic polymers such as polyimide or photoresist serve as the sacrificial planarizing media. A recent work specifically targeted at MEMS applications employed photoresist layers and plasma etch back [27]. Initially these researchers attempted to planarize 150 μm wide trenches approximately 2 μm deep using single and double spin coatings of HPR204 photoresist 2 μm thick. The

unsatisfactory results reported are consistent with the *DOP* predicted by the empirical model presented in the previous section. Recognizing that it was necessary to fill the trenches prior to global planarization, an "image reversal resist" process was developed. Acceptable planarity was acheived for the fabrication of ideally clamped beams in a single mechanical layer. Application of the "image reversal resist" technique for planarization would substantially increase the complexity of a multilayer MEMS process. Each layer would require planarization prior to deposition of subsequent layers to result in a planar top layer. Image reversal after complete fabrication is made impossible by the varying step heights created. But, the ability to create thick planarizing layers of photoresist and use those layers for etch back holds promise.

Instead of being a generally conformal coating, photoresist can be applied as a planar membrane with a planarity that can then be transferred to the desired level by etch back. In a creative application of available materials, Dutch researchers employed thick (38 μm) sheets of dry film photoresist to planarize severe topologies [28]. The thick dry film photoresist used (Ordyl AP838) is primarily intended for printed circuit board fabrication. After lamination to the wafer using pressure (3.5 kg cm^{-2}) and temperature (125°C) the resist layer is etched back by RIE using a CHF etch chemistry to about 7 μm thick. Aluminum is evaporated onto the top of the dry resist film and patterned. The remaining dry resist film is removed by anisotropic RIE leaving aluminum covered photoresist bridges across the deep trenches of this pressure sensor application. Depending on planarity of the etchback and minimum layer thickness possible, a similar approach might be considered for deposition of a metallized polymer mirror facesheet.

2.5.5   Sacrificial Wafer Bonding

Sacrificial wafer bonding combines the features of CMP and the deposition/etch back approaches. The original plane surface of the sacrificial wafer, normally produced by CMP, is transferred indirectly to the wafer to be planarized. The transfer medium is deposited on the sacrificial wafer, the wafers are bonded, then the plane surface is exposed by etching away the sacrificial wafer. The plane surface may become a part of the planarized device structure or may be used as an expendable platform for the fabrication of subsequent layers. A recent work by Dutch researchers illustrates polymer and anodic

sacrificial wafer bonding approaches [29]. Figure 2-2 illustrates a fabrication sequence applicable to both bond types. This work was done by the same researchers and was intended for the same application as the dry film etchback presented in the preceeding section. The only significant difference is use of a sacrificial wafer to "deposit" a planar surface.
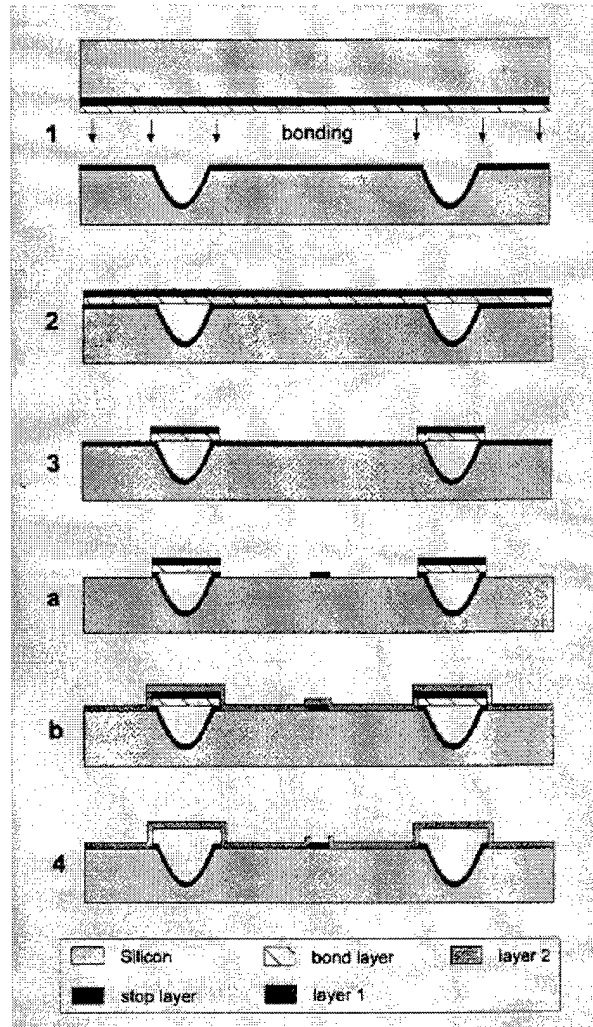
Figure 2-2. Sacrificial wafer planarization process [29].

In the polymer bonding approach, the sacrificial wafer is fabricated with a 0.5 μm thick evaporated aluminum etch stop layer. The bond layer is negative photoresist (3IC Olin Ciba Geigy) which is spin coated to 1.4 μm thickness and prebaked for 140 minutes at 150°C in a nitrogen environment to

2-17

evaporate the solvents from the resist. The two wafers are contacted in a bonding tool at room temperature, then baked for 90 minutes at 150°C in a nitrogen ambient to form the bond. The long prebake minimizes solvent outgassing during bonding. The nitrogen ambient during baking prevents oxidation of the photoresist. Excessive outgassing and resist oxidation were both found to cause failure of the polymer bonds.

The 280 μm thick sacrificial wafers were removed in a 2.5 hour RIE with special precautions to reduce loading effects. As shown in steps 3 and 4 of Figure 2-2 the etch stop and bond layers can be patterned and/or removed in subsequent processing. A similar approach using anodic bonding and potassium hydroxide (KOH) etching was also demonstrated. A 1.4 μm thick borosilicate glass layer sputtered onto the sacrificial wafer serves as both the bond layer and etch stop. The etch back is performed in 25% KOH solution at 78°C. After the etch back, metal is deposited and patterned. The patterned metal serves as the etch mask for removal of the excess glass. The SEM micrograph (Figure 2-3) of a completed device fabricated with polymer sacrificial wafer bonding shows excellent results. The metal bridges span a 100 μm wide, 100 μm deep trench with no apparent sag.
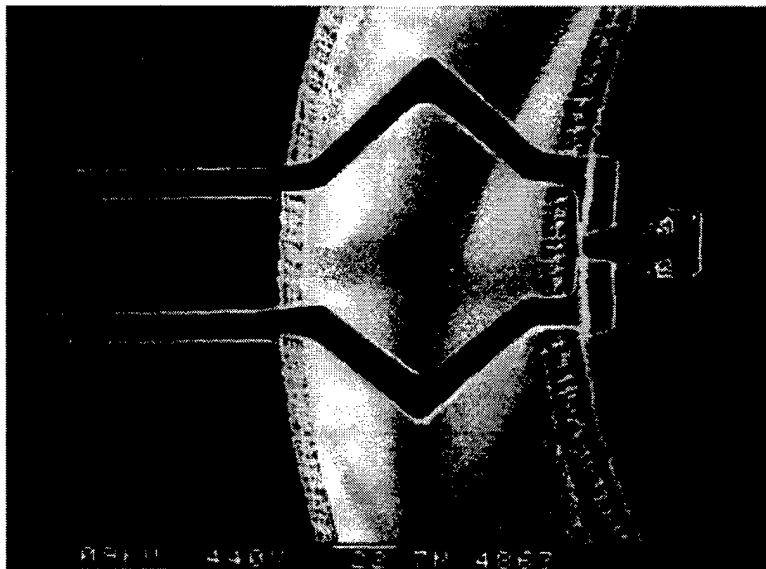
Figure 2-3. Sacrificial wafer planarization. Bridges cross 100 μm wide trench [29].

Use of a sacrificial wafer to provide a temporary plane surface for subsequent fabrication of a mirror facesheet may be of limited utility. To withstand subsequent processing the temporary layer must be thick enough to be mechanically stiff (over a span of 100 μm or more). Holes through this relatively thick layer for attaching the mirror surface to the actuators will perturb the resulting mirror surface. However, if a sacrificial wafer is used to provide the plane mirror surface for a MEMS actuator array, the character of the problem changes considerably. Fabrication of the optically smooth mirror surface is straightforward. Any film material deposited on the CMP processed sacrificial wafer surface will be as smooth and flat as that surface. Unsupported membrane mirrors produced by etching through a wafer to expose a thin sheet of silicon nitride exhibit very good optical quality (see Section 2.6.2). The remaining problem is attaching the plane surface to the MEMS actuators and releasing it from the sacrificial wafer. Polymer, anodic, and eutectic bonding are all low temperature attachment schemes which are compatible with fully processed MUMPs die.

After bonding, the MUMPs die must be protected from the sacrificial wafer etch. Also, the bonds attaching the planar surface must survive the final HF release etch. Very thin anodic bonds might survive if made large enough so that the diffusion limited HF release etch does not completely cut the bonds. Polymer and eutectic bonds can be selected to minimize attack by the HF release etch. An added advantage of sacrificial wafer bonding approaches is that the gap between the actuator attachment and sacrificial oxide need not be filled, providing access for the release etchant. For the Poly1 actuator with Poly2 post example, these channels vary in height from 1.5 to 2.75 μm. Since the DOP does not depend on the underlying layers, a partial release etch leaving just enough oxide to keep the actuator posts in place prior to bonding is also possible. With etch access futher improved and removal of only a small amount of remaining oxide required, the final release etch can be dramatically shortened. Thus the bonds need not survive a long HF etch and etch access holes in the mirror surface are unnecessary. Segmenting the release etch also reduces the total etch time that the outermost actuator structures must survive. Attempts to bond facesheets to MUMPs die are described in Chapter 8.

2.6 Review of Micromirror Designs

The micromirror devices presented here exhibit a wide range of operating characteristics; from arrays of widely spaced but very fast torsion mirrors, to continuous facesheet mirrors with much slower response times. The devices presented were selected from the current technical literature to illustrate different mirror types, fabrication techniques, and optical characteristics.

2.6.1 Cantilever and Torsion Micromirrors

Driven by commercial applications in print and display technology, cantilever and torsion mirrors and mirror arrays dominate the technical literature. Though arrays of torsion or cantilever mirrors are of limited utility for high order aberration correction, single cantilever or torsion mirrors may be candidates for the stabilization/tracking function in an adaptive optic system. The following efforts were selected for discussion because they illustrate two different actuation mechanisms and two different fabrication techniques.

Swiss researchers have fabricated thermally actuated 35μm × 40μm micromirrors compatible with an industrial double-metal CMOS process [30]. An SEM micrograph of the device is shown in Figure 2-4. The mirror and thermally actuated cantilever supports are formed during the 1.2 μm double metal CMOS fabrication process and released in a post-processing etch EDP. The release step requires no additional masking because the etch windows are defined in the CMOS process. Aluminum layers on top of the oxide create a bimorph of materials with different coefficients of thermal expansion. To increase stiffness, the mirror is comprised of both aluminum layers with an oxide layer sandwiched between, and a silicon nitride passivation layer. Upon release, internal stresses cause the mirror structure to bend away from the substrate slightly. Heating the bimorph arms with a buried (not visible in the SEM) polysilicon resistor causes the mirror to move down toward the horizontal position. Upon further heating the mirror moves into the etched cavity.

The analytic theory describing deflection (d) of the thermal bimorph is summarized in the following equation [31]:

$$d = \frac{L^2}{2r} = \frac{L^2}{2}\left\{\frac{6b_1b_2E_1E_2t_1t_2(t_1+t_2)(\alpha_1+\alpha_2)\Delta T}{(b_1E_1t_1^2)^2+(b_2E_2t_2^2)^2+2b_1b_2E_1E_2t_1t_2(2t_1^2+3t_1t_2+2t_2^2)}\right\} \qquad (2\text{-}4)$$

Parameters b_n, t_n, E_n, and α_n are the layer width, thickness, modulus of elasticity, and thermal coefficients of expansion respectively. The length of the cantilever is L, its radius of curvature is r, and ΔT is the thermal heating supplied by the resistor. Extension of this theory to the trimorph case shows good agreement with finite element models and reasonably good agreement with measured results. Other analytic treatments of the multimorph case for CMOS cantilevers show better agreement with measured deflections [32].
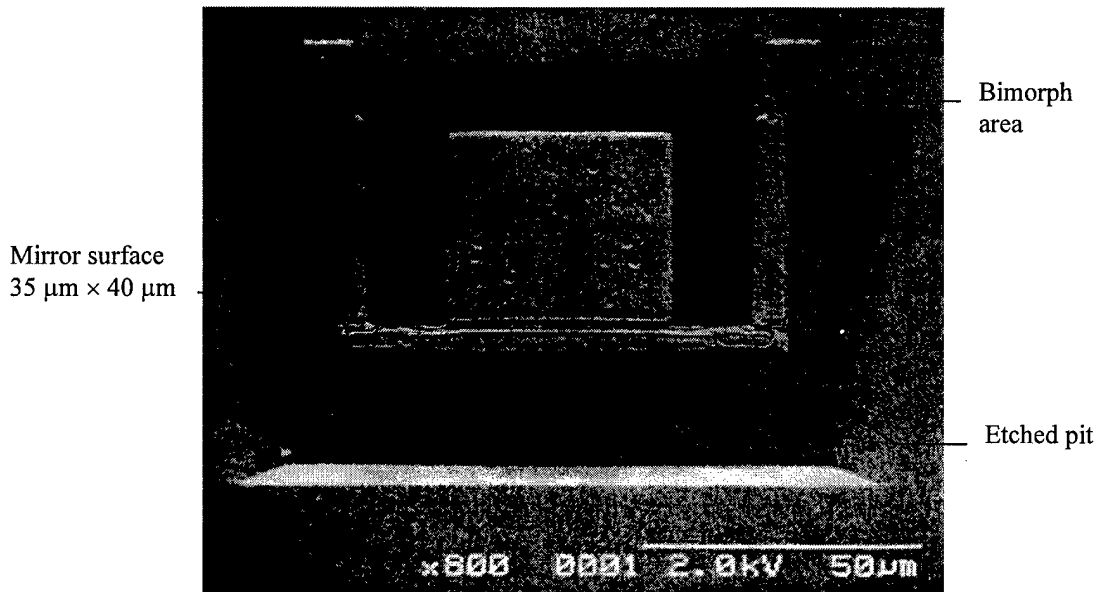
Figure 2-4. Thermally actuated cantilever micromirror [30].

Measured mirror deflections of 4.6° were reported with 4.6 mW of heating power. At this deflection mirror flatness was observed to be 0.2°. The reported dynamic response of the mirrors is 2 ms. When operated with square pulse excitation, the mirror amplitude response deviates less than 15% at frequencies up to 400 Hz. The CMOS process compatibility of these devices makes them attractive for array applications, but may be limited by on-chip heat generation and the low optically active area [30].

Torsion mirrors are perhaps the most ubiquitous micromirror design and closest to wide commercial application. A second group of Swiss researchers have developed a 32 × 32 array of line-

addressable torsion micromirrors fabricated in polysilicon intended as a prototype for printing and projection display applications [33]. A single torsion mirror element and schematic cross-section in Figure 2-5 show the constuction and operating principle. The entire mirror device is fabricated in polysilicon except the approximately 10×20 μm aluminum reflecting surface. The torsion bars are 15 μm long, 2 μm thick, and only 0.4 μm wide. The small torsion bar width requires special dry etch in a surface micromachining process otherwise very similar to MUMPs. A C_2ClF_5/SF_6 plasma etch using a standard photoresist mask exhibits high selectivity, controlled undercutting, and almost vertical sidewalls. Aluminum is sputtered on the active mirror surfaces. The mirrors are released in buffered hydrofluoric acid with glycerin added to increase the selectivity for oxide over aluminum.

The electrical torque required to rotate the mirror is found by integrating the electrostatic force across the width of the address electrode. For small rotation angles the electric torque is approximately the electrostatic force times the distance ($b/2$),

$$T_e = \frac{\varepsilon_0 V^2 mb}{2d^2} \left(\frac{b}{2}\right) = \frac{\varepsilon_0 V^2 mb^2}{4d^2} \tag{2-5}$$

where m is the length of the address electrode into the page. The mechanical torque counteracted by the electric torque is a function of the torsion modulus, polar inertia, rotation angle, and length of the torsion bars. The polar inertia contains terms for the width and thickness of the torsion bar.
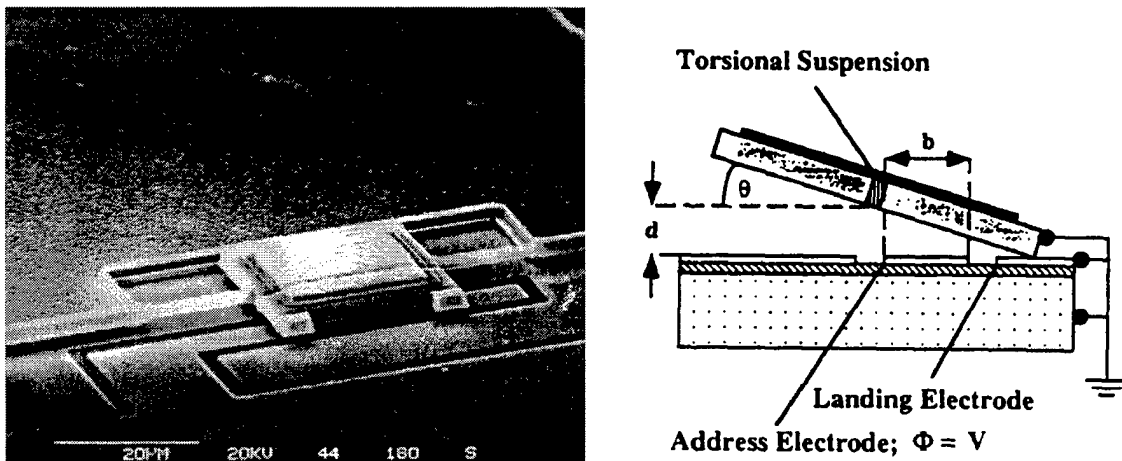
Figure 2-5. Polysilicon torsion mirror SEM micrograph and schematic [33].

Measured mirror deflection angle versus voltage applied shows a V^2 dependence up to about 1/3 of the total displacement. At this point, corresponding to a voltage of about 31 volts, the characteristic "snap through instability" behavior of electrostatic devices causes a sudden full scale deflection. As the applied voltage is decreased, the mirror stays in the fully deflected position until a release voltage of about 16 volts is reached then snaps to the V^2 dependent position. The characteristic hysteresis of the electrostatic actuation mechanism was exploited to create a 32 by 32 array of bistable mirrors with greatly reduced wiring requirements. Each mirror element is individually addressable in the following manner. All mirrors are biased by applying a hold voltage (V_c) midway between the snap through voltage and the release voltage to the columns and ground to the rows. To turn a pixel "on" a voltage $V_c+\Delta$ is applied to the correct column while simultaneously applying a voltage of $-\Delta$ to the correct row. The total potential $V_c+2\Delta$ is greater than the snap through voltage and the pixel fully deflects. Other pixels see at most a potential of $V_c+\Delta$ which is not sufficient to snap the mirror down. The reported maximum mirror deflection for the array device is 7.6 degrees. Direct measurements showed a 97 kHz resonant frequency for small mirror deflections.

2.6.2 Continuous Facesheet Micromirrors

Dutch researchers have reported development of a continuous face sheet membrane micromirror device [34, 35, 36]. A photograph of this device on a test printed circuit board and a diagram showing construction and operating principle are shown in Figure 2-6. The flexible mirror is made from a thin tensile stressed layer of silicon-nitride with aluminum metallization. The membrane is unsupported over the entire 10 mm × 10 mm square active area. Electrodes beneath the mirror membrane are used to electrostatically attract the membrane causing the mirror to deform.

This device is manually fabricated from two die, a surface patterned electrode die and a bulk micromachined membrane die. The membrane is fabricated by depositing a silicon nitride layer nominally 500 nm thick on both sides of a (100) silicon wafer, reactive ion etching mask windows in one side, and anisotropically etching in a 33% potassium hydroxide (KOH) solution at 85°C. Because the silicon nitride

is not etched in KOH only a thin membrane remains. The membrane is cleaned and a 200 nm thick layer of aluminum is deposited by evaporation. Because the deposited silicon nitride conforms to the highly polished wafer surface and its tensile stress is very carefully controlled (10^7-10^8 N/m^2) the resulting membrane mirror has a reported optical flatness of $\lambda/10$ to $\lambda/8$ at 633 nm. The mirror membrane die is manually positioned 25 to 100 μm over the electrode die and glued in place. To reduce mirror deformation caused by the mechanical support (not shown in Figure 2-6), the membrane die is glued at only a single location, which is located as far as possible from the active mirror surface.
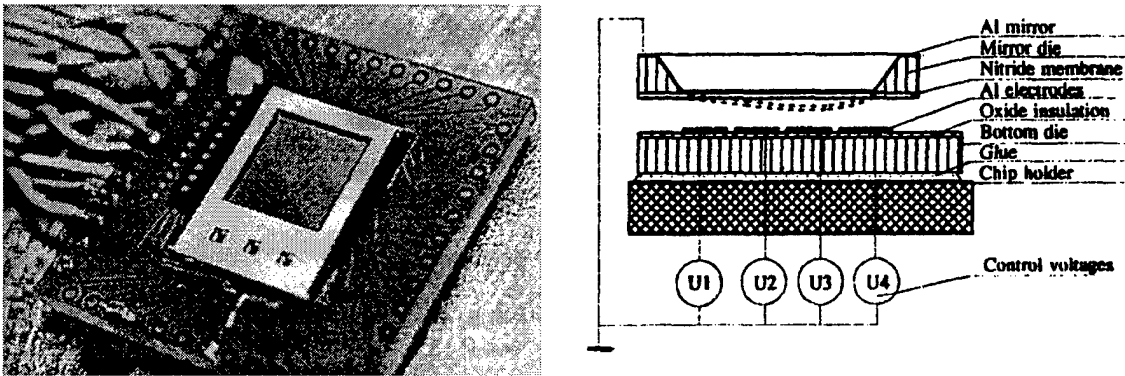
Figure 2-6. Silicon nitride membrane micromirror in test fixture and schematic diagram showing operating principle [34].

The actuation mechanism for membrane mirrors is uni-directional electrostatic attraction of the membrane to the energized electrode(s). Deflection of a membrane under a load is governed by the Laplace equation [37]

$$\nabla^2 z(x,y) = \frac{\partial^2 z(x,y)}{\partial x^2} + \frac{\partial^2 z(x,y)}{\partial y^2} = \frac{-P(x,y)}{T} \quad , \tag{2-6}$$

where $P(x,y)$ is the pressure (force/area) at position (x,y) and T is the tension of the membrane. For known actuator geometry, applied voltages, and electrode to membrane distance (d), the pressure distribution can be approximated by the electrostatic force equation [35]:

$$P(x,y) \approx \frac{\varepsilon_o V^2(x,y)}{2d^2}. \tag{2-7}$$

2-24

Computer modeling using this approximation and the finite difference method to solve the Laplace equation, shows very good agreement with observed images [34].

The relatively low tension of the silicon nitride membrane will allow large deflections provided that the appropriate pressure can be electrostatically applied. No limits on electrostatic deflection were reported, but repeated external loading of the membrane showed elastic deformation of the membrane with up to 50 μm of deflection. Although large deflections are possible, the large mirror to electrode spacing requires correspondingly high control voltages. Dynamic response time measurements yielded estimates that this device could function on the order of a few hundred hertz. The interferometric patterns and reconstructed surface profiles in Figure 2-7 illustrate the good optical quality of the membrane. The figure also illustrates the control limitations for an unsupported uni-directional membrane. High spatial frequency deformations are not possible.
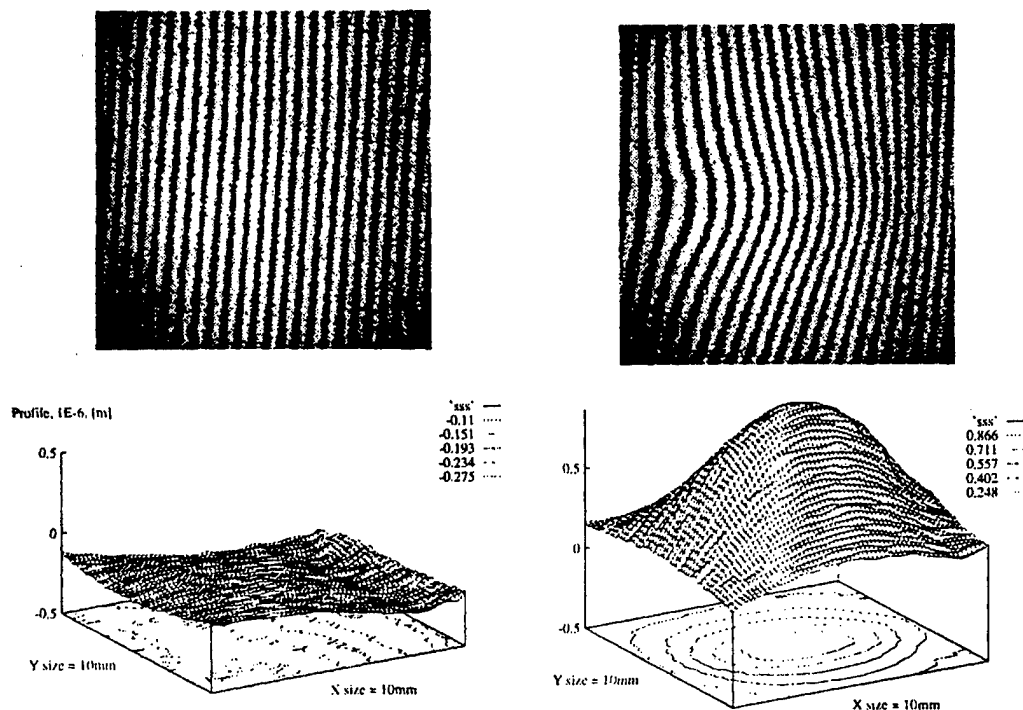
Figure 2-7. Membrane mirror interferometric patterns and reconstructed surface profiles, undeflected (left) and deflected (right) [35].

2-25

In more recent work the same researchers have combined bulk micromachined membrane mirrors up to 4 mm in diameter with printed circuit board (PCB) electrode patterns [38]. Improvements in the membrane fabrication process yield undeflected membranes with optical flatness on the order of $\lambda/20$. Frequency response of the bulk micromachined membrane and PCB hybrid mirrors is reportedly linear from 50 Hz to 1 kHz. Researchers at the Jet Propulsion Laboratory in Pasadena, CA reported a nearly identical membrane mirror and have developed a detailed numerical model for computing control voltages for a desired deflection [39, 40].

Electrostatically actuated continuous facesheet deformable mirrors employing proprietary viscoelastic films have been reported by German researchers [41]. A silicone based elastomer dielectric film damps the electrostatic deflection of a metal membrane. Elastomer damping limits the maximum mirror deflection but permits more precise control of the mirror surface shape. Fluid damping has been used in macro-sized membrane mirrors with large strokes to improve stability and prevent pinning of the membrane to the control electrodes [37].

The viscoelastically supported membrane device was designed to be compatible with a 30 volt CMOS process. Following CMOS processing, oxide and boron oxide layers are deposited and etched back to planarize the wafer surface. The viscoelastic material is spun on to a thickness of 4 to 7 µm after an adhesion promoting treatment. The viscoelastic coating is cured for 2 minutes on a 120°C hot plate. This cure is well below temperatures required to damage the CMOS circuits or metallizations. The surface of the viscoelastic material is hardened in a two step plasma process to prepare it for deposition of the evaporated aluminum mirror metallization. After metal deposition the mirror layer is photolithographically patterned and etched.

Deformation results are provided only for the grating mode where alternating columns of pixels are excited. Peak to peak deformations do not exhibit the characteristic V^2 dependence of electrostatic devices and the deflection appears to be linear with both bias and signal voltage. This is probably the combined result of the viscoelastic damping material and the fact that only a small range of voltage is reported. The deformation time constant for the viscoelastic material is reported as 2 ms, limiting device

operation to less than 500 Hz. The reported reflectivity of the continuous mirror surface is 95% at a wavelength of 550 nm. Performance of the viscoelastically damped membrane mirror was demonstrated in a maskless photolithography application where 0.6 μm lines were defined in photoresist.

Another approach to a continuous facesheet micro-deformable mirror is being pursued by Boston University researchers [42,43,44]. The idealized schematic cross-section shown in Figure 2-8 depicts a continuous (nominally flat) facesheet mirror with electrostatic actuators normal to the mirror surface (axial). Initially designs were implemented in the MUMPs process. Planarity is "drawn in" by careful layout to control the mirror plate topology. Restricting maximum spaces between polysilicon features and oxide cut widths to 1.5 μm resulted in remarkably good mirror plate planarity (~0.25 μm) in the MUMPs process [43]. Electrostatic actuators that are 350×350 μm square double cantilevers have been extensively tested. These actuators, which exhibit V^2 behavior up to about 60V with 0.9 μm deflection, showed 10 nm position repeatability, operated up to 66 kHz, and reportedly had 94.5% yield [42,43]. Segmented mirror arrays and a 560×560 μm continuous facesheet mirror employing 3×3 actuators (200×200 μm) have been designed and tested. Influence function measurements of the continuous mirror with the central actuator deflected show good agreement with model predictions.

Boston University currently has custom fabrication runs underway at MCNC to develop continuous facesheet mirrors with better planarity and greater actuator stroke (2 μm) [45]. To increase actuator stroke a 5 μm thick sacrificial oxide is being used beneath the actuators. The sacrificial oxide between the actuator and mirror membrane is 2 μm thick to achieve the desired stroke and provide adequate self-planarization. Stacks comprised of polysilicon and low stress silicon nitride layers are being used for the membrane layer. A deep reactive ion etch is proposed to provide release etch access holes through the wafer thus avoiding etch access holes in the mirror surface. This backside etch overcomes one of the limitations of the "drawn in" planarizing approach. Because the mirror plate film material must self-planarize to fill in the actuator attachment holes its required thickness is related to the oxide layer thickness and minimum oxide cut size. The facesheet layer must remain relatively thick, requiring large actuator area and/or high control voltages. Though it is doubtful that self-planarized membranes will achieve the

optical flatness of the tensile stressed SiN membranes presented previously, mirror systems using a fabrication approach like this should provide good optical flatness and high order aberration correction capability once the fabrication process is refined.
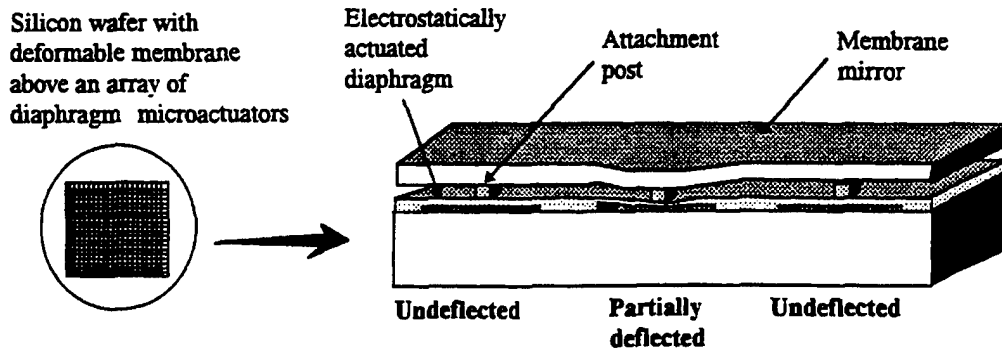
Figure 2-8. Conceptual drawing of continuous facesheet micromirror [42].

2.6.3 Piston Micromirror Arrays

Arrays of "piston only" mirrors approximate a continuous facesheet mirror with axial actuators. The piston mirror arrays reported prior to this research effort were flexure beam designs with the flexure beams and support structure consuming a percentage of the optical surface and increasing the distance between mirror segments. Two representative samples of flexure beam mirror arrays employing different process technologies are presented below. Design of electrostatic piston micromirrors and actuators and the operating principles are covered extensively in Chapter 3.

Texas Instruments (TI) has been investigating flexure beam deformable mirrors since before 1989 [46]. Most recently, TI reported a 128×128 array of metal piston micromirrors designed to be compatible with a 12V CMOS process [47]. Figure 2-9 is a photograph of a portion of the completed array showing the relatively high packing density achieved. A similar 8×8 test array was characterized by Rhoadarmer [48]. One unique feature of the latest TI flexure beam device is that mirrors are addressed through the posts and flexures instead of through the bottom electrodes to reduce capacitive coupling to signal layers beneath the mirror device. The active optical area is reduced somewhat by this requirement because the

2-28

post size must be increased to provide electrical isolation for three of the four flexures attached to it. The completed TI arrays have active optical areas of about 63-74% depending on post size. Assuming a conservative mirror reflectivity of 85% the overall optical reflectivity can be estimated between about 54 and 64%. Dynamic testing at deflections corresponding to π phase shift at 546 nm showed rise and fall times consistent with operation over 100 kHz. The primary contribution to the high frequency of operation is the relatively short, stiff flexures.
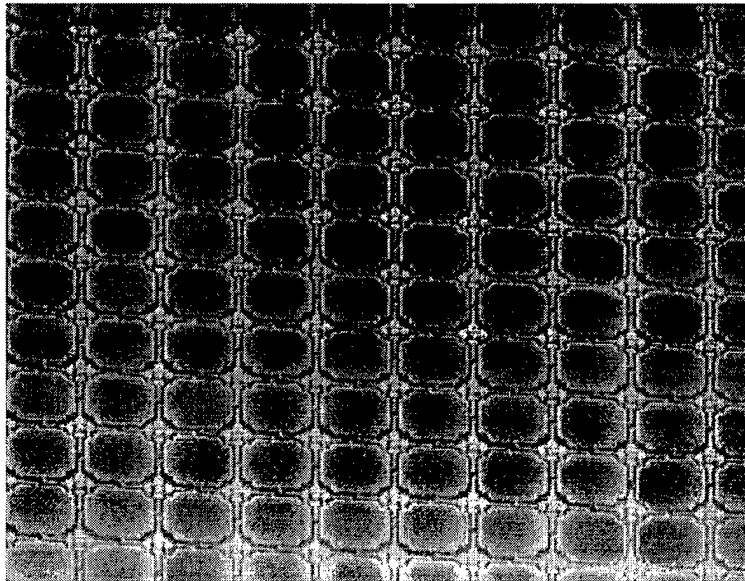
Figure 2-9. Portion of TI flexure beam micromirror array [47].

Hexagonal arrays of 127 piston micromirrors have been developed at the Air Force Institute of Technology (AFIT) [49]. Figure 2-10 is a SEM micrograph showing a portion of an array with 80 μm wide hexagonal elements. This array is fabricated using the MUMPs process. The flexure and upper mirror plate are fabricated in the Poly2 layer which has a nominal thickness of 1.5 μm. MUMPs design rule limitations also force the flexures to be at least 2 μm wide. These size constraints and the relative stiffness of polysilicon force the design of long flexures to reduce the required actuation voltage. The long flexures consume active optical area, add amplitude modulation, and disperse a fraction of the incident light. From the figure the estimated active optical area is 40%. Efforts to mitigate the flexure influence

2-29

include design and on-chip fabrication of a releasable polysilicon cover plate that would mask the flexures while exposing the active mirror faces. Placement of the cover plate is a manual process.
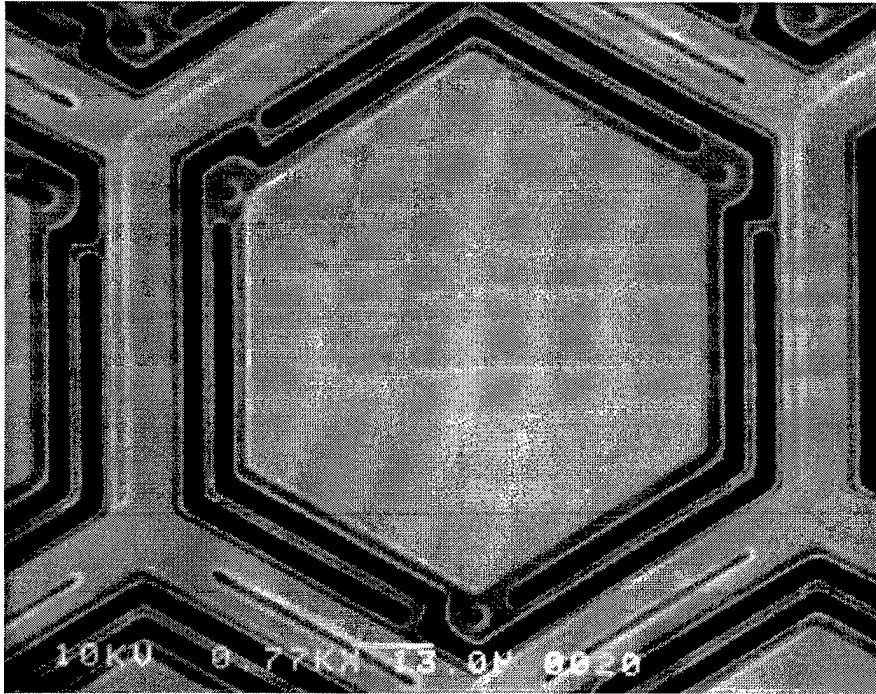
Figure 2-10. SEM micrograph of 80 μm wide hexagonal piston micromirror array.

Recent work has shown the limitations of the AFIT hexagonal array. The low optical efficiency, large nonplanar static background, and curved mirror surfaces all degrade optical phase modulation performance. Microscope interferometer measurements by the author show curvature for the 80 μm wide mirrors greater than 400 nm. One representative measurement is shown in Figure 2-11. Mirror curvature is caused by residual metal tensile stress inherent in the MUMPs process. Despite the limitations of the hexagonal mirror design it was successfully used in the first demonstration of optical aberration correction using a micromirror array [50]. AFIT students P. Roberts and S. Hick demonstrated good agreement between modeled and measured optical aberration correction results with the 80 μm wide hexagonal mirror array [51, 52]. The specific contributions of this author to the hexagonal mirror aberration correction effort were release and packaging of 6 hex mirror arrays, deflection characterization testing, mirror curvature measurement, and documentation support.
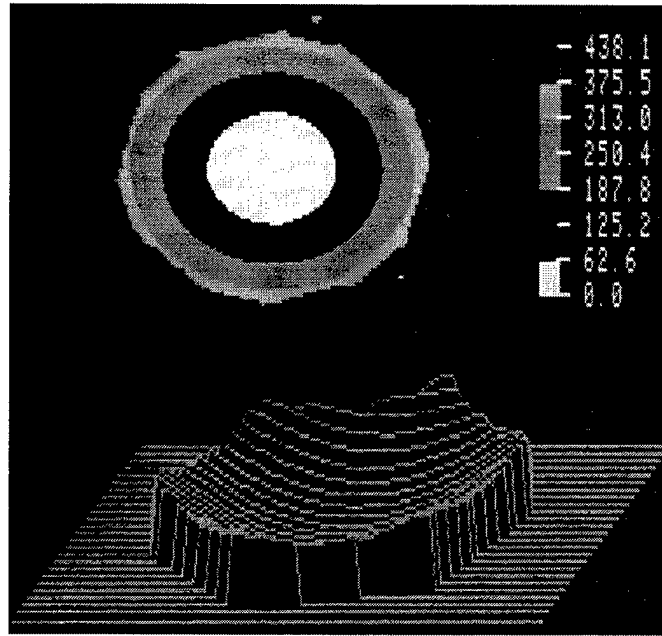
Figure 2-11. Curvature of 80 μm hexagonal mirror.

2.7 Chapter Summary

MEMS fabrication techniques offer the possibility of high performance, low cost deformable mirrors for optical aberration correction. Prior micromirror designs have not achieved the performance requirements of practical high order aberration correction due to either limited optical efficiency or limited correction modes. The principle difficulty faced with microfabrication of deformable mirrors is that of making an optically flat reflecting surface, either continuous or segmented, on a rather severe actuator topography.

Planarization is required to produce a good optical surfaces with sufficient degrees of freedom for high order optical aberration correction. Possible approaches include planarization by design (including self-planarization), addition of a planarization step to the process, or attachment of planar facesheet to an array of actuators. All of these possible approaches have been pursued to some extent in this research effort.

Planarization by design is the least expensive approach because it can be applied to devices fabricated in readily accessible, low-cost foundry processes. Implementation requires only that the

designer recognize and avoid, (or exploit in the self-planarization case), the conformal nature of the layer deposition processes. The authors most successful designs employ this low cost approach.

Development of a full process which includes a planarization step is prohibitively expensive. The already developed SUMMiT process, with its chemical-mechanical polishing should produce mirror surfaces with very good optical quality, but access to this process is somewhat limited. Segmented and continuous facesheet deformable mirrors designed by the author were fabricated in the SUMMiT process and characterized.

Post-foundry planarization of MUMPs die using spin-on film techniques was also attempted. Deposition and etch back approaches were not pursued because RIE equipment was not readily available. Considerable effort was invested in development of a post-foundry process to transfer a planar facesheet from a sacrificial wafer to an array of actuators. Sacrificial wafer bonding is especially attractive for two reasons: (1) All of the difficult processing (i.e. fabrication of a high quality optically flat surface) may be obtained inexpensively from outside vendors; (2) The final release etch is greatly shortened. Only techniques for bonding and release of the planarization layer must be developed "in-house". Although significant progress was made, bonding efforts did not produce functional devices.

References

1   D. A. Koester, R. Mahadevan, and K. W. Markus, *Multi-User MEMS Processes (MUMPs) Introduction and Design Rules, Rev. 4*, July 15, 1996, MCNC MEMS Technology Applications Center, 3021 Cornwallis Road, Research Triangle Park, NC, 27709.

2   J. H. Comtois and V. M. Bright, "Design techniques for surface-micromachining MEMS processes," *Proc. SPIE*, vol. 2639, pp. 211-222, July 1995.

3   R. D. Nasby, D. L. Heatherington, J. J. Sniegowski, C. A. Apblett, J. H. Smith, S. Montgue, C. C. Barron, W. P. Eaton, and P. J. McWhorter, "Application of chemical-mechanical polishing to planarization of surface micromachined devices," *Proceedings of the Solid-State Sensor and Actuator Workshop*, Hilton Head Island, SC, pp. 49-53, June 1996.

4   J. J. Sniegowski, S. L. Miller, G. L. LaVigne, M. S. Rodgers, and P. J. McWhorter, "Monolithic geared mechanisms driven by a polysilicon surface-micromachined on-chip electrostatic microengine," *Proceedings of the Solid-State Sensor and Actuator Workshop*, Hilton Head Island, SC, pp. 178-182, June 1996.

5   B. R. Davies, C. C. Barron, J. J. Sniegowski, and M. S. Rodgers, "SAMPLE (Sandia Agile MEMS Prototyping, Layout tools, and Education)," in *Microelectronic Structures and MEMS for Optical Processing III, Proc. SPIE* , Vol. 3226, pp. 11-21, September 1997.

6   Y. Huang, H. Zhang, E. S. Kim, S. G. Kim, and Y. B Jeon, "Piezoelectrically actuated microcantilever for actuated mirror array applications," *Proceedings of the Solid-State Sensor and Actuator Workshop*, Hilton Head Island, SC, pp. 191-195, June 1996.

7   R. H. Wolf and A. H. Heuer, "Ti Ni (shape memory) films on silicon for MEMS applications," *Journal of Microelectromechanical Systems*, vol. 4, no. 4, pp. 206-212, December 1995.

8   S. M. Sze, *Semiconductor Sensors*, New York: John Wiley & Sons, 1994.

9   O. Tabata, R. Asahi, H. Funabashi, K. Shimaoka, and S. Sugiyama, "Anisotropic etching of silicon in TMAH solutions," *Sensors and Actuators A*, vol. 34, pp. 51-57, 1992.

10   E. H. Klaassen, R. J. Reay, C. Storment, J. Audy, P. Henry, A. P. Brokaw, and G. T. A. Kovacs, "Micromachined thermally isolated circuits," *Proceedings of the Solid-State Sensor and Actuator Workshop*, Hilton Head Island, SC, pp. 127-129, June 1996.

11   J. Shin, S. Chung, Y. Kim, E. Lee, B. Choi, and S. Ahn, "Fabrication of micro mirror supported by electroplated nickel posts," *Proc. SPIE*, vol. 2641, pp. 88-95, July 1995.

12   S. Chung, J. Shin, Y. Kim, and B. Han, "Fabrication of micro mirror supported by electroplated nickel posts," in *The 8th International Conference on Solid-State Sensors and Actuators*, vol. 1, pp. 312-315, June 1995.

13   M. B. Cohn, Y. Liang, R. T. Howe, and A. P. Pisano, "Wafer-to-wafer transfer of microstructures for vacuum packaging," *Proceedings of the Solid-State Sensor and Actuator Workshop*, Hilton Head Island, SC, pp. 32-35, June 1996.

14   A. P. Lee, D. R. Ciarlo, P. A. Krulevitch, S. Lehew, J. Trevino, and M. A. Northrup, "A practical microgripper by fine alignment, eutectic bonding, and SMA actuation," in *The 8th International Conference on Solid-State Sensors and Actuators*, Eurosenors IX, vol. 2, pp.368, June 25-29, 1995.

15   C. L. Chernick, H. H. Claassen, P.R. Fields, H. H. Hyman, J. F. Malm, W. M. Manning, M. S. Matheson, L. A. Quarterman, F. Schreiner, H. H. Selig, I. Sheft, S. Siegel, E. N. Sloth, L. Stein, M. H. Studier, J. L. Weeks, and M. H. Zirin, "Fluorine compounds of xenon and radon," *Science*, vol. 138, pp. 136-138, October 1962.

16   H. F. Winters and J. W. Coburn, "The etching of silicon with XeF_2 vapor," *Appl. Phys. Lett.*, vol. 34, no. 1, pp.70-73, January 1979.

17   F. I. Chang, R. Yeh, G. Lin, P. B. Chu, E. Hoffman, E. J. J. Kruglick, K. S. J. Pister, and M. H. Hecht, "Gas-phase silicon micromachining with xenon difluoride," in *Proc. SPIE*, vol. 2641, pp. 117-128, July 1995.

18   F. I. Chang, "Xenon difluoride etching of silicon for MEMS," *Master's Thesis*, UCLA School of Engineering and Applied Science, Los Angeles, CA 90024-1594, June 1995.

19   M. A. Martinez, "Chemical-mechanical polishing: route to global planarization," *Solid State Technology*, pp. 26-31, May 1994.

20   M. A. Fury, "Emerging developments in CMP for semiconductor planarization," *Solid State Technology*, pp. 47-54, April 1995 and pp. 81-88 July 1995.

21   M. Bhushan, R. Rouse, and J. E. Lukens, "Chemical-mechanical polishing in semidirect contact mode," *J. Electrochem. Soc.,* vol. 142, no. 11, pp. 3845-3852, November 1995.

22   J.-Y. Cheng, T. F. Lei, and T. S. Chao, "A novel planarization of trench isolation using polysilicon refill and etch back of chemical-mechanical polish," *J. Electrochem. Soc.,* vol. 142, no. 10, pp. L187-188, October 1995.

23   A. Schiltz, "An empirical model for planarization with polymer solutions," *Jpn. J. Appl. Phys.,* vol. 34, pp. 4185-4194, August 1995.

24   W. S. Ruska, *Microelectronic Processing.* New York: McGraw Hill, 1987.

25   M. D. Bullwinkel, J. Gu, G. A. Campbell, and P. C. Sukanek, "The effect of molecular weight and solvent type on the planarization of spin-coated films," *J. Electrochem. Soc.,* vol. 142, no. 7, pp. 2389-2394, July 1995.

26   S. Ramaswami and A. Nagy, "Polysilicon planarization using spin-on glass," *J. Electrochem. Soc.,* vol. 139, no. 2, pp. 591-599, February 1992.

27   Y. X. Li, P. J. French, and R. F. Wolffenbuttel, "Plasma planarization for sensor applications," *IEEE Journal of Microelectromechanical Systems*, vol. 4, no. 3, pp. 132-138, September 1995.

28   V. L. Spiering, J. W. Berenschot, and M. Elwenspoek, "Planarization and fabrication of bridges across deep grooves or holes in silicon using a dry film photoresist followed by an etch back," *J. Micromech. Microeng.,* vol. 5, pp.189-192, 1995.

29   V. L. Spiering, J. W. Berenschot, M. Elwenspoek, and J. H. J. Fluitman, "Sacrificial wafer bonding for planarization after very deep etching," *IEEE Journal of Microelectromechanical Systems*, vol. 4, no. 3, pp. 151-157, September 1995.

30   J. Buhler, J. Funk, O. Paul, F.-P. Stiener, and H. Baltes, "Thermally actuated CMOS micromirrors," *Sensors and Actuators A*, vol. 46-47, pp. 572-575, 1995.

31   W. H. Chu, M. Mehregany, and R. L. Mullen, "Analysis of tip deflection and force of a bimetallic cantilever microactuator," *J. Micromech. Microeng.,* vol. 3, pp. 4-7, 1993.

32   B. C. Read, V. M. Bright, and J. H. Comtois, "Mechanical and optical characterization of thermal microactuators fabricated in a CMOS process," *Proc.SPIE*, vol. 2642, pp. 22-30, May 1995.

33   V. P. Jaecklin, C. Linder, N. F. de Rooij, J. M Moret, and R. Vuilleumier, "Line-addressable torsional micromirrors for light modulator arrays," *Sensors and Actuators A*, vol. 41-42, pp. 324-329, 1994.

34   G. Vdovin, S. Middelhoek, and L. Sarro, "Deformable mirror display with continuous reflecting surface micromachined in silicon," in *IEEE Micro Electro Mechanical Systems*, pp. 61-64, 1995.

35   G. Vdovin and P. M. Sarro, "Flexible mirror micromachined in silicon," *Appl. Opt.,* vol. 34, pp. 2968-2972, June 1, 1995.

36   G. Vdovin, S. Middelhoek, and P. M. Sarro, "Thin-film free-space optical components micromachined in silicon," *Digest IEEE/LEOS 1996 SummerTopical Meetings,* Keystone, CO, pp.5-6, August 5-9, 1996.

37   R. K. Tyson, *Principles of Adaptive Optics.* San Diego: Academic Press, 1991.

38   G. Vdovin, S. Middelhoek, and P. M. Sarro, "Technology and applications of micromachined silicon adaptive mirrors," *Opt. Eng.,* vol. 36, no. 5, pp. 1382-1390, May 1997.

39   L. Miller, M. L. Agronin, R. K. Bartman, W. J. Kaiser, T. W. Kenny, R. L. Norton, and E. C. Vote, "Fabrication and characterization of a micromachined deformable mirror for adaptive optics applications," in *Proc. SPIE,* vol. 1945, pp. 421-430, July 1993.

40   P. K. C. Wang and F. Y. Hadaegh, "Computation of static shapes and voltages for micromachined deformable membrane mirrors with nonlinear electrostatic actuators," *IEEE Journal of Microelectromechanical Systems,* vol. 5, no. 3, pp. 205-220, September 1996.

41   H. Kuck, W. Doleschal, A. Gehner, W. Grundke, R. Melcher, J. Paufler, R. Seltmann, and G. Zimmer, "Deformable micromirror devices as phase modulating light valves," in *The 8th International Conference on Solid-State Sensors and Actuators,* vol. 1, pp. 301-304, June 1995.

42   R. Krishnamoorthy and T. Bifano, "MEMS arrays for deformable mirrors," *Proc. SPIE,* vol. 2641, pp. 96-104, July 1995.

43   T. G. Bifano, "Micromechanical arrays for macroscopic actuation of deformable mirrors," *DARPA Semi-Annual Technical Report (II),* September 1996.

44   T. G. Bifano, R. K. Mali, J. K. Dorton, J. Perreault, N. Vandelli, M. N. Horenstein, and D. A. Castanon, "Continuous-membrane surface-micromachined silicon deformable mirror," *Opt. Eng.,* vol. 36, no. 5, pp. 1354-1360, May 1997.

45   T. G. Bifano, "Micromechanical arrays for macroscopic actuation of deformable mirrors," *DARPA Semi-Annual Technical Report (IV),* July 1997.

46   R. M. Boysel, J. M. Florence, and W. R. Wu, "Deformable mirror light modulators for image processing," *Proc. SPIE,* vol. 1151, pp. 183-194, 1989.

47   T. H. Lin, "Implementation and characterization of a flexure beam micromechanical spatial light modulator," *Opt. Engr.,* vol. 33, no. 11, pp. 3643-3648, November 1994.

48   T. A. Rhoadarmer, V. M. Bright, B. M. Welsh, S. C. Gustafson, and T. H. Lin, "Interferometric characterization of the flexure-beam micromirror device," *Proc. SPIE,* vol. 2291, pp. 13-23, 1994.

49   J. H. Comtois, V. M. Bright, S. C. Gustafson, and M. A. Michalicek, "Implementation of hexagonal micromirror arrays as phase-mostly spatial light modulators," *Proc. SPIE,* vol. 2641, pp. 76-87, July 1995.

50   M. C. Roggemann, V. M. Bright, B. M. Welsh, S. R. Hick, P. C. Roberts, W. D. Cowan, and J. H. Comtois, "Use of micro-electro-mechanical deformable mirrors to control aberrations in optical systems: theoretical and experimental results," *Opt. Eng.*, vol. 36, no. 5, pp. 1326-1338, May 1997.

51   S. Hick, "Demonstrating optical aberration correction with a MEMS micro-mirror device," *Masters Thesis*, Air Force Institute of Technology, AFIT/ GAP/ENP/96D-07, 1996.

52   P. Roberts, "Modeling and simulation of optical characteristics of microelectromechanical mirror arrays," *Masters Thesis*, Air Force Institute of Technology, AFIT/ GAP/ENP/96D-09, 1996.

3. Electrostatic Piston Micromirror Arrays

3.1 Chapter Overview

At the start of this research effort the Texas Instruments (TI) flexure beam micromirror array [1], and the AFIT hexagonal micromirror array [2], described in the proceeding chapter represented the state-of-the-art in electrostatic piston micromirror arrays. Despite its promising fill-factor, the TI flexure beam micromirror array has not been demonstrated in applications. As of this writing the TI 128×128 element flexure beam micromirror array project has reportedly been abandoned due to problems individually addressing the elements [3]. Early AFIT hexagonal mirror arrays were used to experimentally demonstrate coherent beam steering and beam shaping by simulated annealing [2, 4]. The most recent AFIT hexagonal array was used in the first successful demonstration of optical aberration correction, but the large reflective static background, and rather severe (~400 nm) mirror curvature proved problematic [5]. The author has advanced the state-of-the-art by developing, in a foundry surface micromachining process, micromirror arrays that exhibit high functional device yield, excellent qualitative deflection uniformity, and good optical quality. The author's micromirror arrays have been successfully demonstrated in optical aberration correction and beam steering experiments.

This chapter presents the design and testing of electrostatic piston micromirror arrays. Arrays of flexure beam electrostatic actuators, on which a facesheet can be added, are also included because of their similar structure. In fact, many of the authors designs will serve both as arrays of actuators or as micromirror arrays. The basic operating principle and design equations for flexure beam devices are presented in Section 3.2. Design trade-offs imposed by the microfabrication process are examined in Section 3.3. The test methods used to characterize array performance are briefly described in Section 3.4, with particular emphasis on the rapid characterization techniques developed by the author. In Section 3.5 the author's many designs are summarized chronologically. The novel digital deflection micromirror devices described in Section 3.6 may represent a large step toward development of an entire deformable

mirror system on a chip. Optical aberration correction with a bare segmented mirror array is shown in Section 3.7. Conclusions and recommendations for future work are offered in Section 3.8.
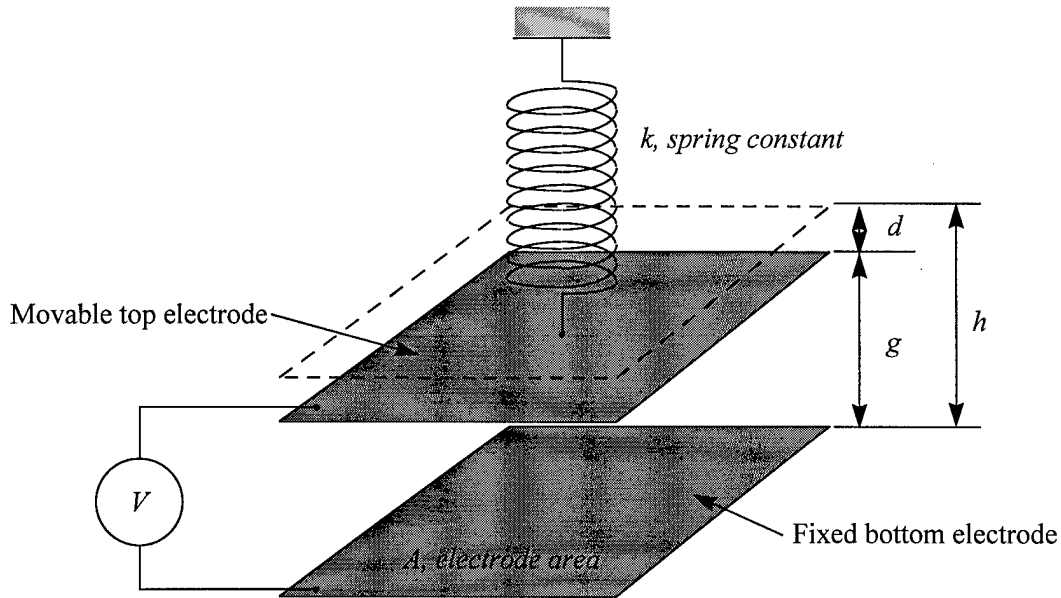
Figure 3-1. Schematic view of basic electrostatic piston micromirror.

3.2 Principle of Operation

As shown in Figure 3-1 the basic piston micromirror structure consists of two parallel-plate electrodes separated by a dielectric gap. Usually the gap is filled with free space or air, but other dielectric media are possible. In Chapter 2 a continuous facesheet mirror employing a gap filled with viscoelastic material was presented. Filling the gap with more thermally conductive gases, such as helium, increases the optical power handling capacity of the micromirror (see Chapter 5). For the development and testing presented in this chapter it is assumed that the gap is filled with air.

To allow piston travel the upper electrode or mirror plate is supported by spring flexures with a total linear spring constant, k. The fixed lower electrode is attached to the substrate. When a voltage (V) is applied across the electrodes the attractive force (F) between the plates is found by integrating the charge

difference across the overlapping electrode areas. For typical piston micromirror geometries, fringing fields and deformation of the mirror plates can be neglected [6]. Integrating the charge yields the electrostatic force,

$$F = \frac{A\varepsilon_0 V^2}{2g^2},$$ (3-1)

where A is the overlapping electrode area, ε_0 is the dielectric constant of air 8.854×10^{-12} F/m, V is the voltage across the electrodes, and g is the gap between the electrodes. Because the upper electrode moves it is represented by the as-fabricated plate height minus the deflection of the plate, $g=h-d$.

$$F = \frac{A\varepsilon_0 V^2}{2(h-d)^2}.$$ (3-2)

For small deflections the counter force applied by the linear spring flexures is $F=kd$, from Hooke's Law. The force balance equation for the system is,

$$kd = \frac{A\varepsilon_0 V^2}{2(h-d)^2}.$$ (3-3)

Solving Equation (3-3) for voltage yields arguably the most useful design equation for electrostatic piston devices,

$$V = (h-d)\sqrt{\frac{2kd}{\varepsilon_0 A}}.$$ (3-4)

Equation (3-4) provides a ready means of calculating the control voltage required for a desired deflection once the electrode area, and spring constant are known.

The spring constant represents the largest source of error in modeling the piston micromirror system. The number of flexures, shape of the flexures, and the mechanical properties of the flexure material determine the total spring constant. Of the factors influencing the spring constant, the mechanical properties of the flexure material comprise the largest uncertainty. Reported elastic modulus values for MUMPs polysilicon range from 150 to 170 GPa [7,8,9]. Reported residual stress values for MUMPs polysilicon also vary from about 3 to 12 MPa compressive. The uncertainty and run-to-run variation in the

mechanical properties of MUMPs films limit the accuracy of design modeling using Equation (3-4), and negate the effectiveness of more complex modeling methods.

For pure piston travel, each of the flexures of length l supporting the movable upper electrode are constrained to have zero slope at both ends. Thus, an n flexure system is modeled as $n/2$ fixed-fixed beams of length $L=2l$, loaded by a force (F) in the beam center. The applied force must then be divided among each pair of flexures so the force supported by each fixed-fixed beam is $2F/n$. From the deflection formula for a fixed-fixed beam substitution yields [1],

$$d = \frac{FL^3}{16Ewt^3} = \frac{(2F/n)(2l)^3}{16Ewt^3} = \frac{Fl^3}{nEwt^3} \; ,$$
(3-5)

where E is the elastic modulus of the flexure material, w is the flexure width, and t is the flexure thickness. Again using Hooke's Law, $d=F/k$, the cross-sectional spring constant from Equation (3-5) is,

$$k_{cs} = \frac{nEwt^3}{l^3} \, .$$
(3-6)

A first order approximation is used to account for the contribution of residual material stress to the total spring constant [1],

$$k_s = \frac{n\sigma(1-\upsilon)wt}{2l} \, ,$$
(3-7)

where σ is the residual material stress, and υ is the Poisson ratio of the flexure material. The total spring constant $k=k_{cs}+k_s$, can be conveniently written as,

$$k = n\left[\frac{Ewt^3}{l^3} + \frac{\sigma(1-\upsilon)wt}{2l}\right] \, .$$
(3-8)

The residual stress, σ, is negative for compressive residual stress, and positive for tensile residual stress, thus decreasing or increasing the spring constant accordingly. Typically, the stress term in the spring constant expression is small compared to the cross-sectional term and can often be neglected for design estimates. Despite the limited accuracy of Equations (3-8) and (3-4), they do provide a quick and easy means of estimating control voltage requirements. All of the mirror and actuator systems developed in this

research effort were designed using these simple equations. Typically measured voltage vs. deflection results are within 20% of the estimated values.

Once the spring constant is known, either from Equation (3-8) or a fit of measured data to Equation (3-4), the resonant frequency of the flexure beam system can be estimated. Using a simple mass suspended by a spring model the resonant frequency in Hertz is given by,

$$F_{Res.} = \frac{1}{2\pi}\sqrt{\frac{k}{M}}, \qquad (3\text{-}9)$$

where k is the total spring constant, and M is the suspended mass. The mass is obtained by summing the volume-material density products of the layers comprising the suspended upper electrode. The density values used for MUMPs layer materials are tabulated below for reference.

Table 3-1. Density of Selected Micromachining Materials

Material	Density kg/m^3	Source/Comments
polysilicon	2.33×10^3	[10], bulk silicon value
oxide	2.20×10^3 2.4-2.8×10^3	[10], SiO$_2$ [11], glass
gold	19.3×10^3	[12], bulk gold value

The resonant frequencies of over 75 piston actuators designed by the author, and fabricated on the 12th MUMPs project run (MUMPs 12) were electronically measured using a network analyzer system [13]. The test actuators had 3 different flexure geometries with 5 flexure widths for each geometry. The measured resonant frequencies were compared to the resonant frequencies predicted by the mass-spring model, using Equation (3-8) to compute the flexure spring constant. The largest error between measured and modeled resonant frequency was 12.2%, and the mean error for all piston actuator data was less than 6% [13,14]. The good agreement observed justifies use of the flexure and the mass-spring models to predict resonant frequencies for similar flexure beam devices.

Equation (3-4) neglects a common phenomenon of electrostatic devices. As the deflection of the upper electrode approaches about 1/3 the total gap distance, the electrostatic force is increasing much more rapidly than the restoring force of the spring flexures. As a result the system becomes unstable, and the

upper electrode snaps down to the fully deflected position [15]. If the upper and lower electrodes come into contact with each other they can be permanently stuck together, destroying the device. This characteristic snap-through instability behavior limits controllable deflection to less than 1/3 the sacrificial oxide layer thickness for surface micromachined devices. For the MUMPs process, device deflection is limited to less than ~0.9 μm for Poly2 only plates, and less than ~0.67 μm for plates employing Poly1. For segmented mirror designs the restricted deflection range has little impact because only a $\lambda/2$ deflection range is required for 2π modulation, and a modulo $\lambda/2$ control scheme can be employed. For continuous facesheet designs the restricted controllable deflection range limits aberration correction ability. Thicker sacrificial oxide layers in a custom process have been proposed to address the deflection limitation [16].

In a recently proposed approach, the controllable deflection range of an electrostatic device is increased by adding a fixed value "feedback" capacitor in series with the variable capacitance of the deflecting device [17]. The feedback capacitance passively controls the voltage across the gap as a function gap size. Theoretical analysis and modeling show that with a feedback capacitance 2 times greater than the zero-voltage capacitance of the movable electrode device, stable deflection over the entire gap is possible. Despite its merits this stabilization scheme is not without drawbacks. Required control voltages are increased substantially. A fixed capacitor stabilized device requires about 1.5 times greater control voltage to achieve $t/3$ deflection. If the same layout geometry is used to construct the feedback capacitance, by simply replacing flexure beams with rigid supports, the footprint of each array element is tripled. Also, the capacitor feedback stabilization scheme does nothing to improve deflection linearity as a function of voltage.

3.3 Micromirror Array Design Trades

Yield, deflection uniformity, and optical flatness are critical if micromirror/actuator arrays are to fully enjoy the cost and performance benefits of microfabrication. The experience gained while developing and testing the many surface micromachined micromirror/actuator arrays fabricated during this research effort

is summarized in this section as design guidelines. Examples of design features resulting from these trades appear in the arrays presented in the following section (and in later chapters).

MUMPs *Trade fill factor, mirror size, array size(wiring depth)*
Metal(0.5 μm) *Self-planarization may help fill factor*
Poly2(1.5 μm)
Oxide2(0.75 μm)
Poly1 (2.0 μm)
Oxide1(2 μm)
Poly0(0.5 μm)
SiN(0.6 μm)
Substrate

SUMMiT *Planarization decouples mirror and actuator design*
MMPOLY3(2 μm)
SACOX3(1.5-2 μm, CMP)
MMPOLY1+2(2.5 μm)
SACOX1(2 μm) etch access holes
MMPOLY0(0.3 μm)
SiN(0.8 μm)
Oxide(0.6 μm)
Substrate

Figure 3-2. Cross-section views of simple flexure-beam micromirror structures fabricated in the MUMPs two releasable layer polysilicon surface micromachining process, and the SUMMiT three releasable layer surface micromachining process.

Cross section views of typical electrostatic flexure-beam micromirror devices fabricated in both the MUMPs and SUMMiT polysilicon surface micromachining processes are shown in Figure 3-2. Without the planarization step available in the SUMMiT process, MUMPs designs require a trade of micromirror/actuator size, flexure geometry, and wiring depth. For a given flexure size and wiring depth, the array fill-factor is improved by making larger mirror elements. The increased electrode area of larger mirror elements also lowers the required control voltage for a given deflection, which is usually desirable. Because the optical input to a micromirror array is readily scaled, the only real limitation to making larger micromirror elements is the requirement to maintain optically flat mirror surfaces. As individual elements become larger it becomes more difficult to control deformation of the mirror surface due to residual material stresses.

While trying to lower control voltage or increase fill-factor it is tempting to decrease flexure width to the minimum feature size allowed, but doing so can adversely impact device yield and deflection uniformity. Nominally flexure beams are viewed as having a rectangular cross-section. But actually, as-fabricated flexure beams exhibit a rounded trapezoidal structure due to overetching and etch enhancement effects at sharp corners. Because overetch and etch enhancement effects can not be precisely controlled, considerable variation in flexure cross-section can occur across an array. By drawing wider flexures, the same etch effects do not significantly change the flexure cross-section. Device yield is reduced when etch effects decrease the stiffness of already weak flexures so that stiction forces in the release and drying process are not adequately countered, and devices stick to the substrate. For the MUMPs process, flexures at least 4 µm wide (2 times the design rule limit) typically exhibit both good yield and deflection uniformity.

Mirror/actuator plate flatness is critical for good electrical, mechanical, and optical performance. If topographic effects are avoided the polysilicon layers used to fabricate the mirror plate are flat prior to release. After release, residual stresses in the polysilicon layers can cause curvature of the actuator plate. Residual stress curvature and the impact of mirror curvature and topography on optical performance are examined in Chapter 4. When the electrostatic force is applied it is possible for the plate to deform if it is not much stiffer than the flexures supporting it. In addition to undesirable optical effects, plate deformation must be avoided for robust devices. In the MUMPs process, Dimple stops hold the upper electrode only 250 nm above an underlying Poly0 address electrode. If the mirror plate is not stiff enough to resist bending when fully deflected, it is possible to short the device and fuse the electrodes together. Low control voltages and native oxides on the polysilicon surfaces help to avoid fusing. Also, a series resistor can eliminate fusing problems, but it is more desirable to build devices that do not require protection resistors. Stacking of polysilicon layers (and the trapped oxide approach) increase the stiffness of the mirror/actuator plate substantially. Because stiffness is a cubed function of thickness, a 3.5 µm thick stacked polysilicon plate is more than 12 times stiffer than a 1.5 µm thick Poly2 only plate.

Without planarization, wiring of the control electrodes for individually addressed mirror or actuator elements can seriously constrain array design. As depicted in Figure 3-2 the wiring consumes a significant fraction of the array area. For the planarized SUMMiT process, wires and actuator structures beneath the mirror surface do not deform the reflecting surface. The fill-factor for micromirror arrays fabricated in the MUMPs process can be improved by employing "self-planarization". In this approach the underlying topography is controlled to minimize print-through deformation of the mirror surface. For the MUMPs process maximum gaps in any layer of 1.5 µm reportedly yield "good" self-planarization results [16]. One risk associated with the self-planarization approach in MUMPs is unreliable etching of small (<2 µm) gaps. The limitations of self-planarization in MUMPs are depicted in Figure 3-3, which shows the attachment of a Poly2 facesheet to a self-planarized Poly1 thermal actuator. Despite as-drawn gaps of only 1.5 µm in the Poly1, the Poly2 surface has visible indentations. In addition, incomplete etching of the Poly1 is observed on the angled gaps. Employing a gap of 2-2.5 µm reduces etch problems results in poorer self-planarization. Despite its limitations self-planarization is helpful in that only the surface areas over underlying gaps are not planar. The planar regions at the same height increase the optical fill-factor, so self-planarization has been used in a number of MUMPs designs.

partial Poly2
self-planarization

1.5 µm wide gaps in Poly1

1.5 µm wide Poly1 anchors

Incomplete etch of Poly1 gap,
1.5 µm wide as-drawn, but mask
stepping can reduce the width
of angled lines
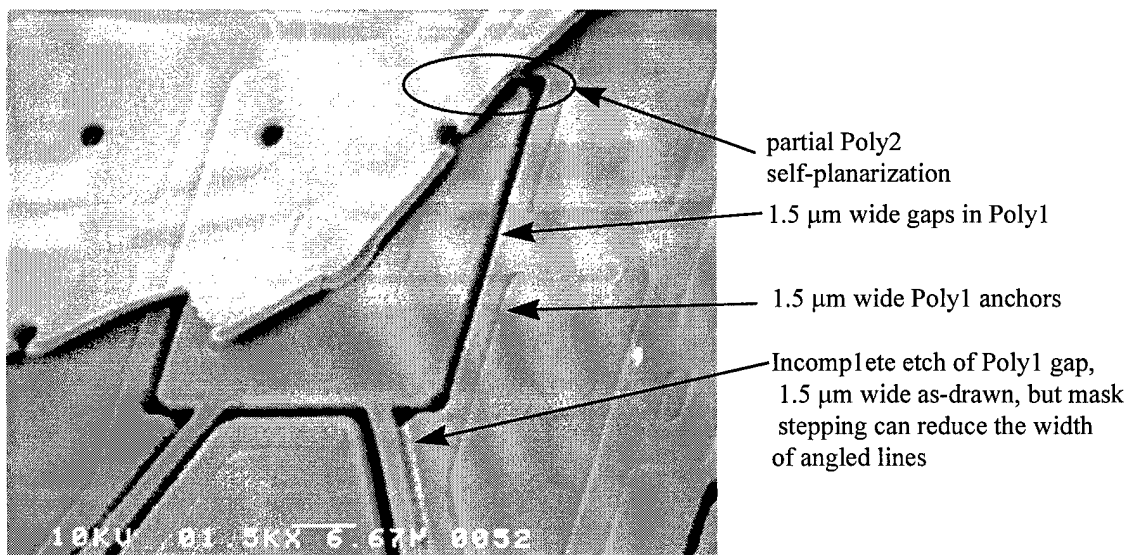
Figure 3-3. MUMPs self planarization of a thermal actuator structure.

3.4 Testing and Device Characterization

One of the principal benefits of microfabrication of micromirror and actuator arrays is the uniformity of device response obtained. Uniformity of device response eliminates the requirement for labor intensive, and expensive, characterization testing of each and every device in the array. Only one device (or a few devices) need to be tested to obtain a single characteristic deflection versus drive voltage response curve that is used to control all of the devices in the array. Two test methods have been used for deflection testing in this research. Initially, devices were tested in the microscope laser interferometer system developed and used extensively by prior AFIT researchers [6,18,19]. Similar interferometer deflection test systems have been developed by others [20,16]. Despite upgrades to the system and analysis software by the author this test method remains a time consuming endeavor. To minimize test time and labor the "static fringe" technique was developed for rapid deflection characterization of piston devices.

The AFIT microscope laser interferometer system is a Michelson interferometer in which the optical path length in the test leg is modulated by the deflection of a micromirror device. The intensity of the central spot of fringe pattern formed by the interfering reference and test beams is measured by a PIN diode detector. The intensity measured at the detector varies as a function of the optical path length difference between the beams. Because only a change in intensity can be accurately measured, only a change in optical path length difference can be measured. Thus, the device under test must be modulated. To mitigate the effect of squeeze film damping on deflection measurements the system is equipped with a vacuum chamber which has an optical window. Micromanipulated probes in the chamber are used to electrically contact the devices under test. Typically, a sinusoidal waveform is used to drive the device under test. Because the system measures only a change on deflection as a function of the change in voltage, the control and detector waveforms must be analyzed to extract device deflection versus drive voltage.

During early laser interferometer testing several problems were encountered with the existing analysis code. The code exhibited data dependent failures which were traced to noise on the input voltage and output intensity (voltage) waveforms. Noise recorded in the input voltage waveform is purely

instrumentation related. Noise on the output waveform is a combined effect of instrumentation (PIN diode, current amplifier, oscilloscope) and mechanical vibration. Previous researchers overcame the mechanical vibration by manually selecting data for analysis. Instrumentation noise was mitigated by waveform averaging and smoothing in the digital oscilloscope, as well as in the analysis code. Based on the assumption that hysteresis effects were insignificant, rising and falling input voltage waveforms (and corresponding output intensity waveforms) were also averaged.
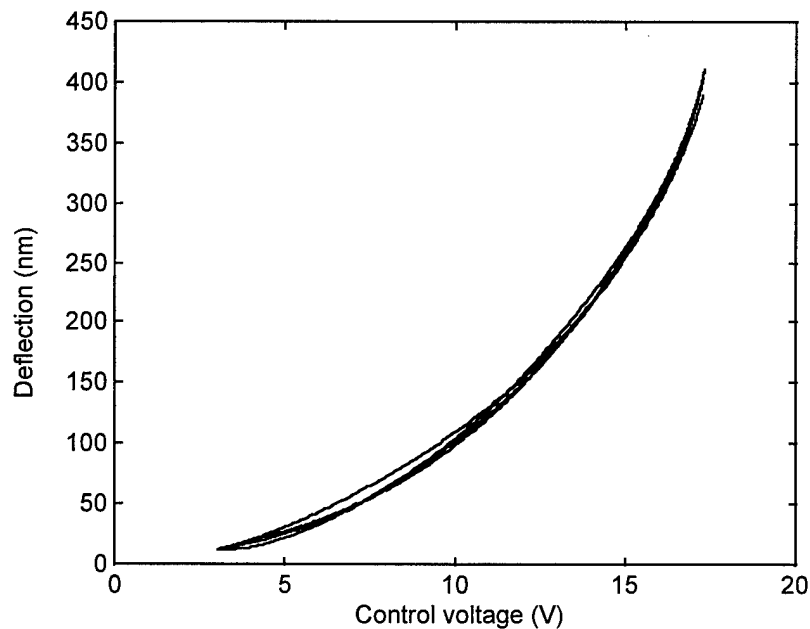
Figure 3-4. Laser interferometer deflection vs. voltage measurements for four MUMPs 17 lenslet mirror test devices.

All microscope interferometer data presented here was processed using new Matlab® analysis codes written by the author. The basic principles described here in general terms are applicable to other implementations. Smoothing of the data is limited to averaging of the complete cycles in a single oscilloscope trace. Averaging is not required and single cycle traces can be analyzed. Only the increasing voltage and increasing deflection segments of the waveform are used to avoid instrumentation hysteresis effects. Digitally filtered versions of the drive and detector voltage waveforms, and their derivatives, are used to automatically locate the maxima and minima which correspond to phase wraps. Using this

information, the averaged output data is unwrapped and the deflection calculated. Although the new codes are substantially more robust and automatically process most data sets, the analysis must be monitored carefully to avoid errors.

The four laser interferometer data sets plotted in Figure 3-4 illustrate both the improved consistency of the authors analysis code and very good device deflection uniformity. The test device is a MUMPs 17 lenslet mirror array (see Figure 3-9). The four test devices reside in one corner of the array and are electrically wired together. Testing was performed in a 20 mT vacuum using a nominal 0 to 18 V sinusoidal drive signal at 5.1 kHz. Note that deflection data below 3 volts has been clipped and each data trace offset to the mean 3 volt deflection. Offsets produced by noise near zero deflection represent the largest error source in analyzing the interferometer data.
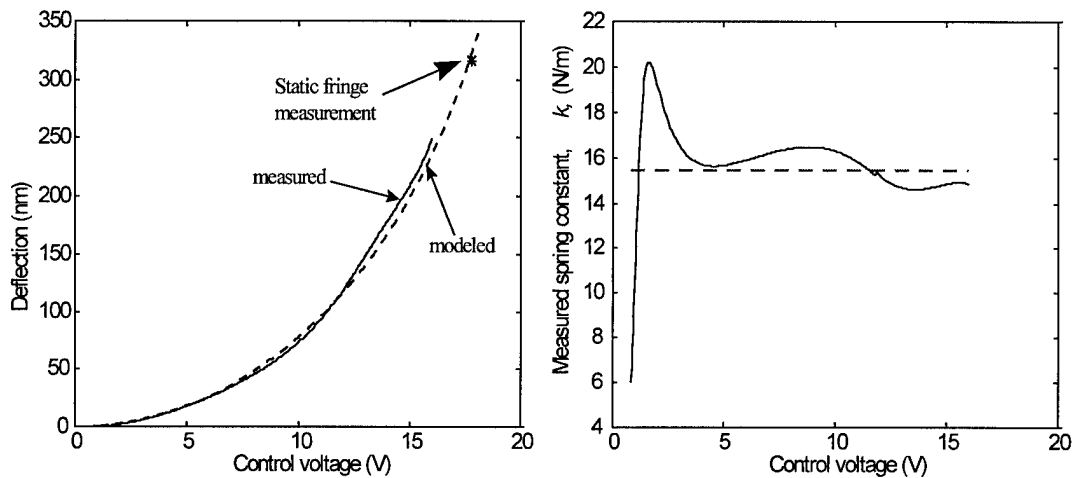
Figure 3-5. Measured and modeled deflection of a MUMPs 17 lenslet mirror (left). Static fringe deflection measurement for the same array is also plotted. Plot of spring constant calculated from measured data points (right). Dashed line is the mean value of the measured spring constant from 5-16 V.

Laser interferometer measurements provide a means of validating the analytical model presented in Section 3.2. Figure 3-7 shows the deflection versus voltage curve obtained for a single MUMPs 17 lenslet mirror array device obtained by laser interferometer testing with a 1.3 kHz sinusoidal drive signal. Also plotted is the deflection curve given by Equation (3-4) using the measured spring constant, $k=15.4$

N/m. The spring constant value was obtained by taking the mean of the spring constant computed from deflection and voltage data between 5 and 15 volts. The measured spring constant is also plotted as a function of control voltage in Figure 3-5 for reference. The estimated spring constant given by Equation (3-8) is 20 N/m, using the as-drawn flexure dimensions and nominal MUMPs film parameters. The 23% discrepancy in measured versus the modeled spring constant is typical, and is attributed to variations in the MUMPs process. Because run-to-run and even wafer-to-wafer process variations can significantly impact device deflection, characterization testing is required for each micromirror or actuator array.

After observing the qualitative fit of measured deflection data to the model, and experiencing the tedium of analyzing microscope laser interferometer data, a new rapid characterization method was developed. The "static fringe" technique employs the Zygo Maxim 3-D, a commercial microscope interferometer with real-time video output, but is adaptable to other interferometric microscopes. The advantages of this technique are that it takes only minutes, is applicable to packaged devices, and requires no data analysis. The static fringe test is elegant in its simplicity. The packaged die are placed in a test circuit board mounted on the laser interferometric microscope (HeNe 632.8 nm). After first leveling the microscope head to the die, the head is intentionally tilted so that 3-4 fringe lines appear on the micromirror reflective surface. Subsequently, DC voltage pulses are applied across the electrodes of the mirror under test. The amplitude of the applied voltage pulse is incremented until the fringe lines no longer move on the microscope video display when the applied voltage is toggled. The static fringe voltage is the voltage required for 316 nm deflection, denoted as V_{316}. The accuracy of the static fringe technique has been verified by directly measuring the deflection of wide flexures on some micromirror designs. A static fringe test result for the MUMPs 17 lenslet micromirror array (V_{316}=17.8 volts) is plotted on Figure 3-7. Extraction of the spring constant for the device, using the single static fringe measurement in Equation (3-4), yields 15.6 N/m which is in excellent agreement with the spring constant obtained from the laser interferometer measurement. Since its development and validation on MUMPs 17 and 18 devices, static fringe testing has supplanted laser interferometer testing for characterization of all of the author's prototype arrays.

The video output of the Zygo laser interferometric microscope also provides a means of quickly checking device yield, and deflection uniformity of an array. To ascertain device fabrication and release yield the die which need not be packaged is leveled to the microscope head and the array is scanned. Stuck down or tilted devices are marked by fringe lines on the flexures and or on the upper plate. To obtain functional yield and qualitative deflection uniformity the array must be packaged and the packaged device mounted in a test circuit board. By selectively actuating devices the functional yield and deflection uniformity can be obtained. Any wiring errors or crosstalk will be apparent as well. If the array controller is available, driving the array in various deflection patterns provides a quick qualitative measure of deflection uniformity and device yield. At larger magnifications the Zygo interferometric microscope also provides a precise measurement of micromirror surface figure. Micromirror surface figure measurements and the effect of micromirror figure on optical performance are described in Chapter 4.

3.5 Micromirror/Actuator Array Designs

During the course of this research more than two dozen micromirror and actuator arrays were designed. Attention span limitations preclude detailed description of every array in this section. Instead, a design chronology is presented with emphasis on the lessons learned from each fabrication run. Descriptions of every array, and the status of remaining die are provided in Appendix 1.

The author's designs of surface micromachined mirror arrays began on MUMPs 11. Prototype square flexure beam mirrors with a nominal 100 μm center-to-center spacing were designed. Several variations on prior AFIT flexure beam designs were explored, including use of only 2 support flexures, stacking of the Poly1 and Poly2 layers to reduce metal stress induced mirror curvature, and use of a removable Poly1 former to increase the controllable deflection range. MUMPs 11 mirrors were used for the study of residual stress induced curvature in Chapter 4. Two flexure mirrors with removable Poly1 formers are shown in Figure 3-6. Use of the manually removed former extends the controllable deflection range to over 1.5 μm.
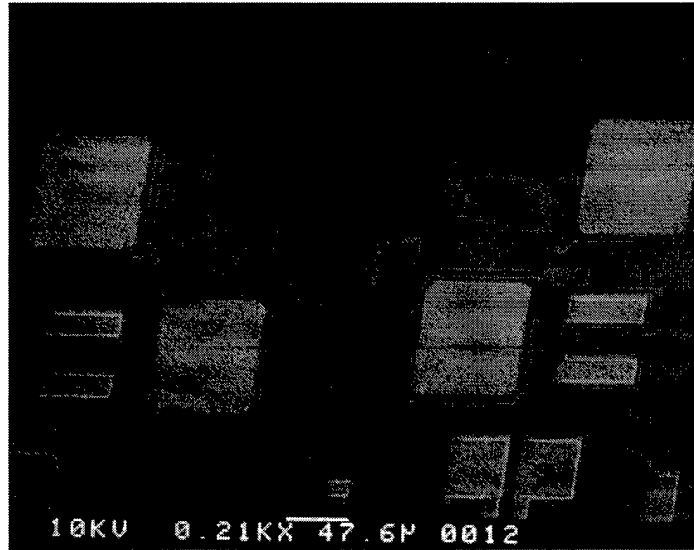
Figure 3-6. MUMPs 11 extended travel piston micromirrors with pull-out Poly1 formers.

On MUMPs 12, four 12×12 arrays of actuators with 100 μm spacing were fabricated on a single MUMPs die for facesheet attachment experiments. A two flexure piston actuator is shown in Figure 3-7(a). Although the M12 arrays were not used for facesheet experiments, test actuators of this type were used extensively for resonant frequency testing [13]. More significantly, the MUMPs 12 actuators showed that with adequate dimple design and a flat upper electrode, very robust electrostatic actuators were possible. While testing the MUMPs 12 piston actuators by fully deflecting the upper electrode at kilohertz rates, not a single device failed. Four different 12×12 arrays of square mirrors with nominal 100 μm spacing were also fabricated on MUMPs 12. A section of one array is shown in Figure 3-7(b). These arrays employ row-column address wiring limiting them to bistable operation [21]. Although mirror curvature and the address scheme limit the utility of these arrays it is worth noting the relatively high fill-factor (~80%) obtained when array wiring is minimized. On MUMPs 14 a 12×12 array, again with 128 addressable elements, employing Poly1 formers was designed. Although the large formers (6×12 elements) have been successfully removed, the former approach to increasing electrostatic deflection is impractical.

3-15

(a)   (b)
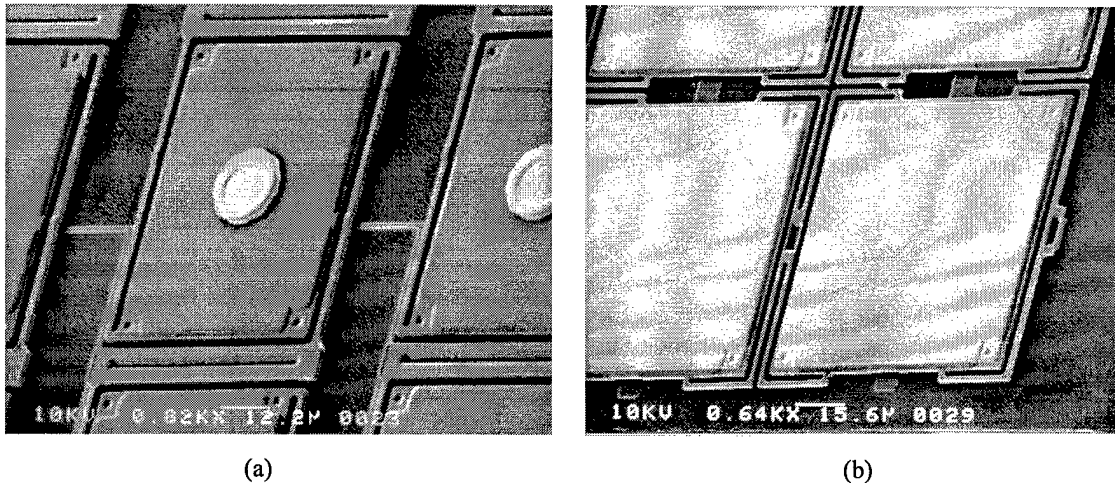
Figure 3-7. MUMPs 12 designs; (a) two flexure piston actuators, and (b) the corner element of a 12×12 row-column addressed micromirror array.

MUMPs 15 marks the transition of array designs to 203 μm center-to-center spacing. The 203 μm spacing was chosen for compatibility with on-hand lenslet arrays. Two 12×12 electrostatic piston mirror arrays were designed and fabricated on MUMPs 15. The arrays are identical except that one array employs the substrate as a common ground electrode and address wires contact the top plates, while the other employs Poly0 address electrodes and the moveable upper electrodes are electrically grounded. Both MUMPs 15 lenslet arrays have 128 individually addressed elements. A MUMPs 15 lenslet mirror is shown in Figure 3-8(a). The reflective mirror surface is 80 μm in diameter. The upper electrode is comprised of a stacked Poly1-Poly2 plate with trapped oxide under the mirror surface. Note the thinning of the 2 μm (as-drawn) flexures due to overetching. Processing problems on MUMPs 15 resulted in significant die-to-die variation in the fabrication of thin lines like these flexures. An especially bad unreleased die is shown in Figure 3-8(b). MUMPs 15 test devices were selected after culling obviously bad die by optical microscope examination. Device yield results for 2 packaged MUMPs 15 die were 89% and 90%. Laser interferometer and Zygo testing showed that using the substrate as a common ground electrode resulted in higher crosstalk, and mirrors sticking down due to dielectric charging effects. As a result the substrate common ground electrode approach was abandoned.
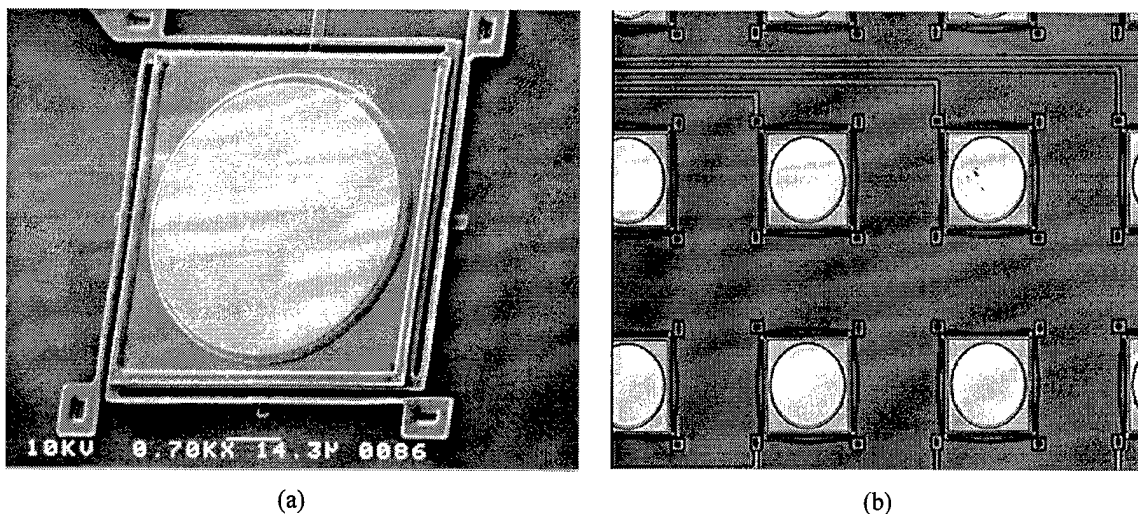
Figure 3-8. MUMPs 15 lenslet micromirror devices; (a) scanning electron micrograph of lenslet mirror, and (b) optical micrograph of unreleased array showing deformed flexures due to fabrication problems. Note the different address wiring schemes. The device in (a) is addressed by an underlying Poly0 address electrode, while the devices in (b) employ a common substrate ground electrode and are selected by wires to the top electrode.
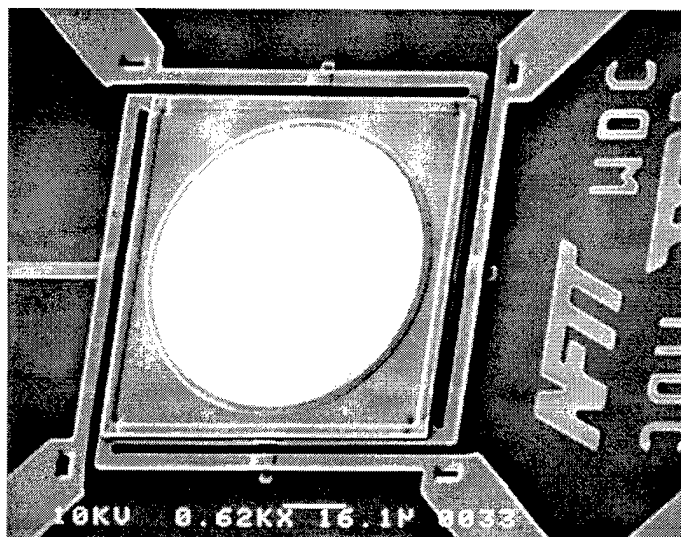
Figure 3-9. MUMPs 17 lenslet mirror. Note that the only change from the MUMPs 15 lenslet design depicted in Figure 3-8 is an increase in flexure width.

A revised version of the MUMPs 15 lenslet mirror array was fabricated on MUMPs 17. The only change to the mirror/actuator structure was widening of the Poly1 flexures to 4 μm. A MUMPs 17 lenslet mirror array device is shown in Figure 3-9. The MUMPs 17 arrays tested exhibited very good deflection uniformity and functional device yields of 100%. Variation in measured device deflection performance from die-to-die was noted. For two similarly released and packaged arrays, the static fringe voltages

3-17

recorded were 17.8 V and 18.5 V. From Equation (3-4) the spring constants corresponding to these voltages are 15.4 N/m and 16.6 N/m respectively. This wafer-to-wafer variation is most likely to thickness variation in the Poly1 layer. Because thickness is a cubed term in the spring constant, relatively small variations in thickness can impact deflection performance. The computed difference in spring constant is,

$$\frac{2(16.6 - 15.4)}{(16.6 + 15.4)} \times 100\% = 7.5\%.$$

Using the spring constant's dependence on thickness cubed, the deviation in Poly1 thickness need only be,

$$\frac{2(\sqrt[3]{16.6} - \sqrt[3]{15.4})}{(\sqrt[3]{16.6} + \sqrt[3]{15.4})} \times 100\% = 2.5\%,$$

to account for the observed difference in device performance. On MUMPs 17 the reported standard deviation of monitor wafer thickness measurements corresponds to a $(528/19739) \times 100\% = 2.7\%$ variation in thickness. MUMPs polysilicon thickness monitor wafers are placed at both ends of the wafer boat during deposition so the reported values represent the wafer-to-wafer thickness variation. Fortunately, thickness variation across a wafer (and across the 1 cm die width) is much lower, so that devices on a die exhibit good deflection uniformity. The comparison above emphasizes the need for a deflection characterization measurement for each array, hence the importance of the static fringe technique.

Although designed primarily as a robust electrostatic actuator array for facesheet fabrication experiments, the MUMPs 18 array shown in Figure 3-10(a) has 60 μm diameter reflective surfaces. The 10 μm wide by 114 μm long Poly1 flexures are stiff compared to previous designs, but the large electrode area lowers the required control voltage. Gaps in the Poly0 address electrodes and array wiring are restricted to 2.0 μm to self-planarize the Poly1 layer. Also, the spaces between actuators are filled by Poly1 segments so that the topography of the array surface varies by only 2.75 μm. The primary purpose of the MUMPs 18 self-planarization efforts was to facilitate facesheet fabrication on the actuators, but the enclosed structure also helps keep dust out of the gaps between electrodes. The MUMPs 18 design proved to be a very high yield, robust and reliable array. Use of the MUMPs 18 array in conjunction with a lenslet array for optical experiments is described in Chapter 5. In contrast, the arrays designed for MUMPs 19 represent an attempt to obtain the maximum fill-factor and mirror flatness. A series of four electrostatic

flexure beam micromirrors with varying top plate construction were fabricated. All four arrays have as-drawn fill-factors of about 70%. With the exception of one array included for comparison, the MUMPs 19 arrays do not use the MUMPs metallization. Post foundry metallization techniques and a study of the impact of mirror surface figure on optical performance are in Chapter 4. Optical experiments using the 12×12 MUMPs 19 design shown in Figure 3-10(b) are described in Section 3.7.

(a)   (b)
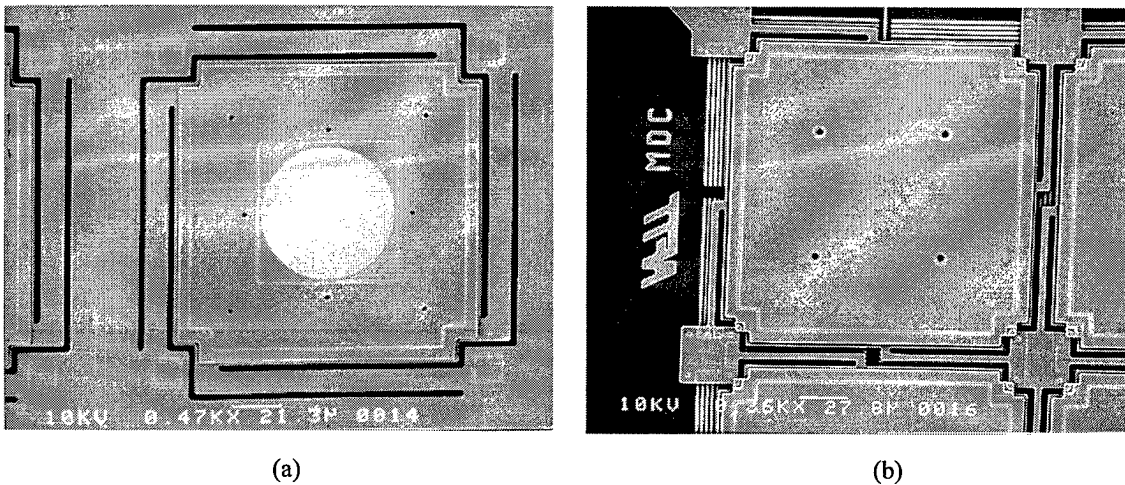
Figure 3-10. Contrasting MUMPs 18 and MUMPs 19 designs. The MUMPs 18 array (a) was designed primarily as a robust actuator array but can be used in conjunction with a lenslet array. The MUMPs 19 (b) design optimizes fill-factor so that lenslets are not required.

Two types of micromirror arrays were fabricated on MUMPs 20. One is basically a 12×12 version of the M19_B design (see Chapter 4) with 128 individually addressable mirrors. The other employs a Poly1 only upper electrode and mirror surface. As shown in Figure 3-11, the design includes a removable Poly2 metallization mask to facilitate post foundry metallization. Residual tensile stress in the MUMPs metal stripes around the edges of the mask cause it to curl up when completely released for easy removal. The as-drawn fill-factor of the MUMPs 20 design with Poly2 metallization mask is 80%. Figure 3-12 shows one of the electrostatic actuators without metal fabricated on MUMPs 21. This array is intended for fabrication of a polymer bonded facesheet. Also fabricated on MUMPs 21 are several continuous facesheet and segmented mirror designs on quarter dies which are discussed in Chapter 9.

Poly2
metallization
mask

MUMPs gold
metallization on
Poly2 mask
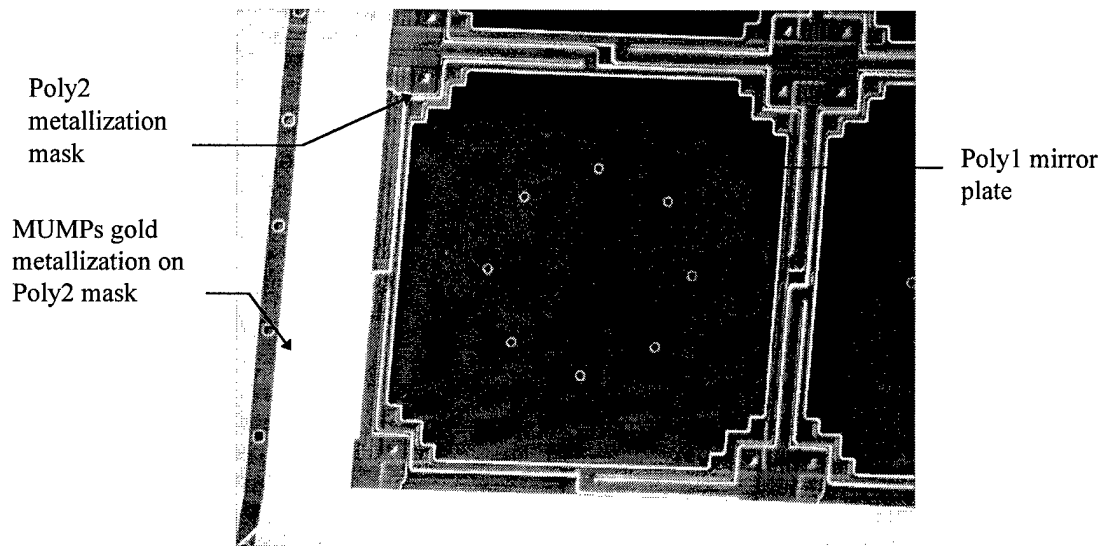
Poly1 mirror
plate

Figure 3-11. MUMPs 20 flexure beam micromirror. Mirror plate (upper electrode) is fabricated with only Poly1. After a partial release etch to expose the Poly1 surface, the array can be metallized using the Poly2 metallization mask. Removal of the mask is assisted by residual metal stress in the MUMPs gold, which causes the mask edges to curl.
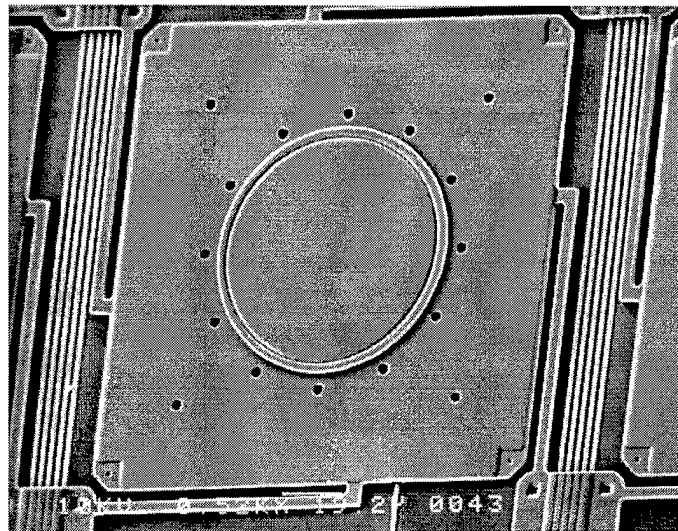
Figure 3-12. MUMPs 21 electrostatic actuator design

The latest MUMPs fabrication runs (22-24) have been primarily devoted to digital deflection mirror arrays discussed in the following section. Two other prototype mirror arrays on these late runs are

worth noting. First, is a series of defocus correctors. The defocus correctors are 12×12 piston micromirror arrays which have elements equidistant from the array center wired together. Only 16 control voltages are required to drive the array, but surface figures are forced to be radially symmetric. The second notable device is an 8×8 micromirror array which employs the feedback capacitor stabilization scheme described in Section 3.2. The extended deflection range of this array (nominally 1.25 μm) makes it a good candidate for infrared (IR) laser steering experiments. The IR array has a ~70% fill-factor, and uses MUMPs metallization for the reflective surface.

3.6 Digital Deflection Micromirrors

This section presents an innovative approach to control of electrostatic micromirrors. Instead of controlling the voltage applied across the electrodes, this approach employs a segmented bottom electrode with N digitally scaled areas. By selectively energizing N electrode areas with a digital control word, 2^N discrete deflections are obtained. The primary contribution of the "digital deflection" approach is elimination of the many digital-to-analog (D/A) converters required to individually control large arrays of micromirror devices. Eliminating the requirement for D/A converters greatly reduces the overall cost of the adaptive optics system, and paves the way for fully integrated deformable mirror systems on a chip. The discrete mirror positions possible with the digital deflection scheme limit aberration correction performance, but simulations show that significant aberration correction is possible with only a few bits of phase control.

The digital deflection micromirror concept is shown in Figure 3-13 which depicts a 4-bit device. The only change from the basic micromirror structure shown in Figure 3-1 is the segmentation of the underlying control electrodes into 4 digitally scaled areas such that $8A_1=4A_2=2A_4=1A_8$. Deflection of the device is controlled by switching the electrodes segments on (V volts) or off (0 volts). Assuming the same on-voltage (V) is used for all electrode segments, solving the force balance Equation (3-3) for deflection yields,

$$d = \frac{\varepsilon V^2}{2k(t-d)^2}(A_1 b_1 + A_2 b_2 + A_4 b_4 + A_8 b_8), \tag{3-10}$$

where $b_8 b_4 b_2 b_1$ is a four bit digital control word. The nonlinear gap term, $(t\text{-}d)^{-2}$, in Equation (3-10) precludes linear deflection versus control word, but discrete deflection is much closer to linear than analog voltage controlled deflection. As a result the digital control scheme yields better position resolution than obtained using a linear D/A with N-bits for voltage control.
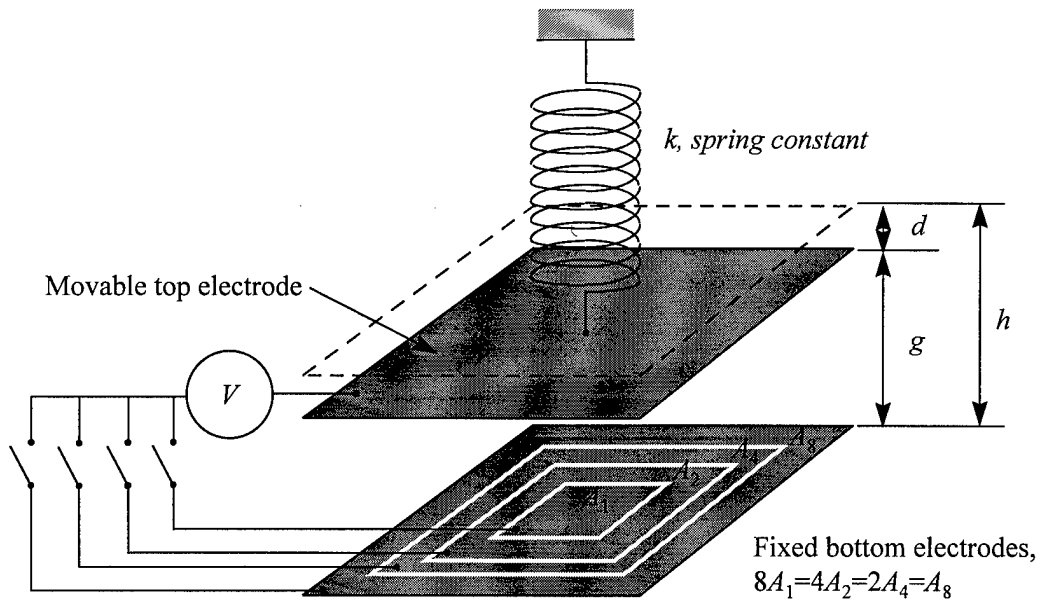
Figure 3-13. Conceptual view of digital deflection micromirror.

Initial prototype 4-bit digital deflection devices were fabricated on MUMPs 21, and have been tested. An annotated scanning electron micrograph of a prototype device is shown in Figure 3-14. Wide flexures were used to insure uniformity and to facilitate static deflection testing. To avoid any curvature of the top plate due to metal stress, the test devices were not metallized. Print-through of the underlying digitally scaled Poly0 electrodes is visible in Figure 3-14. Electrode dimensions and area computation for the MUMPs 21 4-bit prototype digital deflection micromirror device are summarized in Table 3-2.
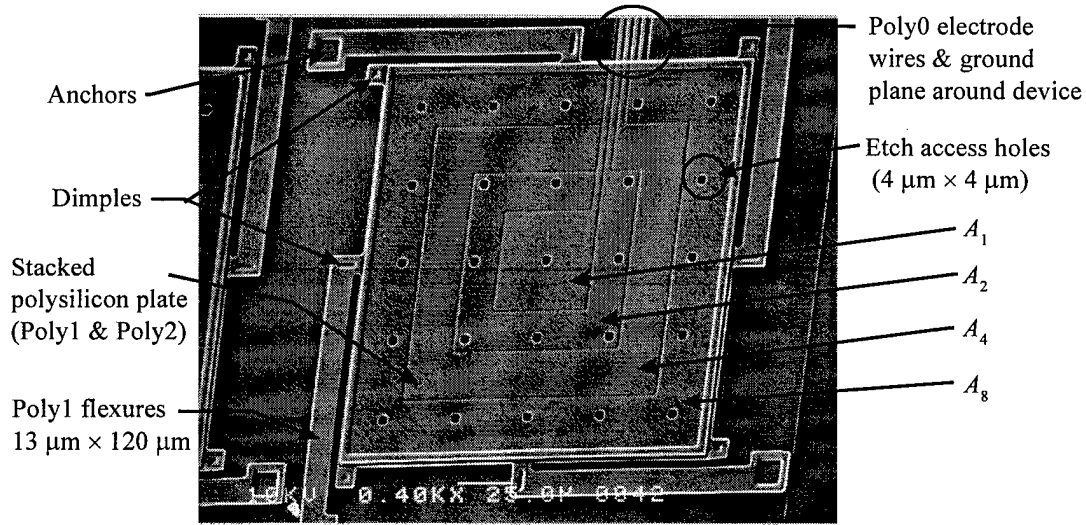
Figure 3-14. Annotated scanning electron micrograph of MUMPs 21 4-bit digital deflection micromirror. Note the outlines of the digitally scaled electrodes.

Table 3-2. MUMPs 21 Digitally Deflection Micromirror Electrode Layout Dimensions

Label	Outside (μm^2)	Inside (μm^2)	Holes (μm^2)	Wire Gap (μm^2)	Area (μm^2)
A_1	50^2	N/A	4^2	N/A	2484
A_2	90^2	54^2	8.4^2	6.36	4840
A_4	138^2	94^2	N/A	10.44	9768
A_8	200^2	142^2	16.4^2	14.58	18768

$$A_T = A_1 + A_2 + A_4 + A_8 = 35860 \ \mu m^2$$

The static fringe technique was used to determine the control voltage required for $\lambda_{HeNe}/2$ deflection with all address electrodes electrically connected in parallel. For the MUMPs 21 digital deflection mirrors with 13 μm wide flexures, $V_{316} \approx 10.4$ V. Similar devices with flexures only 6 μm require a control voltage of only ~7.5 V, suggesting that integration of digital deflection micromirrors with standard CMOS (Complementary Metal Oxide Semiconductor) control logic will be straightforward. For laboratory testing, the simple bipolar NPN transistor circuit shown in Figure 3-15 was breadboarded to provide a convenient means of applying the control voltage to the electrodes. Extrapolating from this circuit to a fully integrated digital deflection mirror system, each electrode requires only a resistor, switching transistor, and register (or memory) cell.
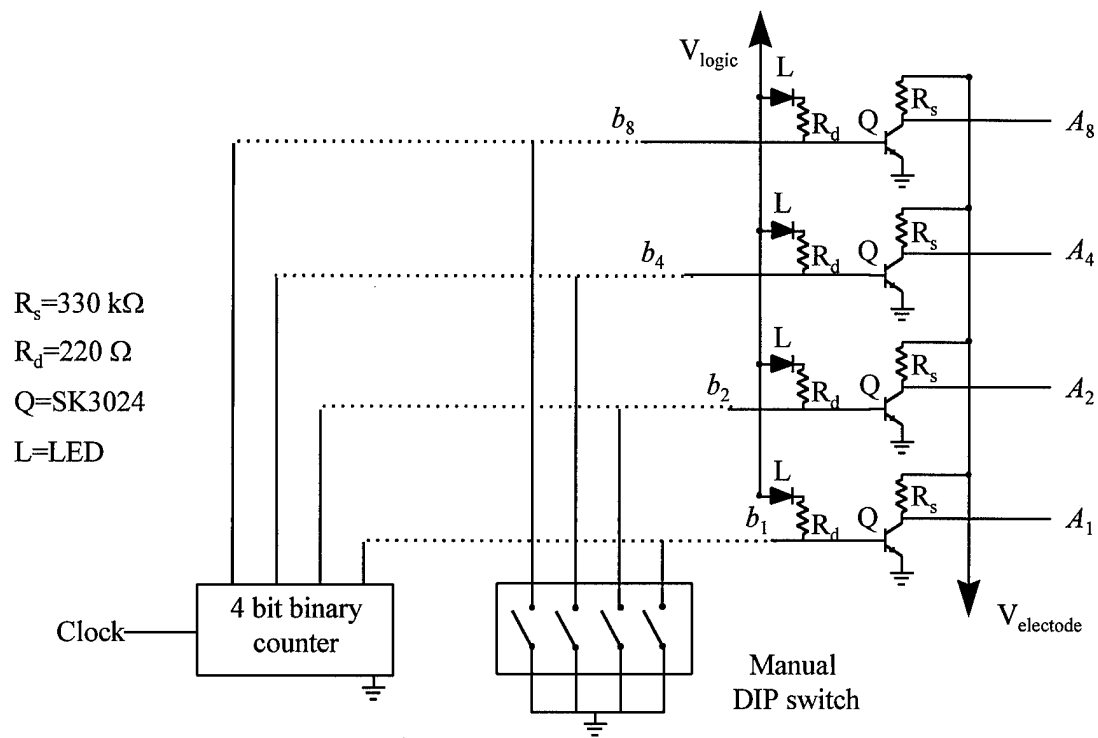
Figure 3-15. Digital deflection micromirror breadboard test circuits.
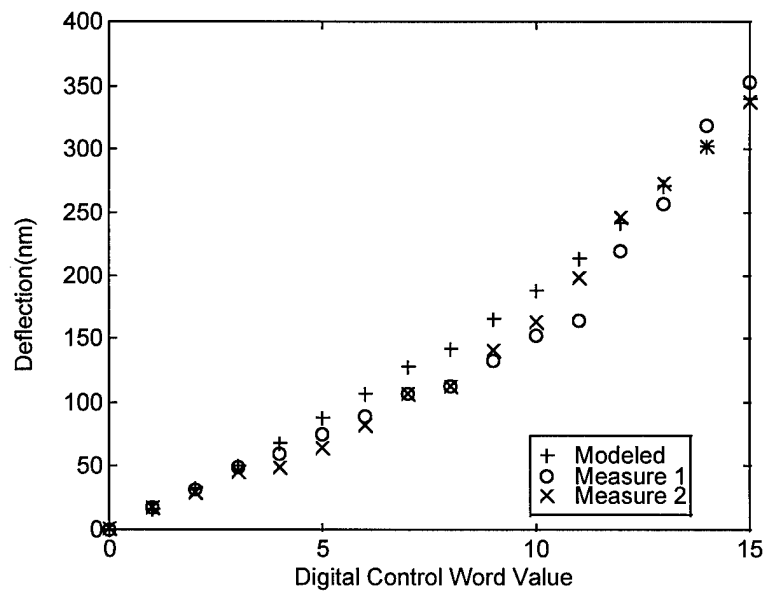
Figure 3-16. Measured deflection data for V=10.4 V (two sets), and modeled deflection using Equation (3-10). The flexure spring constant, k, is calculated from empirical data.

To measure static deflection, the Zygo computer controlled microscope laser interferometer was used to measure the deflection of a flexure for each digital control word. Two sets of deflection data from the MUMPs 21 prototype digital deflection micromirror are plotted in Figure 3-16. The modeled deflection predicted using Equation (3-10) with the measured spring constant is also plotted. An effort was also made during testing to determine if the small deviation in the centroids of the electrode segments would result in tilting of the micromirror surface. Measurements of all four flexures with voltage applied to various electrodes showed that tilting was less than the measurement resolution of a few nanometers.
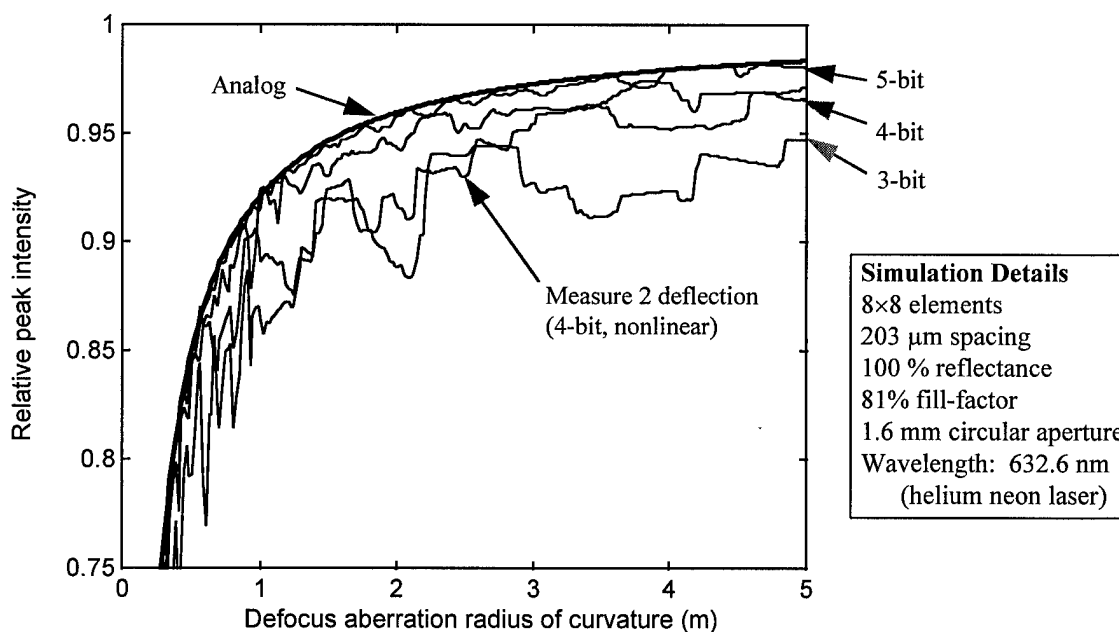
Figure 3-17. Simulated optical aberration correction performance for digital deflection micromirror arrays compared to the analog controlled case. The performance metric plotted is the peak intensity of the optical point spread function (relative to the unaberrated case) versus defocus (spherical) aberration radius of curvature.

The simulations shown in Figure 3-17 demonstrate the efficacy of optical phase control using only a few bits. An 8×8 array of digital deflection micromirrors with 203 μm center-to-center spacing illuminated over a 1.6 mm circular aperture comprises the simulated system. Defocus aberrations (approximated by a spherical wavefront) are corrected by the mirror array with varying deflection constraints imposed on the piston elements. The smooth curve shows the optimal correction case (analog

position control). The shape of the optimal correction curve is defined by the residual phase error due to the finite micromirror element size. For comparison 3, 4, and 5 bit linear deflection are shown. Also shown are simulated correction results obtained when using the measured deflections of the MUMPs 21 prototype mirror.

Though not visible in Figure 3-14 the MUMPs 21 digital deflection test structure is comprised of 3 devices with their electrode segments wired together. Using the digital counter in Figure 3-15, the electrodes were driven with a linear control word ramp while deflection was observed on the interferometric microscope video display. With the head on the interferometric microscope tilted, fringe lines on the moving mirror surfaces appear to smoothly flow in one direction. Using this qualitative method, deflection uniformity of the MUMPs 21 digital devices appears to be excellent.

Layout of the MUMPs 21 prototype digital deflection mirror was accomplished by starting with the smallest electrode and drawing the surrounding electrodes to maintain the required area relationships. To obtain a given element spacing, array designs require that the N electrodes fit into the area defined by the actuator top plate, after layout of the wiring, flexure structure, and dimple protection.

Design of the digitally scaled electrodes to fit into a defined area begins with the digital area relationship. Using the same notation for the digitally scaled areas, for $N=3$,

$$A_4 = 2A_2 = 4A_1 . \tag{3-11}$$

Neglecting the gap between electrodes, the nested square electrodes allow Equation (3-11) to be rewritten in terms of lengths as,

$$(l_4^2 - l_2^2) = 2(l_2^2 - l_1^2) = 4l_1^2 . \tag{3-12}$$

Solving Equation (3-12) the l_2 and l_4 layout dimensions can be written in terms of l_1 as, $l_4 = \sqrt{7} \cdot l_1$, and $l_2 = \sqrt{3} \cdot l_1$. The general form for each digitally scaled electrode is

$$l_{(2^{B-1})} = \sqrt{2^B - 1} \cdot l_1 . \tag{3-13}$$

where B is the bit number from 1 to N, with $B=1$ as the least significant bit, and $B=N$ the most significant bit. Other layout considerations, such as cutouts for dimple landing pads, may require the outside shape of

the largest electrode to be non-square. To fit the digital electrodes into a given area requires $\left[l_{(2^{N-1})} \right]^2 = A_{MAX}$. Plugging this relationship into Equation (3-13) gives l_1 in terms of the number of bits and the maximum available electrode area,

$$ l_1 = \sqrt{\frac{A_{MAX}}{2^{N-1}}} . \tag{3-14} $$

The relationships defined by Equations (3-14) and (3-13) make short work of digital deflection mirror electrode design. Layout is speeded by rounding the computed lengths to the nearest μm and dividing by 2 to provide reference points (from the electrode center) for chopping a continuous electrode. Stretching the corners of chopped segments equally toward (outside edge), or away from (inside edge), the center creates the gap between electrodes while preserving the required area relationships.

Digital deflection prototype mirrors with 3 and 5 bits, and arrays of 3-bit digital deflection micromirrors were fabricated on MUMPs 22 and 23. Quarter die digital deflection micromirror arrays have 21 active 3-bit elements in a 5×5 element array, and are to be packaged in 68 pin Leadless Chip Carrier (LCC) packages. A more aggressive 10×10 element array with 44 active 3-bit devices has also been fabricated. The arrays employ 203 μm element spacing and are self-planarized in an attempt to improve fill-factor. MUMPs metal is not used to avoid stress induced mirror curvature. To simplify post-foundry metallization, a Poly2 mask partially shields the perimeter of the array.

The digital deflection micromirror represents a novel approach to both optical phase control, and position control of electrostatic devices. Although coarse phase discretization may prove inadequate for some applications, the cost savings in control electronics, possible speed advantages, and reduced system complexity may enable new applications. For example, the simulation results shown in Figure 3-17 suggest that more than 90% of the defocus aberration correction possible could be obtained with a 3-bit digital deflection mirror. The remaining 10% of defocus correction is obtained in the AFIT adaptive optics testbed with the expenditure of $10,000 to provide 64 12-bit D/A channels. The basic digital electrode scheme can be extended to other electrostatic devices. One implementation, in which 3 electrostatic cantilever actuators with 3-bit electrodes are employed to control a steering mirror (2^9 positions) is

described in Chapter 9. Digital electrostatic mirror designs to date are limited by the fabrication process. The N-fold increase in wire count, and routing of these wires limit the number of active devices possible and decrease the array optical quality in the MUMPs process. In a planarized process like SUMMiT, increased wire count need not impact the optical quality of a digital deflection mirror array. Wirebonding requirements could limit the size of digital deflection mirror array designs, but can be overcome with advanced packaging concepts such as High Density Interconnect (HDI) packaging [22]. The greatest payoff of the digital deflection micromirror scheme will be realized when the mirror elements, electrode switching circuits, a register (of length $N \times$ #mirrors), and interface circuitry are integrated on a die. The footprint of N switching transistors and resistors will certainly be much smaller than any D/A circuit which can provide equivalent mirror deflection resolution. Processes capable of fabricating an integrated deformable mirror system on a chip using the digital electrostatic deflection scheme exist today [23].

3.7 Micromirror Array Optical Experiments

The AFIT hexagonal array described at the end of Chapter 2 was used in the first reported experimental demonstration of optical aberration correction using a microfabricated mirror device [5]. Measured correction results were limited by the optical characteristics of the hexagonal micro-electro-mechanical deformable mirror (MEM-DM). The hexagonal MEM-DM exhibited low fill-factor (~40%), high mirror curvature (~400 nm) due to residual metal stress, and high static background interference because the support structures were metallized. In addition, only 61 mirror elements were controlled.

Two approaches to improved aberration correction performance were explored in this research; use of a refractive lenslet array to focus light onto the center of MEM-DM elements, and development of segmented MEM-DMs with improved optical characteristics. The use of lenslets greatly simplifies MEM-DM design and fabrication, because the lenslet array defines the fill-factor of the hybrid correcting element, and eliminates background interference with the support structures and wiring. Mirror curvature problems are also mitigated because the mirror surfaces can be smaller. But analysis and experimental results for a lenslet system (Chapter 5) show that the lenslet/MEM-DM hybrid correcting element is not a

3-28

panacea for all optical phase modulation applications. When the incident optical signal is highly aberrated, the lenslet/MEM-DM geometry limit performance of the hybrid correcting element. Another independent analysis confirms that not all systems can effectively employ lenslets [24]. In general, much of the MEM-DM design/microfabrication burden avoided by using a lenslet array is simply transferred to the overall optical system design. At a minimum, use of a lenslet array increases system cost and complexity. Whenever possible, lenslet arrays will be avoided.

The following section describes experimental optical aberration correction using a MEM-DM without lenslets. This experiment was conducted after the lenslet/MEM-DM work described in Chapter 5, and builds on the knowledge gained in that effort. Thus, some readers may find it useful to examine that chapter first.

One element of the MUMPs 19 array used in this effort (hereafter referred to as M19) is shown in Figure 3-10(b). The 12×12 array has 128 individually addressable elements with 203 μm spacing. The design features of the M19 array represent a nearly optimized trade of optical fill-factor, functional device yield, address wiring, and mirror plate flatness. The mirror plate is of trapped oxide construction for maximum stiffness. The Poly2 surface of the mirror plate is degraded only by four (4 μm × 4 μm) etch access holes, and the vias attaching Poly2 to Poly1. Four short flexures (4 μm wide by 65 μm long) centered on the 203 μm cell boundaries support the movable mirror plate. Poly0 address wiring runs lengthwise beneath the flexures to help minimize optically inactive area. Dummy wire segments are drawn under all flexures to ensure flexure uniformity. Dimples and dimple landing areas are avoided by employing the Poly2 tabs on each corner of the mirror plate to limit downward travel. The nominal fill-factor of the M19 array is over 70%. Functional device yields for the array are typically near 100%. Residual stresses in the polysilicon and oxide layers cause convex curvature of the mirror plate. Measured peak-to-valley curvature is ~165 nm across the middle of the mirrors. The M19 array used in this experiment was not metallized to improve the reflectivity of the mirror surface, but other M19 arrays have been successfully metallized in a post-foundry process. Mirror surface figure and post-foundry

metallization are discussed in Chapter 4. The M19 MEM-DM was housed in a pin grid array package (PGA-144) for use in the adaptive optics test bed.

The test bench as configured for M19 testing is depicted in Figure 3-18. This configuration varies somewhat from test bed configuration used for lenslet testing (see Chapter 5). The 18-mW Helium-Neon (HeNe) laser source passes through a variable attenuator before it is collimated and optionally passed through a lens L_a to generate a quadratic aberration. After reflection from the fold mirror (M1), the beam enters a beam splitter (BS1) which reflects the incident wave toward the MEM-DM. The power meter at BS1 guides normalization adjustment of the optical signal incident on the MEM-DM. An afocal telescope (lenses L_l and L_s) between BS1 and the MEM-DM compacts the beam to fill the controllable surface of the array. The MEM-DM is placed at the back focal plane of L_s. An iris located one focal length away from L_l between BS1 and M1 controls the beam diameter. The beam reflected from (and diffracted by) the MEM-DM traverses the afocal telescope (L_s, L_l), BS1, and translating lenses L_{t1} and L_{t2}. At BS2 light is picked off for a CCD camera which records the image of the MEM-DM surface. A second afocal telescope (L_{w1} and L_{w2}) reduces the image size to fit onto the Image camera CCD. A recorded image of the 12×12 M19 array in the circular aperture is shown in Figure 3-19. In the other leg of BS2, a Fourier transforming lens L_F generates the far-field diffraction pattern of the light transmitted by BS2, which is equivalent to the point spread function (PSF) of an imaging system [25]. Another lens L_M magnifies the far-field pattern on the 256×256 pixel array of the PSF camera. Lens focal lengths and nominal positioning dimensions for the bare array configuration are summarized in Tables 3-4 and 3-5 .

The spring constant of the M19 MEM-DM was obtained by static fringe testing. This spring constant was used to compute the voltage required for a desired mirror element deflection. Control voltage files for the MEM-DM were generated by computing the concave spherical deflection pattern required to correct an induced defocus aberration, applying a modulo $\lambda_{HeNe}/2$, then computing the required control voltages. Using this control scheme limits the required travel of the mirror elements to $\lambda_{HeNe}/2$, while permitting corrections of aberrations greater than λ_{HeNe}. A bias voltage of 5.9 V was applied in series with the D/A voltages to obtain 316 nm deflection with the 0-10 V control range of the D/A converters.
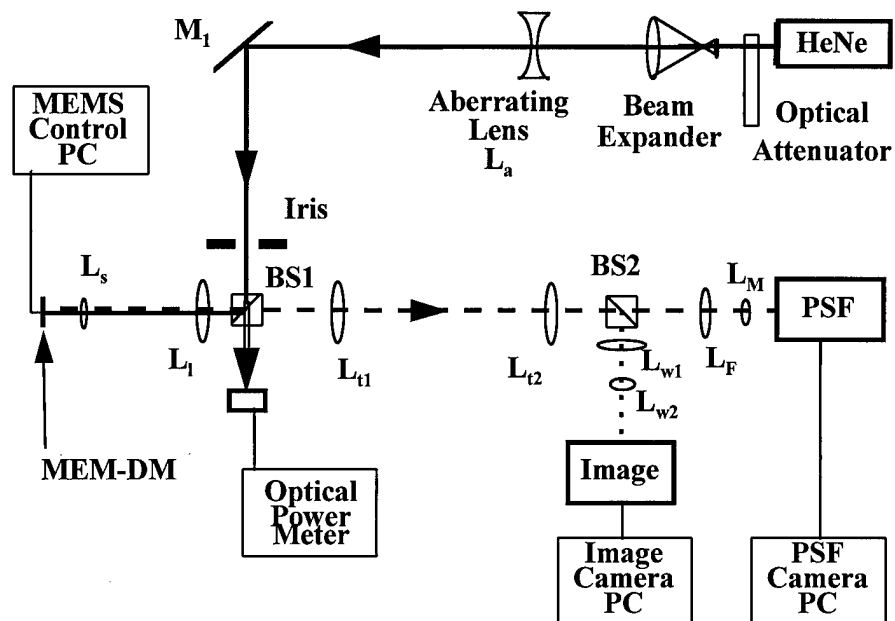
Figure 3-18. Adaptive optics test bed as configured for M19 MEM-DM testing.

Table 3-3. Focal Lengths of Lenses in Adaptive Optical Test Bed for M19 Testing.

Lens labels	Focal length (mm)
L_a	-500, -3500
L_l	250
L_s	100
L_{t1}, L_{t2}	300
L_F	75
L_M	38
L_{w1}	100
L_{w2}	40

Table 3-4. Optical Component Locations in Adaptive Optical Test Bed for M19 Testing.

Distance	Nominal Distance (mm)
L_a to iris	1700
iris to L_l	250
L_l to L_s	350
L_s to MEM-DM	100
L_l to L_{t1}	550
L_{t1} to L_{t2}	600
L_{t2} to L_F	375
L_F to L_M	115
L_{t2} to L_{w1}	400
L_{w1} to L_{w2}	140
L_{w2} to Image camera	40
L_M to PSF camera	770
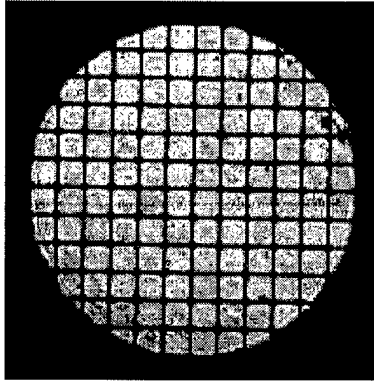
Figure 3-19. Image of M19 MEM-DM captured at test bed Image camera.

The principle objective of this experiment was to provide data for comparing the aberration correction performance of the bare M19 array to lenslet/MEM-DM results. Alignment of the test bed optics and MEM-DM is similar to the lenslet/MEM-DM case but is naturally much easier. After alignment a series of PSF images was recorded as a varying bias voltage was applied to simultaneously deflect all array elements. The measured peak intensity as a function of bias voltage is plotted in Figure 3-20. This plot shows the amplitude modulation effect of interference between the moving mirror surfaces and static background structures (supports, substrate, wires, etc.). The observed 23% intensity variation is consistent with the amplitude modulation expected for a 70% fill-factor device [26].
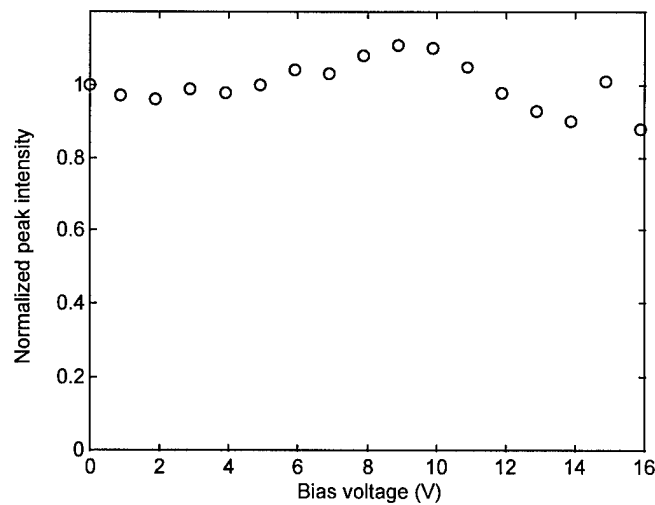
Figure 3-20. Measured peak intensity variation as a function of bias voltage for the M19 MEM-DM.

Defocus aberrations were created by inserting negative focal length lenses into the beam path at a distance of 1.6 m from the MEM-DM. Aberrating lens (L_a) focal lengths of f=-3.5 m, and f=-0.5 m, produce approximately spherical wavefronts at the MEM-DM with curvature radii of 0.8 m and 0.35 m, respectively. Setting the MEM-DM elements to twice the aberration radius of curvature yields best aberration correction results. The factor of 2 between aberration radius of curvature and MEM-DM radius of curvature is due to the "round-trip" optical path length difference obtained using reflective devices.
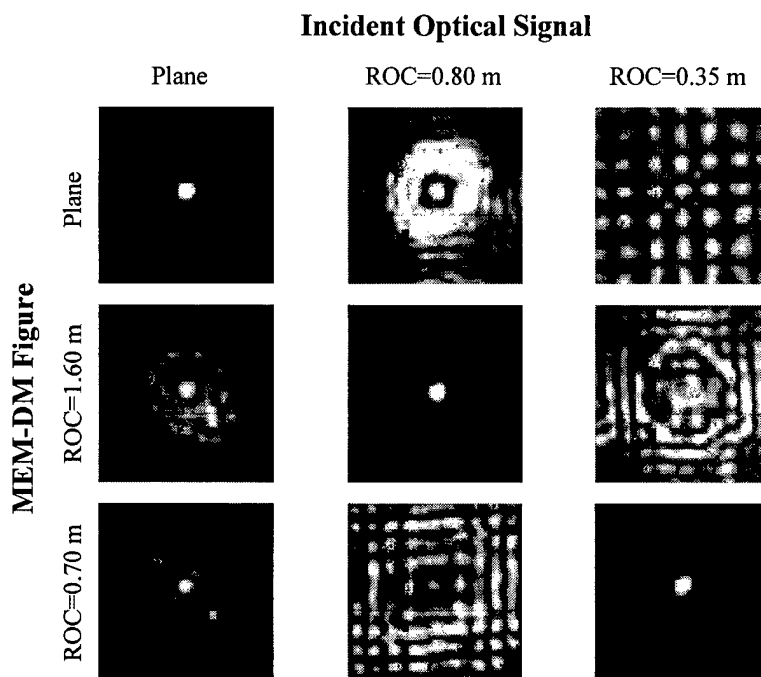
Figure 3-21. PSF images matrix from M19 MEM-DM optical aberration correction experiment. Note that images are independently scaled by camera frame rate and grayscale has been reduced to 64 levels to better show detail of far field diffraction pattern.

Aberration correction results for the M19 MEM-DM experiment are summarized in the image comparison matrix shown in Figure 3-21. For this set of data the incident optical power was normalized by setting the power at BS1 to 1.47 μW for all cases. Image intensity was adjusted by varying the PSF camera frame rate. The variation in PSF camera frame rate provides an indication of the wide dynamic range of the data. Note that the display images are cropped to a 129×129 pixel region around the main lobe, and

the grayscale is reduced to 64 levels to better show details of the far-field pattern. Comparison of the images on the matrix diagonal qualitatively show the excellent aberration correction performance obtained.

The wide range in intensity between aberrated and corrected images complicates quantitative comparison of the peak intensities for all cases. For the lenslet experiment in Chapter 5 optical power meter measurements and optical density filter values were used to scale the data. The new procedure used for the M19 effort was designed to exploit the frame rate adjustment of the PSF CCD camera to scale the data. Empirical calibration measurements confirmed the expected inverse linear relationship of peak intensity to frame rate, provided that pixel saturation was avoided. Restricting maximum peak intensity values to ~80% of full scale results in normalization errors of less than 10% for the calibration data. PSF data was normalized to the incident plane wave, plane MEM-DM case using the recorded camera frame rates. The normalized peak intensity values are listed in Table 3-5, with raw peak intensity values and corresponding camera frame included for reference.

Table 3-5. Quantitative Data for M19 MEM-DM Experiment.

MEM-DM Figure	Incident optical signal		
	Plane	ROC=0.8 m	ROC=0.35 m
Plane	1.00 (208@500 Hz)	0.07 (174 @40 Hz)	0.04 (108@40 Hz)
ROC=1.6 m	0.09 (96@99 Hz)	0.76 (158@500 Hz)	0.05 (121@40 Hz)
ROC=0.7 m	0.18 (91@203 Hz)	0.04 (97 @40 Hz)	0.27 (115 @244 Hz)

Examination of the images and normalized peak intensities indicates consistent performance of the M19 MEM-DM. Introduction of equivalent aberrations to the system, either by inserting an aberrating lens or by applying curvature to the MEM-DM, causes similar decreases in the observed peak intensity. The strongest MEM-DM aberration (plane incident, ROC=0.7 m case) does not induce as strong an aberration as the corresponding lens (ROC=0.35 incident, plane MEMS) due to the modulo $\lambda/2$ control scheme. The observed MEM-DM aberration correction obtained is in good agreement with simulations of the system performance. Simulation results showing the relative peak intensity as function of aberration radius of curvature are plotted in Figure 3-22. The measured M19 MEM-DM aberration correction points from

Table 3-5 are plotted for comparison. Simulation results predict that for correction of the strongest aberration (ROC=0.35 m), residual phase errors, (or the uncorrected phase across a mirror element), reduce the maximum peak intensity obtainable to ~52% of the unaberrated case. The measured MEM-DM corrected value for this case is 27%. The simulated maximum peak intensity for the ROC=0.70 m case and the corresponding measured peak intensity maximum are both 76%.
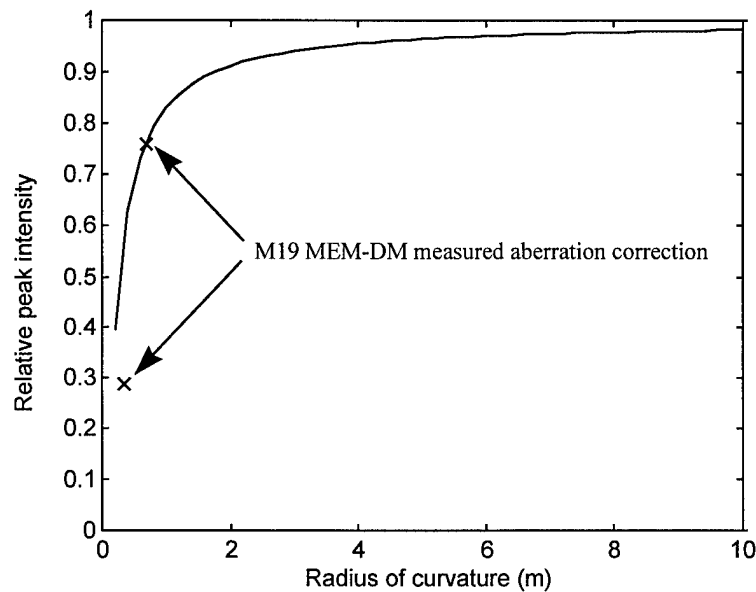
Figure 3-22. Comparison of measured to modeled relative peak intensity for M19 MEM-DM.

Beam steering results for the M19 MEM-DM also appear to be good but were not extensively tested. For a quick demonstration, the control files generated for the MUMPs 18 lenslet array were used to show multiple beam steering. After applying the M18 control voltages to the M19 array, the array bias voltage was manually adjusted to improve the PSF image. The resulting PSF camera images for dual-beam and quad-beam steering are shown in Figure 3-23. For the dual-beam case, the two 64 element control surfaces of the MEM-DM point beams in two directions with the same nominal angle from boresight. To steer four beams, the quadrants of the dual-beam control surfaces were inverted and copied to the opposing quadrants so that four beam directions with equal angles from boresight are formed.
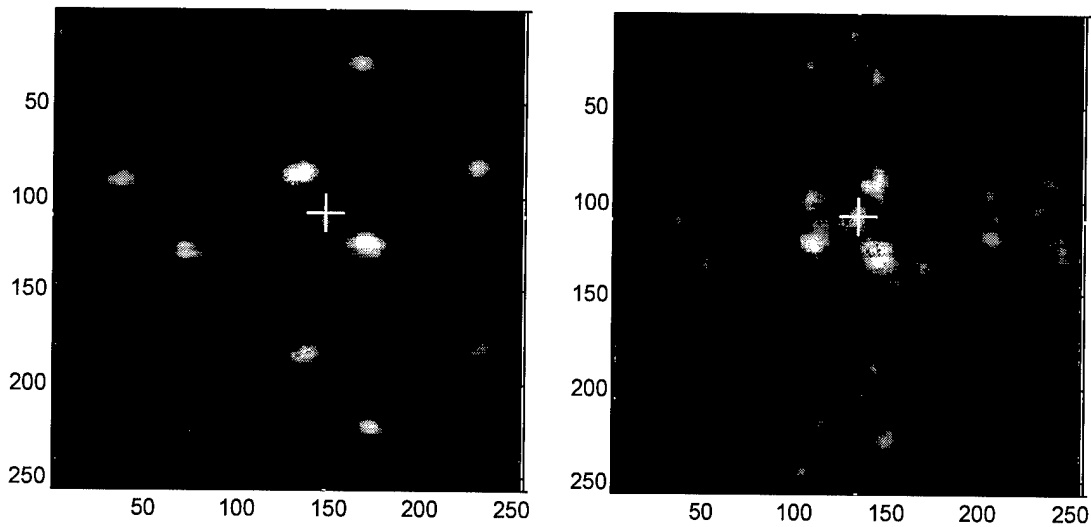
Figure 3-23. Dual-beam (left) and quad-beam (right) steering demonstration using M19 MEM-DM. Axis values are in pixels. Crosses mark the unsteered position for each case.

3.8 Chapter Summary

Electrostatic piston micromirror arrays are arguably one of the most immediately useful applications of microelectromechanical systems. Their almost phase-only modulation characteristics make them especially appropriate for phase conjugate adaptive optics. Microfabricated deformable mirrors represent a substantial cost reduction to adaptive optics systems. In addition to the cost savings achieved by monolithic fabrication, the deflection (or phase modulating) uniformity of microfabricated mirror elements eliminates expensive characterization testing.

Design of piston micromirror arrays is straightforward, but must include the constraints of the micromachining process. The author's micromirror arrays, fabricated in an inexpensive foundry surface micromachining process (MUMPs), exhibit high yield and good deflection uniformity. Without quantitative testing of deflection uniformity, micromirror arrays were characterized using the author's static fringe measurement technique, and then used in a testbed adaptive optics system. The exceptionally good results obtained, and the agreement of those results with theoretical simulations, demonstrate the efficacy of the measurement technique and the deflection uniformity of the array elements.

The digital deflection micromirrors invented by the author pave the way for integration of piston micromirror elements and control circuitry on a single monolithically fabricated chip. Although the number of mirrors and number of control bits of prototype systems to date have been limited by the process and packaging concerns, integrated embodiments will not suffer those same limitations. When one considers the number of wires and transistors in a modern microprocessor, it is easy to envision development of an integrated digital deflection deformable mirror system on a chip with upwards of a thousand individually controlled elements.

References

1   T. H-. Lin, "Implementation and characterization of a flexure-beam micromechanical spatial light modulator", *Opt. Eng.*, vol. 33, no. 11, pp. 3643-3648, November 1994.

2   J. H. Comtois, V. M. Bright, S. C. Gustafson, and M. A. Michalicek, "Implementation of hexagonal micromirror arrays as phase-mostly spatial light modulators", *SPIE*, vol. 2641, pp. 76-87, October 1995.

3   Private communication with R. W. Cohn, 28 January 98.

4   S. C. Gustafson, G. R. Little, V. M. Bright, J. H. Comtois, and E. S. Watson, "Micromirror arrays for coherent beamsteering and phase control", *SPIE*, vol. 2881, pp. 65-74, October 1996.

5   M. C. Roggemann, V. M. Bright, B. M. Welsh, S. R. Hick, P. C. Roberts, W. D. Cowan, and J. H. Comtois, "Use of micro-electromechanical deformable mirrors to control aberrations in optical systems", *Opt. Eng.*, vol. 36, no. 5, pp.1326-1338, May 1997.

6   M. A. Michalicek, V. M. Bright, and J. H Comtois, "Design, fabrication, and testing of a surface-micromachined micromirror device, " *Proceeding of the ASME Dynamic Systems and Control Division ASME 1995*, DSC-vol. 57-2, 1995 IMECE, pp. 981-988, 1995.

7   W. N. Sharpe, B. Yaun, R. Vaidyanathan, and R. L. Edwards, "New test structures and techniques for measurement of mechanical properties of MEMS materials", *SPIE*, vol. 2880, pp. 78-91, Oct. 1996.

8   R. K. Gupta, P. M. Osterberg, and S. D. Senturia, "Material property measurements of micromechanical polysilicon beams", *SPIE*, vol. 2880, pp. 39-45, Oct.1996.

9   J. C. Marshall, D. T. Read, and M. Gaitan, "Analysis of fixed beam test structures", *SPIE*, vol. 2880, pp. 46-55, Oct. 1996.

10   H. H. Lee, *Fundamentals of Microelectronics Processing*, McGraw-Hill, New York, NY, 1990.

11   *Handbook of Mathematical, Scientific, and Engineering Formulas*, Research and Education Association, Piscataway, NJ, 1994.

12   J. A. King, *Materials Handbook for Hybrid Microelectronics*, Artech House, Norwood, MA, 1988.

13   G. C. Dalton II, "Artificial cochlea design using micro-electro-mechanical systems," *Master's Thesis*, Air Force Institute of Technology, Wright-Patterson AFB, OH, AFIT/GCS/ENG/96D-06, December 1996.

14   W. D. Cowan, V. M. Bright, and G. C. Dalton II, "Measuring the frequency response of surface-micromachined resonators", *SPIE*, vol. 3225, pp. 56-67, 1997.

15   P. M. Osterberg, R. K. Gupta, J. R. Gilbert, and S. D. Senturia, "Qualitative models for measurement of residual stress, Poisson ratio, and Young's modulus using electrostatic pull-in of beams and diaphragms", in *Technical Digest, Solid State Sensor and Actuator Workshop*, Hilton Head, SC, pp. 184-188, 1994.

16   R. K. Mali, T. G. Bifano, N. Vandelli, and M. N. Horenstein, "Development of microelectromechanical deformable mirrors for phase modulation of light", *Opt. Eng.*, vol. 36, no. 2, pp. 542-548, February 1997.

17   J. I. Seegar and S. B. Crary, "Stabilization of electrostatically actuated mechanical devices", *Transducers '97, 1997 International Conference on Solid-State Sensors and Actuators*, pp. 1133-1136, June, 1997.

18   T. A. Rhoadarmer, V. M. Bright, B. M. Welsh, S. C. Gustafson, and T. H. Lin, "Interferometric characterization of the flexure-beam micromirror device", *SPIE*, vol. 2291, pp. 13-23, 1994.

19   D. E. Sene, "Design, fabrication and characterization of micro opto-electro-mechanical systems," *Master's Thesis*, Air Force Institute of Technology, Wright-Patterson AFB, OH, AFIT/GEO/ENG95D-03, December 1995.

20   P. B. Chu, P. R. Nelson, M. L. Tachiki, and K. S. J. Pister, "Dynamics of polysilicon parallel-plate electrostatic actuators", *Sensors and Actuators*, A 52, pp. 216-220, 1996.

21   V. P. Jaecklin, C. Linder, N. F. de Rooij, J. M Moret, and R. Vuilleumier, "Line-addressable torsional micromirrors for light modulator arrays," *Sensors and Actuators,* A 41-42, pp. 324-329, 1994.

22   J. T. Butler, V. M. Bright, and J. H. Comtois, "Advanced multichip module packaging of microelectromechanical systems", *Transducers '97, 1997 International Conference on Solid-State Sensors and Actuators*, pp. 261-264, June, 1997.

23   R. D. Nasby, J. J. Sniegowski, J. H. Smith, S. Montague, C. C. Baron, W. P. Eaton, P. J. McWhorter, D. L. Heatherington, C. A. Apblett, and J. G. Fleming, "Application of chemical-mechanical polishing to planarization of surface micromachined devices", in *Technical Digest of the Solid-State Sensor and Actuator Workshop*, pp. 48-53, Hilton Head S. C., June 1996.

24   E. A. Watson, D. T. Miller, and K. J. Barnard, "Analysis of fill-factor improvement using microlens arrays", *Proc. SPIE*, vol. 3276, pp. 123-134, January 1998.

25   J. W. Goodman, *Introduction to Fourier Optics, McGraw-Hill,* New York, 1968.

26   L. J. Hornbeck, "Deformable-mirror spatial light modulators," *SPIE Critical Review Series,* vol. 1271, pp. 51-62, 1990.

4. Micromirror Surface Figure

4.1 Chapter Overview

The flatness of individual mirror elements is critical to the performance of micromirror arrays for both phase and amplitude modulation applications. For surface micromachined mirror arrays two effects determine the quality (or optical figure) of the micromirror surface: curvature due to residual stresses in the fabrication materials, and topography induced by the underlying layers in a conformal process. Surface micromachined mirrors are constructed using thin films and do not have a massive substrate to prevent distortion after release. For single layer micromirrors a stress gradient in the layer will cause curvature. For multilayer mirrors curvature is caused by differing internal stresses of the layers comprising the mirror structure. The amount of mirror curvature experienced can be substantial and can seriously impact system optical performance. Measured peak-to-valley curvature for hexagonal gold on polysilicon mirrors 80 μm across (flat-to-flat) was 400 nm. Optical performance simulations using this measured curvature show over a 97% (15 dB) decrease in the peak intensity of the diffraction pattern from the flat mirror case [1]. Controlling the curvature of individual mirror surfaces in an array of micromirrors is as important to system performance as the fill-factor of the array. The fill-factor and curvature problems are coupled. Fill-factor is improved by increasing mirror size, however larger mirrors exhibit greater curvature due to residual stresses. While the fill-factor of a micromirror array is easily estimated from the design layout, stress-induced mirror curvature is much more difficult to analyze. Without tools to predict the mirror curvature for a given process, optimization of a micromirror array design is impossible.

In addition to stress induced curvature, micromirror topography is influenced by print through of the underlying layers due to the conformal deposition processes employed in polysilicon surface micromachining (i.e. MUMPs). Avoiding the topography effects of print-through on the micromirror surface requires the design trade of mirror size, array size (wiring depth), and fill-factor. Alternatively, self-planarization helps to mitigate the effect of print-through on the micromirror surface [2]. By adding a

planarization step to the fabrication process (i.e. SUMMiT) print-through topography effects can conceivably be eliminated [3].

The first half of this chapter presents successful modeling of the stress-induced curvature of prototype micromirrors fabricated in MUMPs using commercially available software, IntelliCAD [4]. The measurement of MUMPs film stress is detailed in Section 4-2. The prototype MUMPs mirrors that were modeled are described Section 4-3. The curvature measurement technique and measured results are described in Section 4-4. Modeling and simulation results are presented in Section 4-5. The latter half of this chapter presents an optical characterization study of similarly sized micromirror arrays fabricated in both the MUMPs and SUMMiT processes. This experimental study demonstrates the importance of flat micromirror elements. Section 4-6 describes the mirror designs used for optical testing. Section 4-7 describes the post-foundry metallization process used to obtain flat mirrors. Mirror surface characterization results are presented in Section 4-8 and optical measurements are presented in section 4-9. Conclusions regarding surface micromachined mirror array flatness are drawn in Section 4-10.

4.2 Foundry Material Stress Measurement

Perhaps the most challenging aspect of micromachining today is the measurement and control of residual stresses in the materials employed. Accurate, cost-effective measurement techniques are still lacking and existing process control has arguably failed to produce repeatable results (particularly for prototype foundry processes). MCNC uses the wafer bow method to determine residual stress in MUMPs films [5,6]. Although some researchers report good correlation between wafer bow measurements and MEMS device measurements [7], others do not [8]. The wafer bow measurement technique provides only a single value of residual material stress, hence can not describe stress gradients in the film or variations in residual stress across a wafer. The key advantage of the wafer bow method is cost.

Equation (4-1) relates the radius of curvature (or wafer bow) due to the addition of a film to one side of the wafer to the residual film stress [5].

$$\sigma_f = \frac{E_s t_s^2}{6(1 - \upsilon_s) t_f R}, \tag{4-1}$$

where E_s is Young's modulus of the substrate, t_s is the thickness of the substrate, υ_s is Poisson's ratio of the substrate, t_f is the thickness of the film and R is the radius of curvature. This equation is valid where the film is much thinner than the substrate. Two further assumptions are also made, (1) the film stresses are isotropic and constant, and (2) the elastic properties of the substrate plane are transversely isotropic. While E_s and υ_s both vary in the (100) plane of a silicon substrate (the type used in the work described), the quantity $E_s / (1 - \upsilon_s)$ is invariant for cubic crystals so the above equation is justified for this application [6,9]. Bow measurements are currently made using a Tencor FLX-2320, laser scanning thin film stress measurement system. The Tencor measures substrate deflection across a single axis of the wafer and reports radius of curvature and wafer bow. Where wafer bow is much less than the length of the deflection scan (chord), the radius of curvature is defined as

$$R = \frac{L^2}{8B}, \tag{4-2}$$

where L is the scan length and B is the wafer bow.

Wafer bow measurements are performed on dedicated monitor wafers processed with each device wafer lot. Poly1 and Poly2 monitor wafers are specially handled to ensure that the film stresses measured are representative of the film stresses on the device wafers. For example, the Poly1 monitor wafer consists of a substrate on which the Oxide1 layer is deposited followed by the Oxide1 anneal. Then the Poly1 layer and 0.2 μm PSG cap are deposited. The Poly1 monitor wafer is then subjected to the same thermal cycles as the device wafers - Poly1 anneal, Oxide2 anneal, and Poly2 anneal. The Poly2 monitor is also subjected to processing identical to the device wafers. Because films are deposited on both sides of the polysilicon monitor wafers the bow measurement is performed by stripping the test film from one side of the wafer. After removing the cap oxide from both sides of the monitor using a wet etch the bow is measured. Then the test film is removed from one side of the wafer using RIE and the bow is measured again. The difference in bow measurements represents the bow caused by stress in the test film. To monitor metal

stress, the bow of bare silicon substrates is measured before and after being metallized along with the device wafers. Devices fabricated in MUMPs may only have metal deposited on Poly2. In this respect, the metal monitor wafers do not mimic the device wafer processing closely.

Prior to MUMPs 13 an older tool was used to measure wafer bow. Simulations using the initially reported MUMPs 11 metal stress of 20 MPa (tension) were found to be in large disagreement with measured mirror curvatures. Subsequently, the two available MUMPs 11 metal monitor wafers were remeasured on the Tencor system as follows: (1) bow of the metallized wafers was measured, (2) the gold was stripped using Gold Etchant, Type TFA from Transene Company, Inc. , Rowley, MA, (3) the bow of the chromium covered wafer was measured, (4) the chromium layer was stripped using CR7, a commercial chromium etchant manufactured by Cyantec Chemical, (5) the bow of the bare wafer was measured. Using the new wafer bow data (shown in Table 4-1) and Equations (1) and (2) with L=100 mm, $E_S/(1-\upsilon_S)$=180 GPa, t_S=525 μm, yields a mean value of stress for the Cr/Au metal stack of 51 MPa. The residual stress of the chromium layer alone can also be calculated, but results in values (>1200 MPa) which greatly exceed the ultimate tensile strength of bulk chromium (~200 MPa) [10]. This may suggest that the thickness of the chromium layer is actually much larger than intended. Certainly the bow measurements indicate that the chromium layer is the most significant contributor to the overall metal stress. Studies of the metallization process and efforts to reduce metal stress in the MUMPs process are ongoing.

Table 4-1. Bow and Thickness Measurements for MUMPs11 Metal Monitors.

Wafer	Cr/Au Bow (μm)	Cr Bow (μm)	Substrate Bow (μm)	Thickness of Au (Å)	Thickness of Cr (Å)
M21	1.96	2.16	5.69	~5120	~200
M22	-5.65	-5.29	-1.54	~5160	~200

4.3 Device Description

The basic design of the prototype micromirror structures studied in this work was developed previously [11]. In an effort to improve the fill-factor of mirror arrays and decrease the required mirror control

voltage, the original mirror design was stretched to provide a nominal 100 μm square reflecting surface. As it was anticipated that stress-induced curvature of the mirror surface could become problematic, a prototype mirror employing a stacked polysilicon mirror plate was fabricated for comparison. Scanning electron micrographs of both devices after release etch are shown in Figure 4-1. The mirrors consist of a metallized plate suspended above the substrate by either 2 or 4 flexures which wrap around two sides of the perimeter of the plate to reduce flexure stiffness. The Poly2 version employs 2 μm wide Poly2 flexures while the stacked polysilicon version employs 2 μm wide Poly1 flexures. Note that the Poly2 version in Figure 4-1 is stuck to the substrate on one edge. This is not atypical for a large mirror suspended by weak flexures, but sticking problems made yield of the Poly2 devices unacceptably low. Although the mirrors were functionally tested, the focus of this effort was on modeling stress-induced mirror curvature, hence mirror performance data is not reported here.
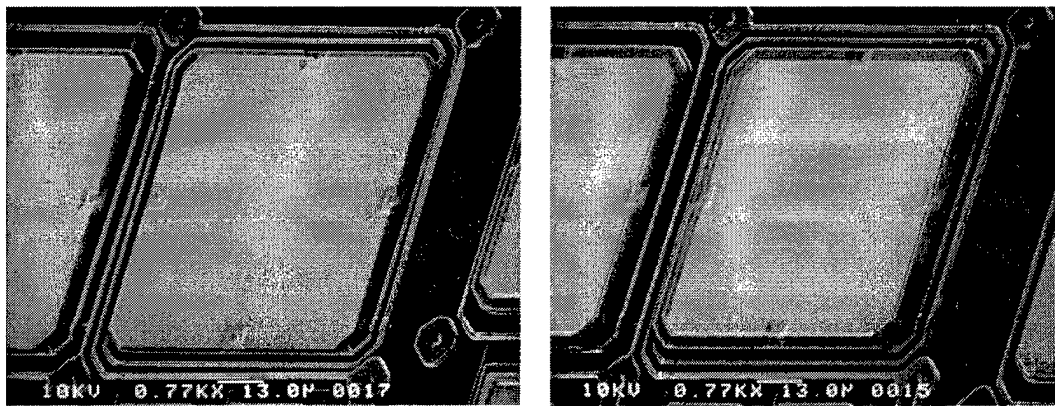
Figure 4-1. Gold/Poly2 (left) and gold/stacked polysilicon (right) piston micromirrors fabricated on MUMPs 11.

4.4 Mirror Curvature Measurements

Stress-induced mirror curvature was measured using a computer controlled Zygo Maxim 3-D laser interferometric microscope [12]. After placing the test die on a block of aluminum on the microscope

stage the microscope head was leveled to the die surface. The measurement region was set to be slightly larger than metallized area using the microscope system's cursor functions. A plane best fitting the raw height data was automatically removed by the system, eliminating any residual die tilt and/or actual mirror tilt. Deflection data was recorded by using the microscope system's scan function to display the curvature in the x and y directions through the approximate mirror center. Figure 4-2 shows the display screen for a representative scan measurement. The peak-to-valley (PV) number indicates the maximum deflection over the scan range. The largest source of measurement error is operator selection of the scan line, but the microscope system's video display facilitated repeatable placement, and discontinuities (due to the dimple structures in the mirror plate) at the end points of the scan provided excellent guides. A series of duplicate measurements verified that manual scans were repeatable within ±5 nm. Four sets of measurements from 3 different die are summarized in Table 4-2. Note that die #2 was measured twice, the second measurement about 5 months after the first.

Table 4-2. Measured Peak-to-Valley Mirror Deflection.

Die Number	Mirror Type	x scan PV (nm)	y scan PV (nm)	Mean PV (nm)
2	Poly2	277	279	278
2	Stacked	66	66	66
9	Poly2	320	330	325
9	Stacked	78	78	78
8	Poly2	302	310	306
8	Stacked	80	78	79
2 redo	Poly2	238	244	241
2 redo	Stacked	57	69	63

Several uncontrolled variables may contribute to scatter in the measurements but the predominant cause is believed to be variation in metal thickness from die to die. Because the die were used for other projects, the release process was not tightly controlled for each test die. The 49% HF release etch may have varied by as much as 1 minute for the devices tested but was most likely 3.5 minutes long. Full release of all the measured mirror devices was confirmed by manual probing. Handling after release varied

also, but none of the die were subject to thermal processes at temperatures greater than hotplate drying at

~125 °C. Die #2 was subjected to no other testing during the 5 month period between measurements. Die

#8 and #9 were also stored for a few months after release before measurements were made. The decrease

in measured deflection observed in die #2 is believed to be attributable to a small change in laboratory

ambient temperature. The fact that the stacked poly mirror structure exhibited less change (4%) than the

gold/Poly2 structure (15%) is somewhat disturbing, and may be indicative of metal creep over time.
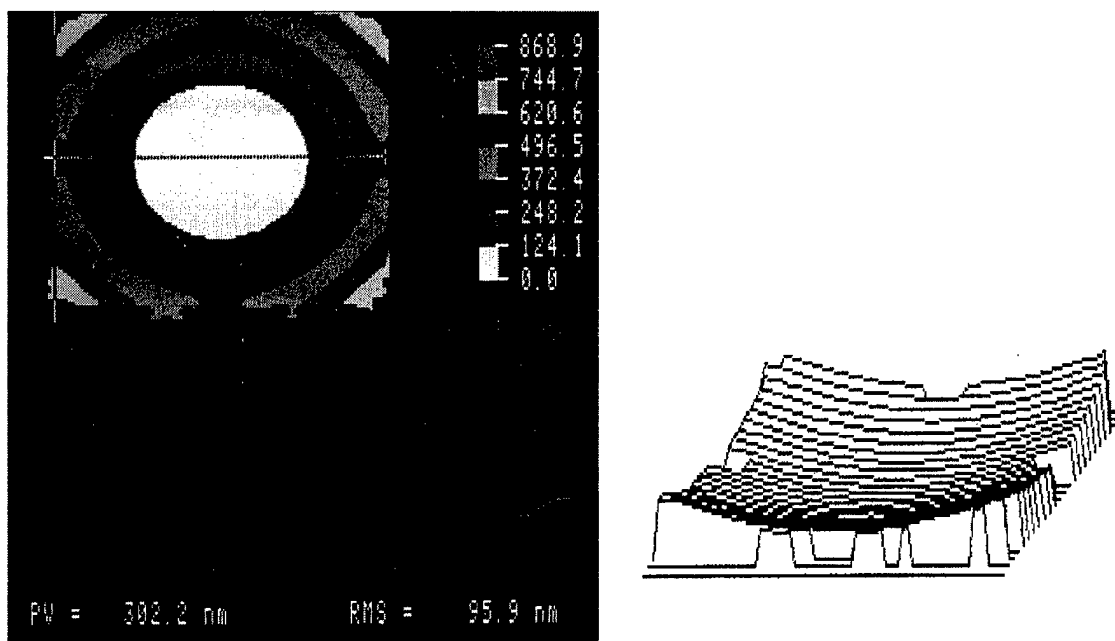
Figure 4-2. Representative interferometric microscope scan measurement of gold/Poly2 micromirror
curvature (left) and reconstructed surface profile (right).

4.5 Modeling

Solid models and subsequent numerical simulations of the mirror devices were created using IntelliCAD, a

commercially available MEMS CAD software package. The first step in this process was simplification of

the modeled geometry by "manhattanizing" the design layout (converting all shapes in the design to

rectangles). A top view scanning electron micrograph of the actual gold/Poly2 device and its manhattanized solid model are shown in Figure 4-3 for comparison. Figure 4-4 shows an isometric view of the solid model of the stacked polysilicon mirror structure. An enlarged view of one of the corners is also shown. The corrugation in the Poly2 layer due to the Poly1 to Poly2 via etch can be clearly seen in this enlarged figure.

The finite element method was used to solve for the deflection of the mirror device. Typical discretizations of the mirror structures are depicted by the mesh lines in Figures 4-3 and 4-4. Parabolic three dimensional solid elements were used. The materials making up the micromirror device were considered to be isotropic. The metallization was treated as a single layer of gold. A Young's modulus of 160 GPa and Poisson ratio of 0.22 were used for the polysilicon layers [13, 14]. A Young's modulus of 83 GPa and Poisson ratio of 0.425 were used for the gold metallization [10]. To ensure that nonlinear geometric effects did not play a role in the problem, the results from a large deformation analysis and results from a small deformation analysis were compared. The nearly identical numerical results confirmed the problem to be linear elastic.
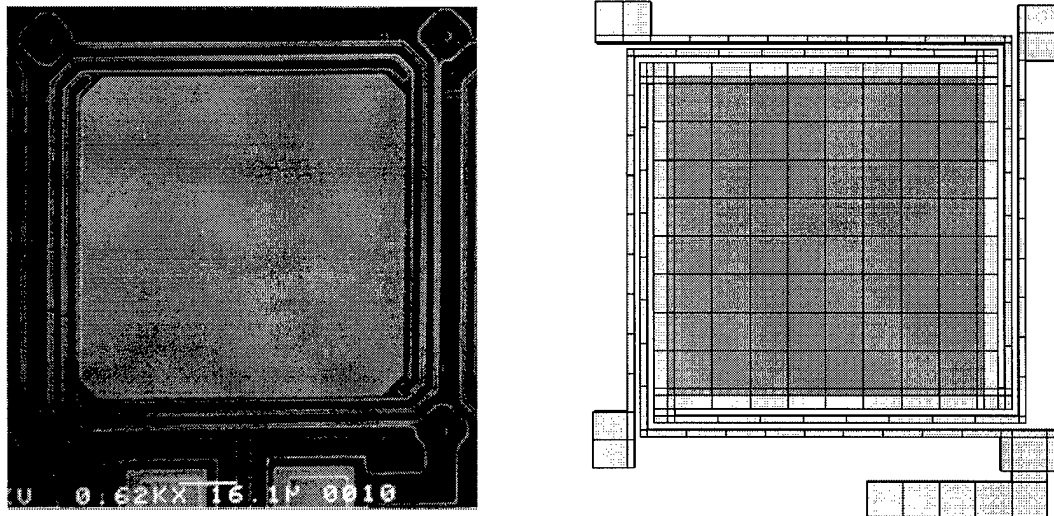
Figure 4-3. Top view scanning electron micrograph of gold/Poly2 micromirror and "manhattanized" solid model.

To start the analyses boundary conditions must be imposed on the finite element models. All points lying on vertical planes of the anchor posts were fixed (no deflection allowed); on facets common to the pads and the flexure beams no prescribed boundary conditions were imposed. These boundary conditions were applied to all models. Internal residual stress fields were applied to the different materials making up the micromirror device. These stresses were assumed to be uniform throughout a material layer. Thus, differing internal stresses between layers are the sole cause of the non-uniform parasitic bowing of the mirror plate. The variation of the parasitic deformation as a function of the MUMPs 11 film parameters was the subject of this investigation. Polysilicon layer thickness values are represented by the mean of all monitor thickness measurements plus/minus one standard deviation. Only three stress measurements were available for each polysilicon layer so the actual maximum and minimum values are used and the nominal value represents the mean of the three measurements. No data was available for metal thickness or stress variation but early simulation results suggested that metal variation might be high. Thus both the thickness and stress of the metal layer were increased by 20 %. Subsequent analysis of the MUMPs metal deposition process suggests that an overall variation of 15 % is reasonable [15]. The numeric values used are summarized in Table 4-3 for reference.

Approximate detail view
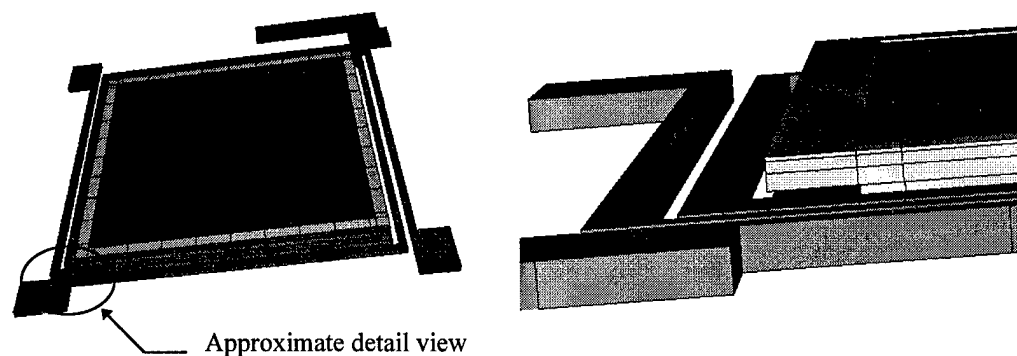
Figure 4-4. Isometric view of the gold/stacked polysilicon micromirror solid model and expanded corner detail showing the corrugation around the edge of the mirror plate. Note that display angles are different.

Table 4-3. Summary of Numeric Values Used in Simulations.

Quantity	Minimum	Nominal	Maximum	Comments
Poly1 thickness (μm)	1.9334	1.9869	2.0404	measured mean ± σ
Poly1 stress (MPa)	-2.7	-4	-5.0	measured (see text)
Poly2 thickness (μm)	1.4599	1.5154	1.5709	measured mean ± σ
Poly2 stress (MPa)	-8.3	-11	-14.8	measured (see text)
Metal thickness (μm)	0.8*Nominal	0.5340	1.2 * Nominal	estimated (see text)
Metal stress (MPa)	Not used	50.7	1.2 * Nominal	estimated (see text)

(negative stress implies compression, σ is standard deviation)
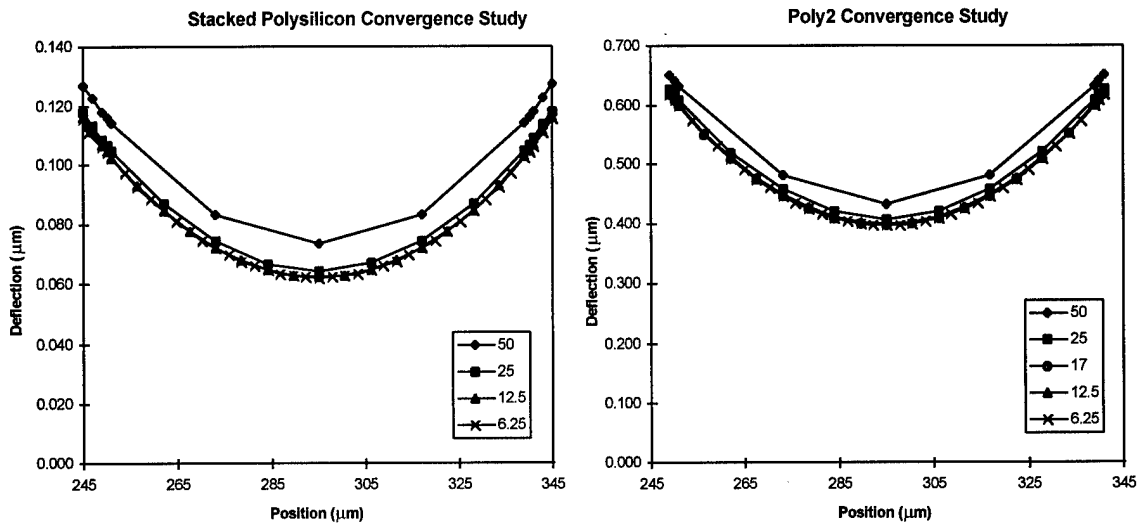
Figure 4-5. Convergence studies for both micromirror structures showing that a nominal 12.5 μm mesh (see text) yields accurate results with the minimum number of nodes.

4.5.1 Convergence Study

To ensure that simulation results are valid a sufficiently fine numerical finite element mesh must be used. To this end a convergence study of the discretization was performed using the minimum polysilicon film parameter values and nominal gold film values from Table 4-3. Deformation of the upper gold surface on a line passing through the center of the mirror plate and parallel to one of the flexure beams was computed for various mesh sizes. Figure 4-5 plots results for both the Poly2 and stacked polysilicon convergence studies. The points in these figures correspond to mesh nodes and each curve corresponds to meshes containing different numbers of elements and hence nodes. Figure 4-5 shows that as the mesh is refined,

the deflection of the gold layer (indeed the entire solution) converges. It is evident that using a mesh with a maximum element size of 12.5 μm for both types of problems is adequate. Note that only the largest elements have x and y dimensions of 12.5 μm. Elements which intersect the device boundaries are smaller. The z dimension of all elements is defined by the corresponding layer thickness. The 12.5 μm mesh was subsequently used to perform all the simulations and is the mesh shown in Figures 4-3 and 4-4. The mesh for the gold/Poly2 mirror contains 2872 nodes, and the gold/stacked polysilicon mirror contains 4764 nodes.

(a)   (b)
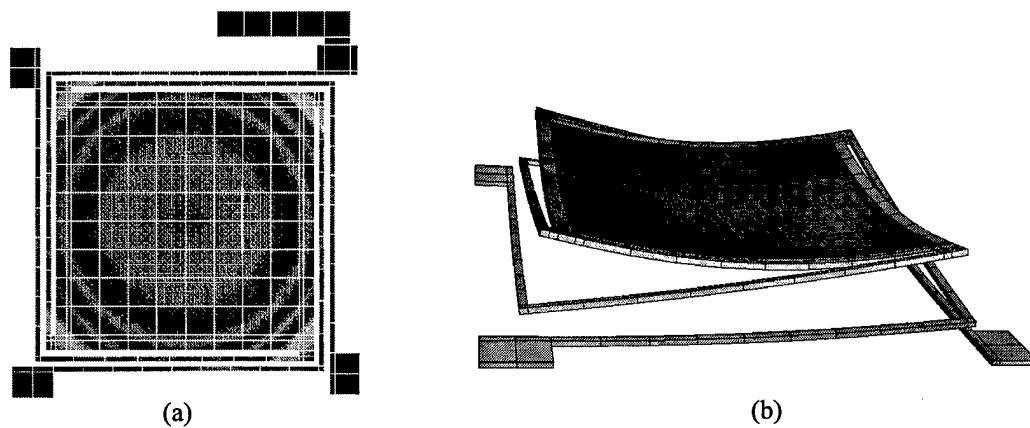
Figure 4-6. Representative simulation results for gold/Poly2 micromirror displayed as false gray scale image (a), and as solid model with deflection scale magnified by factor of 25. Note the good qualitative agreement with measured data in Figure 4-2.

4.5.2 Polysilicon Variation Study

Initially, simulations focused on variation of only the thickness and stress parameters for the polysilicon layers because metal variation data was not available. The internal stresses considered for each polysilicon layer were the maximum and the minimum values in Table 4-3. Variation of these parameters results in 4 cases for the gold/Poly2 structure and 16 cases for the gold/stacked polysilicon structure. Figure 4-6(a) is a false gray scale image depicting the simulated deflection of the mirror structure. Figure 4-6(b) shows the solid model result with the deflection scale magnified by a factor of 25. Note the good qualitative agreement with the measurements in Figure 4-2. To reduce the quantity of simulation data, the elevation of

the top surface of the gold layer on a line passing through the center of the device and parallel to one of the flexure beams was automatically extracted. By subtracting the minimum value of each curve the lowest point is set to zero and the simulation data can be compared directly with the measured interferometer data. Data from all of the polysilicon variation cases is plotted in Figure 4-7 along with measured deflection values.
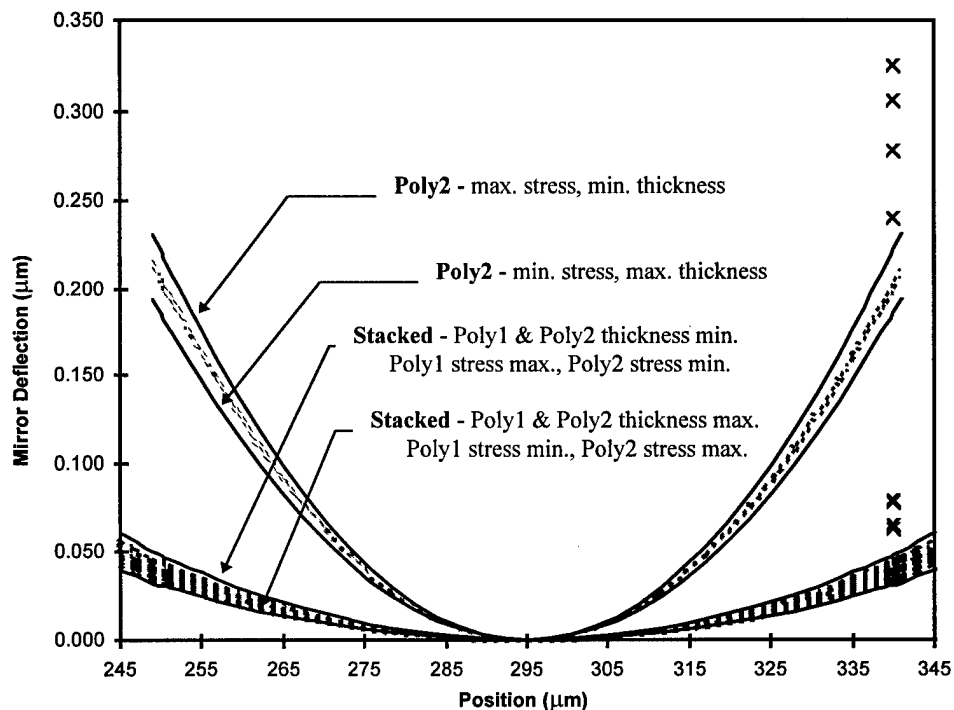
Figure 4-7. Simulation results for all polysilicon variations with measured data plotted at the 340 μm position.

Qualitatively, the results of the polysilicon variation study are intuitive. For the bilayer mirror case (gold/Poly2) the maximum parasitic deflection corresponds to the case when the thickness of the Poly2 layer is minimum while the internal stress is maximum. The minimum deflection corresponds to the case when the thickness of the polysilicon layer is maximum while the internal stress is minimum. For the three layer device the largest deflection corresponds to the case of both polysilicon layers having minimum thickness with maximum internal stress in the Poly1 layer and minimum stress in the Poly2 layer. The smallest deflection corresponds to the case of both polysilicon layers having maximum thickness with

minimum internal stress in the Poly1 layer and maximum stress in the Poly2 layer. In general, the thicker the mirror plate (polysilicon layers) the smaller the parasitic deformation. Further, placing the internal stress away from the neutral surface (the surface which does not undergo any extension or contraction during bending) increases the deformation. Although the position of the neutral surface was not computed in this study, it is expected to be within the Poly2 layer. Hence having the maximum internal stress acting in the Poly1 layer (away from the neutral surface) produces the maximum deformation.

For comparison the measured results are plotted at the 340 μm position (45 μm from the mirror center) which corresponds to the inner edge of the dimple in the design layout of the measured devices. For both the Poly2 and stacked polysilicon cases the model underpredicts the magnitude of mirror deflection. The range of simulation values at the 340 μm position for the stacked polysilicon case (17 nm) is very close to the range of measured values (16 nm). The range of measured values for the Poly2 mirror case is considerably larger (84 nm) and is not matched by the range of simulated values (36 nm). Using mean deflection values the simulations predict a factor of 5.1 improvement by stacking the polysilicon layers but the measured results show only a factor of 4 improvement.
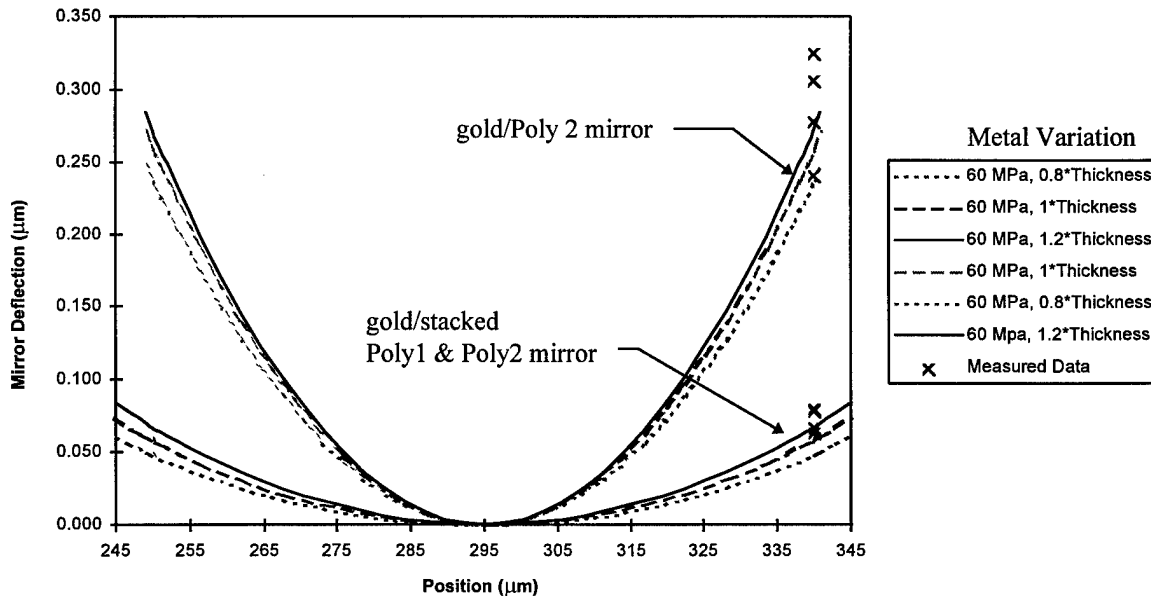
Figure 4-8. Simulation results for metal thickness variation with increased metal stress.

4.5.3 Metal Stress Variation Study

Comparison of resonant frequency measurements with analytical predictions computed using MUMPs polysilicon film parameters provided confidence in the polysilicon stress values used in the preceding simulation [16,17]. Other work also tends to confirm the residual stress values for MUMPs polysilicon films [14,18]. Thus, a limited number of simulations were performed to explore the effect of metal stress and thickness variation. Without any empirical data available a metal thickness variation of ±20% was chosen to bound the problem. Metal stress was increased by 20% to ~60 MPa (tension). Examination of metal stress measurements from MUMPs 5-15 indicates that this value is not unreasonable. For both mirror structures the maximum deflection polysilicon cases were used as the baseline for metal studies. Results of the metal variation simulations are plotted in Figure 4-8, again with measured deflection values for comparison. Agreement of the model with measured data is improved substantially. In particular, the ratio of the Poly2 deflection (272 nm) to stacked polysilicon deflection (67 nm) when both metal thickness and stress are increased is 4.1 which is much closer to the improvement factor observed experimentally.
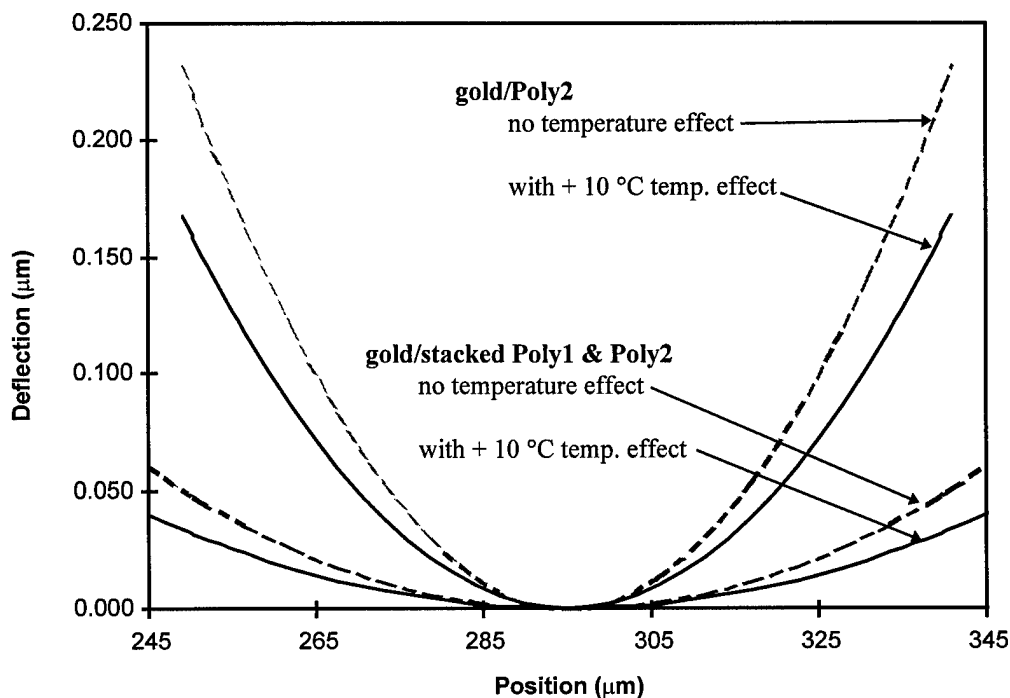
Figure 4-9. Simulated temperature effect (+10 °C) reduces mirror curvature due to internal stresses. Thermal coefficient of expansion values at room temperature (300 K) used.

4.5.4 Temperature Effects

Another set of simulations was performed to ascertain the impact of temperature on mirror curvature measurements. The thickness of polysilicon layers was set to the minimum values and the gold layer thickness was set to the nominal value. The residual stress of all layers was set to zero so that the deformation was due to differing thermal coefficients of expansion of gold (14.2 $\times 10^{-6}$/K [10]) and polysilicon (2.6 $\times 10^{-6}$/K for silicon [10]) when a temperature change was imposed. As expected, increasing the temperature caused the initially flat mirror structures to bow downward (perimeter lower than center). The temperature induced deformation was applied to the maximum curvature polysilicon case for each type of mirror structure by summing the corresponding residual stress-induced deflection and the temperature induced deflection curves. This summation is permissable because the problem is linear elastic. The results are plotted in Figure 4-9. Deflections with and without temperature effects were compared at the 340 μm position. The gold/Poly2 structure exhibits a 28% decrease in deflection and the gold/stacked polysilicon structure exhibits a 34% decrease in deflection with a 10 °C temperature increase. Thus the simulation predicts that both mirror structures should exhibit a similar percentage decrease in deflection as the ambient temperature is increased. The repeat measurements recorded for die number #2 do not agree with this prediction, indicating that metal creep may occur over time.

4.6 Mirror Designs for Optical Testing

In an effort to examine the effects of mirror surface topography on optical performance, similar arrays were designed in the MUMPs and SUMMiT surface micromachining processes. All of arrays tested are designed with nominally square reflecting elements on a 203 μm square grid. Annotated scanning electron micrographs showing individual elements of each design are shown in Figures 4-10 and 4-11. All of the piston micromirror arrays studied here are electrostatically actuated flexure beam designs similar to designs developed by AFIT and other researchers. Each mirror element consists of a mirror plate suspended above the substrate by 4 straight polysilicon flexures. In an effort to improve the array fill-factor the area of the nominal reflecting surface is maximized. It was anticipated that metal stress-induced curvature of the

mirror surface could become problematic so the MUMPs designs employed a stacked polysilicon layer structure [3]. Although the mirrors were functionally tested, the focus of this effort was on optical performance so electrical performance data is not reported here.

The MUMPs 19 designs shown in Figure 4-10 are all quite similar, with the primary difference being the details of the reflective surface fabrication. These details of the mirror surface structure in the MUMPs designs lead to substantial differences in optical performance shown by optical testing (Section 5). Figure 4-10(a) depicts a single element of a 12×12 mirror array design designated M19. In an effort to maximize fill-factor, Poly0 wires to the individual mirror electrodes in the M19 design run directly under the Poly1 flexures. To ensure flexure uniformity identically drawn "dummy" Poly0 wires are included under all four flexures so that all flexures are equally embossed. The M19 mirror plate is comprised of Poly1, "trapped" Oxide2, and Poly2. Around the edges of the mirror plate and around each of the four 9 μm diameter etch access holes Poly1 and Poly2 are connected. Between the two polysilicon layers Oxide2 is trapped and is not attacked during the release etch. The use of trapped oxide provides the thickest possible releasable structure in MUMPs. The thicker mirror plate better resists curvature due to residual stress in any metallization applied. The M19 design does not use MUMPs metallization for the reflective surface and requires post-foundry metallization. Assuming 100% reflectance of the flat Poly2 surface, the as-drawn fill-factor of the M19 array is 67.0%.

The MUMPs 19 designs shown in Figure 4-10(b) through 4-10(d) employ similar wiring, electrodes, and Poly1 flexure structures but avoid wiring beneath the flexures. The M19_A design in Figure 4-10(b) is very similar to the M19 design discussed in the preceding paragraph. A trapped oxide plate is employed with a single 10 μm × 10 μm etch access hole in the center of the mirror. M19_A is the only design tested which employs the standard MUMPs metallization. The as-drawn fill factor of the M19_A design, computed using the nominally flat gold surface area (again assuming 100 % metal reflectance) is 67.4%.

M19_B shown in Figure 4-10(c) also employs a trapped oxide mirror plate but has four 9 μm diameter etch access holes. MUMPs metal is not used so this array requires post-foundry metallization.

The as drawn fill-factor of M19_B of 67% is computed using the nominally flat Poly2 surface area on which metal can readily be deposited.

M19_C shown in Figure 4-10(d) employs a different mirror plate attachment strategy. Here the Poly2 mirror surface is attached to the underlying Poly1 actuator by 21 vias through the Oxide2 layer, each 3 μm square. The Oxide2 between the Poly1 and Poly2 layers is exposed to the release etch and removed. Four 9 μm diameter etch access holes facilitate oxide removal. Subtracting the area consumed by the vias the flat Poly2 surface area of the M19-C design yields a 71.9% as-drawn fill-factor.
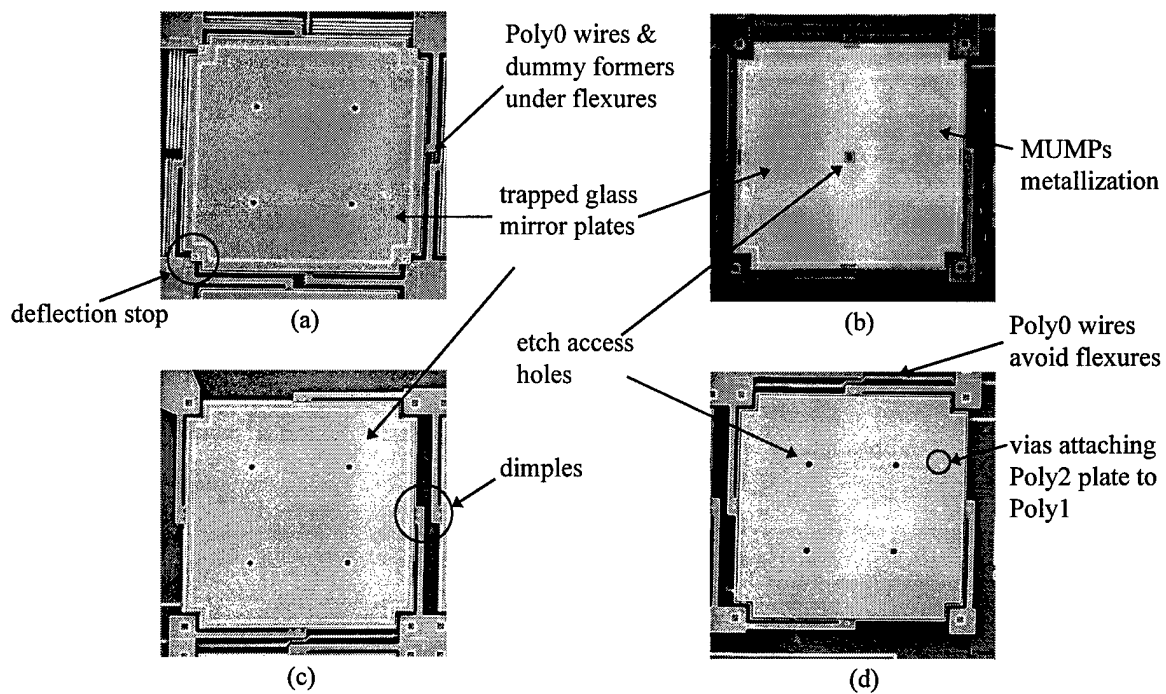
Figure 4-10. Scanning electron micrographs of piston micromirror designs with nominal 203 μm center-to-center spacing fabricated in MUMPs; (a) M19, (b) M19_A, (c) M19_B, (d) M19_C.

The addition of a planarization step in the SUMMiT process completely decouples actuator and reflective surface design. Actuator size can be shrunk to allow space for address wiring which runs under the reflective surface. At the same time fill-factor of the reflective surface is limited only by the minimum (MMPOLY3) cut size, release etch access hole requirements, and vias to connect the mirror plate to the underlying actuator. Figure 4-11 shows an early AFIT micromirror array design for the SUMMiT process.

The reflective surface was deleted in the layout drawing (left side of Figure 4-11) to show actuator and wiring design detail. The nominally 100 μm × 100 μm actuator plate is supported by flexures 2 μm wide. The 2.5 μm thick flexures and upper actuator electrode are fabricated in stacked polysilicon (MMPOLY1 and MMPOLY2). Attached to the movable upper electrode by four 10 μm × 10 μm vias is a MMPOLY3 mirror plate. The 200 μm × 200 μm mirror plate is perturbed only by the vias and 49 etch access holes, each 3 μm × 3 μm. Because the SUMMiT process does not have a metallization step the SUMMiT arrays require post-foundry metallization. To facilitate metallization of the SUMMiT array after the release etch the design includes a MMPOLY2 frame under the mirror edges. This frame prevents metal from shorting the array wiring. The as drawn fill-factor computed using the nominally flat MMPOLY3 surface area of the SUMMiT arrays is 95%.
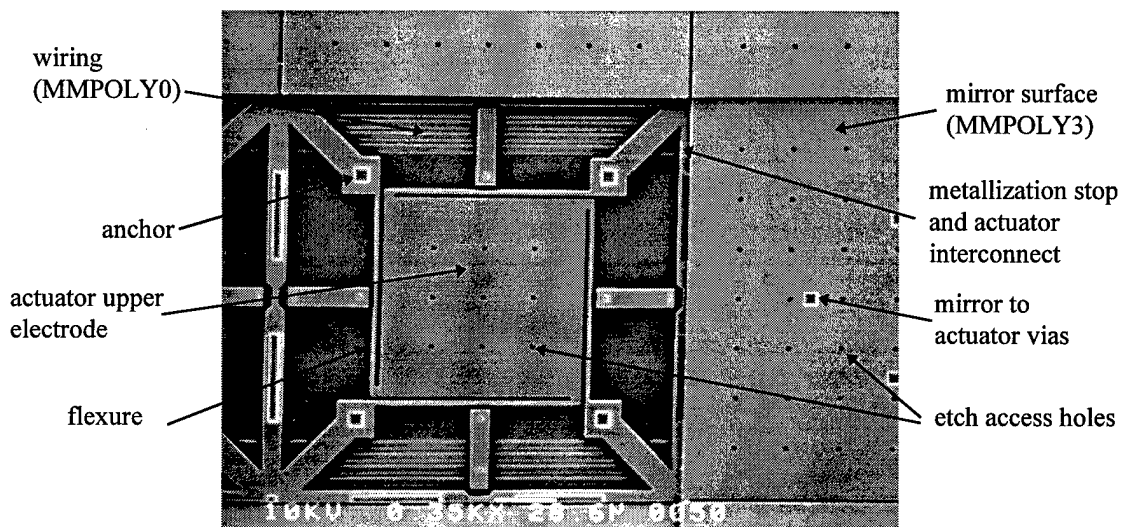
Figure 4-11.   Scanning electron micrograph of piston micromirror array fabricated in the SUMMiT process showing design details.

4.7 Post-Foundry Metallization

With the exception of the M19_A array which used the standard MUMPs metallization, all of the tested arrays required post foundry metallization to improve reflectivity. Because metallization procedures were still being developed, the metallizations used for the test devices were not consistent. The SUMMiT arrays

were designed for metallization after the sacrificial oxide release etch. Acceptable results were obtained for 2 SUMMiT test arrays using a shadow mask to deposit ~600 angstroms of gold in a Ladd benchtop sputtering system. Metal was deposited immediately after the release etch. Optical microscope examination of the metallization qualitatively showed good reflectance but probing of the pure gold metallization showed poor adhesion (as expected with no adhesion layer).

Post foundry metallization of the MUMPs test die was integrated with the release etch procedure. To avoid generating a mask and photolithography step the following maskless metal deposition process was used successfully. First, the MUMPs protective shipping resist was removed using acetone, the die cleaned in methyl alcohol, and dried on a 50 °C hotplate. Metal was deposited in a Denton DV602 sputtering system using an aluminum foil shadow mask. A two layer metallization consisting of a chromium adhesion layer 40-100 angstroms thick and a gold layer ~500 angstroms thick was typical. After removal of the foil shadow mask, the die were mounted in chip carrier packages for ease of handling. The packaged die were then given a partial release etch in 49% HF for ~20 seconds. Breaches in the metallization along the edges of Poly2 structures allow the etch to attack the oxide underneath. After the partial release etch the packaged die were subjected to 2 minutes of ultrasonic agitation to break off the undercut metal. The release etch was then completed in gently stirred HF with the packaged die held upside-down. The gravity-assisted lift off helps prevent the undercut metal from sticking to the substrate. As in the case of the SUMMiT die, metallization success was judged only qualitatively under an optical microscope. The sputtered chromium/gold metallizations exhibited both good reflectivity and good adhesion.

4.8 Micromirror Surface Characterization

The topography of all test mirror surfaces was characterized using a computer controlled Zygo Maxim 3-D laser interferometric microscope [12]. Packaged die were placed in a test socket on the microscope stage and the microscope head leveled to the die surface. The measurement area was set to be slightly larger than the nominal surface area of a single micromirror element using the microscope system's cursor

functions. With background subtraction and averaging to reduce noise the manufacturer specified measurement accuracy is 3 nm RMS. A plane best fitting the data was automatically removed by the system eliminating and residual die tilt and/or actual mirror tilt. Figure 4-12 is copy of the microscope display screen showing the M19_A mirror surface in both a gray scale image and mesh drawing. To obtain a single value characterizing the micromirror surface the microscope system's scan function was used to display the curvature (or topography) on a line parallel to the mirror edge through the approximate mirror center. The scan line was shifted slightly to avoid etch access holes and vias in the center of some mirror designs. The scan measurement is also depicted in Figure 4-12. The peak-to-valley (PV) number indicates the maximum height over the scan range.

The interferometric microscope scan measurements for the test devices are summarized in Table 4-4. The concave curvature of the M19_A micromirror is due to residual metal stress. For MUMPs 19 the residual metal stress reported by MCNC is 57 MPa (tensile). The trapped glass mirror plates of the M19 and M19_B devices exhibit a convex curvature even after metallization. The convex curvature is due to differing residual stresses and/or residual stress gradients in the polysilicon/oxide layers. The reported stress value for both Poly1 and Poly2 on MUMPs 19 is 10 MPa (compressive). The stress value for the Oxide2 layer, which is normally removed is not available.

Comparing curvature measurement results for the MUMPs 19 devices metallized with the maskless chromium/gold suggests that sputtered metallizations can be precisely controlled to exactly counter an initially convex mirror plate curvature. The curvature of the two metallized M19 devices is almost 2 times less than the bare M19 device. From thickness monitor measurements at the time of deposition the M19 metallization is 44 angstroms of chromium and 505 angstroms of gold. The M19_B devices which exhibits a similar curvature before metallization were sputtered with 100 angstroms of chromium and 532 angstroms of gold. This metallization reduced M19_B mirror plate curvature by almost a factor of 3. The resulting M19_B mirror plate exhibits better than $\lambda/10$ flatness at 632.8 nm HeNe wavelength. The same 100/532 angstrom metallization caused the initially convex 70 nm curvature of the

4-20

M19_C mirror plate to change to 65 nm concave because the mirror plate without trapped oxide is less

resistant to bending.

Scan

Gray scale image surface height (nm)

Scan line peak-to-valley: 303.4 nm

Mesh of surface figure
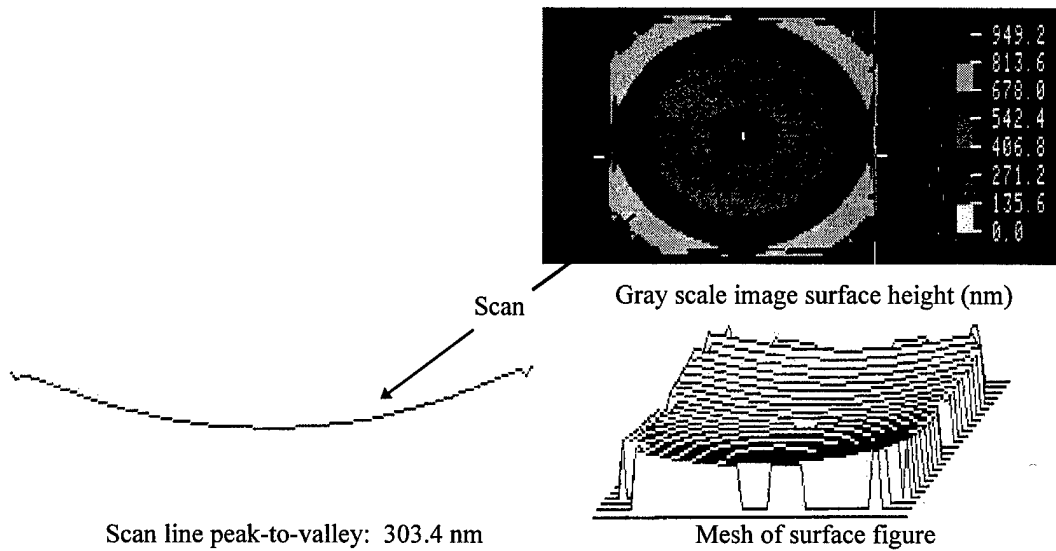
Figure 4-12. Interferometric microscope measurement of the M19_A device which employs MUMPs metallization.

Scan

Gray scale image of surface height (nm)

Scan line peak-to-valley: 291.1 nm

Mesh of surface figure
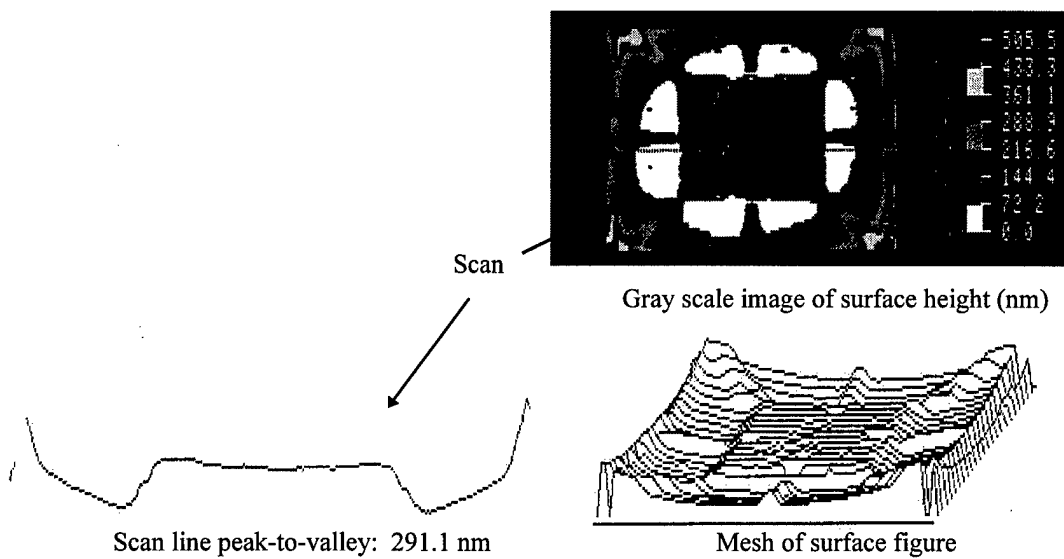
Figure 4-13. Interferometric microscope measurement of SUMMiT mirror surface showing print-through.

The mirror surface of the SUMMiT devices was studied extensively after it was found that the nominally flat mirror surface exhibited significant print-through of the underlying layers. Figure 4-13 shows the print through phenomenon for a gold metallized SUMMiT device. Ideally, the CMP planarization process should completely eliminate print-through. Thus, the observed print-though suggests incomplete planarization. To confirm that the observed print-through was not a measurement artifact (i. e. light transmission through the mirror surface), laser interferometric microscope measurements of an unreleased device were compared to Dektak stylus surface profilometer measurements. Results for both measurement methods were identical, confirming the print-through phenomenon. It should be noted that the SUMMiT devices used in this work were from two early process runs. The incomplete planarization for structures of this type may have already been corrected. In addition to print-through, the released SUMMiT micromirrors show some upward curling of the edges. Because it appears in unmetallized devices, this curling is attributed to differing residual stresses or stress gradients in the polysilicon layers. Comparing metallized devices to unmetallized devices indicates that the sputtered gold only metallization does not significantly increase surface curvature.

Table 4-4. Micromirror Surface Characterization.

Mirror Description	Measured Peak-to-Valley Curvature (nm)	Comments
M19 No Metal	165.6	convex
M19_A MUMPs Metal	303.4	concave
M19 AFIT Metal 1	90.2	convex
M19 AFIT Metal 2	98.3	convex
M19_B AFIT Metal	55.6	convex
M19_C AFIT Metal	65.4	concave
SUMMiT No Metal, Unreleased	129.8	print-through of underlying layers
SUMMiT No Metal	187.9	print-through plus concave
SUMMiT AFIT Metal 1	291.1	print-through plus concave
SUMMiT AFIT Metal 2	159.4	print-through plus small convex

4.9 Optical Measurements

The truest measure of piston micromirror array quality is obtained by reflecting a coherent optical beam off the micromirror array surface and observing the far-field diffraction pattern. For an array of undeflected mirrors the measured on-axis intensity of the far-field diffraction pattern is function of the array fill-factor, individual mirror surface quality including reflectance, and array surface quality (alignment of the mirror surfaces).

The testbed shown in Figure 4-14 was used to measure the far-field diffraction pattern for the micromirror arrays tested. A collimated 18 mW Helium-Neon (HeNe) laser at 632.8 nm provides the optical signal source. After reflection from the fold mirror (M1), the beam enters a beam splitter (BS1) which reflects the incident wave toward the micromirror array labeled as MEM-DM. An afocal telescope (lenses L_l and L_s between BS1 and MEM-DM) compacts the beam to fill the surface of the MEM-DM. An iris located a focal length away from L_l between BS1 and M1 controls the beam diameter on the MEM-DM. The beam reflected from (and diffracted by) the MEM-DM traverses the afocal telescope (L_s, L_l), BS1, and translating lenses L_{t1} and L_{t2}. At BS2 light is picked off for a CCD camera which records the image of the MEM-DM surface. In the other leg a Fourier transforming lens L_F generates the far-field diffraction pattern of the light transmitted by BS2. To within a scale factor applied to the axes the far-field pattern is equivalent to the point spread function (PSF) of an imaging system, hence the label used in the test bench diagram [19]. Another lens L_M magnifies the far-field pattern on the 256×256 pixel array of the PSF camera. This test bed has proved very flexible and has been used for a number of MEM-DM optical experiments.

The test bed optics were initially aligned using a plane alignment mirror in place of the MEM-DM. The plane alignment mirror consists of a MUMPs die with a large (0.5 cm square) metallized Poly2 plate anchored to the substrate. After initial alignment, the plane mirror was replaced with the first test array. Using the iris closest to BS1, the incident beam diameter was set to just fill an 8 × 8 mirror array section. The resulting incident beam diameter was ~1.6 mm. The setting of the iris remained fixed for the duration of the experiment. In turn, each of the test arrays was installed and aligned to the aperture by x

and y translation adjustments. Tip and tilt adjustments were used to center the far-field pattern on the PSF

camera. The Imaging camera provided feedback for translation adjustments in the z (propagation)

direction.
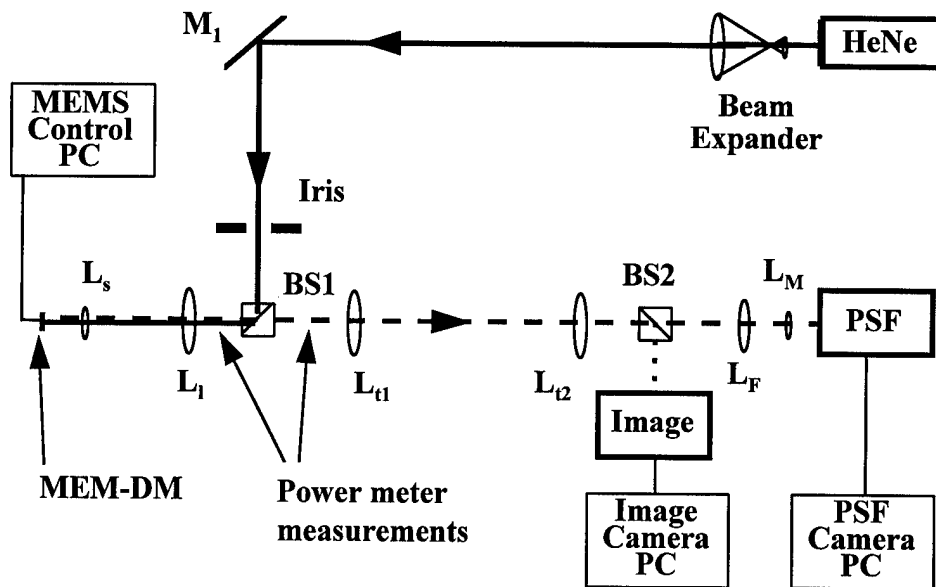
Figure 4-14. Test bench used for optical measurements.

Images and PSFs were recorded for each test array and the plane mirror. Image and far-field data

for the M19_B array with post-foundry metallization are shown in Figure 4-15. For comparison the same

data for the M19_A device is shown in Figure 4-16. Note that although the array images are similar, the

PSFs in Figures 4-15(b) and 4-16(b) differ markedly, and represent the best and worst case PSFs,

respectively. The flat mirror surfaces of the M19_B array (Figure 4-15(b)) produce a high on-axis peak

and sidelobes that are barely discernible (even with only 16 gray scale levels). In contrast, the curved

surfaces of the M19_A device shift almost all of the optical energy into the sidelobes of the PSF. Most of

the energy shows up in the diagonal sidelobes (the four corner spots of the PSF image in Figure 4-16(b).

This effect is consistent with the measured stress-induced mirror curvature which is highest in the corners

of each micromirror element (see Figure 4-12). The PSFs for the other arrays tested lie between these two

extremes. For each of the PSFs the peak intensity and the two dimensional FWHM of the main (on-axis)

lobe were found. Two optical power meter measurements were also made for each test mirror; one

4-24

between BS1 and L_1 to get the incident beam power, and one between BS1 and L_{t1} to measure the optical power reflected from the test mirror. Because the incident beam power varied by about 15% over the course of the optical measurements the incident laser power readings were used to normalize peak intensity measurements to each other. The test data are summarized in Table 4-5.

(a) Image   (b) PSF
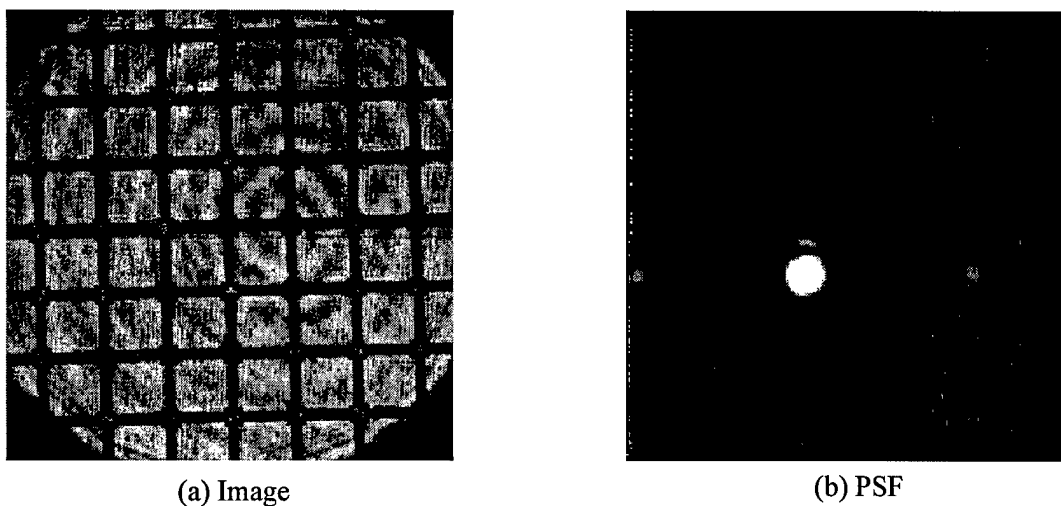
Figure 4-15. Image and far-field (PSF) camera images for the post-foundry metallized M19_B device. Note that PSF image has been scaled to only 16 gray scale levels to better show detail.

(a) Image   (b) PSF
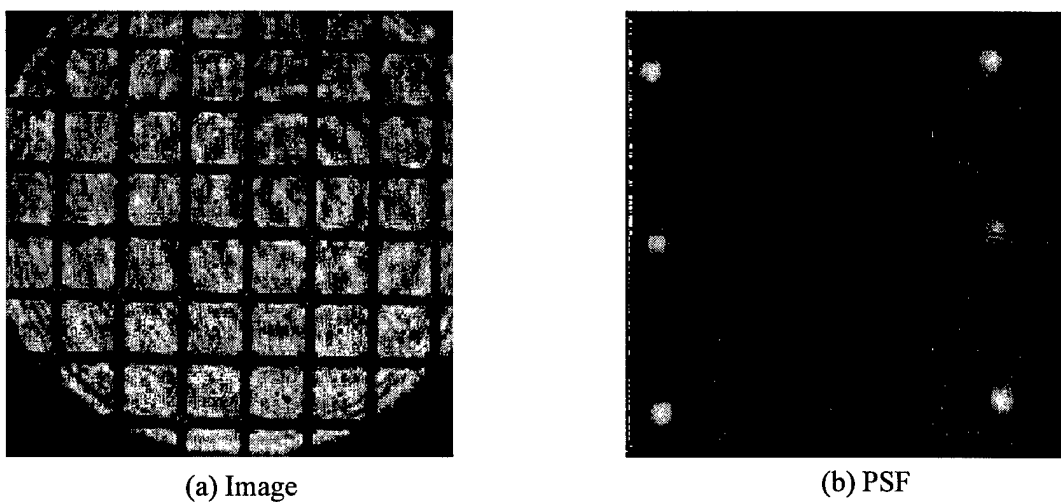
Figure 4-16. Image and far-field (PSF) camera images for foundry metallized M19_A device. Note that PSF image has been scaled to only 16 gray scale levels to better show detail.

Table 4-5. Summary of Optical Measurements.

Mirror Description	Reflected Optical Power, %	Optical Efficiency Normalized to Plane Mirror Case, %	PSF Peak Intensity Normalized to Plane Mirror Case, %	Effective Fill Factor, %	FWHM Normalized to Plane Mirror Case, %
MUMPs Plane Mirror	76.3	100	100	100	100
M19 No Metal	29.2	38.3	5.2	22.8	104
M19_A MUMPs Metal	56.9	74.5	1.0	10.0	221
M19 AFIT Metal 1	62.6	82.0	24.9	49.9	98
M19 AFIT Metal 2	60.8	79.7	25.8	50.8	99
M19_B AFIT Metal	53.6	70.2	35.7	59.8	105
M19_C AFIT Metal	30.0	39.3	7.8	28.0	117
SUMMiT No Metal	44.0	57.7	7.8	28.0	116
SUMMiT AFIT Metal 1	66.0	86.5	7.2	26.7	109
SUMMiT AFIT Metal 2	67.5	88.4	6.9	26.2	111

Notes:

$$\text{Reflected Optical Power} = \frac{\text{Measured Reflected Power}}{\text{Measured Incident Power}}$$

$$\text{Optical Efficiency} = \frac{\text{Reflected Optical Power}}{\text{MUMPs Plane Mirror Reflected Optical Power}}$$

$$\text{PSF Peak Intensity} = \frac{(\text{Measured Peak Intensity})(\text{Measured Incident Power})}{(\text{Plane Mirror Inc. Power})(\text{Plane Mirror Peak})}$$

$$\text{Effective Fill Factor} = (\text{PSF Peak Intensity})^{0.5}$$

$$\text{FWHM} = \frac{(\text{Measured FWHM})}{(\text{Measured Plane Mirror FWHM})}$$

Using the peak intensity of the plane mirror far field diffraction pattern (an Airy disk) as the measurement baseline, the normalized peak intensity for each case was calculated. Taking the square root of the normalized peak intensity yields an effective fill-factor for each array. This effective fill-factor represents the fill-factor of an array of ideally flat mirror elements which would yield an identical on-axis peak intensity in the PSF. Note that the effective fill-factors computed using the MUMPs metallized plane

mirror as a baseline assumes that the reflectivity of the mirror surface is identical to the MUMPs gold. Prior measurements of the MUMPs gold reflectance show a reflectance of 91.5% for HeNe illumination [20]. Power meter measurements for the MUMPs metal plane mirror were checked against this value. Using a nominal 0.96 transmission for the afocal telescope lenses (two passes) and beam splitter gives $(0.96)^5 \times 91.5 = 74.6\%$, which compares very favorably with the measured power meter value 76.3%. FWHM data were also normalized to the plane mirror case to facilitate comparison. With the exception of M19_A (which essentially had no on axis peak intensity), the FWHM for all cases was within 17% of the plane mirror. The normalized FWHM data expressed as a percentage is also listed in Table 4-5. In general the FWHM data correlate well with the measured peak-to-valley curvature data listed in Table 4-4.

With the exception of the M19_C device the maskless post-foundry metallization used for the MUMPs die shows good results. In particular, comparison of the unmetallized M19 device to the two AFIT metallized M19 die shows a marked (and consistent) improvement in effective fill factor. With optimization of the sputtered chromium/gold post-foundry metallization effective fill-factors very close to the as-drawn fill-factor should be obtainable. Metallization results for the M19_B device were excellent. Only the metallized M19_C results were poor. Subsequent examination of the M19_C die showed that many of the array elements were tilted and stuck down to the substrate. Tilted mirrors are consistent with both the low reflected power and peak intensity measured. The sputtered gold only metallization used on the SUMMiT die showed improvement only in optical efficiency, but results were consistent for the two die tested.

4.10 Conclusions

This analytic and experimental efforts described in this chapter clearly demonstrate that design tools and processes exist for the manufacture of micromirror arrays with high quality optical surfaces. Available computer aided design tools can be used to predict the stress-induced curvature of surface-micromachined micromirror devices, and can be used to optimize micromirror array designs. The accuracy of CAD

4-27

simulation of stress-induced curvature is dependent on the accuracy and run-to-run consistency of process residual stress data.

Characterization of the MUMPs process by means of wafer bow measurements is actually better than originally anticipated. In particular, the careful duplication of process conditions for the polysilicon layer monitor wafers produces values for residual stress which appear to be accurate. Simulation results suggest that device level residual metal stress is actually somewhat higher than that obtained by wafer bow measurements. Possible causes for the discrepancy are wafer-to-wafer film thickness variation, imprecise measurement of the absolute thickness of the chromium and gold layers, and the effect of depositing the metal monitor film on a silicon substrate rather than a polysilicon film. Stress variation across a wafer also can not be ruled out as the wafer bow measurement technique yields only an average value.

The impact of micromirror surface quality on optical performance was demonstrated using several similar mirror designs fabricated in two polysilicon surface micromachining processes. The optical performance data collected leads to several observations. First, optical efficiency in terms of power is not a good measure of imaging performance. The M19_A array, despite a 74% optical power efficiency, is not a viable device for aberration correction applications. Second, control of mirror surface quality appears to be the most important factor in fabricating piston micromirror arrays. Although the SUMMiT arrays have a high (~95%) as-drawn fill-factor and the highest measured optical power efficiency, the imaging performance suffers considerably due to the print-through deformation of the mirror surface. It is expected that the observed print-through can easily be remedied by increasing the thickness of the oxide deposition prior to the CMP step slightly. Post-foundry metallization results using a maskless sputtered chromium/gold metallization are encouraging. A viable manufacturing approach for high quality piston micromirror arrays may be to design in a small convex mirror plate curvature which is corrected by tailoring the final reflective surface metallization. This would require release and measurement of a sample wafer to determine the metallization, but the remainder of the wafer lot could be batch processed.

References

1   M. C. Roggemann, V. M. Bright, B. M. Welsh, S. R. Hick, P. C. Roberts, W. D. Cowan, and J. H. Comtois, "Use of micro-electromechanical deformable mirrors to control aberrations in optical systems: theoretical and experimental results", *Opt. Eng.*, Vol. 36, No. 5, pp. 1326-1338, May 1997.

2   T. G. Bifano, R. K. Mali, J. K. Dorton, J. Perreault, N. Vandelli, M. N. Horenstein, D. A. Castanon, "Continuous-membrane surface-micromachined silicon deformable mirror," *Opt. Eng.*, Vol. 36, No. 5, pp. 354-1360, May 1997.

3   B. R. Davies, C. C. Barron, J. J. Sniegowski, and M. S. Rodgers, "SAMPLE (Sandia Agile MEMS Prototyping, Layout tools, and Education)," in *Microelectronic Structures and MEMS for Optical Processing III, Proc. SPIE* , Vol. 3226, pp. 11-21, September 1997.

4   IntelliCAD, CAD system for MEMS, Intellisense Corp., 16 Upton Drive, Wilmington, MA 01887.

5   G. G. Stoney, "The tension of metallic films deposited by electrolysis", *Proc. Roy. Soc. (London)*, Vol. 9, pp. 172-175, 1909.

6   P. Krulevitch, G.C. Johnson, and R.T. Howe, "Stress and microstructure in phosphorus doped polycrystalline silicon", *Mat. Res. Soc. Symp. Proc.*, Vol. 276, pp. 79-84, 1992.

7   Y. B. Gianchandani and K. Najafi, "Bent beam strain sensors", *Journal of Microelectromechanical Systems*, Vol. 5, No. 1, pp. 52-58, March 1996.

8   M. Boutry, A. Bosseboeuf, and G. Coffignal, "Characterization of residual stress in metallic films on silicon with micromechanical devices", in Proc. SPIE, Vol. 2879, pp. 126-134, 1996.

9   W. A. Brantley, "Calculated elastic constants for stress problems associated with semiconductor devices", *J. Appl. Phys.,* vol. 44, pp. 534-535, 1973.

10   J. A. King, *Materials Handbook for Hybrid Microelectronics*, Artech House, Norwood, MA, 1988.

11   M. A. Michaliacek, D. E. Sene, and V. M. Bright, "Advanced modeling of micromirror devices," *Proc. International Conference on Integrated Micro/Nanotechnology for Space Applications*, NASA & Aerospace Corp. Publications, Oct. 1995.

12   *Zygo Maxim 3D Operation and Maintenance Manual*, Zygo Corp., Laurel Brook Road, Middlefield, CT, May 1988.

13   W. N. Sharpe, B.Yaun, R. Vaidyanathan, and R. L. Edwards, "New test structures and techniques for measurement of mechanical properties of MEMS materials", *SPIE*, Vol. 2880, pp. 78-91, Oct. 1996.

14   R. K. Gupta, P. M. Osterberg, and S. D. Senturia, "Material property measurements of micromechanical polysilicon beams", *SPIE,*Vol. 2880, pp. 39-45, Oct.1996.

15   Private communication with David A. Koester, MUMPs Process Engineer, MEMS Technical Applications Center, Research Park, NC.

16   G. C. Dalton, "Artificial cochlea design using micro-electro-mechanical systems," *Masters Thesis*, Air Force Institute of Technology, AFIT/GCS/ENG/96D-06, 1996.

17   W. D. Cowan, V. M. Bright, and G. C. Dalton, "Measuring the frequency response of surface-micromachined resonators", *Proc. SPIE* ,Vol. 3225, pp. 56-67, 1997.

18   J. C. Marshall, D. T. Read, and M. Gaitan, "Analysis of fixed beam test structures", *SPIE*, Vol. 2880, pp. 46-55, Oct. 1996.

19   J. W. Goodman, *Introduction to Fourier Optics*, McGraw-Hill, New York, NY, 1968.

20   D. M. Burns and V. M. Bright, "Investigation of maximum optical power rating for micro-electro-mechanical device," in *Transducers '97*, International Conference on Solid-State Sensors and Actuators, Chicago, IL, pp. 335-338, June 1997.

5. Optical Phase Modulation Using a Lenslet Array and MEM-DM

5.1. Chapter Overview

Using a lenslet array to focus the incident light onto only the reflective surface of the MEM-DM greatly improves the effective fill-factor with a corresponding decrease in interference effects. In the experimental and theoretical work described in this chapter a refractive lenslet array is used with a very low fill-factor MEM-DM (~7%) to comprise a correcting element which behaves like a 70-80% fill factor device. The MEM-DM has 128 active piston micromirror elements. Experiments employing the hybrid correcting element demonstrate single beam steering, dual beam steering, and optical aberration correction. A thermal circuit model is developed to estimate optical power handling capability of the MEM-DM. A conservative estimate of maximum optical power for this particular MEM-DM is 4 Watts per element when operated in a helium ambient, suggesting that relatively high power laser control applications are feasible.

The remainder of this chapter is organized as follows. A theoretical model of the lenslet and micromirror combination is developed in Section 5-2. Design of the micromirror device and the test bed setup are described in Section 5-3. Test procedures and results are detailed in Section 5-4. In Section 5-5 the optical efficiency of the lenslet/micromirror arrangement is examined, and a simplified thermal circuit model is used to estimate optical power handling capability. Conclusions are drawn in Section 5-6.

5.2. Modeling the Lenslet/MEM-DM Configuration

Predicting the far field diffraction pattern resulting from a lenslet/MEM-DM hybrid correcting element is very similar to the bare MEM-DM case, with additional consideration of the lenslet and mirror geometry required. In this section we first examine the lenslet/micromirror geometry. The results of the geometric

analysis are used to define the optical field emerging from the lenslets after reflection from the micromirrors. Scalar diffraction theory is then used to predict the far-field pattern.
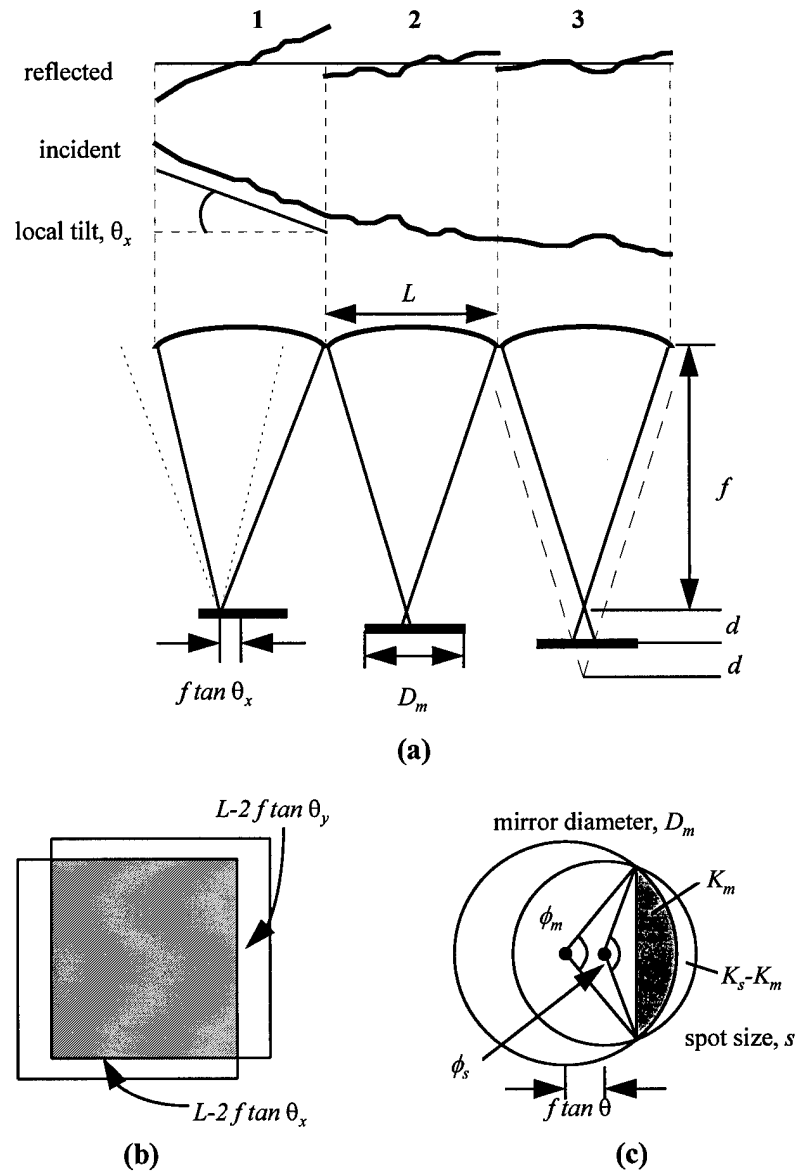
Figure 5-1. (a) Schematic side view of lenslet/micromirror geometry, (b) top view of incident and reflected light for a single lenslet, and (c) intersection of optical spot and reflective mirror surface geometry.

The basic lenslet/micromirror concept is depicted in Figure 5-1(a). The system aperture is divided by the lenslets into a collection of subapertures. In each subaperture the lenslet focuses the incident optical signal onto the micromirror surface. The light entering each subaperture is reflected by the mirror surface,

and re-emerges from the lenslet. Regardless of micromirror position the exiting light is an inverted or flipped version of the incident signal. As depicted in Figure 5-1(a), wavefront aberrations spatially smaller than the lenslet dimensions are simply inverted. This is characteristic of all aberration correction schemes; aberrations spatially smaller then the correcting element spacing can not be corrected. With the lenslet scheme, lenslet size not micromirror size, establishes corrector element spacing. The light which exits the lenslet is a function only of the lenslet dimensions ($L \times L$ square), lenslet focal length (f), and the mirror deflection (d). If the piston mirror is not deflected the exiting light is simply the incident light inverted and delayed by $2f$. When the mirror is deflected the phase delay is $2(f+d)$ and some light is "lost" around the edges of the lenslet. The width of the reflected beam $L_R = L(f + 2d)/f$, is readily found by comparing the similar triangles formed by the incident and reflected light (see Figure 5-1(a) lenslet 3). Assuming all reflected light outside the lenslet aperture is lost, the irradiance after reflection (I_R) from a deflected micromirror is proportional to the areas of incident and reflected beams at the lenslet,

$$I_R = \frac{L^2}{L_R^2} = \left(\frac{f}{f + 2d}\right)^2 \times I_{incident} \tag{5-1}$$

From Equation (5-1) it is apparent that for focal lengths much greater than the deflection very little light is lost. For typical lenslet focal lengths of millimeters and micromirror deflections measured in microns I_R is approximately equal to $I_{incident}$. Thus for incident plane waves the lenslet/micromirror combination behaves as a pure phase modulation element.

When the incident optical signal is not a plane wave (as in aberration correction applications) the local tilt of the wavefront across the lenslet subaperture must be considered. Local tilt causes the spot on the micromirror to deviate from the center of the micromirror. The light reflected from the mirror "misses" the lenslet from which it entered by twice the local tilt angle. In Figure 5-1(a) lenslet number 1 depicts this phenomenon in the x dimension, while Figure 5-1(b) shows the effect of missing in two dimensions. Considering the three dimensional geometry the reflected irradiance due to local tilt is:

$$I_{tilt} = I_{incident} \left(\frac{(L - 2f \tan\theta_x)(L - 2f \tan\theta_y)}{L^2} \right) \tag{5-2}$$

5-3

where θ_x and θ_y are the local tilts in the x and y directions, respectively.

The irradiances computed to this point treat the both the incident and reflected light as a point source on the micromirror surface. Because the light incident on the mirror has a finite spot size we must also consider the effect of this spot "walking" either partially or completely off the mirror surface due to local tilt. The spot size on the mirror due to the square lenslet aperture surface is approximately $s \approx 2 f \lambda / L$. For ease of computation we use a circle of diameter, s, to estimate the light loss due to "walkoff". The geometry associated with the walkoff phenomenon is shown in Figure 5-1(c). When the local wavefront tilt is such that,

$$f \tan \theta \geq \left(\frac{D_m}{2} + \frac{s}{2} \right) \tag{5-3}$$

where D_m is the mirror diameter and θ is the total local tilt, the spot is completely off the mirror surface and it is assumed that all of the incident light is lost. When the spot is not completely off the mirror surface the amount of light returned is directly proportional to the area of the spot remaining on the mirror. The chord c, depicted in Figure 5-1(c) defines the circular segments that comprise the area of the spot remaining on the mirror. The length of c is readily found using Heron's formula to analyze the general triangle formed by the mirror and spot radii, and the local tilt induced spot shift [1];

$$c = \frac{4}{f \tan \theta} \sqrt{b \left(b - \frac{D_m}{2} \right) \left(b - \frac{s}{2} \right) (b - f \tan \theta)} \text{ , with } b = \frac{1}{2} \left(\frac{D_m}{2} + \frac{s}{2} + f \tan \theta \right). \tag{5-4}$$

The areas of each circular segment depicted in Figure 5-1(c) are then [1];

$$K_m = \frac{1}{2} \left(\frac{D_m}{2} \right)^2 (\phi_m - \sin \phi_m), \text{ where } \phi_m = 2 \sin^{-1} \left(\frac{c}{D_m} \right)$$

$$K_s = \frac{1}{2} \left(\frac{s}{2} \right)^2 (\phi_s - \sin \phi_s), \text{ where } \phi_s = 2 \sin^{-1} \left(\frac{c}{s} \right)$$

Calculating the area of the spot (A_{spot}) remaining on the mirror using these circular segments depends on the position of the spot center defined by $f \tan \theta$. Considering all possible cases the spot area is;

$$A_{spot} = \begin{cases} = \pi\left(\dfrac{s}{2}\right)^2, \text{ for } f\tan\theta \le \dfrac{D_m}{2} - \dfrac{s}{2} \\[3mm] = \pi\left(\dfrac{s}{2}\right)^2 - K_s + K_m, \text{ for } \left(\dfrac{D_m}{2} - \dfrac{s}{2}\right) < f\tan\theta \le \dfrac{D_m}{2} \\[3mm] = K_s + K_m, \text{ for } \dfrac{D_m}{2} < f\tan\theta \le \left(\dfrac{D_m}{2} + \dfrac{s}{2}\right) \\[3mm] = 0, \text{ for } f\tan\theta > \left(\dfrac{D_m}{2} + \dfrac{s}{2}\right) \end{cases} \qquad (5\text{-}5)$$

Again, the irradiance due to mirror walkoff is proportional to the ratio of the areas of the spot remaining on the mirror surface to the whole spot,

$$I_{walkoff} = I_{incident}\left(\frac{A_{spot}}{\pi(s/2)^2}\right). \qquad (5\text{-}6)$$

For known aberrations the local tilt at each lenslet and fixed geometry of the hybrid correction element permit computation of the irradiance terms for each lenslet using Equations (5-1 to 5-6). Coherence of the incident signal allows the irradiance terms computed using Equations (5-1), (5-2), and (5-6) to be combined into a total transmission or amplitude value for each active array element,

$$A_{Lenslet} = \sqrt{I_{Lenslet}} = \frac{\sqrt{I_R I_{tilt} I_{walkoff}}}{I_{incident}}, \qquad (5\text{-}7)$$

where the product terms under the radical represent the fraction of incident irradiance remaining for each geometric effect considered. The square root in Equation (5-7) converts the total irradiance value to an amplitude value used to define the field emerging from the lenslet/MEM-DM hybrid correcting element. The amplitude of the field emerging from a lenslet/MEM-DM correcting element can be substantially reduced for high local tilts, and predictably reduce the peak intensity in the far field.

Applying scalar diffraction theory, the field $U_0(\xi,\eta)$ creates a disturbance in the far field $U_1(x,y)$, given by [2]

$$U_1(x,y) = \frac{e^{ikz}}{i\lambda z}\exp\left[i\frac{k}{2z}\left(x^2 + y^2\right)\right]\cdot \mathrm{F}\{U_0(\xi,\eta)\}\,\Big|_{\omega_\xi = x/\lambda z,\,\omega_\eta = y/\lambda z}, \qquad (5\text{-}8)$$

where $F\{\cdot\}$ is the Fourier transform operator, λ is the analysis wavelength, $k=2\pi/\lambda$, z is the propagation distance from source (or ξ, η) plane to observation plane, and (ω_ξ, ω_η) are the spatial frequencies in the ξ and η directions in the object plane. The coordinate pairs (x, y) and (ξ,η) represent parallel coordinate systems with origins on the optical axis z. The far-field intensity of $U_0(\xi,\eta)$ is given by $I(x,y) = |U_1(x,y)|^2$. To within a magnification factor, the far-field intensity is equivalent to the point spread function (PSF) of an imaging system having an aperture defined by $U_0(\xi,\eta)$ [2]. Thus the far-field pattern is referred to as the PSF in the remainder of this chapter. In the bare MEM-DM case the initial optical disturbance $U_0(\xi,\eta)$ is defined immediately after reflection from the mirror surfaces. To model the lenslet/MEM-DM case computation of the PSF is simplified by defining the initial disturbance $U_0(\xi,\eta)$ as the field emerging from the lenslets after reflection from the MEM-DM. Essentially the lenslet/MEM-DM is treated as a system that modulates both the phase and amplitude of the incident optical signal. For incident plane waves the amplitude for each mirror is identical and the phase is determined by micromirror deflections. For aberrated incident waves the phase is defined as the residual phase, or phase remaining after correction, and the amplitude for each lenslet/micromirror element is defined by the results of the geometric analysis from Equation 5-8. Let the incident wavefront be a unit amplitude wave represented by $U_i(\xi,\eta) = \exp[i\phi(\xi,\eta)]$, where $\phi(\xi,\eta)$ represents the wavefront aberration, if any. Then the initial field can be written as,

$$U_0(\xi,\eta) = U_i(\xi,\eta) \cdot a(\xi,\eta) \exp\left[i\frac{4\pi h(\xi,\eta)}{\lambda}\right] \tag{5-9}$$

where $a(\xi,\eta)$ represents the amplitude modulation and $h(\xi,\eta)$ represents the relative height of the micromirrors in the array. The extra factor of 2 in the argument of the complex exponential accounts for the round trip nature of phase modulation using reflective devices. We treat $h(\xi,\eta)$ as a function only of mirror deflection and have not found it necessary to include either propagation effects, or the effects of the lenslet surface for acceptable modeling results. The values of $a(\xi,\eta)$ are determined by the geometric

analysis presented earlier, with the value across a given lenslet/micromirror element constant. To represent the gap between lenslets corresponding portions of $a(\xi,\eta)$ are set to zero.

(a)   (b)
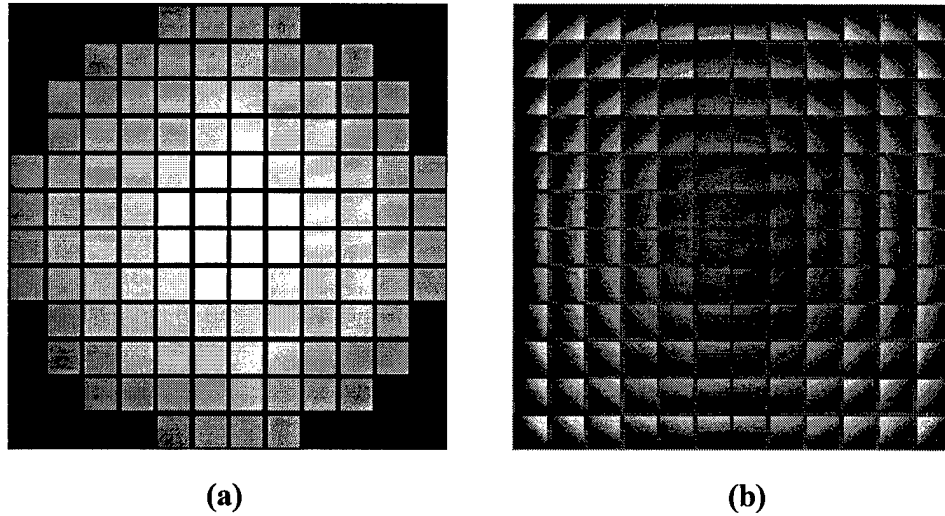
Figure 5-2. (a) Modeled amplitude, $a(\varepsilon,\eta)$, and (b) height, $h(\varepsilon,\eta)$, functions depicted in grayscale.

For the incident plane wave case $a(\xi,\eta)$ is uniform across all the modulation elements and computation of the PSF is straight forward. More interesting is the case when a highly aberrated incident wave with correspondingly high local tilts is applied. Then amplitude variation across the array due to geometric effects can significantly influence the peak intensity of the PSF. Consider for example correction of a defocus aberration (or spherical wavefront) with a 0.35 m radius of curvature using the lenslet/MEM-DM geometry defined. The amplitude $a(\xi,\eta)$ and residual phase errors of the field $U_0(\xi,\eta)$ are shown as grayscale images in Figure 5-2 (a) and (b) respectively. Simulation results show that the peak intensity of the PSF for this field is 34% that of the incident plane wave case. Simulation of the residual phase error alone reduces the peak intensity to 58% of the plane wave case, so we see that the geometric amplitude effects are substantial. A Matlab® model incorporating the geometric analysis for spherical aberrations has been developed. Figure 5-3 plots the simulated relative peak intensity of the PSF after correction as a function of applied spherical aberration radius of curvature. From this curve we can see the importance of the geometric analysis in establishing performance limits of lenslet/MEM-DM for aberration

correction applications. Measured peak intensity data from aberration correction experiments is also plotted in Figure 5-3, but will be discussed in Section 5-4.
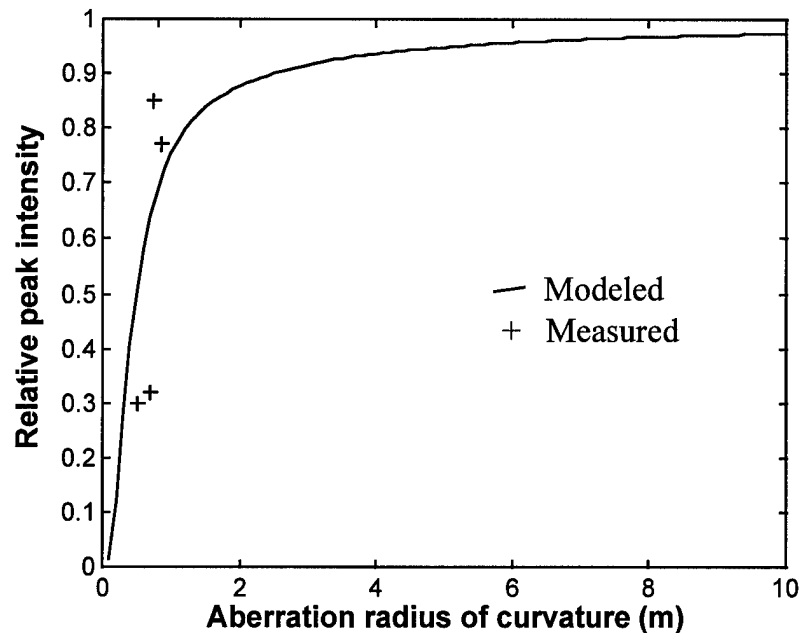
Figure 5-3. Modeled and measured relative peak intensity of the point spread function (PSF) as a function of defocus aberration radius of curvature.

5.3. Device and Test Bed Description

One driver for pursuing the lenslet/MEM-DM approach is to achieve high optical efficiency without a specialized microfabrication process. By focusing light on a smaller reflective surface several microfabrication challenges are avoided. All of the chip area not dedicated to the reflective surfaces is available for the actuator structure and wiring without regard for the optical effects, thus control of the underlying topography and/or planarization are avoided. By making the mirror surfaces small, curvature induced by differing material residual stresses is minimized (see Chapter 4). Because fielded electrostatic micromirror systems will likely require an optical window to protect the microscopic moving parts from dust, moisture, and handling, the addition of a lenslet array which also serves as a protective window is not especially burdensome.

The MEM-DM used in this work was designed specifically for use with an available lenslet array having 203 μm center-to-center spacing. Scanning electron micrographs of the MEM-DM array and a single micromirror element are shown in Figure 5-4. The array shown is comprised of 12×12 elements on a 203 μm square grid. Four elements (2×2) in each corner of the array are wired together serving only as test devices (16 total). The remaining 128 elements are individually controllable. The micromirror arrays were fabricated in the DARPA supported Multi User MEMS Processes (MUMPs) [3]. MUMPs is a polysilicon surface micromachining process with 2 releasable polysilicon layers.
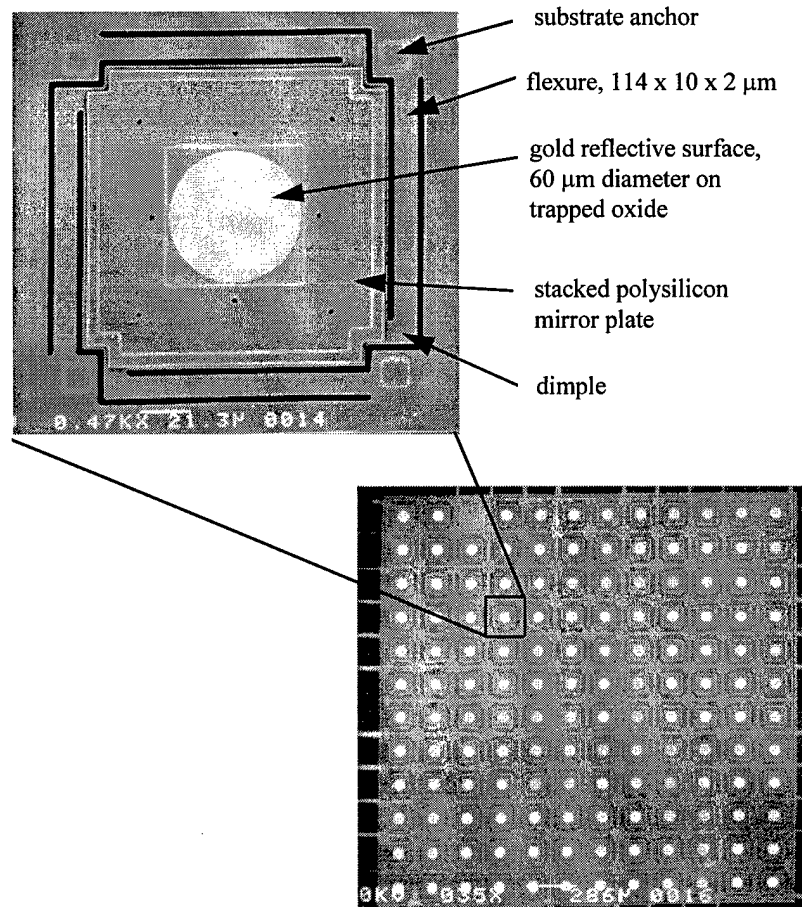
Figure 5-4. Annotated scanning electron micrographs showing MEM-DM construction.

Several design features are incorporated to improve the device deflection uniformity, yield, robustness, and optical characteristics of this particular MEM-DM design. The stacked polysilicon (3.5 μm thick) mirror plate area is made as large as possible to decrease the maximum control voltage required. Stacking of the polysilicon layers greatly increases the stiffness of the plate which is a function of the thickness cubed. Under the 60 μm diameter gold reflective surface a 0.75 μm thick layer of oxide is also trapped between the two polysilicon layers. Curvature of the mirror surface is minimized by keeping the reflective surface as small as possible and making the underlying structure as stiff as possible. Despite a high residual tensile stress in the metallization (typically ~50 MPa), measured mirror curvature is less than 30 nm across the mirror surface. By maximizing the mirror plate area, which also serves as the movable upper electrode of the electrostatic structure, the flexures supporting the plate can also be made relatively stiff. Stiff flexures improve device yield by better resisting stiction forces during the release process. The four flexures of this MEM-DM design are 10 μm wide, 114 μm long, and 2 μm thick. We have found that wide flexures (greater than 4 μm) greatly improve device-to-device deflection uniformity for micromirrors fabricated in the MUMPs process. Wide flexures minimize the impact of overetching, or rounding of the corners, on the total cross-sectional area of the flexures. Not visible in Figure 5-4 are dimples at the end of each flexure which protect the device from overdriving. Electrostatic devices exhibit a characteristic "snap-through" instability behavior when deflected past about 1/3 the nominal plate separation distance [4]. This occurs because the linear restoring force of the flexures can not counter the rapidly increasing electrostatic force which is a function of both the applied potential and separation distance. If not adequately protected by dimples, parallel plate electrostatic devices typically stick down in the fully deflected position if overdriven. Another design feature of note is the minimal access to the air gap between the electrodes. Although the primary purpose of closing the entire top plate structure was self planarization for post-process facesheet fabrication, it has the added benefit of minimizing exposure of the gap to contaminants such as dust and moisture. The devices in this MEM-DM have been (intentionally and unintentionally) overdriven repeatedly. Not a single device failure has been observed in several months of testing in room air. The die were mounted in a 144 PGA package using a hot melt adhesive prior to the

release etch. The sacrificial oxide layers were removed in a 2 minute and 30 second etch in 49% hydrofluoric acid. After soaking in methyl alcohol for 20 minutes to stop the release etch and displace water the die were dried on a 60 °C hot plate. Following the release process the devices were ultrasonically wirebonded.

To fully enjoy the cost advantages of microfabrication, device deflection uniformity must be sufficient to eliminate the requirement for characterization testing of each and every device. Testing of similar electrostatic designs has shown that such uniformity is achievable in the MUMPs polysilicon micromachining process [5]. The MEM-DM used for the lenslet experiments was subjected to only minimal quantitative testing and qualitative verification of device uniformity. Uniformity of device deflection response was not quantitatively tested. During static fringe testing the four electrically parallel test devices in one corner of the array showed no discernible difference in deflection response. To qualitatively test yield and deflection uniformity the MEMS control computer with 128 D/A converter channels was connected to the MEM-DM while it was on the interferometric microscope. One by one all 128 devices were driven with a 9.99V control signal while observing mirror deflections on the microscope video monitor. This test confirmed 100% functional device yield and verified control computer to micromirror array wiring. Subsequently, various figures were applied to the MEM-DM array while monitoring the video display. Qualitatively, device deflection uniformity was observed to be excellent.

Prior micromirror characterization work has shown that deflection is accurately represented by $d=kV^2$ where k is a constant that incorporates the physical characteristics of the device structure, i.e. electrode area, relative dielectric in the space between electrodes, and total flexure spring constant. Using the voltage required for 316 nm deflection (V_{316}=13.8 V) obtained using the static fringe measurement technique k is computed as $k = d / V_{316}^2 = (316 \text{ nm}) / (13.8 \text{ V})^2 = 1.66 \text{ nm} / \text{V}^2$. The maximum stable deflection of the sample MEM-DM mirrors was also measured. By slowly stepping the control voltage for the test mirrors while observing deflection on the microscope interferometer a maximum stable deflection of ~600 nm at 15 V was obtained. This shows reasonable agreement with the 1/3 the gap distance rule of thumb, but more importantly establishes the usable deflection range of the MEM-DM for optical

modulation. To work within the stable deflection range of the micromirror devices, a modulo λ/2 is applied to the desired deflection profile before computing the control voltage for each MEM-DM element. By so doing the mirrors move at most 316 nm modulating the optical beam by up to one wavelength in reflection. The modulo λ/2 deflection scheme overcomes the process imposed deflection limitations of the mirror design. To obtain 316 nm deflection with the 0 to 9.99V range of the D/A converter boards the control range is offset using a bias voltage. The required bias voltage is found by iterating to find V_{Bias} (to the nearest 0.1 V) that satisfies the equation $316/k = (V_{Bias} + 9.99)^2 - V_{Bias}^2$. The measured value of V_{316} is provided as an input to a Matlab® script which computes k and V_{Bias}, then generates control voltages for any desired MEM-DM deflection profile using the modulo π deflection scheme.

The packaged MEM-DM is mounted in the test bench depicted in Figure 5-5. An 18 mW Helium-Neon (HeNe, 632.8 nm) laser is collimated to provide the optical signal source. For aberration correction experiments the beam passes through a lens L_a to generate a quadratic aberration. After reflection from the fold mirror (M1), the beam enters a beam splitter (BS1) which reflects the incident wave toward the MEM-DM. A pair of afocal lenses L_l and L_s between BS1 and MEM-DM compacts the beam to fill the controllable surface of the MEM-DM. The refractive lenslet array LL is placed at the back focal plane of L_s, and the MEM-DM is located at the back focal plane of LL. An iris located a focal length away from L_l between BS1 and M1 controls the beam diameter. The beam reflected from (and diffracted by) the MEM-DM/lenslet combination traverses the afocal telescope (L_s, L_l), BS1, and translating lenses L_{t1} and L_{t2}. At BS2 light is picked off for a CCD camera which records the image of the lenslet surface. In the other leg a Fourier transforming lens L_F generates the far-field diffraction pattern of the light transmitted by BS2, which is equivalent to the point spread function (PSF) of an imaging system. Another lens L_M magnifies the far-field pattern on the 256×256 pixel array of the PSF camera. Lens focal lengths and nominal positioning dimensions are summarized in Tables 5-1 and 5-2.
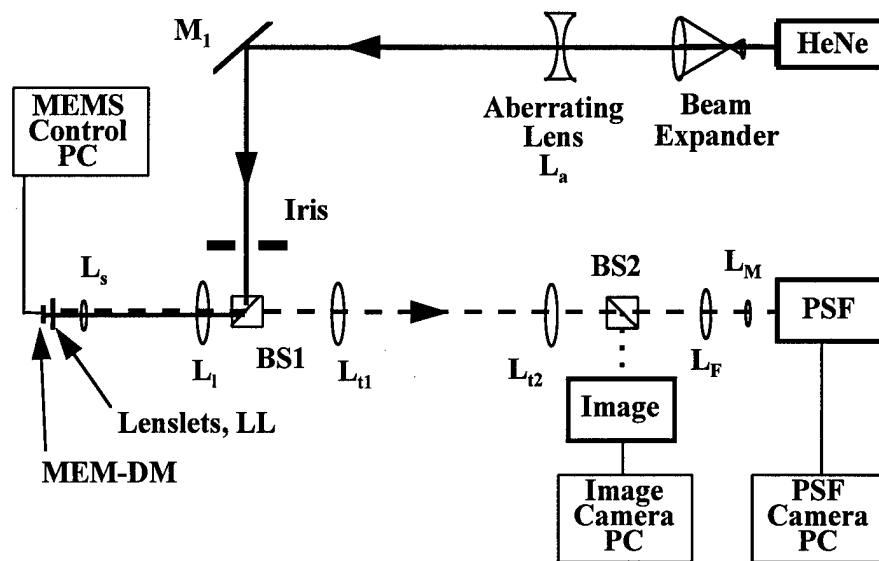
Figure 5-5. Optical test bed layout. Note drawing is not to scale. Lens focal lengths and dimensions are provided in Tables 5-1 and 5-2 respectively.

Table 5-1. Focal Lengths of Lenses in Adaptive Optical Test Bed.

Lens labels	Focal length (mm)
L_a	-500
L_l	250
L_s	100
LL	7.8
L_{t1}, L_{t2}	300
L_F	75
L_M	11

Table 5-2. Optical Component Locations in Adaptive Optical Test Bed.

Distance	Nominal Distance (mm)
L_a to iris	1700
iris to L_l	250
L_l to L_s	350
L_s to LL	100
LL to MEMS-DM	7.8
L_l to L_{t1}	550
L_{t1} to L_{t2}	600
L_{t2} to L_F	375
L_F to $_{LM}$	89
L_M to CCD camera (PSF)	50

5.4.   Test Procedure and Results

The test bed optics are initially aligned with a plane mirror in place of the lenslet array and MEM-DM by making use of the reflections from lens surfaces and the "ghost" reflections from the beam splitter cubes.   The MEM-DM is then installed (without the lenslets in place) and aligned to obtain a far-field pattern on the PSF camera.   The MEM-DM is then moved back by the lenslet focal length and the lenslet array is installed.   The Image and PSF cameras proved extremely useful for alignment of the lenslet array to the MEM-DM.   While watching the Image camera display the MEM-DM/lenslet pair is positioned for maximum optical through-put and uniform lenslet illumination, while maintaining the position of the zeroth order on the far field camera.   Baseline images of the far field diffraction pattern and lenslet array surface (recorded at the PSF and Image cameras respectively) are shown in Figure 5-6.   Note that the Image camera shows inversion or flipping of the beam(s) expected from passage through the lenslet.

(a)   (b)
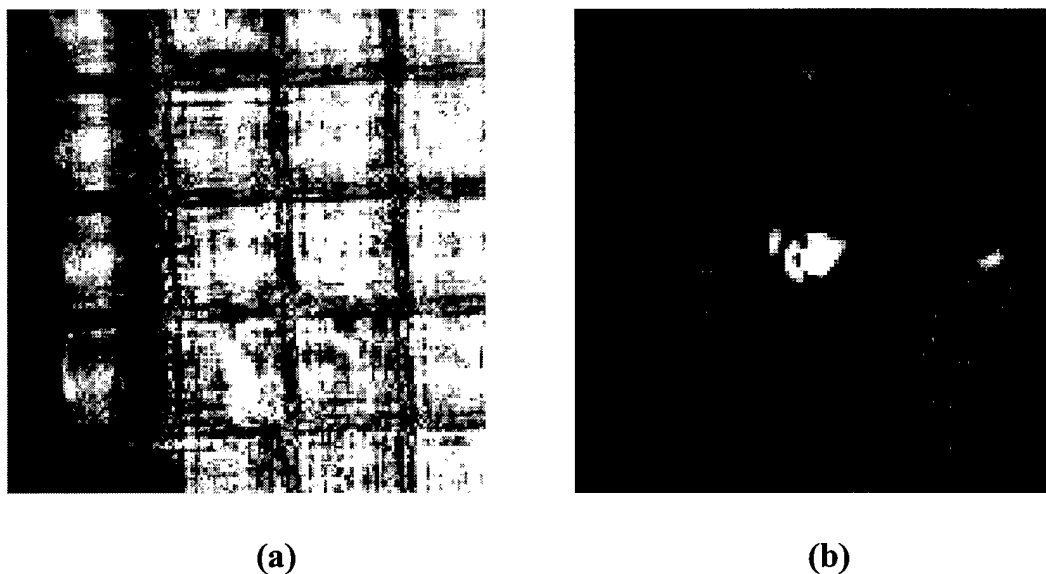
Figure 5-6. Baseline Image and PSF camera images. The image of lenslet surface near aperture edge (a) shows the expected image inversion. Note that the PSF camera image (b) is reduced to only 16 grayscale levels to show grating lobes of the diffraction pattern.

Background interference effects were measured prior to experimentation. All elements in the array were simultaneously deflected by slowly increasing the array bias voltage while monitoring the PSF camera. The main lobe peak intensity was observed to vary by 30% due to interference effects with a single minimum occurring at about $3\lambda/4$ deflection. In contrast, similar testing of bare MEM-DMs (with low fill factor) shows that background interference can completely null the main lobe of the PSF. Even for bare micromirror arrays with relatively high fill factor (80%), interference with the static background structure can cause significant (30%) amplitude modulation [6]. Thus, lenslets improves the effective fill-factor of the micromirror array and correspondingly reduces static background interference phenomenon. In addition, the deflection range was limited to $\lambda/2$ (316 nm) thus avoiding the background interference minimum.

The first experiment performed with the lenslet/MEM-DM combination demonstrates optical beam steering. In one dimension an optical phased array of n elements, with uniform phase shift spacing (between elements) from 0 to 2π steers a beam to an angle $\theta_S = \lambda/(nL)$, where L is the spacing of the elements (the lenslet dimension in this case), and λ is the operating wavelength [7]. Control voltage files corresponding to mirror deflections approximating tilted planes were generated. Using the modulo $\lambda/2$ scheme each tilted plane consists of 1, 2, 3, 4 or 6 "slats" comprised of 12, 6, 4, 3, and 2 elements respectively, with 0 to 316 nm total deflection across each slat. Rotated versions of each slat voltage control file were generated to steer the beam in the $+x$, $-x$, $+y$, $-y$ directions. Control voltage files approximating a plane tilted 0.15 mrad in both x and y were also generated to demonstrate beam steering non-orthogonal to the rectangular diffraction pattern. Each of the 24 voltage control files was applied in turn and the resulting PSFs recorded.

The PSF camera was calibrated by measuring the mean distance in pixels between the zeroth order peak and the four orthogonal first order peaks in the diffraction pattern with a plane wave incident on a flat MEM-DM. The first order diffraction peak occurs at $\theta_1 = \lambda/L$, so the angle per pixel on the PSF camera is given by

$$\theta_{pixel} = \frac{\lambda}{x_p L} \text{ radians / pixel} \qquad (5\text{-}10)$$

where, x_p is the measured mean distance in camera pixels between the zero and first order peaks in the far field diffraction pattern. Using the calibration method the PSF camera exhibits an angular resolution of 56 to 66 μrad. A summary of beam steering position results is plotted in Figure 5-7. For comparison with theory the mean steering angles and mean peak intensity values for the orthogonally steered sets are listed in Table 5-3. Note that the top row in Table 5-3 is the no steering case with all micromirrors at the same height. Steering angle measurements show excellent agreement with 1-D beam steering theory. The theoretical predictions are listed in the table for comparison. In the 6 slat case the micromirror array surface approximates 2 planes tilted in opposite directions because the slats are only 2 elements wide. Thus two beams of roughly equal intensity are formed each ~1.5 mrad from boresight.
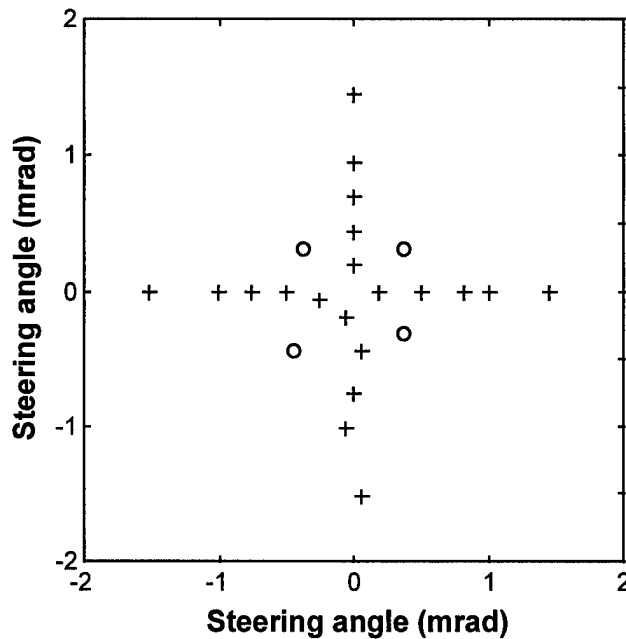
Figure 5-7. Summary plot of single beam steering results. Crosses denote the data points which were averaged to produce the numeric results in Table 5-3.

Table 5-3. Beam Steering Measured and Theoretical Results.

# Slats	Elements per slat	Theoretical steering angle (mrad)	Measured mean steering angle (mrad)	Mean peak intensity (camera counts)	Theoretical peak intensity (%)	Measured peak intensity (%)
1	12	N/A*	N/A*	253	100	100
1	12	0.259	0.21	225	97	89
2	6	0.518	0.48	200	91	80
3	4	0.778	0.77	183	81	72
4	3	1.03	1.01	189	68	74
6	2	1.56	1.50	120	40	53

* unsteered case which serves as baseline for all cases

The peak intensity of the steered beams follows the diffraction envelope of a single element, $\text{sinc}^2(\pi L \sin\theta / \lambda)$, where θ is the angle from boresight [8] For small angles where $\theta \approx \sin\theta$ this simplifies to $\text{sinc}^2(\pi/n)$, where again n is the number of elements with uniformly spaced phase shift between 0 and 2π. Measured mean peak intensity values show relatively good agreement with theory. A 2-dimensional full width half maximum (FWHM) was also computed as a measure of beam quality. From phased array theory the beam width increases as $1/\cos\theta$ for small steering angles [9]. Negligible beam spreading is expected over the small steering angles possible. The measured FWHM values for all steering cases were within 12% of the flat MEM-DM case. The variation observed does not correspond to steering angle and is attributed to measurement noise.

One potential application of the lenslet/MEM-DM system is projection of laser beacons for adaptive optics. With a sufficiently large segmented mirror system the mirror can be partitioned to create multiple independently steered beams. With appropriate control of the MEM-DM the number, position, and relative intensity of laser beacons can be varied in real time. To illustrate this capability in the test bed system the MEM-DM is partitioned into two control surfaces, creating two beams which are independently steered. Both steered positions are not aligned to the rectangular grid of the diffraction pattern to demonstrate the flexibility of the MEM-DM for multiple beam steering. The steering angles were chosen

so that $\theta_{x1}=-\theta_{y2}$ and $\theta_{y1}=-\theta_{x2}$, yielding beams with the same total angle from boresight to obtain beams of similar intensity. PSF camera images of the central region for the unsteered beam (a) and dual steered beam case (b) are shown in Figure 5-8. Peak pixel locations are annotated. From peak to sidelobe measurements θ_{pixel} =66 µrad using Equation (5-10). The peaks of the steered beams are located at angles of θ_{x1}=0.330 mrad, θ_{y1}=0.792 mrad and θ_{x2}=-0.792 mrad, θ_{y2}=-0.396 mrad with respect to the peak of the unsteered beam. The total steering angles for Beam1 and Beam2 are 0.858 mrad and 0.885 mrad, respectively. The peak intensity of Beam2 is 46% the peak intensity of the unsteered beam, while Beam1 is 25% the peak intensity of the unsteered beam. The difference in measured peak intensities for the steered beams is attributed primarily to slight misalignment of the aperture on the lenslet/MEM-DM. The relative efficiency of the nominal 6 × 12 mirror control surfaces for the respective beam directions is also probably a factor but has not been studied closely. There was no significant change in the FWHM of the steered beams (all FWHM within 20%), suggesting that beam quality is preserved. This experiment demonstrates that a single lenslet/MEM-DM can replace the optical power splitter and multiple steering elements required to generate multiple laser beacons.
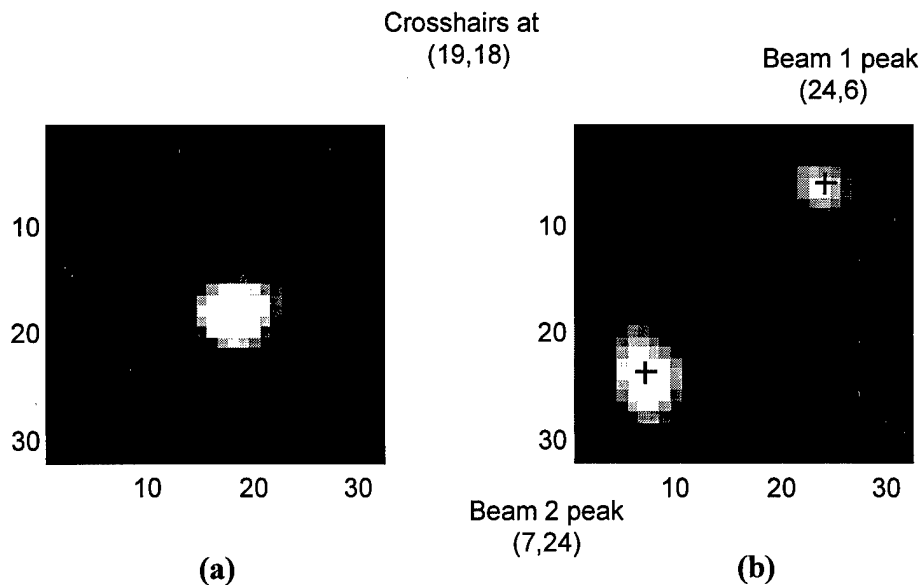
Figure 5-8. Dual beam steering results with annotated peak intensity locations. Upper image is unsteered beam whose peak intensity defines crosshairs on both images. Lower image depicts two steered beams nominally equidistant from the crosshair origin.

For aberration correction experiments an aberration lens is placed in the incident beam between the beam expander and turning flat M1. The aberrating lens L_a produces a defocus aberration at the lenslet surface. Applying the lens equation twice, the radius of curvature of the spherical wavefront surface is given by

$$R_{aber} = f_s - \left(\frac{f_s f_l^2 - f_s o_1 + f_s f_l}{f_l^2} \right),$$
(5-11)

where the object distance o_1 is the distance from L_a to L_1 minus the focal length of the aberration (f_a), and f_s and f_l are the focal lengths of the lenses comprising the afocal telescope. The distance from the aberrating lens (L_a) to the afocal telescope (L_1) is 1.92 m. The lens focal lengths are listed in Table 5-3. By varying both the focal length of L_a and its position on the test bed a continuously varying range of quadratic aberrations can be produced.
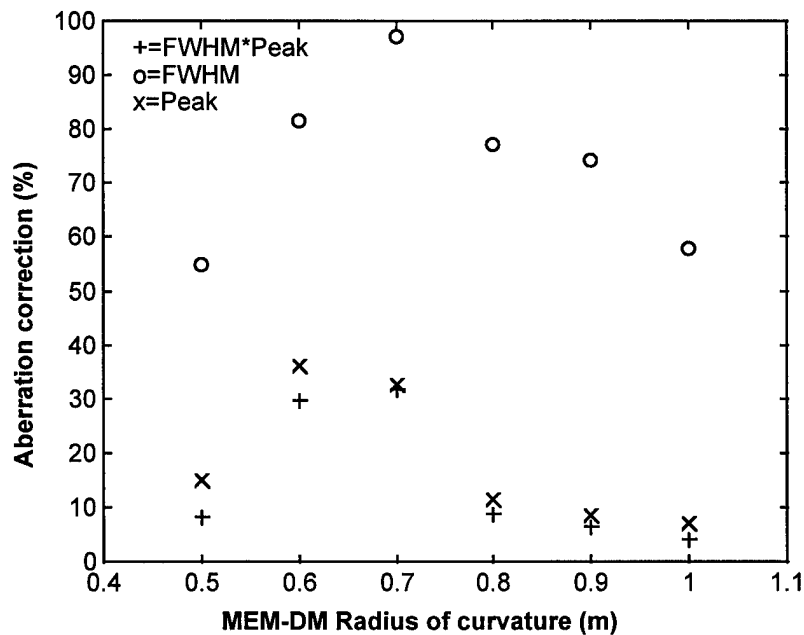
Figure 5-9. Aberration correction results for a 0.35 m radius of curvature aberration as a function of the radius of curvature applied to the MEM-DM. Best correction is obtained for $R_{MEM-DM}=2R_{aber}$.

Aberration correction experiments were conducted by inserting the aberrating lens and estimating R_{aber} using Equation (5-11). Several spherical figures with radius of curvature near $2R_{aber}$ were subsequently applied to the MEM-DM. PSF camera images were recorded for MEM-DM figure applied. Plotted in Figure 5-9 are the relative correction (FWHM unaberrated/FWHM corrected) and peak intensity (normalized to the unaberrated case) for several applied MEM-DM radii of curvature with a rather severe spherical aberration, R_{aber}=0.35 m. Also plotted is the product of the two metrics. As expected, best resolution performance (and highest combined metric) is achieved with a 0.7 m radius of curvature concave spherical figure applied to the MEM-DM. The FWHM of the corrected signal main lobe is 0.98 that of the unaberrated case showing that near diffraction limited imaging resolution is achievable. The peak intensity of the main lobe is 32% the peak intensity of the unaberrated case in excellent agreement with the model presented in Section 5-2.

Aberrated and corrected PSF images for other quadratic aberrations are shown in Figure 5-10. In all cases the MEM-DM figure applied for correction is a concave spherical surface with a radius of curvature equal to $2R_{aber}$. The 256 level grayscale of each image in Figure 5-10 is independently adjusted to show detail. The measured FWHM in camera pixels, and peak intensity relative to the unaberrated case are annotated beside each image for comparison.

The relative peak intensities for all aberration correction cases (including some not shown) are also plotted on the model curve in Figure 5-3. While the measured relative peak intensities confirm the presence of a steep performance drop off predicted by the model the measured data is somewhat scattered due to experimental errors. The largest source of error is normalization of the incident optical power after inserting the aberrations. The beam divergence induced by the aberrating lens results in less optical power entering the system aperture. Scale factors to compensate for the reduced optical power were obtained by recording power meter measurements between the Iris and BS1 for all cases. In addition to the optical power scaling, it was necessary to scale the PSFs to account for the optical density filters used to prevent camera saturation. These scaling errors are present only in comparisons of aberrated and corrected results to the unaberrated case and to each other. Before and after correction results for a given aberration, such as

the three sets shown in Figure 5-10, were recorded without changing the optical power or optical density

filters.

Plane Wave/Flat MEM-DM

FWHM=4.97
Peak=100%

Aberrated   Corrected

R_{aber}=0.8 m
FWHM=6.48
Peak=20%

FWHM=5.17
Peak=~100%

R_{aber}=0.75m
FWHM=8.06
Peak=17%

FWHM=5.17
Peak=85%

R_{aber}=0.5 m
FWHM=13.7
Peak=9%

FWHM=6.38
Peak=30%
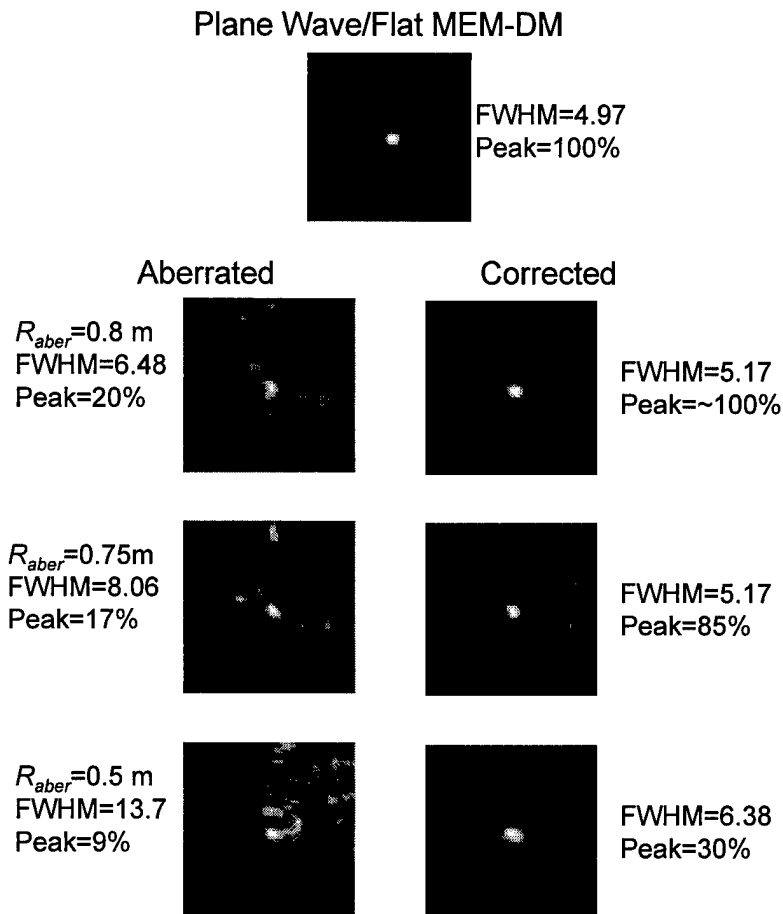
Figure 5-10. PSF camera images showing plane wave incident on undeflected MEM-DM and quadratic aberration correction results. Note that each image is independently scaled to 256 grayscale levels to better show PSF structure. FWHM and peak intensity relative to the plane wave/plane MEM-DM are provided for comparison.

In addition to beam steering and quadratic aberration correction several other experiments were

conducted to explore the characteristics of the lenslet/MEM-DM correcting element and the test bed. With

a plane wave incident on the correcting element any figure applied to the MEM-DM should theoretically

reduce the peak intensity of the main lobe and increase the width of the main lobe. As expected, convex

and concave curvatures of equal magnitude on the MEM-DM produce similar effects in the PSF. When

small random deflections ranging from 0 to $\lambda/10$ are applied to the MEM-DM with an incident plane

wave, there are discernible effects in both the main lobe peak intensity and FWHM of the main lobe. The results remain consistent as the random deflection pattern is rotated on the MEM-DM. From this we conclude that the MEM-DM is indeed very flat (all elements in phase) when at rest. We also can infer that the measurement techniques are sensitive to relatively small optical phase variations. When random deflections of $\lambda/4$ are applied to the MEM-DM and the deflection pattern rotated, structures in the PSF are observed to rotate with the deflection pattern indicating good deflection uniformity. Composite MEM-DM figures comprised of x, y tilts, radius of curvature, and a random component have also been applied to the MEM-DM with good results. For system applications requiring both low order (tip, tilt) compensation over small angles and high order aberration correction the segmented MEM-DM/lenslet system may provide both in a single adaptive element. Initial precompensation experiments have also been conducted. With an aberrating lens ($\sim$-3.5 m focal length) placed between BS1 and L_{t1} the main lobe peak intensity of the PSF is reduced to 11% of the unaberrated case. Applying a 100 cm radius of curvature to the MEM-DM precompensates the incident plane wave, increasing the measured peak intensity of the PSF to 67% of the unaberrated value.

5.5.   Optical Efficiency and Power Handling

Having demonstrated the utility of the lenslet/MEM-DM for beam steering and aberration correction the following section considers the system integration issues of optical efficiency and power handling. The principal goal of the lenslet array in the lenslet/MEM-DM system is improvement of the optical efficiency (fill-factor) of the correcting element. The fill factor computed from layout dimensions of the bare MEM-DM used in this work is less than 7%. Comparison of the light and dark areas in Figure 5-2 suggests a maximum fill-factor of about 70-80% for the lenslet/MEM-DM case. For an empirical measurement of lenslet/MEM-DM optical efficiency, power meter readings were recorded between BS1 and L_{t1} with and without a plane mirror (99% reflective) inserted in front of the lenslet array. The highest measured optical efficiency of the lenslet/MEM-DM corrector using this method was 59%. The discrepancy between

estimated and measured optical efficiencies is attributed to misalignment between the lenslet array and
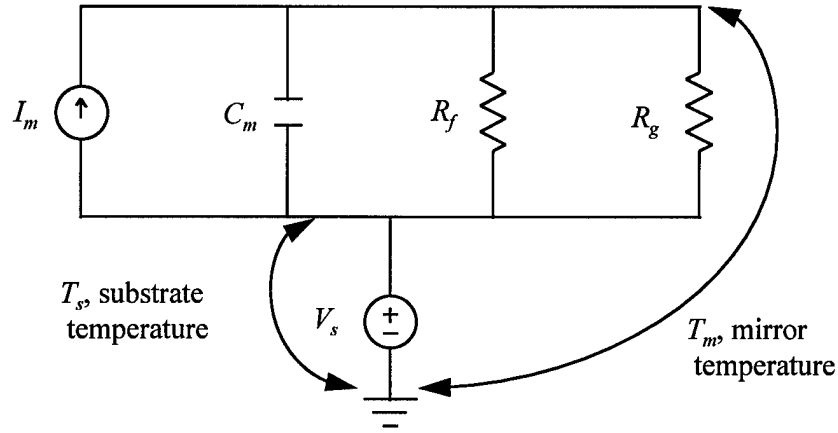
MEM-DM.

Figure 5-11. Thermal equivalent circuit model used to estimate optical power handing capability of MEM-DM.

For beam projection applications the optical power handling capability of the micromirror structure is a critical issue. The thermal circuit model shown in Figure 5-11 provides a straightforward means of estimating the maximum optical power handling capability of the MEM-DM. Similar thermal circuit models have been used to model the behavior of lateral thermal actuators and thermal piston micromirrors [10] (also see Chapter 6).   The power into the system, represented by the current source I_m , is the optical power (P_O) not reflected by the micromirror surface;

$$I_m = P_O\left(1 - \mathrm{R}_{mirror}\right),$$ (5-12)

where R_{mirror} is the reflectance of the mirror surface. Laboratory measurements of the mirror surface under HeNe laser illumination show a reflectance of 91.5% [11]. The thermal energy deposited on the mirror plate is conducted to the substrate only through the polysilicon flexures (R_f) and the volume of gas directly beneath the mirror plate (R_g). Three assumptions are incorporated to permit the simple lumped element model: (1) the mirror plate is highly conductive and its temperature remains uniform; (2) the substrate is an infinite heat sink at room temperature (25 °C); and (3) heat loss or transfer due to radiation is assumed negligible. The value of flexure thermal resistance is given by

$$R_f = \frac{L_f}{N\kappa_{poly}A_f}, \qquad\qquad (5\text{-}13)$$

where N is the number of flexures, L_f is the flexure length, A_f is the cross-sectional area of the flexure, and κ_{poly} is the thermal conductivity of polysilicon (30 W/m-K). Likewise the thermal resistance representing the gas volume is,

$$R_g = \frac{L_g}{\kappa_{gas}A_g}, \qquad\qquad (5\text{-}14)$$

where L_g is the gap between the mirror plate and substrate, A_g is the cross-sectional area of the gas volume, and κ_{gas} is the thermal conductivity of the gas media. For a conservative estimate of optical power handling capability L_g is set to the nominal 2.0 μm as-fabricated height, and A_g is set to the area of the mirror plate neglecting gas conduction along the flexures. C_{mirror} represents the thermal capacity of the mirror plate found by summing the volume-density product for the materials which make up the plate structure. The mirror thermal capacity is not a factor for a steady-state (thermal equilibrium) solution but is included for model generality. Writing the temperature (voltage) of the mirror plate in terms of the current source and solving for optical power yields,

$$P_O = \frac{T_m - T_s}{\left(1 - R_{mirror}\right)\left[\dfrac{R_f R_g}{R_f + R_g}\right]}, \qquad\qquad (5\text{-}15)$$

where T_s and T_m are the substrate and mirror temperatures, respectively. For a given maximum mirror temperature, device structure, and ambient media, Equations (5-13) to (5-15) provide an estimate of the maximum optical power a single micromirror can tolerate before failure. The estimated values produced by the thermal circuit model are in excellent agreement with values produced using the experimentally verified (in vacuum) and more rigorously developed thermal equilibrium model in Reference 25. Thermal testing of MUMPs mirrors has shown degradation of the mirror surface reflectivity at temperatures greater than 250 °C.[25] Using 250 °C as the maximum tolerable mirror temperature (T_m) and a substrate temperature (T_s) of 25 °C the computed maximum optical power for the MEM-DM used in this work is 56 mW per mirror element if operated in a vacuum ($R_g \to \infty$). Significantly higher incident optical power is

possible if the gas media surrounding the MEM-DM has high thermal conductivity. For example if the MEM-DM is surrounded by helium at 1 atmosphere (κ_{gas} =0.152 W/m-K) [12], the thermal circuit model yields an estimated maximum optical power of 3.98 W per mirror element. Assuming uniform illumination of the 112 active elements in the MEM-DM aperture incident optical beams of over 400 W can conceivably be controlled. The maximum operating speed of the mirrors will be reduced somewhat by squeeze film damping but kilohertz operation is still feasible with low viscosity gas media.

5.6. Conclusions

This chapter presented results of optical test bed experiments employing a refractive lenslet array and microfabricated deformable mirror phase conjugating element. The lenslet array has the desired effect of significantly increasing achievable fill-factor, and mitigating static background interference effects. The importance of lenslet and MEM-DM geometry in establishing performance limits for the hybrid correcting element has been demonstrated. The experimental results are well understood and are in good agreement with theoretical predictions. A simple thermal circuit model for estimating the optical power handling has been proposed. Maximum optical power handling estimates from this model are encouraging. In particular the experimental results suggest use of lenslet/MEM-DM systems for beam projection applications in which a plane incident wavefront virtually eliminates the geometric effects that must be considered for aberration correction applications.

References

1   *CRC Standard Mathematical Tables*, CRC Press, Boca Raton, FL, 1990.

2   J. W. Goodman, *Introduction to Fourier Optics*, McGraw-Hill, New York, NY, 1968.

3   D. A. Koester, R. Mahadevan, and K. W. Markus, "Multi-user MEMS processes (MUMPs): introduction and design rules, rev. 4," Technical Report, MCNC MEMS Technical Applications Center, 3021 Cornwallis Road, Research Triangle Park, NC 27709, 1996.

4   P. M. Osterberg, R. K. Gupta, J. R. Gilbert, and S. D. Senturia, "Quantitative models for the measurement of residual stress, Poisson ratio, and Young's modulus using electrostatic pull-in of beams and diaphragms," in *Technical Digest, Solid State Sensor and Actuator Workshop*, Hilton Head, SC, pp. 184-188, 1994.

5   R. Krishnamoorthy, T. Bifano, and G. Sandri, "Statistical performance evaluation of electrostatic micro actuators for a deformable mirror," in *Proc. SPIE*, vol. 2881, pp. 35-44, 1996.

6   L. J. Hornbeck, "Deformable-mirror spatial light modulators," in *Spatial Light Modulators and Applications III, Proc. SPIE*, vol. 1150, pp. 86-102, 1990.

7   S. D. Gustafson, G. R. Little, V. M. Bright, J. H. Comtois, and E. S. Watson, "Micromirror arrays for coherent beam steering and phase control," in *Proc. SPIE*, vol. 2881, pp. 65-74, 1996.

8   E. Hecht and A. Zajac, *Optics*, Addison-Wesley, Reading, MA, 1975.

9   M. I. Skolnik, *Introduction to Radar Systems*, McGraw-Hill, New York, NY, 1980.

10   J. Butler, V. M. Bright, and W. D. Cowan, "SPICE modeling of polysilicon thermal actuators," in *Micromachined Devices and Components, Proc. SPIE*, vol. 3224, pp. 284-293, 1997.

11   D. M. Burns and V. M. Bright, "Investigation of maximum optical power rating for micro-electro-mechanical device," in *Transducers '97, International Conference on Solid-State Sensors and Actuators*, Chicago, IL, pp. 335-338, 1997.

12   F. P. Incropera and D. P. DeWitt, *Fundamentals of Heat Transfer, 2nd Edition*, John Wiley & Sons, New York, NY, 1981.

6. Thermally Actuated Piston Micromirror Arrays

6.1 Chapter Overview

This chapter describes design and characterization testing of thermally actuated piston micromirror arrays. The micromirrors were fabricated in the DARPA-sponsored MUMPs polysilicon surface micromachining process. The power averaging characteristic of thermal actuation is exploited in a novel line addressing scheme which reduces wiring for an n^2 array to $2n$ wires. Mirror deflections were measured with a microscope laser interferometer system equipped with a vacuum chamber. Data presented includes device uniformity, frequency response, and deflection vs. drive power for varied ambient pressure. Test results confirm that thermally actuated piston micromirrors offer several advantages over more common electrostatic designs. Thermally actuated micromirrors offer greater deflections at drive voltages compatible with CMOS circuitry. Measured thermal piston micromirror deflection vs. drive voltage is nonlinear, but does not exhibit the "snap through instability" characteristic of electrostatic devices. Operation of thermally actuated devices in rarefied ambient significantly decreases power dissipation. For a given deflection range, the power reduction facilitated by vacuum operation makes larger arrays feasible. Frequency response of thermally actuated devices is limited by the ability of the device to dissipate heat, but operation at 1 kHz rates is feasible.

Arrays of piston micromirrors have been demonstrated in adaptive optics applications [1]. Piston mirror designs to date employ electrostatic actuation. Advantages of electrostatic actuation include low power dissipation, and fast response time. But for applications requiring analog position control over a specified range several characteristics of electrostatic actuation emerge as design and microfabrication challenges. Electrostatic actuation exhibits a V^2 behavior because the electrostatic force between two charged bodies is function of the distance squared. As the specified range of motion is increased, required drive voltages may become impractical. Moreover, electrostatic devices exhibit a characteristic "snap through instability" behavior which limits the analog position control range to about 1/3 of the plate

separation [2]. Thus the plate separation, established in electrostatic micromachined devices by a sacrificial layer, must be at least 3 times the desired deflection range.

Since each element must have only $\lambda/2$ deflection range in an array of segmented piston mirrors, the constraints of electrostatic actuation are not particularly burdensome. But addition of a continuous facesheet to an array of actuators to improve optical efficiency dramatically increases required actuator travel and force requirements. The actuator force required is a function of the facesheet material, facesheet thickness, and desired influence function [3]. Required actuator travel or stroke is defined by the aberrating or correcting ability desired of the mirror system. For correction of atmospheric aberrations in a telescope system typical actuator deflection values range from ~2 to >6 μm [4,5]. Achieving even the low end of this deflection range presents microfabrication challenges, and requires a large electrostatic actuator area for acceptably low control voltages.

In general, thermal actuators provide greater force and larger deflections than similarly sized electrostatic actuators [6]. Both lateral and vertical thermal actuators have been designed and extensively tested by Air Force Institute of Technology (AFIT) researchers [7,8]. This chapter describes arrays of vertical piston micromirrors (or actuators) driven by thermal excitation, and presents characterization data for three prototype elements. Section 6-2 describes the basic operating principle and presents electrical and thermal models. Section 6-3 defines the fabrication process employed and design features of the prototype devices. Test procedures and device characteristics are presented in Section 6-4. Section 6-5 presents conclusions based on test results to date and briefly describes ongoing research efforts.

6.2 Principle of Operation

Figure 6-1 shows schematically a top view and diagonal cross section of the generic piston micromirror element examined in this paper. Electrically the element appears as a purely resistive load to the control source. Due to the small device dimensions parasitic capacitance is negligible. Device resistance is determined by the physical dimensions and doping of the polysilicon legs. When current is passed through

the legs, resistive heating induces thermal expansion. As the legs increase in length the mirror plate is forced to deflect. With no former, as shown in Figure 6-1(a), residual metal stress in the mirror plate initiates downward deflection. By adding a former, as shown in Figure 6-1(b), upward deflection of the mirror plate can be insured. The small electrostatic force caused by the potential difference between the mirror plate and substrate is negligible for sufficiently low control voltages.
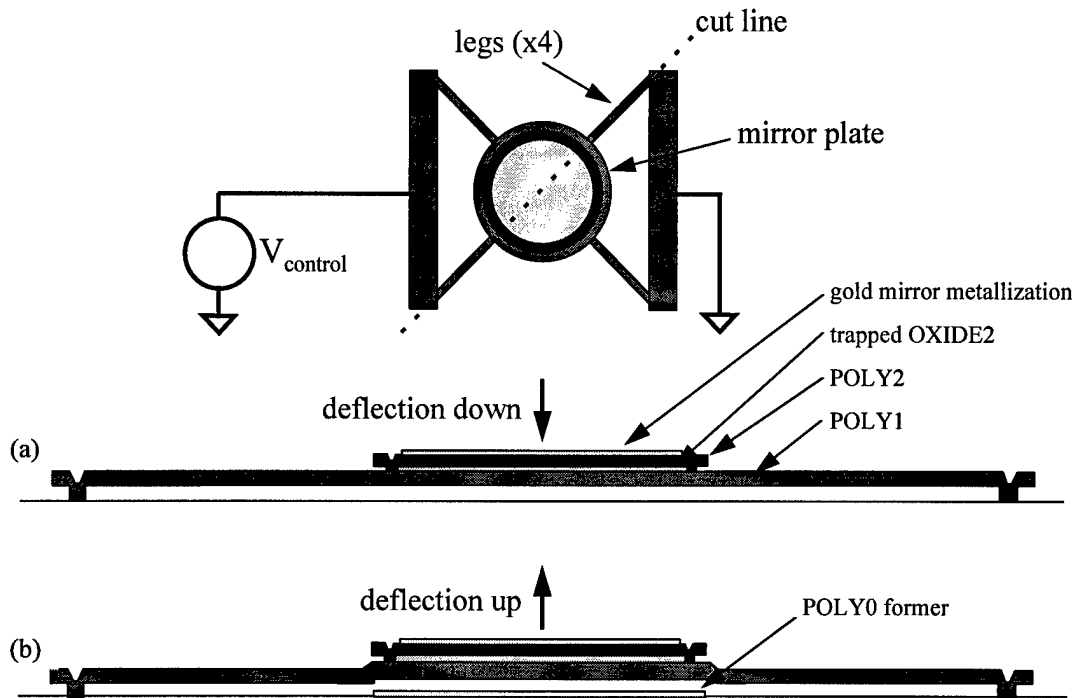
Figure 6-1. Schematic view of basic thermal piston micromirror fabricated in a polysilicon surface micromachining process. Diagonal cross-sections (a) and (b) show topographic detail. Note the use of a POLY0 former in (b) to insure deflection upward away from the substrate.

Analysis and modeling of the thermal and mechanical behavior of the piston micromirror is substantially more complex than the electrical circuit. All parts of the structure much be represented by thermal resistance and capacitance. If we neglect the mirror plate in the cross section view (and consider only one pair of legs), the structure is that of a polysilicon microbridge. Microbridges were extensively studied by Mastrangelo in his doctoral work [9]. Using a finite difference approach, Mastrangelo developed a convenient method of modeling the thermal behavior of the microbridge using SPICE circuit simulation. Extending his work to the micromirror case is straightforward. The four legs are modeled as

identical polysilicon microbridges attached to the thermal ground (substrate) at one end and the mirror plate at the other. The mirror plate is modeled as a wide microbridge section with increased thermal capacity to account for the stacked layers, and no resistive heating which is precluded by the mirror metallization. Inclusion of the mirror plate area is especially critical for accurate simulation of the device operation in non-vacuum ambient due to its large cooling surface. Each microbridge must be represented by at least 10 discrete segments for accurate simulation results [9].

Electrical Branch
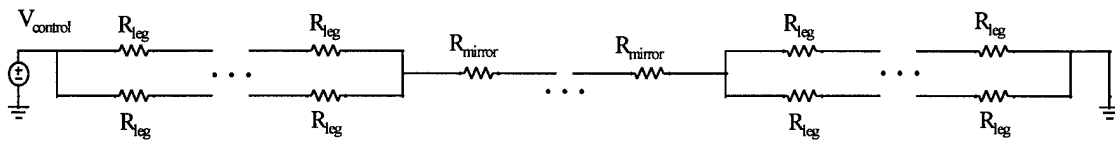
Thermal Branch
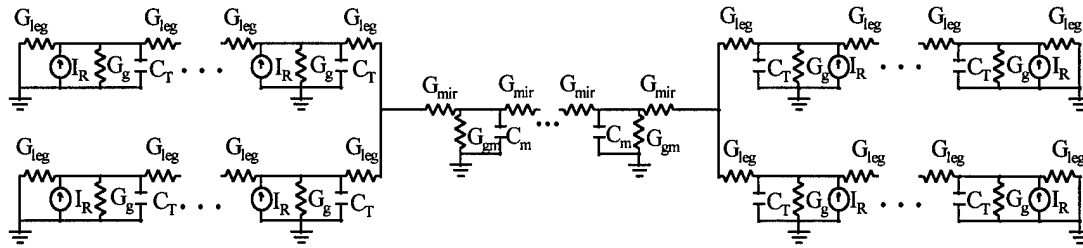
Figure 6-2. Electro-thermal circuit model for piston micromirror elements.

An overview of the combined electrical-thermal circuit model is shown in Figure 6-2. Not indicated in the figure is the temperature dependence of the polysilicon resistors but the SPICE model includes this effect [9]. Once the temperature of each element is known, the expansion of each leg segment is computed using the thermal coefficient of expansion for silicon. The thermal coefficient of expansion for silicon varies from about 2.6×10^{-6} K^{-1} at room temperature to 4.2×10^{-6} K^{-1} at 1000 K [10]. Summing the expansion of each segment yields the total leg expansion. Deflection of a microbridge which is fixed at both ends is defined by beam buckling equations. For a micromirror with sufficiently long legs, trigonometry provides reasonable deflection estimates. While the maximum operating temperature of the

legs is limited by the melting of polysilicon, the mirror plate temperature must not exceed 363 °C. At this temperature the gold mirror metallization and polysilicon irreversibly form a Au/Si eutectic with reduced optical reflectivity. Model parameters are computed using the physical dimensions of the device and the material properties. The electrical resistance of the leg segments is,

$$R_{leg} = \frac{\rho_{poly} l}{wtn},$$ (6-2)

where n is the number of segments, ρ_{poly} is the electrical resistivity of the polysilicon, and l, w, t are the length, width and thickness of the leg respectively. R_{mirror} is assumed to be zero due to the gold mirror metallization. The power dissipated in each leg segment is the current source I_R for the corresponding segment in the thermal branch. The thermal conductance of each 1/2 leg segment in the thermal branch is given by,

$$G_{leg} = \frac{2\kappa_{poly} wtn}{l},$$ (6-3)

where κ_{poly} is the thermal conductivity of the polysilicon legs. Reported values for κ_{poly} range from 17 to 30 W m^{-1} K^{-1} depending on the doping level and deposition process [11-16]. For the MUMPs process the more common value of 30 W m^{-1} K^{-1} appears to work well. The thermal conductance of the mirror plate segments, G_{mir}, are similarly defined using the mirror plate dimensions. Heat flow through the ambient media (gas) to the substrate is represented by conductances G_g and G_{gm}. G_g is given by

$$G_g = \frac{\eta \kappa_{gas}(P) wl}{sn},$$ (6-4)

where κ_{gas} is the thermal conductivity of the gas which is a function of pressure, s is the separation between the microbridge structure and the substrate, and η is an excess flux coefficient which accounts for the fringing heat flux. The thermal conductivity of the gas between the mirror plate and substrate, G_{gm}, is similarly defined. Strictly speaking, the values of the G_g elements in the model must vary as a function of the mechanical response (deflection) of the thermal micromirror system for accurate simulation in non-vacuum ambients. Development of a complete electro-thermal-mechanical model is beyond the scope of this work but developers of commercial computer aided design tools have shown an interest in doing so

[17]. Acceptable qualitative simulation results have been obtained using constant values for G_g, and G_{gm} in the SPICE electro-thermal model. The thermal heat capacity of the leg elements are found using the specific heat and density of polysilicon, and the leg dimensions.

$$C_T = density \cdot specific\ heat \cdot w \cdot t \cdot l\ /\ n \tag{6-5}$$

C_m is found similarly by summing the thermal capacities of the layers comprising the mirror plate.

Because thermal actuators are electrically just resistive elements they are inherently power averaging devices. For any a.c. or pulse drive signal faster than the device thermal response, the device will deflect to the position corresponding to the average power of the signal. This characteristic can be exploited in a number of control schemes. Analog positioning using all-digital control has been demonstrated using modulated pulse width or a varied number of pulses. Alternatively, pulse amplitude modulation can be used to position elements in large arrays in a multiplex fashion.
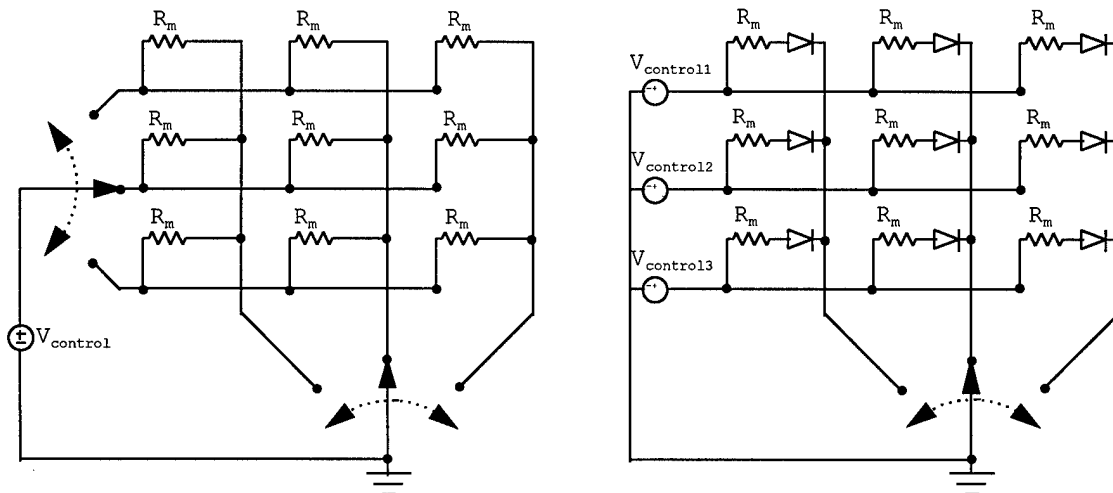
Figure 6-3. Simplified schematic of present row/column addressing scheme (left), and true line address capability (right) requiring only rectifying diodes for a 3 × 3 array.

The ability to multiplex drive signals is critical for development of large arrays. True multiplexing requires active components which are currently not available in MEMS foundry processes. Using the fact that the deflection of thermal piston micromirrors is a strong function of drive current (see Section 6-4) a

novel row/column address scheme was devised. With readily predicted cross-coupling, this approach reduces the number of control line and D/A converters for and $n \times n$ array to $2n$. This scheme is shown pictorially for a 3×3 array in Figure 6-3. When any element in the array is selected the current $V_{control}/R_m$ flows through the selected device. Parallel resistive paths from $V_{control}$ to ground result in undesired currents through the unselected array elements. The undesired current $0.4 \cdot V_{control}/R_m$ flows through the 4 elements connected to either the selected row or column, and the current $0.2 \cdot V_{control}/R_m$ flows through the 4 elements not connected to either the selected row or column. For any array size the undesired currents are given by:

$$\left| I_{off-row,off-column} \right| = V_{control} / \left[(\#rows + \#cols - 1) \cdot R_m \right]$$
$$\left| I_{off-row,on-column} \right| = \left[(\#cols - 1) \cdot V_{control} \right] / \left[(\#rows + \#cols - 1) \cdot R_m \right] \quad (6-6)$$
$$\left| I_{on-row,off-column} \right| = \left[(\#rows - 1) \cdot V_{control} \right] / \left[(\#rows + \#cols - 1) \cdot R_m \right]$$

The relationships in Equation 6-6 show that for square arrays the undesired current of any element can not exceed 50% of the current through the desired device. Conceptually, the mirror array control processor can compute the undesired currents using Equations (6-6) and factor the contribution of the undesired currents control signals driving the array. A better solution is to eliminate the non-selected current flow entirely. This can easily be accomplished by adding a series diode to each mirror cell. Diode requirements are minimal, and result in true line address capability. Because drive voltages for thermal piston micromirror devices are compatible with CMOS processes this approach may represent a near-term solution for producing large micromirror arrays.

6.3 Device Description

All of the thermal piston devices presented here were fabricated in the DARPA-sponsored Multi-User MEMS Process (MUMPs). MUMPs is described in Chapter 2. The MUMPs process characteristics which most impact design of the thermal piston micromirrors are the doping of the polysilicon legs and the gold metallization. Because only the power dissipated in the legs contributes to deflection it would be desirable

to selectively dope each leg at a lower level than the polysilicon used for wiring to maximize deflection as a function of power. Residual tensile stress in the gold metallization causes undesirable curvature of the mirror plate. Though specifically developed for the MUMPs process, the thermal piston micromirrors presented are readily adaptable to other processes.

Figure 6-4 is a scanning electron micrograph of a thermal piston micromirror fabricated on MUMPs 15. The mirror plate is 80 μm in diameter and each leg is 40 μm long and nominally 3 μm wide. The mirror plate is comprised of stacked POLY1, trapped OXIDE2, POLY2 and gold to reduce mirror curvature. Interferometric microscope measurements of the mirror plate show less than 40 nm curvature when at rest. While stacking effectively improves mirror flatness and plate stiffness, it also increases thermal capacity substantially. Visible in Figure 6-4 is disk of POLY0 under the mirror plate. This former raises the mirror plate 0.5 μm above the legs and insures piston travel upward when power is applied to the legs. Figure 6-5 is a scanning electron micrograph of the 3 × 3 row/column addressed array fabricated on MUMPs 15. Sections of POLY0 wiring in the elements of two columns equalize the resistive paths for all elements in the array. This resistive matching is critical for predictable operation of arrays employing the row/column addressing scheme. If the resistive paths to each element are not equal, the undesired current relationships in Equation (6-6) no longer hold true.
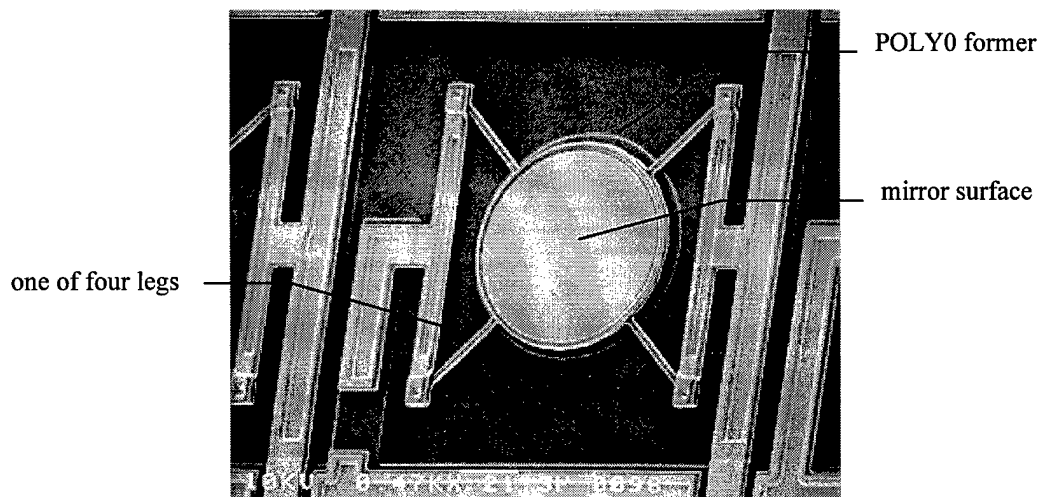
Figure 6-4. MUMPs 15 thermal piston micromirror element.

POLY0 resistors
to equalize
resistive path
of each mirror
element
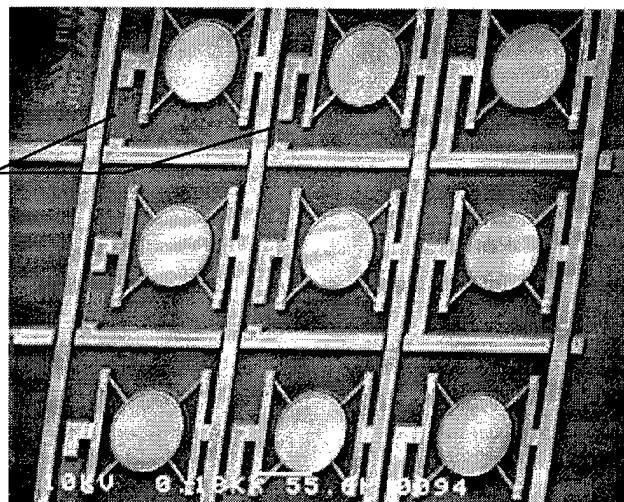
Figure 6-5. Prototype 3 × 3 array employing row/column address scheme.

Optically oriented readers may note the exceptionally low "fill-factor" of this array. In fact all of the arrays presented here were designed for operation with a refractive lenslet array having 203 μm center-to-center spacing. Using a lenslet array the optical efficiency of all arrays approaches 100% with the exception of diffractive effects caused by the edges of the lenslets. Alternatively, a segmented or continuous facesheet can be added to improve optical efficiency.

Depicted in Figure 6-6 is a somewhat more complex thermal piston micromirror element from 12 × 12 arrays fabricated on MUMPs 16. This design was developed primarily to test techniques for lowering power dissipation and improving frequency response. Leg length is maximized by allowing the mirror center to differ from the cell center while maintaining 203 μm center-to-center spacing of the mirrors in the array. The 61 μm long, 4 μm wide legs are not at 45 degree angles, but do not need to be. The cross ties were included to prevent the legs from bowing out but are probably only necessary when the width of the leg is smaller than the thickness. The critical design requirement to insure piston motion without tip or tilt is preservation of symmetry in the thermal circuit. Note that this design preserves thermal symmetry of the legs, and leg attachments to the substrate and mirror plate.
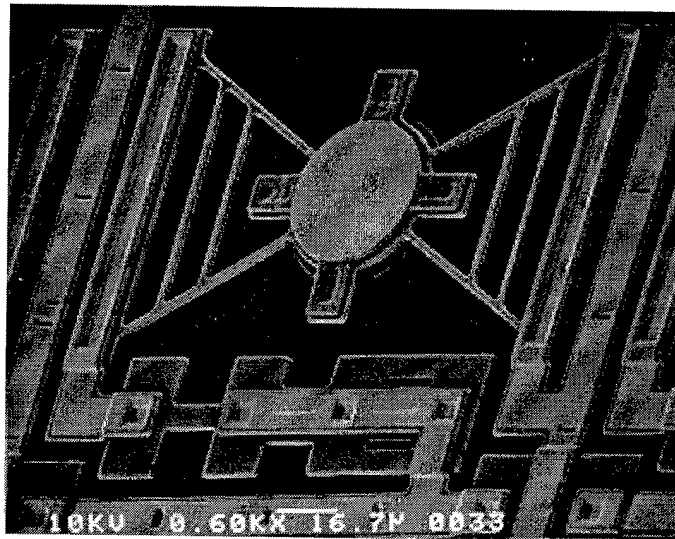
Figure 6-6. MUMPs 16 thermal piston micromirror element.

Since the device response speed is limited by thermal capacity, higher frequency operation requires reducing the thermal capacity of the structure. In this design the gold/POLY2 mirror plate is attached to the underlying POLY1 by four vias, and there is no trapped oxide. This reduces the thermal capacity of the mirror plate by eliminating the OXIDE2, and isolates the POLY2 and gold contribution to plate thermal capacity by the thermal resistance of the vias. The vias are placed outside the mirror plate to maximize the mirror surface area. The mirror metallization is 45 μm in diameter. Lacking the increased stiffness of the stacked/trapped oxide structure, the mirror curvature measures ~75 nm. Although a POLY0 former is used, the deflection direction is downward toward the substrate because residual metal stress causes an initial "cupping" of the mirror plate.

To avoid the computational burden associated with driving row/column addressed arrays, 128 element arrays of individually addressed thermal piston micromirrors were fabricated on MUMPs 17 and 18. Figure 6-7 shows scanning electron micrographs of a single element and a section of the MUMPs 17 array. This mirror design has a 50 μm diameter reflective surface and legs 63 μm long and 4 μm wide. The relatively wide legs were employed to increase stiffness of the mirror structure when used as an

actuator for a continuous facesheet mirror. Again stacked polysilicon and oxide layers are used to reduce mirror surface curvature due to residual metal stress. Measured mirror curvature is 30 nm. Each micromirror element is addressed by a single gold on POLY2 low resistance wire. The highly conductive substrate serves as a common ground. Due to bond pad limitations only 128 elements of the 12 × 12 array are wired. Four elements in each corner of the array (16 total) are inactive. In fact, the key difficulty with expanding individually addressed designs such as this one is wiring. While multi-level wiring may permit relatively large arrays, wiring to off-chip control sources will ultimately limit designs. Large arrays (~1000 elements) will require either on-chip control sources or novel packaging concepts. One viable option currently being researched at AFIT is the use of High Density Interconnect technology for packaging MEMS [18].
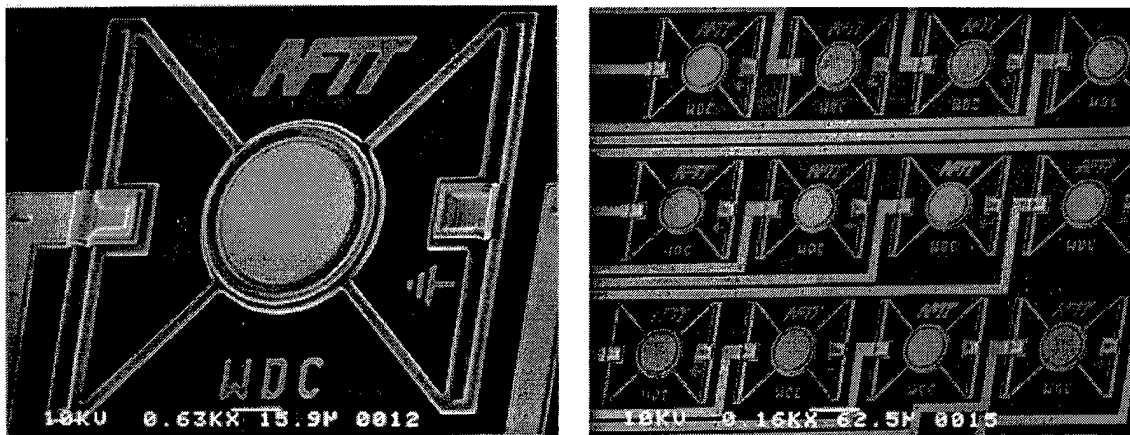
Figure 6-7. MUMPs 17 thermal piston micromirror array.

6.4 Testing and Device Characteristics

Critical to the use of thermal piston micromirror arrays in adaptive optics applications is characterization of deflection, frequency response, device uniformity, and mirror flatness. Although ongoing, test results to date indicate that thermal piston devices may be an attractive alternative to the more common electrostatic designs.
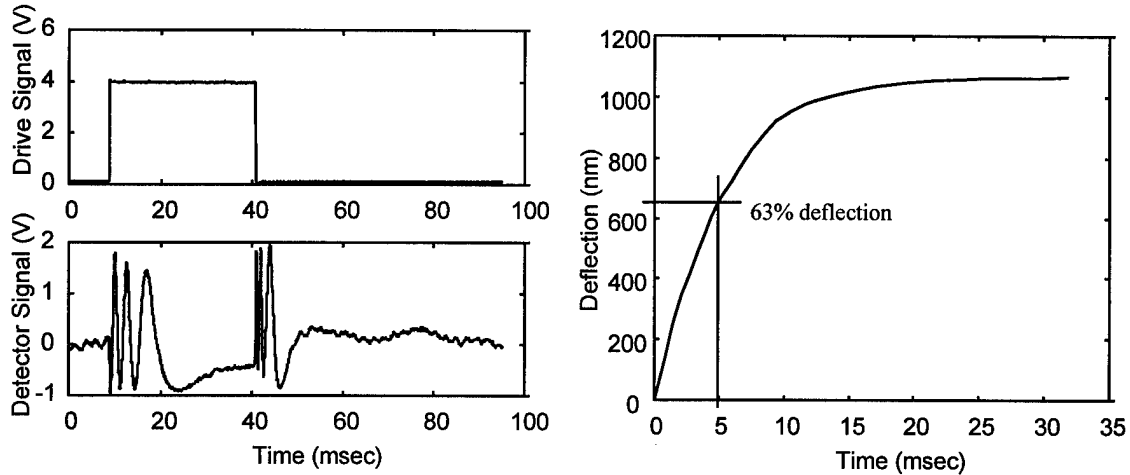
Figure 6-8. Raw drive signal and detector signal from laser interferometer (left), and deflection vs. time (right) produced by data analysis. Also shown is measurement of thermal time constant. MUMPs 15 device in 20 mT vacuum.

Deflection was measured using a laser interferometer system previously used to test electrostatic piston devices [19, 20]. This system is equipped with a four probe pressure vessel allowing testing to be performed at pressures of 20 mT to 1000T in a nitrogen ambient. The interferometer system requires dynamic motion of the mirror under test to produce accurate deflection measurements. The periodic drive waveforms usually used for testing electrostatic devices can lead to erroneous deflection results for thermal piston micromirrors, because thermal actuation is a function of average power. Unless the drive signal is much slower than the thermal time response, allowing the device to cool completely between cycles, deflection data will be erroneous. In addition, the larger deflections possible with thermal piston mirrors complicate the interferometer's detector signal (Figure 6-8). Multiple phase wraps occur and the intensity of the wrap points in the signal are not constant due to limited microscope depth of focus. Existing AFIT analysis software was unable to process thermal piston micromirror data.

Thus, a new measurement technique and analysis software were developed specifically for thermal mirror measurements. Deflection measurements were performed by driving the mirror with a single pulse of set amplitude and recording the transient response of the interferometer's detector diode. The detector signal was then unwrapped to produce a mirror deflection vs. time curve using two criteria;

(1) at time zero the deflection is zero, and (2) phase wraps (detector signal maxima and minima) occur at $\lambda_{HeNe}/2$ phase. Deflections of at least $\lambda/4$ are required to facilitate unwrapping of the detector signal. Figure 6-8 shows the raw drive signal and PIN detector diode response for one transient measurement of a MUMPs 15 device in 20 mT vacuum. Also shown is the resulting deflection vs. time curve as the mirror moves to the powered position. The thermal time response (analogous to an RC time constant) of the device can be read directly from the deflection vs. time curve as annotated in the figure. Peak deflections and drive pulse amplitudes for a set of measurements are plotted to produce a static deflection curve. Matlab® scripts automate processing of laser interferometer data sets.
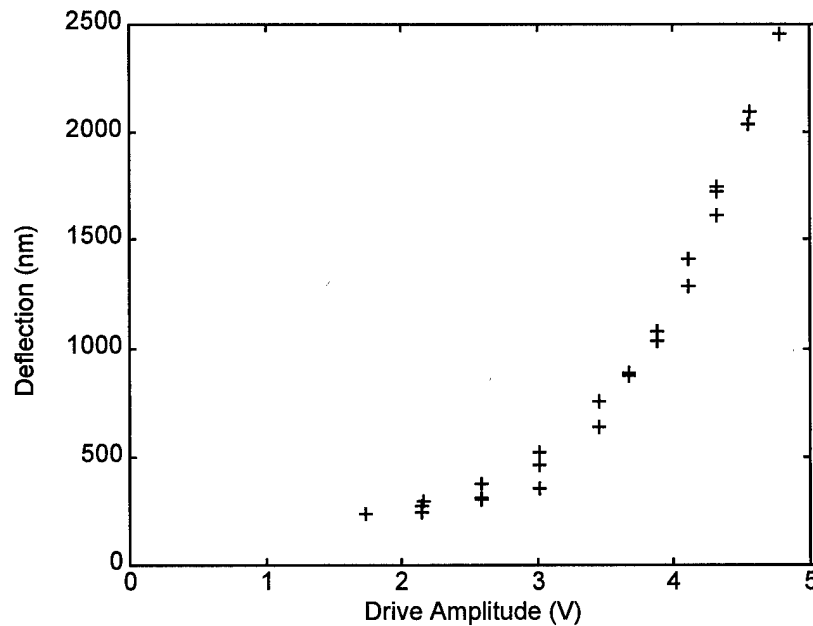
Figure 6-9. Deflection vs. drive voltage measurements for MUMPs 15 thermal piston micromirror in vacuum (20 mT).

Plotted in Figure 6-9 are 25 automatically processed deflection vs. voltage measurements for a MUMPs 15 device (shown in Figure 6-4) operating in a 20 mT vacuum. Between 2 and 4.6 V measurements were repeated 2 or 3 times using the same nominal drive signal. Using the mean deflection at each repeated drive amplitude as a true deflection, the computed root mean squared error is 46 nm. This quantity represents the combined measurement and deflection uncertainty. Inspection of the raw data

indicated that most of this uncertainty is attributable to noise on the detector signal (see Figure 6-8). Thus, the positioning uncertainty is estimated to be about 10 nm. Also note that the maximum deflection is greater than 2 µm. This shows that the mirror plate is pistoning upward because downward travel is limited to 2 µm by the sacrificial layer (OXIDE1) thickness. This illustrates the efficacy of the POLY0 former.

Determination of the exact power dissipated in the mirror device is complicated by the row/column address wiring arrangement which prohibits direct measurement of the device resistance. Selectively breaking away all but one row of devices on the test array permitted direct measurement of the of mirror resistance and path resistance. The resulting mirror resistance of 170 Ω agrees reasonably well with the value computed using MUMPs 15 film parameters (126 Ω). The discrepancy is attributable to an as-fabricated leg width that is somewhat smaller than the as-drawn width. The mean path resistance (R_{path}=515 Ω) measured from a row bondpad to a column bondpad includes wiring resistance (POLY0 cross-unders), mirror resistance R_{mirror}, and POLY0 balance resistors. The measured path resistance is significantly higher than the resistance computed using MUMPs film parameters and as-drawn dimensions. The source of the discrepancy was traced to the POLY0 cross-unders and balance resistors which measured 3 times higher (115 Ω/resistor) than expected. Each path consists of 3 series POLY0 resistors plus the mirror resistance ($3 \cdot 115 + 170 = 515\Omega$). The measured path resistances for the three intact mirrors differed by only 7 Ω. To account for the path resistance and corresponding voltage drop, the measured resistance values were used to compute the power dissipated in the mirror by $(V/R_{path})^2 \cdot R_{mirror}$. From the plot in Figure 6-10, a 1 µm mirror deflection requires ~8 mW of power in a vacuum. The primary reason for this relatively high power requirement is the short legs of this particular mirror design.

The power averaging characteristic of thermal devices is also illustrated in Figure 6-10. Pulse width modulated signals were generated by varying the duty cycle of a 100 kHz square wave which was applied in a burst for the transient deflection measurement. Bursts of a 50% duty cycle, 100 kHz square wave were used to verify amplitude modulated pulse drive. All power computations were performed using the measured device resistance.
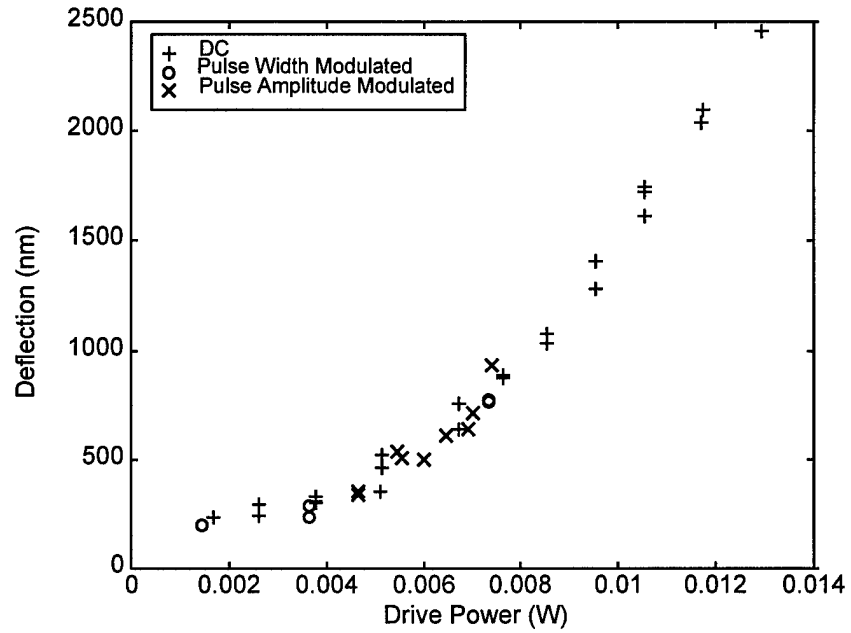
Figure 6-10. Deflection vs. power for a MUMPs 15 thermal piston micromirror operating in vacuum (20 mT). DC drive values correspond to data in Figure 6-9 corrected for path and mirror resistance.
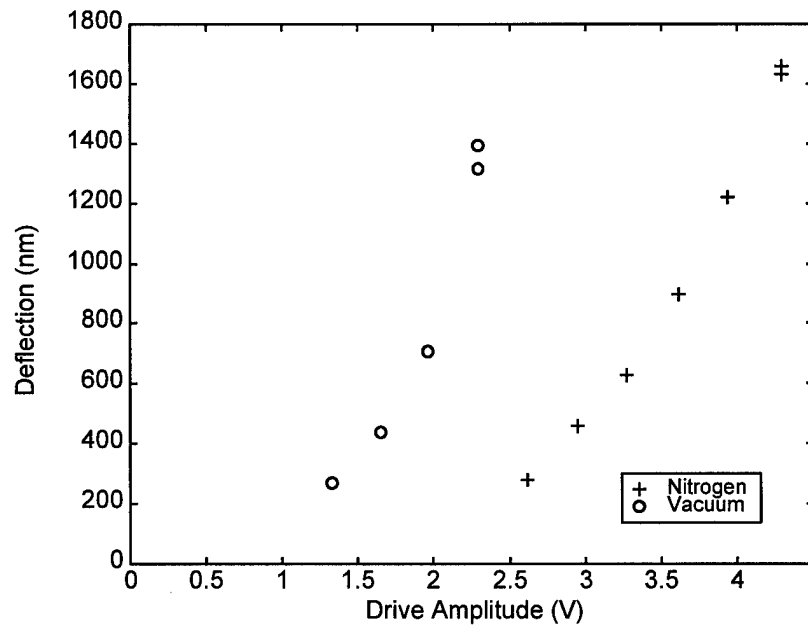
Figure 6-11. MUMPs 16 thermal piston micromirror deflection vs. voltage in 20 mT vacuum and 1000 T nitrogen ambient.

Operation in vacuum substantially reduces the drive voltage (hence power) required for thermal devices. Figure 6-11 shows deflection vs. drive voltage for a MUMPs 16 thermal piston micromirror (of Figure 6-6) when measured in a 20 mT vacuum and 1000 T nitrogen ambient. Comparing the squared drive voltage indicates that drive power is reduced by approximately a factor of 9 for a 1 μm deflection. The mean value of the thermal time constant measured in nitrogen ambient is 403 μsec indicating that kilohertz operation is feasible. The 12 × 12 row/column addressed arrays of this device were wired as dual 12 × 6 arrays to reduce the space required for balance resistors. The asymmetry of the arrays causes undesired row currents to be unacceptably high. Despite these shortcomings, the MUMPs 16 device illustrates that as long as thermal symmetry is preserved, a pure piston motion can be obtained. Interferometric microscope measurements of the device while deflecting show no tilting of the mirror.

The individually actuated thermal piston micromirror array fabricated on MUMPs 17 (and shown in Figure 6-7) is closest to application in an adaptive optics experiment. Although the measured resistance of devices (including the wiring) in the array varies by up to 10%, mirror deflection as a function of drive power is remarkably consistent. This deflection uniformity is illustrated in Figure 6-12 which plots deflection vs. power measurements for three devices operating in nitrogen at 1000 T. Also shown is a 0 to ~250 nm deflection measurement for one device modulated with a 100 Hz sinusoidal drive signal.

Power is computed in all cases using the device measured resistance (measured from its bond pad to the substrate bond pad). By simply measuring and storing the resistance value of each device an array of identically deflecting micromirrors can be achieved. Power dissipation is comparable to the MUMPs 15 device, with 60 mW required for 1μm deflection in nitrogen. The primary design contribution to this high power is the 4 μm leg width used for increased stiffness. Some power may also be dissipated in the wiring and substrate return path. Deflection is toward the substrate because no POLY0 former was used. The plot appears to show evidence of cooling at large deflection - a slight flattening of the deflection vs. power curve. This is attributable to increased thermal conductivity (G_g) when the mirror plate and portions of the heated legs are physically close to the substrate.
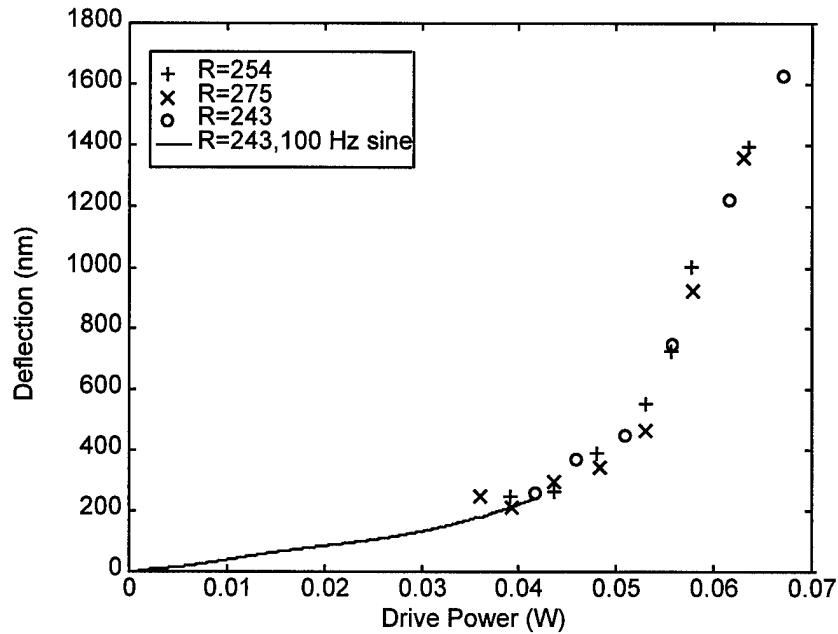
Figure 6-12. Measured deflection vs. drive power for three MUMPs 17 thermal piston micromirrors in the same array operating in nitrogen at 1000 T.

The drive voltage for maximum deflection in nitrogen (or air) is less than 5V making the MUMPs 17 devices especially well suited for demonstration of all-digital control using pulse width modulation. The mean thermal time constant from the automated analysis of 20 measurements in Figure 6-12 was 0.74 ms, indicating the feasibility of kilohertz system operation. While driving one mirror with a maximum deflection signal, adjacent devices (particularly those with wires close to the driven mirror) were checked for deflection. No crosstalk between devices was detectable.

6.5 Conclusions

Initial tests results for three prototype devices indicate that arrays of thermal piston micromirrors and/or piston actuators of similar design may be an attractive alternative to electrostatic designs for optical phase modulation applications. In particular, the large controllable deflection range and force expected of thermal piston actuators will be useful for development of microfabricated continuous facesheet

deformable mirrors. Preservation of thermal symmetry insures tilt-free piston travel. Ongoing research focuses on reducing device power dissipation which may be a limiting factor for large arrays. Development and validation of a complete electrical-thermal-mechanical model will facilitate optimization and system development efforts.

References

1   M. C. Roggemann, V. M. Bright, B. M. Welsh, S. R. Hick, P. C. Roberts, W. D. Cowan, and J. H. Comtois, "Use of micro-electromechanical deformable mirrors to control aberrations in optical systems", *Opt. Eng.*, vol. 36, no. 5, pp.1326-1338, May 1997.

2   P. M. Osterberg, R. K. Gupta, J. R. Gilbert, and S. D. Senturia, "Qualitative models for measurement of residual stress, Poisson ratio, and young's modulus using electrostatic pull-in of beams and diaphragms", in *Technical Digest, Solid State Sensor and Actuator Workshop*, (Hilton Head, SC), pp. 184-188, 1994.

3   M. A. Ealy and J. A. Wellman, "Deformable mirrors: design fundamentals, key performance specifications, and parametric trades", in *Proc. SPIE on Active and Adaptive Optical Components*, vol. 1543, pp. 36-52, 1991.

4   R. K. Mali, T. G. Bifano, N. Vandelli, and M. N. Horenstein, "Development of microelectromechanical deformable mirrors for phase modulation of light", *Opt. Eng.*, vol. 36, no. 2, pp. 542-548, February 1997.

5   R. L. Clark, "Adaptive optics: aims for earthly applications", in *Photonics Spectra*, pp. 100-106, April 1997.

6   J. H. Comtois, "Structures and techniques for implementing and packaging complex, large scale microelectromechanical systems using foundry fabrication processes", *Ph. D. dissertation*, Air Force Institute of Technology, Wright-Patterson AFB, OH, June 1996.

7   J. H. Comtois, V. M. Bright, and M. W. Phipps, "Thermal microactuators for surface micromachining processes", in *Proc. SPIE*, vol. 2542, pp. 10-21, 1995.

8   J. R. Reid, V. M. Bright, and J. H. Comtois, "Force measurements of polysilicon thermal micro-actuators", in *Proc. SPIE*, vol. 2882, pp. 296-306, 1996.

9   C. H. Mastrangelo, "Thermal applications of microbridges", Ph.D. dissertation, University of California, Berkeley, 1991.

10   Y. Okada and Y. Tokumaru, "Precise determination of lattice parameter and thermal expansion coefficient of silicon between 300 and 1500 K", *J. Appl. Phys.*, vol. 56(2), pp. 314-320, 1984.

11   O. Paul, M. von Arx, and H. Baltes, "Process-dependent thermophysical properties of CMOS IC thin films", in *Transducers '95-Eurosensors IX*, 37-A4, pp. 178-181, 1995.

12   C. Mastrangelo, Y.-C. Tai, and R. Muller, "Thermophysical properties of low-residual stress, silicon-rich, LPCVD silicon nitride films", *Sensors and Actuators*, A21-A23, pp. 856-860, 1990.

13   M. von Arx, O. Paul, and H. Baltes, "Determination of the heat capacity of CMOS layers for optimal CMOS sensor design", *Sensors and Actuators*, A46-47, pp. 428-431, 1995.

14   O. M. Paul, J. Korvink, and H. Baltes, "Determination of the thermal conductivity of CMOS IC polysilicon", *Sensors and Actuators*, A41-42, pp. 161-164, 1994.

15   Y. C. Tai, C. H. Mastrangelo, and R. S. Muller, "Thermal conductivity of heavily doped low-pressure chemical vapor deposited polycrystalline silicon films", *J. Appl. Phys.*, vol. 63, no. 5, pp.1441-1447, 1988.

16   F. Volklein, and H. Baltes, "A microstructure for measurement of thermal conductivity of polysilicon thin films", *J. Microelectromechanical Systems*, vol. 1, no. 4, pp.193-196, December 1992.

17   Private communication with Dr. Joost Von Kirk, *Microcosm*, developers of MEMCAD.

18   J. T. Butler, V. M. Bright, and J. H. Comtois, "Advanced multichip module packaging of microelectromechanical systems", to be published in *The Ninth International Conference on Solid-State Sensors and Actuators, Transducers 97*.

19   T. A. Rhoadarmer, V. M. Bright, B. M. Welsh, S. C. Gustafson, and T. H. Lin, "Interferometric characterization of the flexure beam micromirror device", in *Proc. SPIE*, vol. 2291, pp. 13-23, 1994.

20   M. A. Michalicek, V. M. Bright, and J. H. Comtois, "Design, fabrication, and testing of a surface micromachined micromirror device", *Proceedings of the ASME Dynamic Systems and Control Division ASME 1995*, DSC-vol. 57-2,1995 IMECE, pp. 981-988, 1995.

7. Beam Steering Mirrors

7.1 Chapter Overview

This chapter presents novel micro-opto-electro-mechanical (MOEM) beam steering mirrors. Although applications and operating characteristics of the micromirror systems vary widely, all of the systems employ a lift mechanism to raise the mirror above the substrate. This ability to lift the steered mirror surface higher than the as-fabricated position is critical for obtaining practically large steering angles in surface micromachined devices. Without lifting, the maximum steering angle is restricted by mirror size and sacrificial oxide thickness. Two innovative lifting mechanisms have been exploited: backbent vertical thermal actuators, and metal stress cantilevers.

Most of the systems presented employ backbent vertical thermal actuators for lifting. The high force and large deflection of backbent vertical thermal actuators are useful in many applications, particularly when a single large deflection is required for device setup. For example, backbending two actuators driven in parallel flips a 250 μm square mirror to 45 degrees off the substrate. The actuators can then be driven to permit scanning over 45 degrees. In another example, 3 backbent actuators are used to position an electrostatically actuated optical beam steering mirror 10 μm off the substrate thereby increasing the maximum steering angle by a factor of 5. Critical to applications like these is predictable and repeatable operation of the actuators. The experimental data presented in this chapter represents the first quantitative characterization data for backbent thermal actuators. Vertical actuators were ideal for this characterization because deflection measurements with ±5 nm precision are possible using interferometric microscope techniques. Although nonlinear, the relationship of backbending deflection to drive power is predictable and repeatable enough for many micro-positioning applications.

One characteristic of using backbent vertical thermal actuators for MOEM systems is that a setup step must be performed after release of the mechanical structures. This setup requirement may be advantageous in some cases; for example in MOEM systems that are deployed and not setup until needed.

For most applications the setup step requirement of thermal actuators is a disadvantage, imposing additional cost in labor and/or automated equipment. Metal stress cantilevers require no additional processing or setup, and perform the same lifting functions as backbent vertical thermal actuators without power. Although only a few systems to date have employed metal stress cantilevers, the yield and uniformity of this lifting mechanism appears to be exceptionally good. As a result almost all new designs which require vertical lifting employ metal stress cantilevers.

The remainder of this chapter is organized as follows. The vertical thermal actuators tested are described in Section 7-2. Test procedures and characterization results are presented in Section 7-3. Several MOEM systems employing backbent thermal actuators are described in Section 7-4. The metal stress cantilever concept is described in Section 7-5, and beam steering mirror applications exploiting metal stress cantilevers are presented in Section 7-6.

7.2 Vertical Thermal Actuator Description

Thermal actuators provide greater force and deflection than equivalently sized electrostatic actuators, albeit with significantly higher power dissipation and lower operating frequency [1,2,3]. By using backbent thermal actuators for setup or one time positioning applications the large deflection and force possible can be exploited without the penalty of long term high power dissipation. Although backbending of lateral actuators was noted and used to some extent in previous research efforts, no attempt was made to characterize the repeatability and predictability of the backbending phenomenon.

The vertical thermal actuators used here were developed to provide an initial upward deflection in self assembly applications [4]. A representative vertical thermal actuator fabricated in the MUMPs process is shown in Figure 7-1. Resistive heating caused by current flow in the 4 µm wide Poly2 hot arms, induces thermal expansion. The Poly0 former (0.5 µm thick) and sacrificial Oxide2 thickness (0.75 µm) make the center of the hot arms 1 µm higher than the center of the cantilever bar, so this expansion drives the actuator tip toward the substrate. The downward deflection range is limited to 1.25 µm; the Oxide1

thickness (2 μm) minus the Dimple etch. A much greater deflection range is obtained by "backbending"

the actuator. At sufficiently high drive current, with the downward tip deflection stopped by contact with

the substrate, the hot arms bow upward. Upon removal of the drive current the hot arms rapidly "freeze" in

the bowed shape and shrink, pulling the tip of the actuator upward. The deformation of the hot arms is

permanent and the tip of the actuator remains deflected upward without applied power. An identical

actuator after backbending is also shown in Figure 7-1. It is this characteristic which makes backbent

actuators ideal for setup or one-time positioning applications.
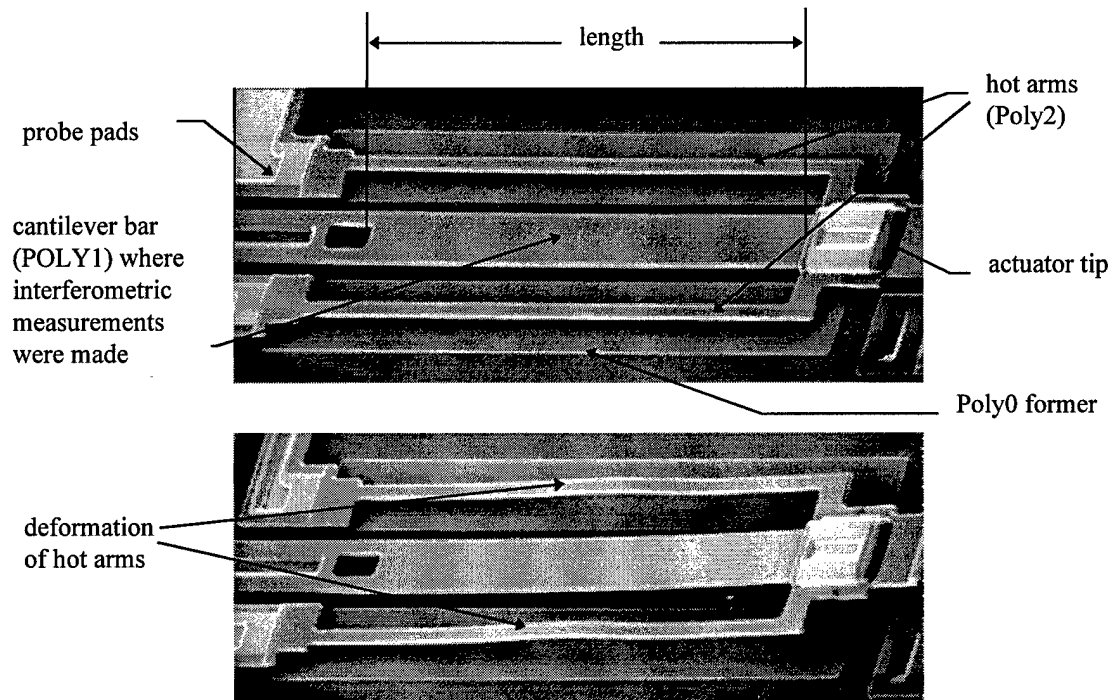
Figure 7-1. Annotated scanning electron micrographs of a vertical thermal actuators fabricated in MUMPs.
Top view is as fabricated. Bottom view is after backbending with approximately 4.5 mA current flow
through the hot arms.

After backbending, the actuator is still functional with an expanded deflection range defined by

the distance from the tip to the substrate. Upward tip deflections of over 12 μm have been observed for

150 μm long actuators after backbending. Thus, backbending yields a nearly ten-fold increase in

deflection range. Backbending is a complex thermal-mechanical problem and no effort was made in this

work to analyze or model the phenomenon. Instead, a series of measurements were performed to empirically characterize the predictability and repeatability of backbending for MOEM applications.

7.3 Backbending Characterization

Several experiments were conducted to determine the backbending characteristics of vertical thermal actuators. In all cases individual devices were carefully backbent by applying a constant voltage power supply across the hot arm probe pads for 5 seconds. The duration of the backbending pulse was chosen only as a convenient time period for manual control and recording of the drive voltage and current flow. Much shorter pulses (just sufficient for the structure to achieve thermal equilibrium) are recommended for automated backbending. Using the series drive approach no current flows through the cantilever bar and the current through each hot arm is identical. Alternatively the cantilever bar probe pad can be used to drive the hot arms in parallel. Parallel drive is often used in the applications to lower the required backbending voltage. Initially backbending was performed on a probe station with the devices exposed to room air. Later backbending efforts were performed in a nitrogen filled probe chamber.

After backbending, the deflection of each actuator was measured on an interferometric microscope using HeNe laser illumination [5]. After leveling the sample die, a bare section of the substrate (silicon nitride) was used to record a reference frame. Subtraction of this reference frame from subsequent measurements removed any remaining tilt and system optical aberrations, thus allowing accurate deflection measurements. Averaging of the reference (4 frames) and measurement (2 frames) results in a manufacturer specified vertical measurement accuracy of 1.5 nm (peak-to-valley) with 0.7 nm (RMS) repeatability [5]. Deflection data was recorded using the microscope system's scan function to display the height of the cantilever bar from the hole to the edge of the tip structure (see Figure 7-1). This portion of the cantilever bar is a smooth, discontinuity-free surface permitting interferometric measurement without ambiguity. Figure 7-2 is a copy of the display screen for a representative scan measurement. The peak-to-valley (PV) number indicates the change in height of the cantilever bar over the scan range. The largest

7-4

source of measurement error is operator selection of the scan line, but the microscope system's video display facilitated repeatable placement, and sharp discontinuities at the end points of the scan provided excellent guides. A series of duplicate measurements verified that manual scans were repeatable within ±5 nm.
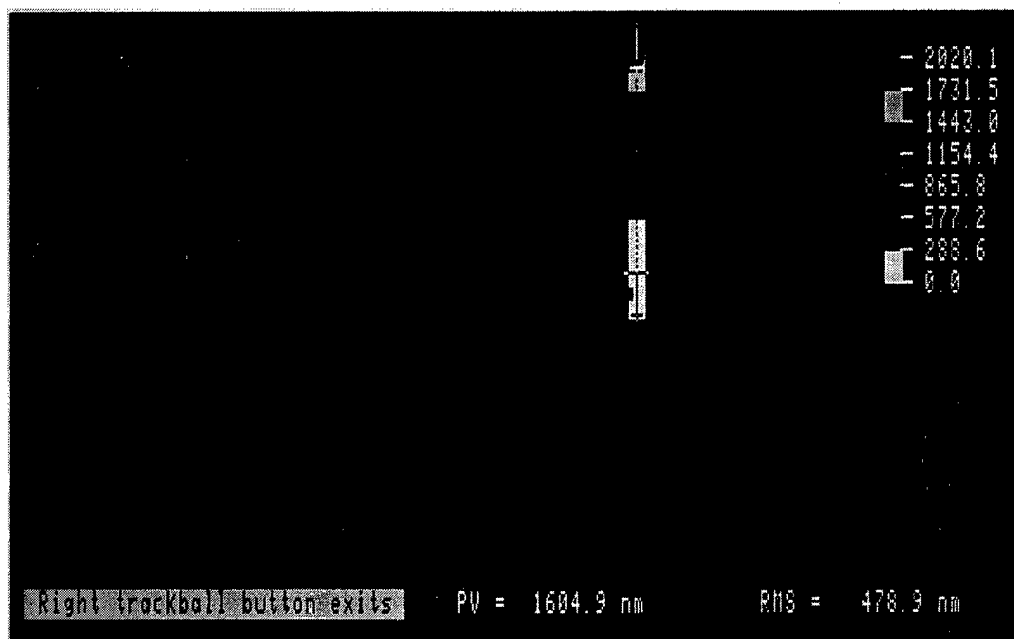
Figure 7-2. Interferometric microscope operator display during manual scanning of cantilever bar.
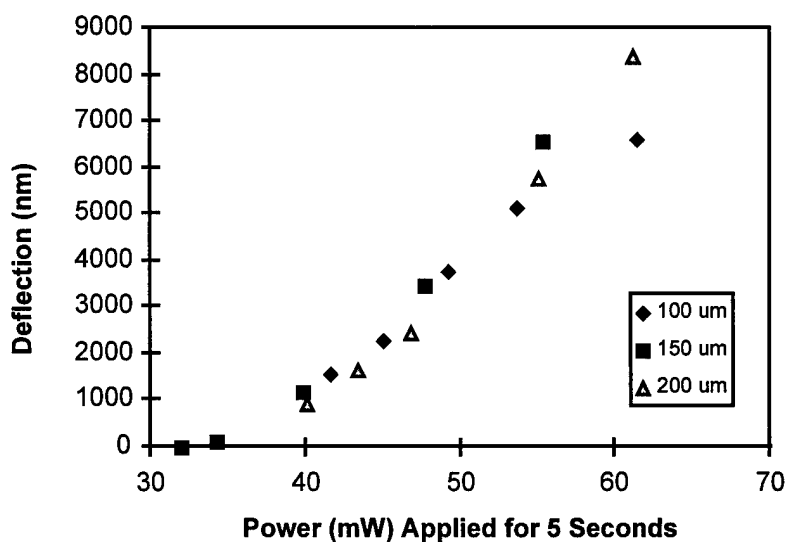
Figure 7-3. Measured deflection after backbending in room air for vertical thermal actuators of 3 different lengths as a function of applied power.

Otherwise identical vertical thermal actuators of three different lengths (100, 150, and 200 µm lengths measured as shown in Figure 7-1) were tested. To determine backbending as a function of applied electrical power, the supply voltage was varied for five devices of each length. All of the test devices for this experiment were on the same MUMPs 11 wafer and backbending was performed in air. No attempt was made to obtain maximum deflections. The data is plotted in Figure 7-3. Although nonlinear, the relationship of backbending deflection to drive power is well behaved, therefore predictable.

Two experiments were performed to quantify backbending repeatability. The first was conducted on an open probe station in air at atmospheric pressure and room temperature. One device of each length was driven to failure with a manually increased drive voltage to determine the maximum drive signal. Then a drive voltage of roughly half the failure value was used to backbend a set of 5 identical vertical actuators in turn. Due to small variations in probe contact and hot arm resistance, the actual power applied varied slightly. Deflection versus applied power (computed from the measured voltage and current) for actuators backbent in air is plotted in Figure 7-4(a). All measured deflections are within 10.5% of the mean value for that device type.
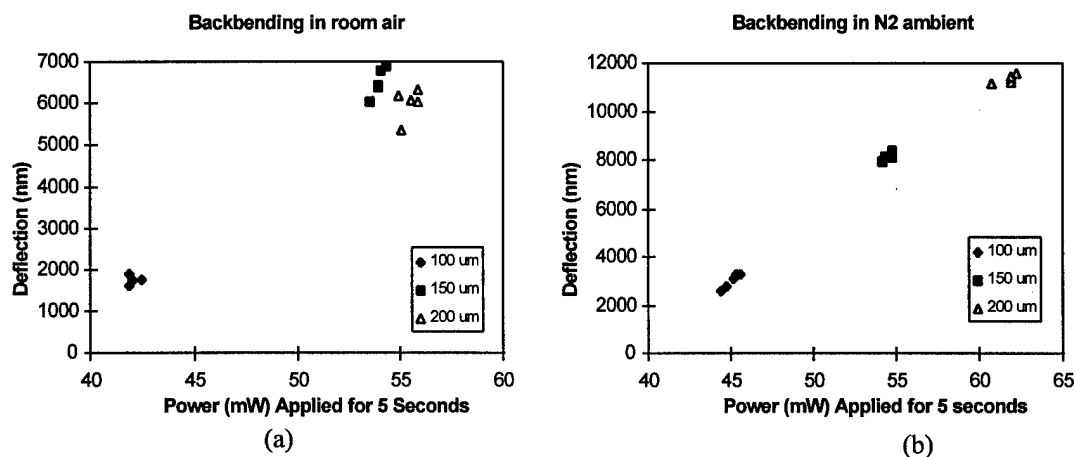
Figure 7-4. Results of two backbending repeatability experiments. Differences in the backbending procedures for each experiment are described in the text.

In an effort to eliminate some of the uncontrolled variables a second backbending uniformity experiment was conducted. Devices were backbent in a probe chamber filled with room temperature nitrogen at 1 Torr. A programmable power supply with digitally switched output was used for more precise control of the power applied. Backbending voltages of about 80% of the maximum drive voltage (as determined in the first experiment) were used to backbend 6 devices of each length for larger nominal deflections. The resistance of each device was recorded before and after backbending. For each device length the starting resistance values varied by about ±1%. The measured deflection vs. applied power is shown in Figure 7-4(b). Backbending uniformity for the 150 and 200 μm actuators was significantly improved in nitrogen, with all measurements within 2.4% and 2.6% of the means, respectively. Results for the 100 μm length actuators worsened somewhat (~15%). This is attributed to two devices in the set which displayed higher resistance (lower current flow) during backbending. Both anomalous devices also exhibited a smaller decrease in resistance. Comparison of device resistance measurements recorded before and after backbending suggest that the backbending process is very similar to polysilicon resistor trimming [6] and can readily be automated for production applications. With a controlled ambient environment and an automated backbending process it is expected that positioning uniformity better than 1% is achievable.

7.4 MOEM Applications

With the demonstrated predictability and repeatability, the high force/large deflection of backbent vertical thermal actuators is useful in numerous applications. In the MOEM examples presented here, backbending is used principally for one-time setup or positioning applications. It is important to remember that after backbending the vertical thermal actuators are still functional. Fine positioning in one direction from the nominal backbent position is possible with relatively low power dissipation. Thus final position accuracy is limited only by the measurement and control capability of the overall system.

Figure 7-5 shows a 250 μm square mirror flipped to about 45 degrees off the substrate using dual backbent vertical thermal actuators. The principal design purpose for this device is coupling of normally

incident optical signals onto the substrate plane. After fabrication and the release etch, the parallel-wired vertical thermal actuators are simultaneously backbent, flipping the mirror plate to an angle of greater than 45 degrees from the substrate. Small Poly2 flexures prevent the mirror from flipping too far and keep the mirror plate engaged with the actuators through a novel hinge/lever arrangement. Subsequent drive of the actuators permits trimming of the mirror's angular position. Greater than 45 degree positioning was verified using the microscope interferometer as an illumination source. After flipping the mirror into position the reflection from the normally incident laser beam was visible across the face of the die. Although not intended for scanning applications, the mirror can be scanned from 0 to >45 degrees with a 0-8 V signal.
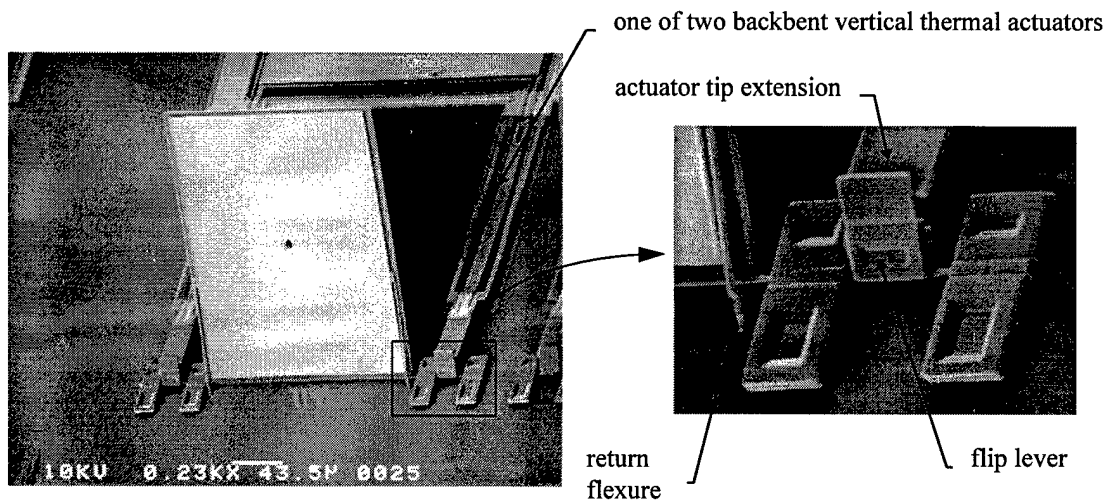
Figure 7-5. Scanning electron micrograph of 250 mm square mirror flipped to a 45 degree angle with the substrate using two backbent vertical thermal actuators and detail of the hinge/return flexure mechanism.

Figure 7-6 shows a surface micromachined beam steering mirror system which employs backbent vertical thermal actuators for setup. Here a hexagonal plate 200 μm across (corner to corner) is raised from a nominal as fabricated position of 2 μm off the substrate to about 10 μm high using 3 backbent actuators driven in parallel. The plate is comprised of stacked Poly1 and Poly2 to increase stiffness. In addition, Oxide2 is intentionally trapped between the polysilicon layers under the 100 μm across metallized mirror

surface. Measured corner-to-corner mirror curvature is less than 40 nm. After setup, the mirror plate is grounded and three Poly0 electrodes under the plate are used to deflect the plate electrostatically. The control electrodes do not extend under the metallized mirror surface to avoid induced topography in the reflective surface.
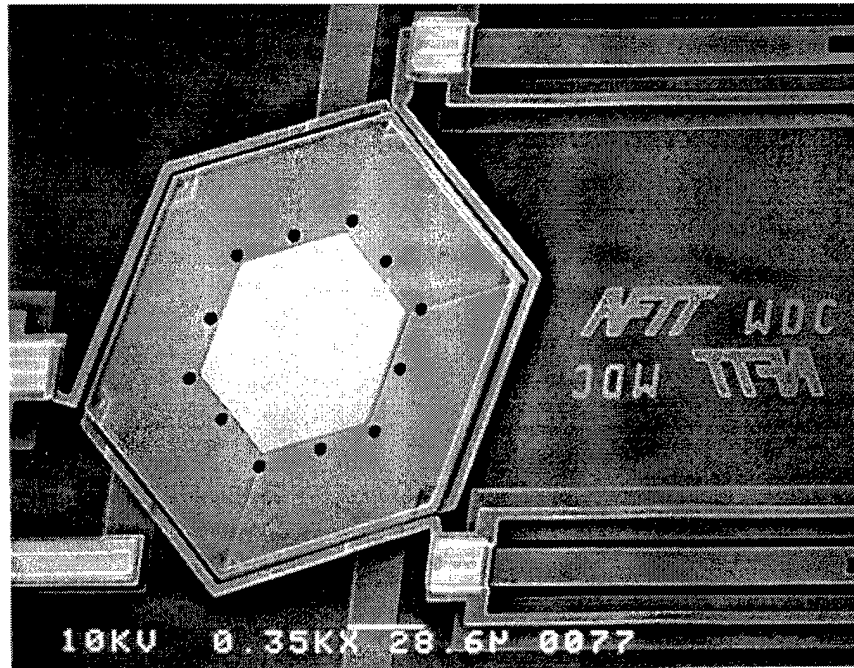
Figure 7-6. MUMPs 16 version of electrostatically controlled beam steering mirror positioned 10 mm above substrate by 3 backbent vertical thermal actuators driven in parallel.

By proper control of the electrode voltages piston and/or angular deflection are possible. Increasing the electrostatic gap by a factor of 5 increases the maximum controllable steering angle by a factor 5 also. Using 1/3 the gap distance (to avoid snap through) and the center to plate corner dimension of 100 µm results in a computed maximum steering angle of 30 mrad. For a first order approximation of beam steering speed the mirror system may be modeled as a mass (the stacked plate structure) suspended by a spring (three Poly1 flexures 4 µm wide, 200 µm long) see (Chapter 3). The estimated resonant frequency of this mirror system is 6.7 kHz using this simplified model.

Where minimum power dissipation and high frequency response are less important system requirements than maximum steering angle, the large deflection of vertical thermal actuators can be

directly exploited. Figure 7-7 is a micrograph of a thermally actuated beam steering mirror fabricated on

MUMPs 16. The device is comprised of a 80 μm diameter gold mirror attached to 3 vertical thermal

actuators by Poly1 flexures. The mirror plate is trapped oxide (Poly1, Oxide2, Poly2) to increase its

stiffness. The stacked mirror plate effectively eliminates metal stress induced curvature of the mirror (<30

nm), limits bending of the plate due to actuator forces, and reduces cross-coupling of the actuators. After

fabrication and release the 3 individually wired actuators are driven in parallel to backbend them equally.

Backbending raises the mirror plate about 10 μm of the substrate surface. Independent control of the

actuators then permits angle and/or piston modulation of an optical beam. Initial microscope

interferometer measurements of the deflection show a maximum steering angle of 125 mrad. Maximum

operating frequency of thermally actuated devices is limited by the ability of the structure to dissipate heat.

Based on experience with similarly sized lateral thermal actuators and thermal piston micromirrors the

maximum operating frequency is estimated to be in the 100's of Hz [7].
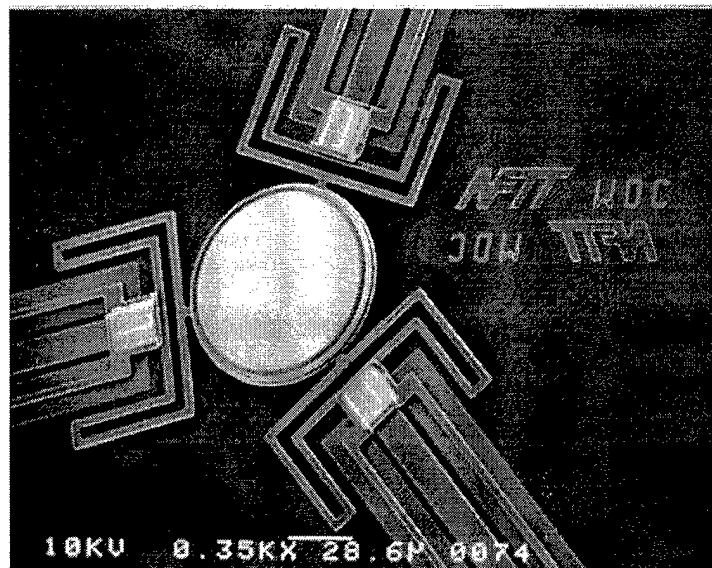
Figure 7-7. Thermally setup and actuated beam steering mirror fabricated on MUMPs 16.

Micromirror systems with large numbers of elements employ bistable actuation to simplify the

control scheme [8, 9]. Generally, the bistable deflection of the mirror elements is determined by the

fabrication process. A sacrificial layer thickness normally determines maximum piston travel. For tilting mirrors the angular deflection is determined by a sacrificial layer thickness and the mirror structure's lateral dimensions. Although fabrication processes can conceivably be tailored for any particular application, use of vertical thermal actuators as post-process positioning elements for bistable mirrors offers the potential of low-cost foundry fabrication, and system flexibility. The following micromirror prototypes fabricated in MUMPs illustrate these features.
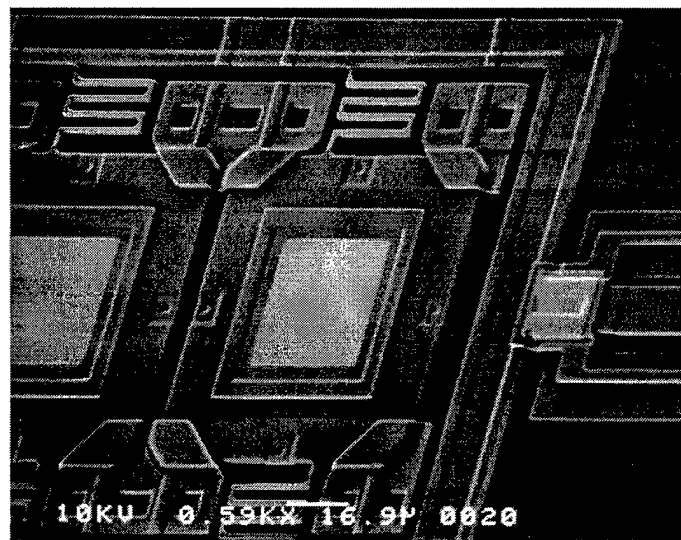
Figure 7-8. Portion of 10 element linear array of adjustable bistable piston mirrors.

Shown in Figure 7-8 is a portion of a linear array of 10 piston micromirror elements that is positioned for bistable operation by means of vertical thermal actuators. If backbent, the vertical thermal actuators pull the Poly1 mirror plate up against the Poly2 stops. By applying an electrostatic potential (~20 V) between the mirror plate and the underlying Poly0 address electrode the plate can be snapped down so that the dimples rest on the substrate. The dimples, stacked poly plate for added stiffness, and relatively low operating voltage prevent destruction of the device when snapped down. The deflection distance in this mode of operation is nominally 2.0 μm (Oxide1 thickness + Oxide2 thickness - Dimple etch). After backbending, the thermal actuators can be operated in the forward mode to vary the bistable deflection

distance from 0 to 2.0 μm. The voltage required to pull the mirror plate down is a squared function of the gap distance so small deflections require correspondingly lower control voltages. For this particular design π modulation of a normally incident HeNe beam requires only ~5 V. Post-fabrication electrical adjustment of the bistable deflection distance allows the same device to be used in phase modulation applications with different operating wavelengths, permits fine tuning, and could conceivably be used to vary the bistable modulation "on-the-fly".
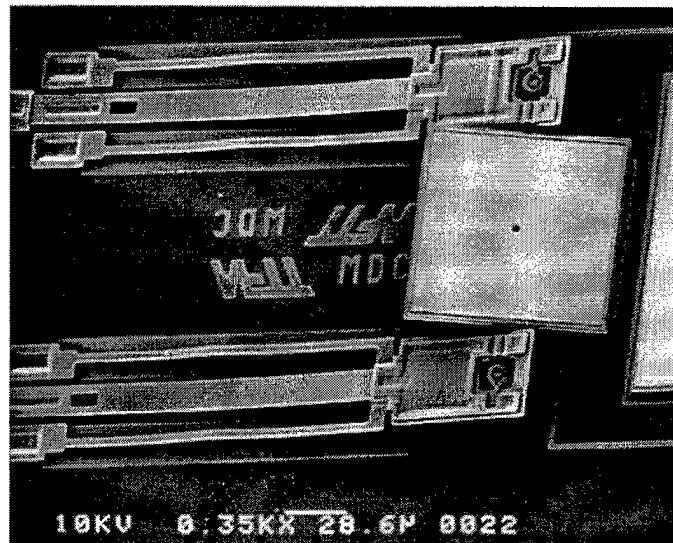
Figure 7-9. Electrostatically controlled bistable switching mirror setup by backbent vertical thermal actuators.

Backbent vertical thermal actuators have also been used to position bistable tilting mirrors for amplitude modulation applications. The initial prototype single 100 μm square mirror shown in Figure 7-9 illustrates the basic design. The unique floating hinge mechanism facilitates bistable operation for large steering angles at reasonable control voltages because the mirror plate rotates freely. Only frictional (and possibly stiction) forces need to be countered by the electrostatic force to toggle the mirror plate. After release this mirror has a beam switching angle of only 1.14 degrees. Using the backbent vertical actuators to lift the mirror plate 10 μm off the substrate yields a switch angle of 22.6 degrees. The maximum switching angle is controlled at setup by the degree of backbending applied. The characterization

measurements of Section 7-3 suggest that setup tolerances on the order of 1-2% are feasible. Certainly this degree of repeatability is adequate for many display applications.
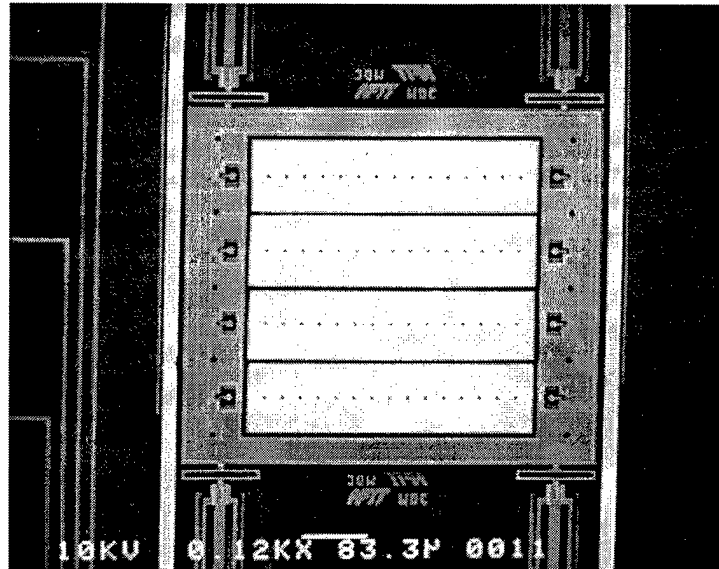
Figure 7-10. Electrostatically toggled mirror slats (100 x 400 mm) setup using backbent vertical thermal actuators.

Electrical drive of the backbent actuators permits adjustment of the steering angle from 0 to the maximum switching angle. This adjustment may be a part of the system setup, tuning, or an integral part of the optical modulation scheme. Prototype systems of multiple switching mirrors have also been fabricated. One example is shown in Figure 7-10. In this system 4 vertical thermal actuators driven in parallel raise a stacked polysilicon frame in which four 100 μm $\times$ 400 μm mirrored slats are supported by hinges. The electrostatic pads for each slat are wired together so that the slats move in unison.

7.5 Metal Stress Cantilevers

Exploitation of metal stress cantilevers was a natural evolution of the efforts to model the curvature induced by residual metal stress on micromirror structures (Chapter 4). Beginning on MUMPs 16 test structures comprised of cantilever beams of varying layer composition were included on each run to

monitor residual material stresses. The pronounced tip deflection of gold on Poly2 cantilevers in particular, suggested use of similar cantilever structures in lieu of vertical thermal actuators for lifting applications. Metal stress cantilevers offer two distinct advantages over vertical thermal actuators. First, the lifting process requires no external electrical or mechanical power. Second, lifting occurs in the release etch helping to mitigate stiction effects. Laboratory yields of 100% for properly designed metal stress cantilever devices have been observed.
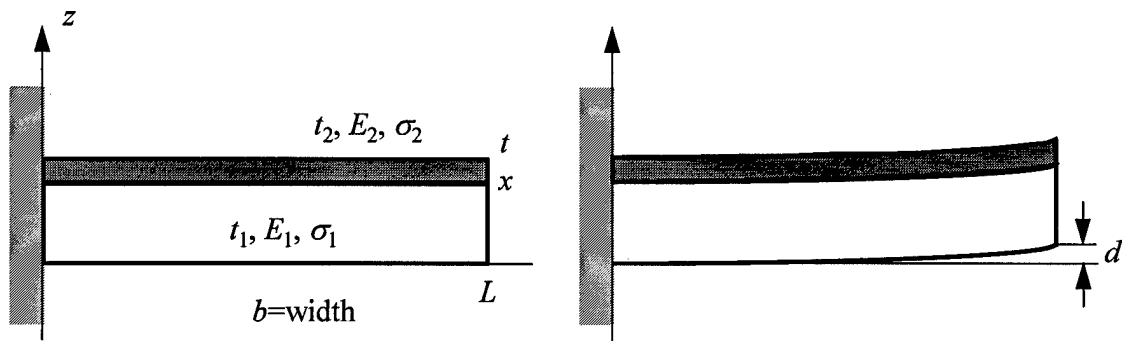
Figure 7-11. Bilayer cantilever structure deflected upward due to residual material stresses.

Design of metal stress lift cantilevers to date has been performed using only the most rudimentary analysis, and intuition based on the observation of metal cantilever test structures. Although a seemingly simple structure, the uncertainty of material properties complicates accurate analysis of the bilayer cantilever structure. Accurately predicting the tip deflection of bilayer cantilevers which are not mechanically attached to other structures should be possible using composite structural analysis techniques [10]. Critical to employment of composite analysis techniques is knowledge of the thermal expansion coefficients of materials comprising the structure, and the thermal processes used for fabrication. Finite element modeling will most likely be required for metal stress cantilevers which are attached to other structures. For single material beams, a linear strain gradient is generally assumed and a bending moment, M, due to material stresses is found by integrating through the thickness of the cantilever [11]. The deflection, d, of a cantilever of length, L, with an applied end moment is,

$$d = \frac{ML^2}{2EI},\qquad\qquad\qquad (7\text{-}1)$$

where E is the elastic modulus of the beam material, and I is the moment of inertia about the zero strain axis. For the bilayer cantilever case, computation of the bending moment is precluded because the stress distribution through the beam thickness is not known. In addition, both the effective elastic modulus and moment of inertia of the composite beam are functions of the layer materials and thicknesses. The results of simplified mechanical analyses to date have not shown good agreement with measured stress cantilever test structures, typically underpredicting deflection by over 40%. Measured tip deflections for cantilevers of differing length do show the L^2 relationship suggested by Equation (7-1). A lack of dependence on cantilever width, which cancels from the M and I terms in Equation (7-1) has also been observed. Although more accurate mechanical modeling is certainly possible, there seems to be little payoff in developing such a design model unless material parameters are controlled and known precisely (see Chapter 4). In practice, it is more expedient to "overdesign" the stress cantilevers for a given lifting application by making them longer than deemed necessary. Stops can be employed if an application requires that structures be lifted to a specific height.

7.6 Stress Cantilever Beam Steering Mirrors

Following demonstration of the MUMPs metal/Poly2 stress cantilever by the author, many AFIT designs have incorporated this simple mechanism in self-assembly applications [12]. So called "stress engineering" has been exploited to some extent by other researchers for fabrication of surface-micromachined turbine blades and microvalve structures [13,14]. The beam steering mirrors described in this section represent an innovative application of stressed cantilevers as both a lifting mechanism and actuator structure.

A second-generation version of the stress cantilever beam steering mirror is shown in Figure 7-12. In this device the 250 μm diameter mirror plate is lifted off the substrate by 3 metal stress cantilevers actuators positioned at 120 degrees with respect to each other. The mirror plate is comprised of Poly1 and

Poly2 with trapped oxide to minimize metal stress deformation of the mirror plate. Gold covered Poly2 cantilevers 300 μm long by 100 μm wide are the top plates of the three electrostatic actuators. The 3 actuator top plates and the mirror structure are grounded to the substrate. Underlying Poly0 address electrodes (not visible in the micrograph) allow each actuator to be driven independently. The flexures attaching the mirror plate to the actuators are critical because they absorb the torsion between the actuator tip and mirror plate. Without torsion relief flexures lifting is inhibited. Anchored Poly1 structures midway down the length of the cantilever and at the cantilever tip prevent shorting of the actuator if overdriven.
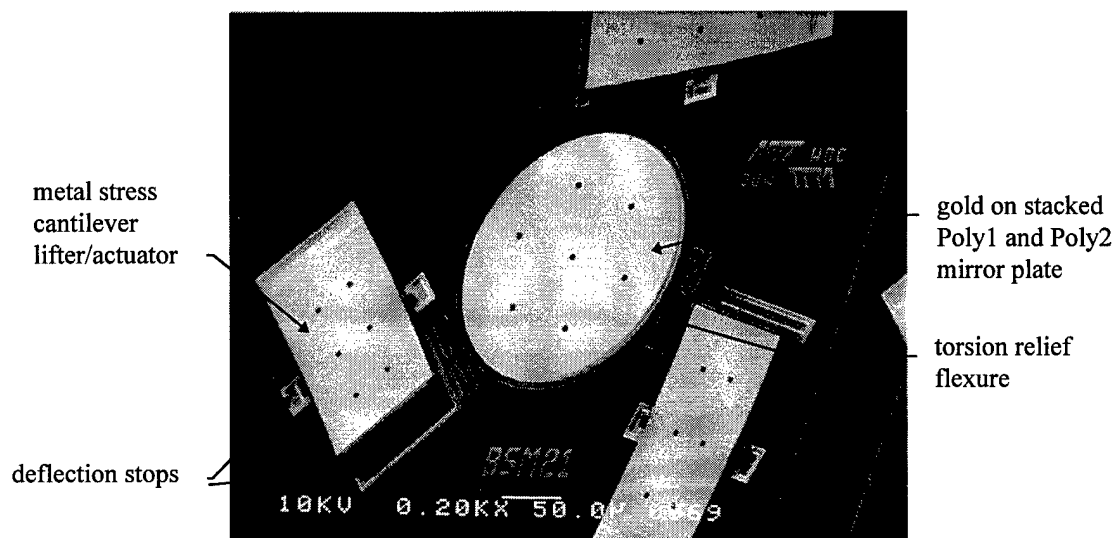
Figure 7-12. Annotated scanning electron micrograph of beam steering micromirror employing metal stress cantilevers to lift the mirror off the substrate. Note bending of torsion relief flexure.

Initial test results for the metal stress cantilever beamsteering mirrors demonstrate the advantages of the metal stress cantilever design approach. From Figure 7-12 the height of the mirror plate is estimated at ~21 μm. As a reference the lettering "BSM21" in the micrograph is 28 μm tall. The maximum stable deflection for a single actuator is approximately 7 μm, using the 1/3 the gap rule of thumb. When a single actuator is deflected the mirror pivots on the line defined by the other two actuator attachment points. The distance between adjacent attachment points is found using the mensuration formula for an equilateral triangle with sides of length, s, circumscribed by a circle of diameter D is $s=D$ sin 60° [15]. For the 250

μm mirror diameter s=108 μm. The distance from the energized actuator attachment point to the pivot line is 93.5 μm. The maximum tilt angle θ_{max}=tan^{-1}(7/93.5)=4.3° (or 74 mrad) yields a maximum steering angle of 8.6° off boresight, which is over 10 times greater than this same mirror would have without the lifting of the metal stress cantilevers. Comparison of the BSM21 design employing metal stress cantilever actuators to the beam steering mirror design which employed thermal actuators for setup (Figure 7-6) further illustrates the advantages. The BSM21 design provides twice the maximum steering angle and more than 6 times the reflective surface area, with no setup step required.
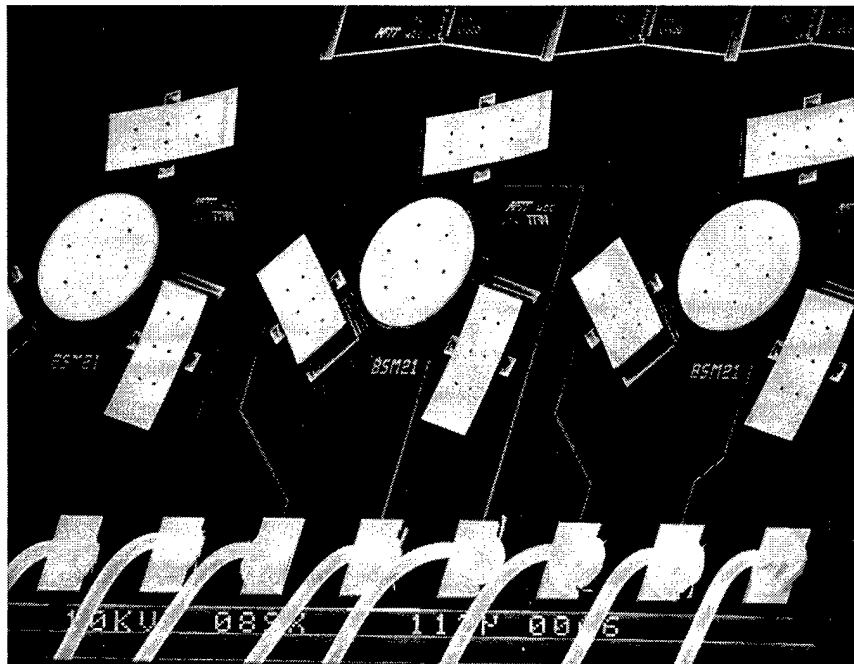
Figure 7-13. Scanning electron micrograph of 3 self-assembled beam steering mirrors employing metal stress cantilevers for lifting and actuation. Note the height uniformity of the cantilevers and mirrors.

Yield for properly designed metal stress cantilever systems appears to be excellent. On the MUMPs 21 die tested, all five BSM21 steering mirrors on the die self-assembled perfectly. Three self-assembled mirrors are shown in Figure 7-13. Interferometric microscope examination of the released die showed that all mirrors erected to a position parallel to the substrate. This observation suggests that metal stress induced curvature provides very uniform lifting, at least for the MUMPs process. Experience using

metal stress cantilevers for other applications suggests two guidelines for proper metal stress cantilever design. First, a few dimples (or other down stops) are required to prevent sticking of the cantilever to the substrate. Second, the metal layer must not unintentionally overlap the sides of the cantilever. In the MUMPs process in particular, gold stringers seem to exacerbate stiction problems, and were observed to greatly reduce metal stress cantilever yield [11].

Only minimal electrical testing of the BSM21 design has been performed, because the large electrostatic gaps provided by the metal stress cantilever actuators require fairly high actuation voltages. Testing was performed in the Zygo laser interferometric microscope. After first leveling the die/mirror surface to the microscope the height of the mirror surface at rest (no voltage applied) was recorded as a reference frame. Subsequently, the maximum available 100 V control signal was applied to one electrode and the new mirror height recorded after subtraction of the reference frame. The peak-to-valley measurement of the reference subtracted height data (1.64 μm) yields a mirror tilt of $tan^{-1}(1.64/250)= 0.37°$ (or 6.5 mrad). Nearly identical tilt results were obtained for the other electrodes. A video recording of the interferometric microscope camera shows this deflection uniformity as the electrodes are manually switched. As expected the large mirror surface of the BSM21 design exhibits significant metal stress induced curvature despite use of stacked Poly1 and Poly2 for the mirror plate. Measured mirror curvature is ~1.7 μm peak-to-valley. Using the bow formula (Equation 4-2) this curvature corresponds to a mirror focal length of 4.6 mm. An optimized process for beam steering mirrors employing the metal stress cantilever lifter/actuator would require two distinct metallizations; a high stress metal for the cantilevers, and a very low stress but highly reflective metallization for the mirror surface.

7.7 Conclusions

Both vertical thermal actuators and metal stress cantilevers provide a means of obtaining practical maximum steering angles for surface micromachined beam steering mirrors. The experimental results demonstrate that backbending of surface micromachined polysilicon actuators is predictable and

repeatable. Future work should focus on modeling of the backbending phenomenon and development of automated control of the backbending process. Extension of the techniques used for trimming of polysilicon resistors appears to be a viable starting point for automated backbending. The large force and deflection characteristics of backbent actuators are useful in an unlimited number of MEMS applications. The practical use of backbent vertical thermal actuators for setup and positioning of micro-opto-electro-mechanical devices has been demonstrated in several prototype systems.

Though not yet exploited to the extent that vertical thermal actuators have been, metal stress cantilevers offer several advantages over vertical thermal actuators. They can provide even greater lift height, with excellent yield and uniformity, and do not require any setup process. For fabrication processes which have a tensile stressed metal layer available (like MUMPs) metal stress cantilevers can (and perhaps should) replace vertical thermal actuators entirely. Despite the advantages of metal stress cantilevers, vertical thermal actuators will continue to have a place in MEMS systems fabricated in surface micromachining processes which do not have a tensile stressed metal layer, like Sandia's SUMMiT process.

References

1   J. H. Comtois, V. M. Bright, and M. W. Phipps, "Thermal microactuators for surface micromachining processes", *Proc. SPIE*, vol. 2642, pp. 10-21, May 1995.

2   J. R. Reid, V. M. Bright, and J. H. Comtois, "Arrays of thermal micro-actuators coupled to micro-optical components", *Proc. SPIE*, vol. 2865, pp. 74-82, Aug. 1996.

3   J. R. Reid, V. M. Bright, and J. H. Comtois, "Force measurements of polysilicon thermal micro-actuators", *Proc. SPIE*, vol. 2882, pp. 296-306, Oct. 1996.

4   J. H. Comtois and V. M. Bright, "Surface micromachined polysilicon thermal actuator arrays and applications", *Proc. 1996 Solid State Sensor and Actuator Workshop*, Hilton Head, SC, pp. 174-177, 2-6 June, 1996.

5   *Zygo Maxim 3D Operation and Maintenance Manual*, Zygo Corp., Laurel Brook Road, Middlefield, CT, May 1988.

6   D. W. Feldbaumer and J. A. Babcock, "Theory and application of polysilicon resistor trimming", *Solid-StateElectronics*, Vol. 38, No. 11, pp. 1861-1869, Nov. 1995.

7   W. D. Cowan and V. M. Bright, "Thermally actuated piston micromirror arrays", *to be published in Proc. SPIE*, vol. 3131, July 1997.

8   J. M. Younse, "Projection display systems based on the Digital Micromirror Device™ (DMD™)", Proc. SPIE, vol. 2641, pp. 64-75, July 1995.

9   V. P. Jaecklin, C. Linder, N. F. de Rooij, J. M Moret, and R. Vuilleumier, "Line-addressable torsional micromirrors for light modulator arrays", *Sensors and Actuators A*, vol. 41-42, pp. 324-329, 1994.

10   B. D. Agarwal and L. J. Broutman, *Analysis and Performance of Fiber Composites*, John Wiley & Sons, Inc., New York, 1990.

11   M. Madou, *Fundamentals of Microfabrication*, CRC Press, Boca Raton, FL, 1997.

12   P. E. Kladitis, "Self-Assembly of Microstructures", *Masters Thesis*, Air Force Institute of Technology, AFIT/GE/ENG/97D-02, November 1997.

13   C.-L. Tsai and A. K. Henning, "Surface micromachined turbines", in *Transducers '97*, proceedings of the 1997 International Conference on Solid-State Sensors and Actuators, vol. 2, pp. 829-832, June 1997.

14   J. Haji-Babaei, C. Y. Kwok, and R. S. Huang, "Integrable active microvalve with surface micromachined curled-up actuator", in *Transducers '97*, proceedings of the 1997 International Conference on Solid-State Sensors and Actuators, vol. 2, pp. 833-836, June 1997.

15   *CRC Standard Mathematical Tables*, 25 th Edition, CRC Press, Boca Raton, FL, 1980.

8. Microfabricated Continuous Facesheet Deformable Mirrors

8.1 Chapter Overview

The best reported atmospheric aberration correction results to date have been obtained with axially actuated continuous facesheet deformable mirrors. Typical conventionally manufactured deformable mirrors employ an array of piezoelectric (or electrostrictive) actuators to deform a relatively thin glass facesheet [1]. Conventionally manufactured continuous facesheet deformable mirrors are expensive, with a typical cost of $1000 per actuator. Microfabrication in a foundry process can potentially reduce the cost of continuous facesheet deformable mirrors by a factor of 1000 or more. The principal challenge is development of a microfabrication process which yields actuators with sufficient stroke, and acceptable facesheet planarity.

Ongoing efforts to develop a micromachining process specifically for deformable mirror fabrication appear relatively close to success [2-6]. This MUMPs-like process employs thicker sacrificial oxides to both increase actuator stroke and improve self-planarization of the polysilicon/silicon nitride facesheet. Perhaps the biggest microfabrication challenge is controlling the residual material stress of layer or layers comprising the facesheet. Because the facesheet is a large structure, residual material stresses can cause large deformations of the facesheet surface when the structure is released. The Boston University researchers have observed cracking at facesheet attachment posts due to residual tensile stresses in a silicon nitride membrane [4]. The author's continuous facesheet designs fabricated in MUMPs exhibit significant deformation due to residual compressive stress in the Poly2 facesheets. Similar continuous facesheet prototypes recently fabricated in the SUMMiT process do not exhibit stress-induced facesheet deformation.

The remainder of this chapter is organized as follows. Continuous facesheet design is examined in Section 8.2. Prototype continuous facesheet designs fabricated in the MUMPs and SUMMiT surface micromachining foundry processes are presented in Sections 8.3 and 8.4, respectively. Attempts to add a continuous facesheet to MUMPs actuator arrays are described in Section 8.5. Conclusions and

recommendations for future continuous facesheet deformable mirror microfabrication research are offered in Section 8.6.

8.2 Foundry Design Limitations

The characteristics of currently available foundry processes, specifically MUMPs and SUMMiT, impose constraints on micromachined continuous facesheet deformable mirrors. In addition to the planarity and residual stress problems mentioned in the proceeding section, the thicknesses of the polysilicon layers are not particularly well suited to good continuous facesheet deformable mirror fabrication. The brief examination of continuous facesheet deformable mirror design equations below provides a basic understanding of these process imposed constraints and suggests process changes for continuous facesheet DM fabrication.

The influence function of a continuous facesheet deformable mirror element is a function of the force applied by the actuator (F), actuator spacing (b), and facesheet stiffness. Beam theory approximations show good agreement with measured influence functions and finite element models of macro-sized deformable mirrors [7]. Using beam theory approximations the shape of the influence function is given by

$$y = \frac{F}{k_{FS}^{CC}}\left[2\left(\frac{x}{b}\right)^3 - 3\left(\frac{x}{b}\right)^2\right], \tag{8-1}$$

for the clamped-clamped case, and by

$$y = \frac{F}{k_{FS}^{CF}}\left[\frac{1}{2}\left(\frac{x}{b}\right)^3 - \frac{1}{3}\left(\frac{x}{b}\right)^2\right], \tag{8-2}$$

for the clamped-free case, where y is the deflection of the facesheet at a distance x from the actuator. The force, F, applied by an electrostatic parallel-plate actuator is given by Equation (3-2). Depending on the approximation used, the stiffness of the facesheet is either [7],

$$k_{FS}^{CC} = \frac{16Et^3}{b^2} \text{ or } k_{FS}^{CF} = \frac{8Et^3}{b^2}, \tag{8-3}$$

where t is the thickness of the facesheet, and E is the elastic modulus of the facesheet material. The actuator spacing, b, varies as a function of direction for square grids with the spacing in the 45° direction increasing to $\sqrt{2}$ times the nominal grid spacing. The implications of a nonsymmetrical influence function are beyond the scope of this discussion. Suffice to say that many high performance deformable mirrors employ square actuator grids. Equations (8-1) through (8-3), and Equation (3-2) permit computation of the influence function for a given microfabricated deformable mirror geometry.

Which beam deflection approximation case is most applicable for calculation of the influence function is primarily determined by the relative stiffness of actuators and facesheet. If the actuators are very stiff when compared to the facesheet, the clamped-clamped is more appropriate, and vice versa if the relative stiffnesses are reversed. These relative stiffnesses also define the interactuator coupling, which is computed as [7].

$$Actuator\ Coupling = \frac{1}{4\left(\frac{k_{act}}{k_{FS}}\right)+1} \times 100\% \qquad (8\text{-}4)$$

For a flexure beam actuator, k_{act} is the spring constant computed in Equation 3-8. Typical values for MUMPs Poly1 flexure beam actuators and Poly2 facesheet yield high actuator coupling. Stiffer actuator structures can reduce interactuator coupling to less than 5% but require very high control voltages. A more practical approach is to reduce the stiffness of the facesheet material by reducing the thickness and or elastic modulus, and possibly increasing the distance between actuators.

Reducing the stiffness of the facesheet also lowers the maximum operation frequency of the deformable mirror. The natural frequency of a continuous facesheet membrane supported by axial actuators is given by [8]

$$f_n = \frac{10.21t}{2\pi b^2}\sqrt{\frac{E}{12\rho\left(1-\upsilon^2\right)}} \qquad (8\text{-}5)$$

where ρ and υ are the density and Poisson ratio of the facesheet material respectively. For a MUMPs Poly2 membrane (t=1.5 μm, E=170 GPa, υ=0.22, ρ=2330 kg/m^3) supported by actuators with 203 μm spacing, Equation (8-5) yields a resonant frequency over 165 kHz. Since adaptive optics systems for atmospheric aberration correction only require a closed loop bandwidth of about 1 kHz, it is clear that facesheet stiffness can be substantially reduced to obtain microfabricated continuous facesheet deformable mirrors with low control voltages.

8.3 MUMPs Continuous Facesheet Designs

Despite the known limitations of the MUMPs process for continuous facesheet deformable mirror fabrication, a number of prototype systems were developed and functionally tested. The optical quality of the MUMPs prototypes is degraded by incomplete self planarization, etch access holes, and residual stress in the Poly2 layer. Controllable actuator stroke is limited to about 1/3 the Oxide1 thickness, or 0.67 μm, limiting the magnitude of aberrations that can be corrected. None of the successful MUMPs designs use the MUMPs gold metallization. Forces caused by residual stress in the MUMPs gold are sufficient to rip apart Poly1 vias, and pull flexure beam actuator structures upward.

(a)   (b)
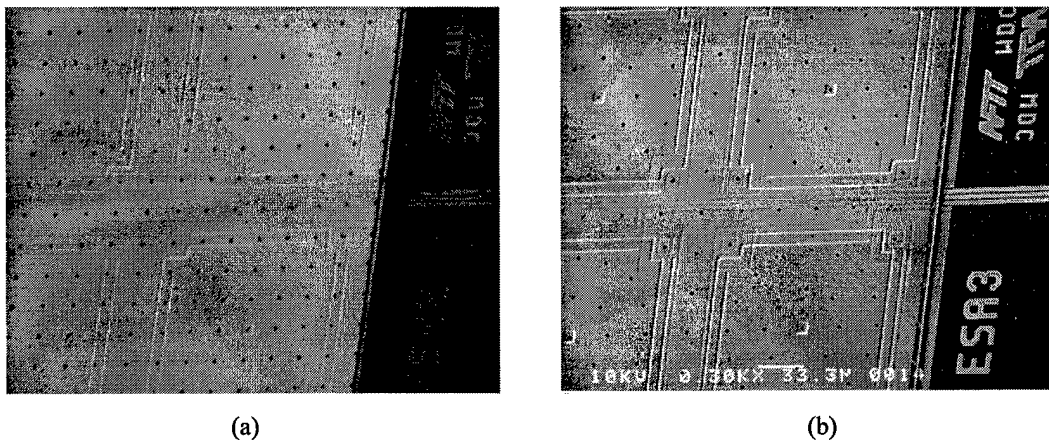
Figure 8-1. Scanning electron micrographs of similar MUMPs self-planarized continuous facesheet deformable mirrors with (a) and without (b) metal. Note metal stress-induced actuator pull-up in (a).

Stress driven actuator pull up of a metallized MUMPs 19 prototype is visible in the scanning

electron micrograph of Figure 8-1(a). For comparison, the micrograph of a similar device without MUMPs

metal in Figure 8-1(b), shows no evidence of deformation. Interferometric microscope testing of the

unmetallized device depicted in Figure 8-1(b) does show deformation of the Poly2 surface due to residual

compressive stress, but the device is still functional. Interferometric microscope images of the MUMPs 19

device with two different actuators pulled down are shown in Figure 8-2.

(a)   (b)
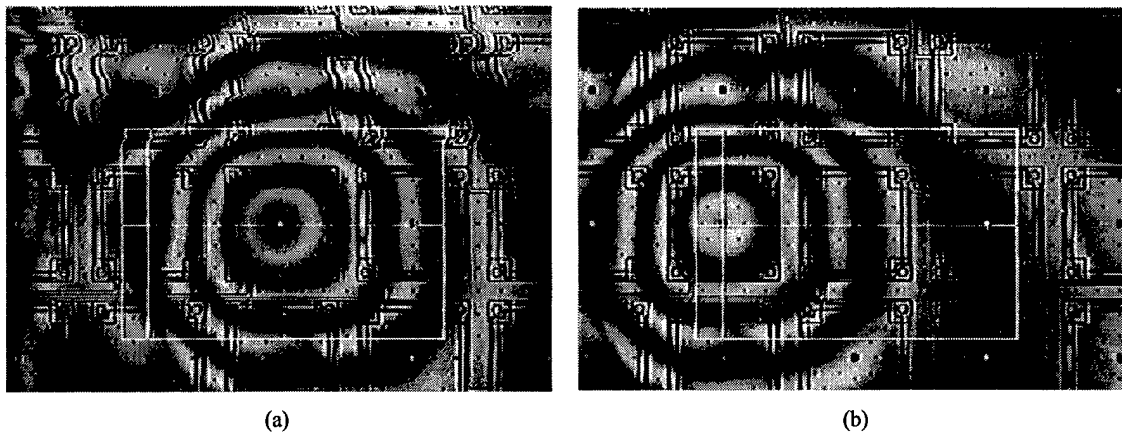
Figure 8-2. Interferometric microscope images of MUMPs 19 continuous facesheet deformable mirror
with two adjacent actuators fully pulled down by 21 V control signal. Measurements from scan line in (b)
are shown in Figure 8-3.

Influence functions were measured using the reference subtraction feature of the computer

controlled interferometric microscope. With the mirror under test at rest, the surface height is recorded and

stored as a reference. Subsequent reference subtracted measurements with control voltage applied to an

actuator are a direct measurement of influence function. Measured influence functions with 18 V and 21 V

applied are shown in Figure 8-3. The scan lines depicted start at the center of the controlled actuator, and

span 2 actuators (406 μm). Note that for the 21 V measurement, the actuator is fully deflected to the

dimple steps. These measurements indicate that interactuator coupling is about 40%. This value agrees

reasonably well with the coupling estimated by Equation (8-4).
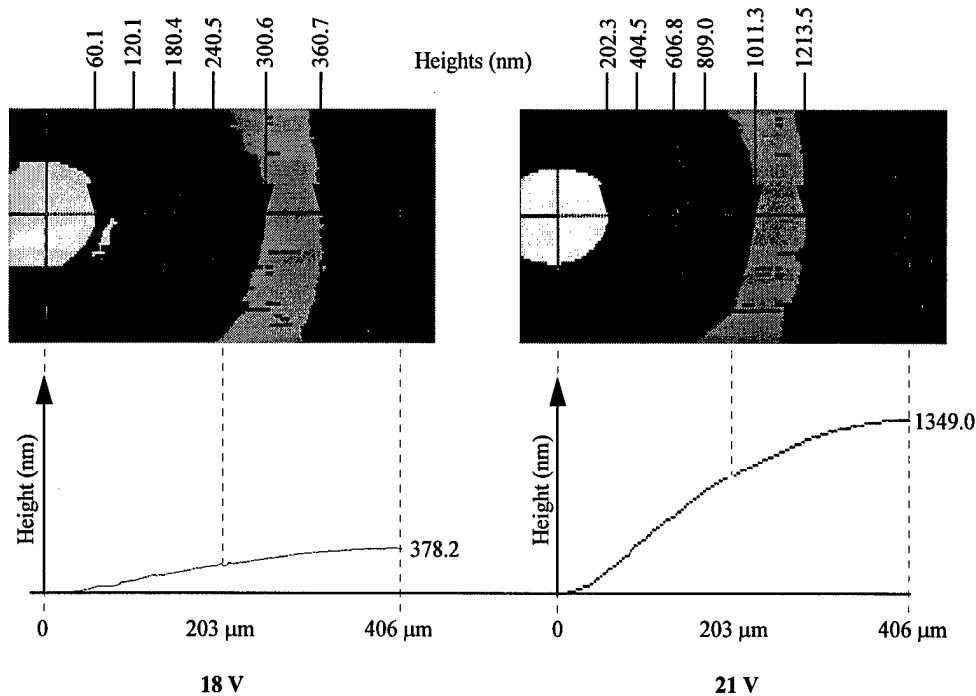
Figure 8-3. Measured influence functions for MUMPs 19 continuous facesheet deformable mirror with 18 V and 21 V applied to the actuator. The measurement scan corresponds to (b) in Figure 8-2. Note that the scan lines have been scaled to the same vertical axis for side by side comparison.

The same basic MUMPs 19 unmetallized continuous facesheet design was employed on 2 stand-alone die fabricated on MUMPs 21 and 22. The MUMPs 21 version is a quarter die containing a 12×12 actuator continuous facesheet deformable mirror. The actuators are individually controllable. One element of the MUMPs 21 design is shown in Figure 8-4. The self-planarization of the Poly2 facesheet is reasonably good. On MUMPs 22, a 12×12 actuator version of the continuous facesheet deformable mirror was implemented as a defocus corrector. Like the segmented defocus corrector described in Chapter 3, actuators equidistant from the mirror center are wired together. Only 16 control voltages are required to drive the defocus correctors. The 12×12 continuous facesheet defocus corrector resides alone on a quarter die (5 mm × 5 mm) for convenient packaging.

Shown in Figure 8-5 are interferometric microscope images of the continuous facesheet defocus corrector with and without control voltages applied to selected actuators. Deformation of the mirror surface due to residual compressive stress in the Poly2 layer is significant. Pinning of the unused corner

actuators exacerbates the stress induced deformation. Allowing the 4 unused actuators in each corner to "float" would allow the actuator flexures to absorb the lateral deflection of the facesheet, and reduce the amount of upward buckling. Laser surgery to remove the 16 Poly2-Poly1 vias will improve the facesheet flatness of the MUMPs 22 defocus correctors, and is recommended for any devices used for future experimentation. With selected actuators near the defocus corrector driven, the interferometric images suggest that it is possible to flatten the facesheet. Pending development of controller and setup (flattening) procedure, the continuous facesheet defocus correctors should be capable of focusing from infinity down to about 1 meter.
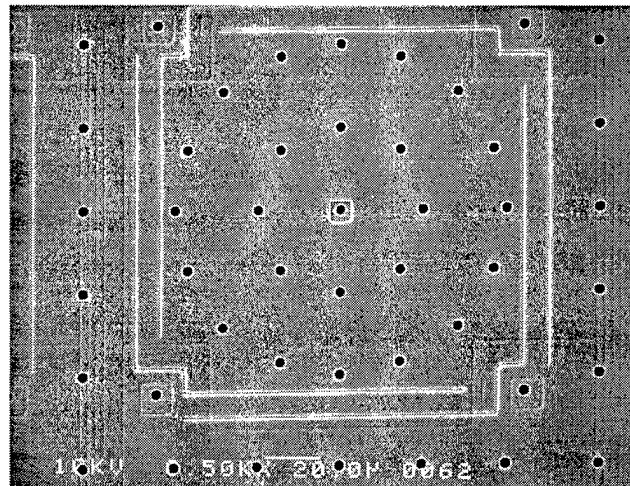
Figure 8-4. Scanning electron micrograph of MUMPs 21 self-planarized continuous facesheet deformable mirror element.

(a)   (b)   (c)
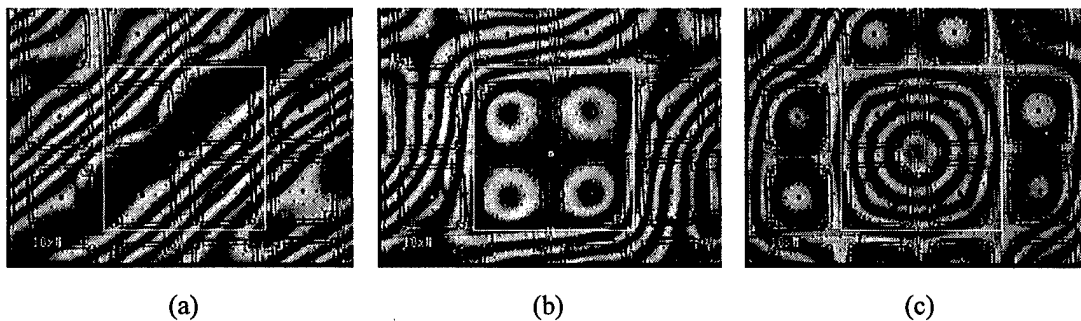
Figure 8-5. Interferometric microscope images of continuous facesheet defocus corrector; with no actuation (a), with 4 central actuators pulled down (b), and with 8 actuators equidistant from center pulled down.

The digital deflection concept described in Section 3.6 has also been applied to a continuous facesheet deformable mirrors fabricated in MUMPs. The first prototype fabricated on MUMPs 22 is shown in Figure 8-6. The actuator top plate, flexures, and self-planarization structure of the continuous facesheet digital deflection design are nearly identical to previous analog controlled designs. The single Poly0 address electrode of analog controlled designs has been replaced by a 3-bit digitally scaled design (see Section 3.6). All but the four corner actuators of the 5×5 element digital design are active. The four corner actuators are not fixed. Due to the smaller size of the facesheet (~ 1 mm) and the lack of hard attachment points, the Poly2 facesheet of digital deflection design is expected to be relatively flat. Prior to release, a metallized Poly2 frame surrounds the array surface and covers the Poly0 wiring. This structure comprises a self removing mask that floats off the die in the release process. The combination of the self-removing mask to define facesheet edges, and a crude aluminum foil shadow mask to protect the remainder of the chip, should make post foundry metallization of the digital deflection continuous facesheet mirrors fairly easy.
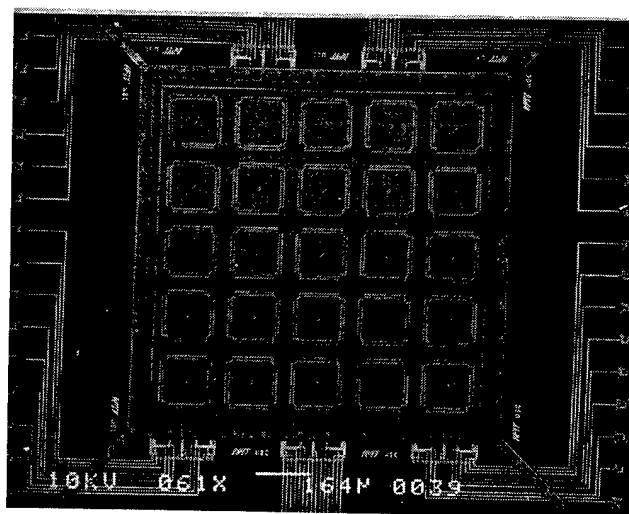
Figure 8-6. Continuous facesheet deformable mirror employing 21, 3-bit digital deflection actuators. Corner elements are inactive.

Another type of continuous facesheet deformable mirror is shown in Figure 8-7. This MUMPs design employs only a Poly2 membrane supported by a 12×12 array of flexures. The Poly0 actuating

electrode for each element surrounds the support post. The self-planarization of the Poly2 layer using the PolyO wiring layer, Oxide 1 and Oxide 2 is quite good. The modulation characteristics of this device are expected to be closer to an unsupported membrane than an axially actuated continuous facesheet. The nominal stroke of the Poly2 facesheet is approximately 0.9 μm, using the 1/3 gap rule of thumb. Initial MUMPs 21 prototypes suffered severe surface deformation upon release due to residual compressive stress in the Poly2 and have not been tested. Removal of the hard point attachments in the corners of the membrane should help reduce stress induced deformation somewhat.
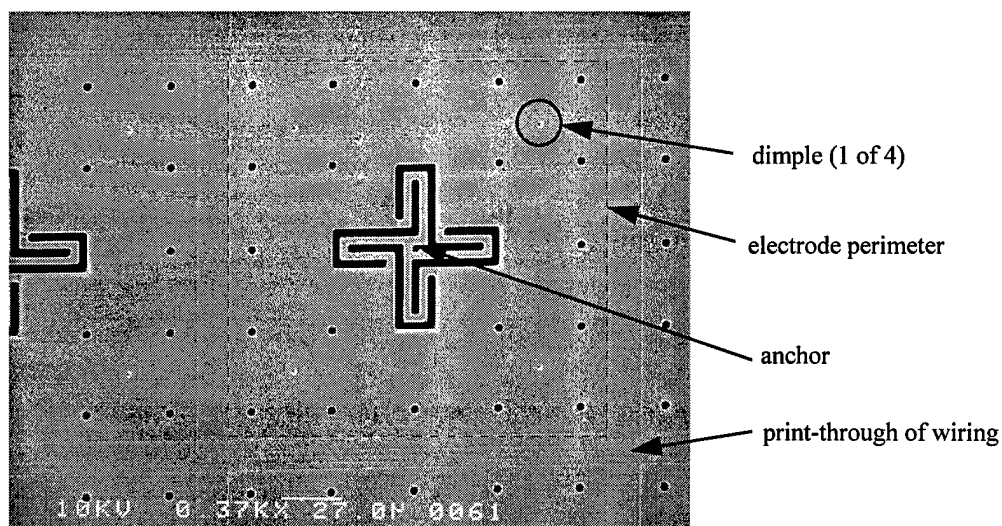
Figure 8-7. MUMPs 21 supported membrane mirror. Each element is supported by a central flexure.

8.4 SUMMiT Continuous Facesheet Designs

At first blush, the SUMMiT process with its CMP planarization step seems almost tailor made for continuous facesheet deformable mirror fabrication. Unfortunately, the same deformable mirror design limitations imposed by layer thicknesses apply to the SUMMiT process. The stroke of an electrostatic actuator defined by the first sacrificial oxide thickness is ~0.67 μm, identical to the MUMPs process. Stacked MMPOLY1 and MMPOLY2 structures are nominally 2.5 μm thick and must deform a 2.0 μm thick MMPOLY3 facesheet.

A prototype continuous facesheet mirror fabricated in the SUMMiT process is shown in Figure 8-8. This mirror, is a direct extension of the author's segmented design shown in Chapter 4, and employs an actuator structure very similar to that shown in Figure 4-11, with wider (4 µm) flexures. The layout drawing was produced by the Phillips Laboratory, hence the graffiti in the micrograph. Although the facesheet surface appears very flat in the scanning electron micrograph, the print-through of underlying layers described in Chapter 4 was observed. The measured peak-to-valley surface irregularity is 176 nm. Ignoring print-through, the facesheet is very flat across the 5×7 element array, due to the essentially stress-free MMPOLY3 layer produced in more recent SUMMiT fabrication runs.

(a)   (b)
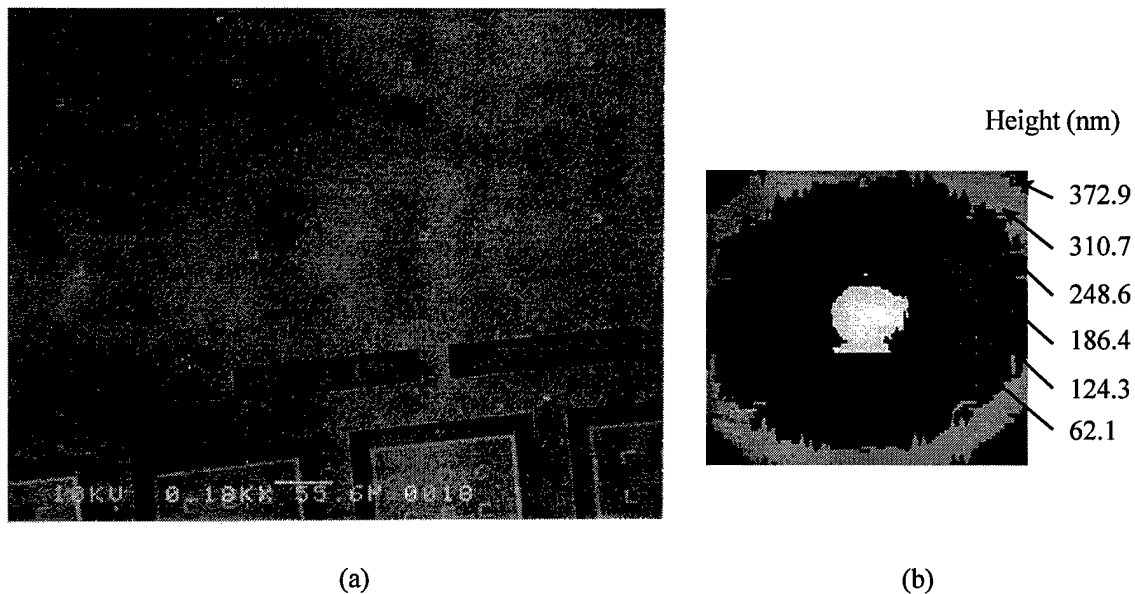
Figure 8-8. SUMMiT continuous facesheet deformable mirror. Scanning electron micrograph (a) shows facesheet surface. Measured influence function with 50 V applied to the underlying actuator (b).

Interferometric microscope testing of the SUMMiT continuous facesheet showed that the influence function is dominated by the stiff facesheet, as expected. A reference subtracted false grayscale image of the influence function is shown in Figure 8-8 (b) with 50 V applied to a single actuator. These initial test results suggest that with relatively minor modifications, the SUMMiT process could be used to produce very good continuous facesheet deformable mirrors.

8.5 Post Foundry Facesheet Fabrication

To fully overcome the continuous facesheet deformable mirror design limitations improved by foundry processes, requires development of a specialized process. Developing a microfabrication process is expensive, and was deemed to be beyond the scope of this research effort. Instead, actuator arrays were designed and fabricated in the MUMPs foundry process, and post-foundry techniques to add a continuous facesheet were explored. Although these efforts have not yet produced fully functional devices, the partial successes obtained suggest that post-foundry facesheet fabrication be explored further. This section summarizes the achievements and pitfalls of the author's post-foundry facesheet fabrication effort. These "lessons learned" provide a good starting point for future efforts. Two approaches to facesheet fabrication were attempted; eutectic bonding of membranes and actuator arrays fabricated in the MUMPs process, and polymer planarization of a MUMPs actuator array before deposition of a facesheet.

8.5.1 Eutectic Bonding

The initial approach to facesheet fabrication was to use gold/silicon eutectic bonding to attach a membrane (fabricated in MUMPs) to a MUMPs actuator array. Gold/silicon eutectic bonding is described in Section 2.4. After attachment, a sacrificial wafer etch removes the membrane die, but leaves the membrane structure attached to the actuator array. The first problem encountered with the eutectic bonding approach was alignment of the two MUMPs die containing the membrane and the actuator array. MUMPs dicing tolerances preclude mechanical alignment of the die edges unless mating structures are very large. Therefore, an infrared microscope (Research Devices) was used to align metallized features on the membrane and actuator die. The normally unpolished backside of MUMPs die must be polished to enable infrared alignment. The backside of MUMPs die were manually polished using successively finer silicon carbide polishing papers (600, 800, 1200 grit) mounted to glass plates. Polishing was performed prior to removal of the protective shipping resist so that the topside structures were not damaged or contaminated

by handling. After stripping the protective resist in acetone, the backside polished die are clean, with no grinding residue evident under optical microscope examination. This polishing procedure results in good visibility through 2 MUMPs die, using only the IR microscope's 10 W bulb for illumination, and permits alignment of the gold features.

A second problem solved is that of heating the MUMPs die to the gold/silicon eutectic temperature (363 °C) in a vacuum. The apparatus shown in Figure 8-9 employs two 250 W quartz lamps to heat the MUMPs die. Similar quartz lamp vacuum heating approaches have been used by other researchers for Au/Si bonding [9,10]. The quartz halogen bulbs and fixtures were scavenged from an inexpensive ($10 total) surplus outdoor security light. The quartz lamp heater performed remarkably well. A J-type thermocouple mounted between two MUMPs die reaches 370 °C after 2.5 minutes in a 2×10^{-5} Torr vacuum, if both lamps are operated at full power. To verify thermocouple readings, eutectic formation was confirmed by visually inspecting test die through the glass bell jar. With a test die face up on the heater, the lamps were powered until the thermocouple reading exceeded the eutectic temperature (370-390 °C). After turning off the lamp power, the color of metallized regions on the die were observed to be a silver-gray color. Under optical microscope examination, both die for several bond attempts showed good eutectic formation but no evidence of adhesion.

two quartz halogen lamps in fixtures

thermocouple mounted between two MUMPs die

thermocouple vacuum feedthrough

AC power vacuum feedthrough
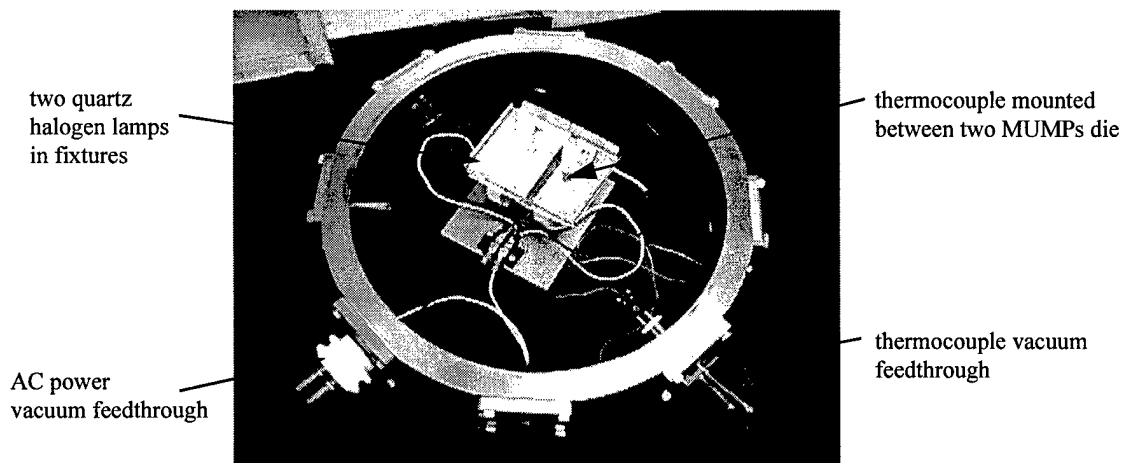
Figure 8-9. Quartz lamp heater developed for eutectic bonding experiments in Denton DV-602.

Fixturing to hold the 2 die in intimate contact proved to be the most vexing problem. A number of clamping arrangements were devised and tested, but no adequate solution was found. Trying to mate the chips and align in a non-clean room environment is also inadvisable. Micron size dust particles can prevent intimate contact of the bonding surfaces. After considerable fruitless effort, the eutectic bonding facesheet fabrication approach was abandoned due to the practical problems of fixturing and cleanliness. This approach may still be viable but should be undertaken only if a clean room environment is available. Also a reliable means of clamping the two die for infrared alignment and subsequent heating must be developed. Holding and clamping of two wafers together is probably more practical and has been demonstrated for selective eutectic bonding of MEMS structures [9-12].

8.5.2 Polymer Planarization

Planarization of MEMS topologies with a spin coated polymer were examined in Section 2.53. A photosensitive polyimide manufactured by DuPont (Pyralin® PD, PI-2721) was selected for polymer planarization experiments primarily because thick (over 10 μm) layers can be deposited in a single spin coating [13]. The photosensitive polyimide simplifies post-foundry processing. The polyimide layer is spun on and patterned much like a positive photoresist. Exposure to ultra violet (UV) illumination initiates crosslinking (imidization) of the polymers. After UV illumination, the developer (DE-6018) dissolves the unexposed polyimide. A rinse (RI-9045) stops the developing process. The two basic approaches to fabrication of a continuous facesheet using polymer planarization are shown in Figure 8-10. The first case shown in, Figure 8-10(a), relies on selective exposure of posts which attach the facesheet membrane to the actuator structures. Thus, the polyimide serves as both a planarization layer and a structural material. After exposure of the posts and facesheet deposition, the unexposed polyimide is removed by the developer. In the second approach depicted in Figure 8-10(b), the polyimide serves only as a planarizing sacrificial layer. After deposition of the facesheet material, all of the polyimide is removed. The facesheet in the latter approach is degraded by the actuator attachment vias through the sacrificial polyimide layer.

Initial polyimide planarization tests on an unreleased MUMPs die were encouraging. Step heights of 2.25 μm were reduced to 0.25 μm (DOP=88%) with a 4.5 μm thick layer of pre-baked polyimide. Slower spin speeds produced prebaked layers over 12 μm thick on bare silicon wafers.

Facesheet fabrication attempts using both polyimide planarization schemes failed. In the polyimide post case, the developer was unable to remove the unexposed polyimide after sputter deposition of a chromium/gold facesheet onto the planarized die. It was determined through diagnostic experiments that the sacrificial regions of polyimide were partially crosslinked while sputtering the facesheet. The cross-linking observed is attributed to either UV exposure from the sputtering plasma or increased temperature. Attempts to remove the polyimide sacrificial layer were also complicated by the partial crosslinking of the sacrificial media. Two proprietary photoresist strippers ACT CMI and ACT1 manufactured by Ashland Chemical were tried. Both removers attack and dissolve the polyimide, but in doing so cause a swelling of the polymer layer. This swelling damages the fragile facesheet.
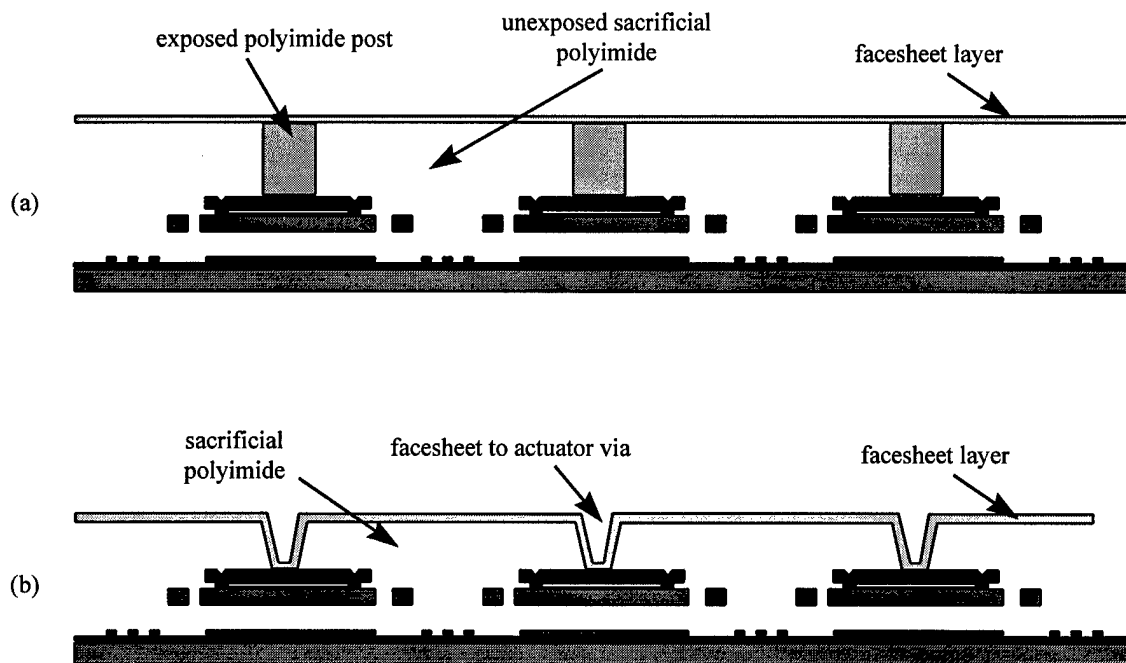
Figure 8-10. Polymer facesheet planarization approaches. The approach shown in (a) requires a photosensitive polyimide which can be hardened to form structural posts that remain after removal of the sacrificial polyimide. In (b) the polymer serves only as a sacrificial planarizing media.

Although polymer planarization experiments did not produce a functional deformable mirror device, the author's results are encouraging. By limiting the topography of the actuator array using self-planarization techniques, and applying a sufficiently thick layer of polyimide, very planar sacrificial surfaces for facesheet fabrication should be possible. Both the polyimide post and sacrificial layer approaches warrant further investigation. In particular, use of a dry etch to remove a sacrificial layer of polyimide should be explored. Other MEMS researchers have successfully used long duration (3 to >5 hour) oxygen plasma etches to remove sacrificial polyimide layers [14,15]. This avenue was tentatively explored for facesheet fabrication, but the available oxygen plasma etching system proved ill suited for long etch times.

8.6 Conclusions and Recommendations

Currently available foundry processes are not well suited to fabrication of continuous facesheet deformable mirrors. Lack of a planarization step, and residual stresses in the MUMPs process limit the planarity of the optical surface obtained. Pending refinement of the CMP planarization step, the SUMMiT process will produce exceptionally good optical surfaces because the facesheet layer is virtually stress-free. To maintain low control voltages, the stiffness of the final polysilicon (facesheet) layer in both processes must be reduced. Reducing the thickness of the final poly layer to ~0.5 µm is an easy process modification with huge benefits for continuous facesheet deformable mirror designs. Alternatively, the thickness of the top polysilicon layer can be reduced by a post-foundry silicon etch before the foundry fabricated die are released. Post-foundry planarization and facesheet fabrication are options worthy of further research. In all approaches attempted, practical problems, (such as fixturing, cleanliness, and lack of more sophisticated etching equipment), and not fundamental design flaws prevented successful facesheet fabrication.

Within the constraints of the MUMPs foundry process, several functional microfabricated continuous facesheet deformable mirror systems were produced. In hope that these devices can be made

available for future cooperative research efforts, the general characteristics are summarized here. Maximum actuator stroke is limited to less than 0.6 μm unless the actuator is fully deflected to the dimple stops. When fully deflected, the facesheet contacts the Poly1 support (and self-planarization) structure in all working designs. All designs employ a square actuator grid with 203 μm center-to-center spacing. MUMPs continuous facesheet actuators require a maximum control voltage of less than 30 V, but survive overdriving. The optical surface of the MUMPs continuous facesheet designs is corrupted by etch holes, actuator attachment vias, and print-through of the underlying structures, but the flat in-phase optical surface exceeds 90%. Optical energy diffracted by these small structures should be widely scattered. Some designs include self-removing masks to facilitate post-foundry metallization with a shadow mask. The low stress sputtered chromium/gold metallization discussed in Section 4-7 should work well for MUMPs continuous facesheet designs.

References

1   B. R. Oppenheimer, D. Palmer, D. Dekany, A. Sivaramakrishnan, M. Ealy, and T. Price, "Investigating a Xinξtics Inc. Deformable Mirror", *SPIE*, vol. 3126, pp. 569-579, 1997.

2   T. G. Bifano, "Micromechanical arrays for macroscopic actuation of deformable mirrors", *Semi-annual Technical Report (II)* submitted to the Defense Advanced Research Project Agency, September 1996.

3   T. G. Bifano, "Micromechanical arrays for macroscopic actuation of deformable mirrors", *Semi-annual Technical Report (III)* submitted to the Defense Advanced Research Project Agency, February 1997.

4   T. G. Bifano, "Micromechanical arrays for macroscopic actuation of deformable mirrors", *Semi-annual Technical Report (IV)* submitted to the Defense Advanced Research Project Agency, September 1997.

5   R. K. Mali, T. G. Bifano, N. Vandelli, and M. Horenstein, "Development of microelectromechanical deformable mirrors for phase modulation of light", *Opt. Eng.*, vol. 36, no. 3, pp. 542-548, February 1997.

6   T. G. Bifano, R. K. Mali, J. K. Dorton, J. Perreault, N. Vandelli, M. K. Horenstein, and D. Castanon, "Continuous-membrane surface-micromachined silicon deformable mirror", *Opt. Eng.*, vol. 36, no. 5, pp. 1354-1360, May 1997.

7   M. A. Ealy, and J. A. Wellman, "Deformable mirrors: design fundamentals, key performance specifications, and parametric trades", *SPIE Active and Adaptive Optical Components*, vol. 1543, pp. 36-51, 1991.

8   R. K. Tyson, *Principles of Adaptive Optics*, San Diego: Academic Press, 1991.

9   A. P. Lee, S. Lehew, C. Yu, D. Ciarlo, E. Schmidt, and M. A. Northrup, "Selective Au-Si bonding for Si-based MEMS applications", in *Proceedings of the Third International Symposium on Semiconductor Wafer Bonding: Physics and Applications, Electrochemical Society Proceedings*, vol. 95-7, pp. 518-527, 1995.

10   M. B. Cohn, Y. Liang, R. Y. Howe, and A. P. Pisano, "Wafer-to-wafer transfer of microstructures for vacuum packaging", in *Proceedings of the Solid-State Sensor and Actuator Workshop, Hilton Head, SC*, pp. 32-35, June 1996.

11   A. P. Lee, D. R. Ciarlo, P. A. Krulevitch, S. Lehew, J. Trevino, and M. A. Northrup, "A practical microgripper by fine alignment, eutectic bonding and SMA actuation", in *Proceedings of the 8th International Conference on Solid-State Sensors and Actuators, and Eurosensors IX*, Stockholm, Sweden, pp. 368-371, June 1995.

12   R. F. Wolffenbuttel and K. D. Wise, "Low-temperature silicon wafer-to-wafer bonding using gold at eutectic temperature", *Sensors and Actuators*, A43, pp. 223-229, 1994.

13   *Pyralin® PD Polyimide Coatings: PI-2700 Processing Guidelines*, DuPont Photopolymer and Electronic Materials, Experimental Station 334/127, Wilmington, DE, 19880-0334.

14   C. W. Storment, D. A. Borkholder, V. Westerlind, J. W. Suh, N. I. Maluf, and G. T. Kovacs, "Flexible, dry-released process for aluminum electrostatic actuators", *Journal of Microelectromechanical Systems*, vol. 3, no. 3, pp. 90-96, September 1994.

15   A. B. Frazier, "Recent applications of polyimide to micromachining technology", *IEEE Transactions on Industrial Electronics*, vol. 42, no. 5, pp. 442-448, October 1995.

9. Other MEMS Devices

9.1 Chapter Overview

The course of any research effort presents many avenues for further exploration. That many of the world's greatest discoveries, penicillin to name but one, were happened upon while pursuing some other objective suggests that researchers must always remain open minded to such opportunities. While it is often not possible or advisable to explore these tangential research areas completely, it would be unwise to ignore them completely. In particular, the MEMS field is young enough that new devices, fabrication approaches, and applications are of interest. The goal of this chapter is to document some of the author's new MEMS devices in enough detail to perhaps inspire future research efforts.

Surface micromachined thermal conductivity pressure gauges are presented in Section 9.2. Several test structures specifically targeted at characterization of the MUMPs foundry process are presented in Section 9.3. Two new motion systems, a scratch drive actuated rotor, and a novel electrostatic cantilever motor structure, are described in Sections 9.4 and 9.5 respectively. Two new micro-relay designs developed by the author in support of another research effort are described in Section 9.6. Recommendations for future research for the devices presented are offered in Section 9.7.

9.2 Pressure Gauges

MEMS, particularly electrostatically actuated devices are susceptible to contamination from dust and moisture. In addition, the maximum frequency of moving micromechanical systems is limited by squeeze film damping when operated in air. For long life and maximum operation frequency micromirror systems may be packaged in a vacuum. To increase maximum optical power handling capability it may also be desirable to package micromirror systems in a gas media, such as helium, with increased thermal conductivity. Thermal conductivity pressure gauges that provide a means of non-destructively monitoring the ambient are an important feature for packaged micromirror systems. Although a number of thermal

conductivity pressure gauges have been developed for CMOS processes [1, 2, 3], a literature search did not find any pressure gauges fabricated in a surface micromachining process.

The author's examples of thermal conductivity pressure gauges, fabricated in the MUMPS surface micromachining process, are shown in Figure 9-1. Both examples shown employ 4 suspended polysilicon resistors in a Wheatstone bridge configuration, and a heater resistor in close proximity (1.5 - 3.0 μm) to one of the bridge resistors. To operate the gauge, current is applied to the heater resistor. The ohmically generated heat is coupled to the sense resistor by the thermal conductivity of the gas media in the gap, (and parasitically by the substrate attachments). Increasing temperature in the sense resistor causes an increase in its resistance. The change in sense resistance unbalances the bridge resulting in a differential voltage across the readout terminals.
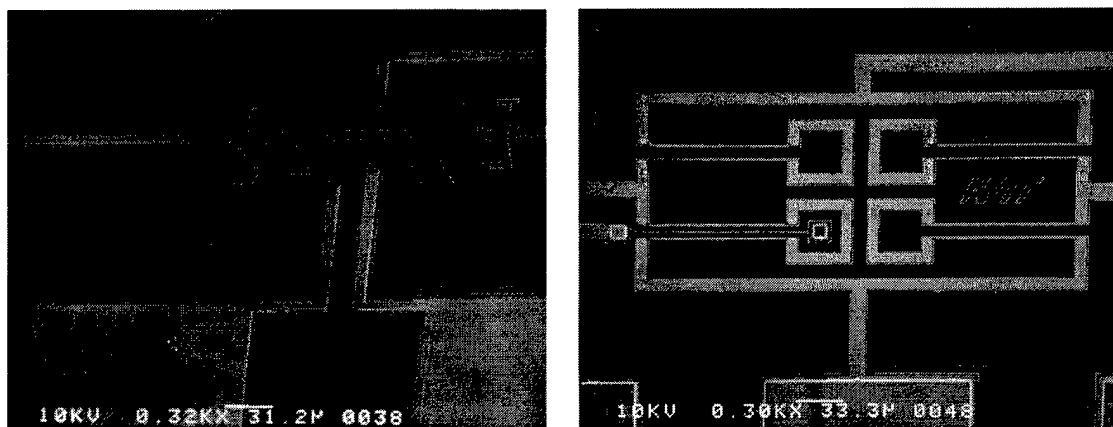
Figure 9-1. Surface micromachined thermal conductivity pressure gauges.

Proof-of-concept testing of a MUMPs 14 surface micromachined pressure gauges was performed using the simple apparatus shown in Figure 9-2(a). The test device was a VG1 type shown on the left side of Figure 9-1. The small aluminum vacuum chamber is sealed to the surface of a 144 PGA chip carrier package by a rubber O-ring. The aluminum housing was kept in place for both low and atmospheric pressure readings to eliminate any illumination effects. To simplify testing, an ohmmeter was used to measure the sense resistor value directly while the heater voltage was varied from 0 to 2.5 volts.

The raw test data plotted in Figure 9-2(b), shows that a surface micromachined polysilicon resistor structure can be used to sense vacuum. Sensitivity of the VG1 structure is not particularly good because the heater and sense resistors share a common ground wire and are thermally coupled by the mechanical connection. Improved pressure gauge designs were fabricated on MUMPs 16. An example of the improved design is shown in Figure 9-1(b). Note that the sense resistor has been segmented into two parts which surround the heater resistor, and the shared electrical/mechanical contact has been illuminated. There is still a mechanical-thermal connection of the heater and sense resistances through the substrate attachments. The revised designs should be substantially more sensitive but have not been tested.
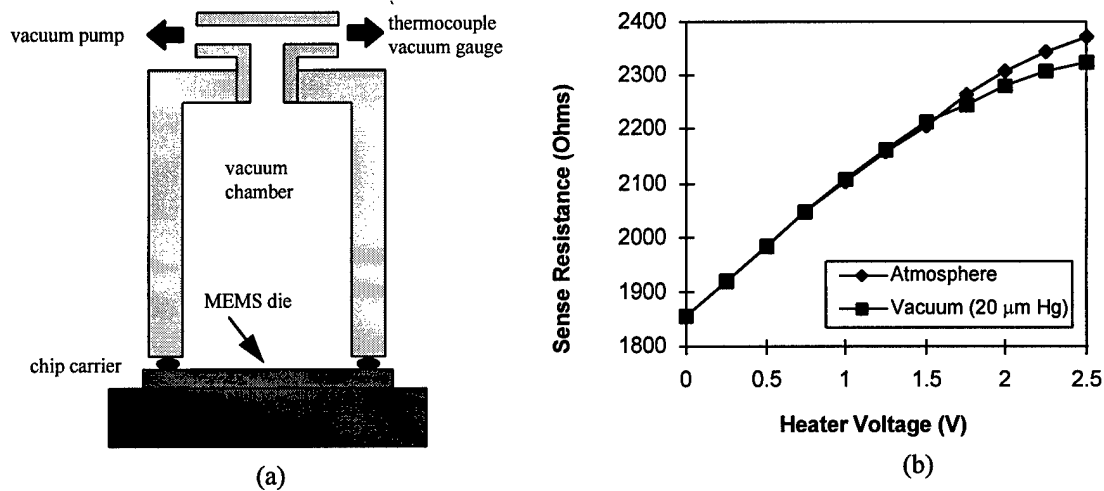
Figure 9-2. Vacuum gauge proof-of-concept test setup (a), and initial test data (b).

9.3 Test Structures

Despite extensive efforts by the MEMS community, design modeling of microelectromechanical structures is still limited by the control and measurement of the mechanical properties of MEMS materials. For the most part, "successful" MEMS models reported in the literature are obtained by adjusting the mechanical properties of the materials employed to force the structure model to reflect observed or measured device behavior. Until designer's can develop and model the behavior of microfabricated structures with the reasonable expectation that the fabricated device will perform as modeled, the full potential of MEMS will

not be realized. The author's study of stress-induced micromirror curvature (see Chapter 4), and experience with other foundry fabricated MEMS prompted an interest in test structures to characterize mechanical properties. For the most part these test structures were designed and fabricated but not extensively tested. The primary purpose of this section is to simply describe and state the availability of these test structures. Because the test structures are available on multiple test die over several MUMPs runs they could serve as the basis for a family detailed study of the mechanical properties of the materials used in the MUMPs process.

One common method of determining the residual stress of MEMS material layers is through use of fixed-fixed beam structures of various length [4-7]. Strain induced by residual material stress causes beams longer than the critical buckling length to deform. Beam buckling is most readily observed using an interferometric microscope, but optical and scanning microscopy work also. The beam buckling equation solved for length, L, is [6]

$$L = \sqrt{\frac{\pi^2 t^2 E}{3\sigma}} \qquad (9\text{-}1)$$

where t is beam thickness, σ is residual stress, and E is the elastic modulus of the material. Using Equation (9-1), the nominal thicknesses of MUMPs Poly1 (2.0 μm) and Poly2 (1.5 μm), E=169 GPa [8], and a stress range covering the reported MUMPs polysilicon values (2-20 MPa) arrays of beams were designed as stress monitors. Poly1 beams range from 310 μm to 1100 μm and Poly2 beams from 110 μm to 900 μm, both sets with 10 μm steps. All beams are nominally 10 μm wide. Buckling beam test structures were included on MUMPs 20 and 21, but were discontinued thereafter because they consume such a large die area. The observed critical buckling lengths for one MUMPs 20 die were 160 μm for Poly2, and <310 μm for Poly1 (all beams were buckled). The respective residual stresses computed are 46 MPa for Poly2 and >22 MPa for Poly1. The reported residual stress values for MUMPs 20 were 8(C) for Poly1 and 9(C) for Poly2. One possible explanation for the large discrepancy between wafer curvature measurements and buckled beam observations is stiction in the drying process after release.

Shown in Figure 9-3 is a variation of the buckled beam test structure with only 6 beams 250 µm to 500 µm in 50 µm increments. Also included in this test cell are parallel plate resonators with support beams of the same lengths and widths divided into four segments. Note that in this scanning electron micrograph all of the beams appear to be buckled and stuck down to the substrate but resonators are not. This suggests that stiction during the drying process caused the observed deformation of beams. Even though the total lengths of the overall resonators are longer (by the 100 µm plate width), protection dimples on the plate prevent pull down of the beams due to surface tension.

250-500 µm beams
stuck to substrate
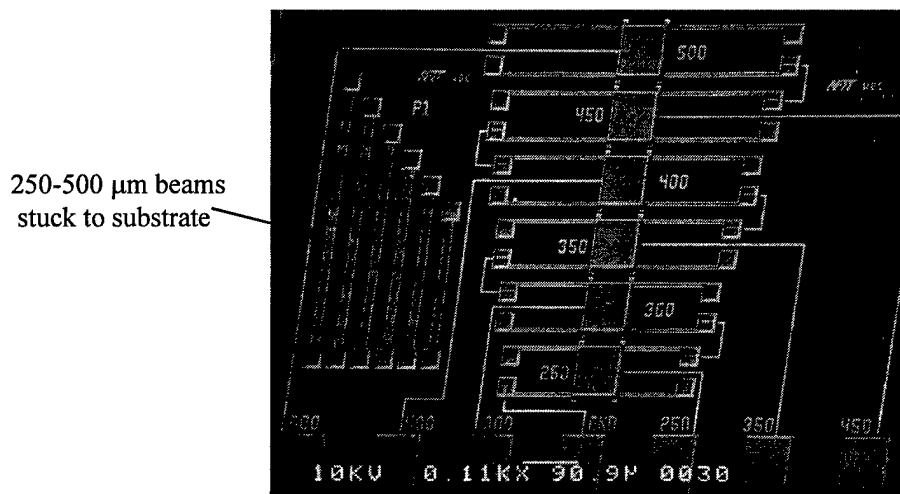
Figure 9-3. Buckled beam and resonator test structure. Note that beams are stuck to the substrate but resonators employing flexures of the same overall length are not.
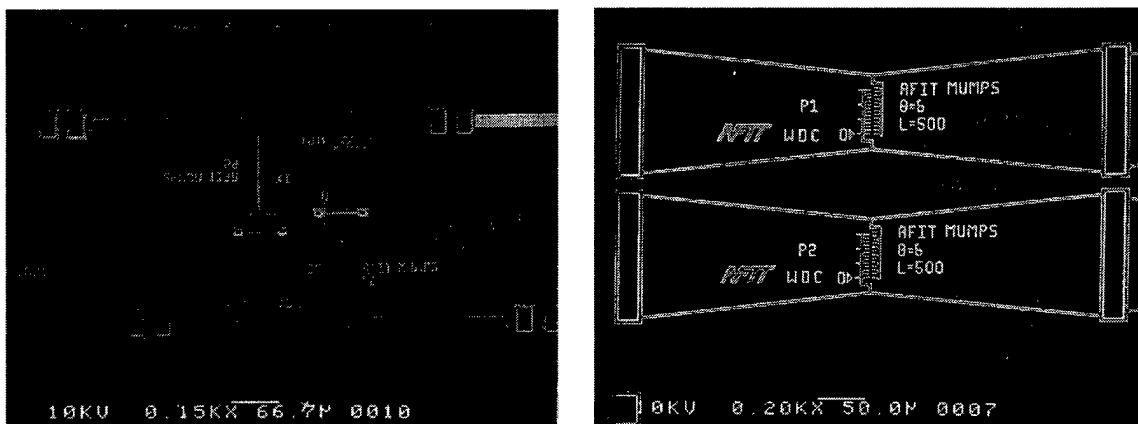
Figure 9-4. Gas-gauge and bow tie strain gauges fabricated in MUMPs.

Other micromechanical structures developed for stress measurement include "gas gauge" [9] and "bow tie" [10] structures. Examples of these strain measuring structures fabricated in the MUMPs process are shown in Figure 9-4. Both structures employ a vernier readout to obtain a deflection resolution of approximately 0.25 μm. No attempt was made to read either the gas gauge or bow tie structures because of stiction problems. Stiction can be avoided by making vernier readings on an optical microscope while the test structures are still immersed in deionized water.

Cantilever beams have been used to measure stress gradients in MEMS material layers [11]. Taking this concept a step further, a series of cantilever beams comprised of varying MUMPs layers were designed. With appropriate analytical models to predict the deflection of cantilevers with 1, 2, 3 and 4 material layers it should be possible to extract the residual stresses of each layer. This test structure is very compact (430 μm × 275 μm) when compared to other stress/strain test structures, and has been included on almost all of the author's MUMPs die since MUMPs 18. Measurement of cantilever deflection is best accomplished using an interferometric microscope.
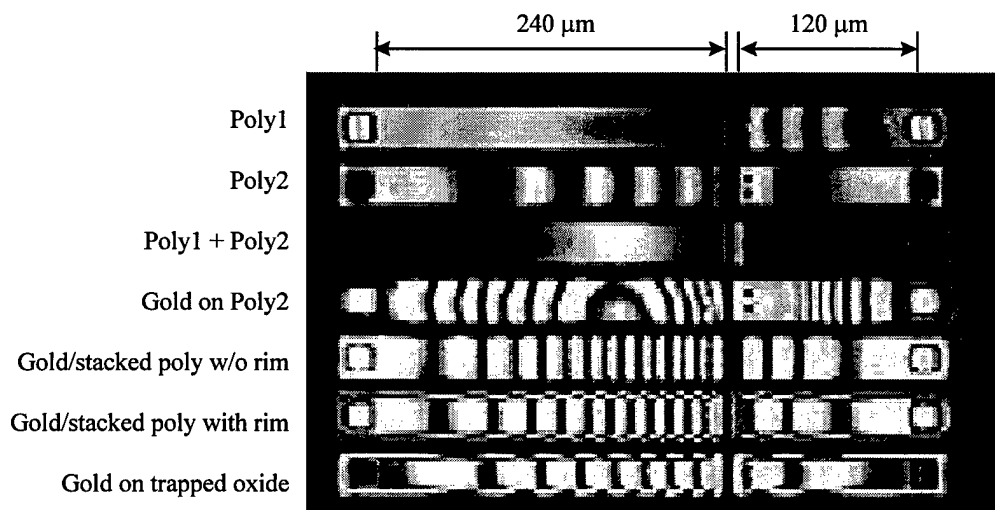
Figure 9-5. Interferometric microscope image of MUMPs stress test structure comprised of single and multi-layer cantilevers.

Shown in Figure 9-5 is an annotated image captured from the Zygo interferometric microscope video display of the stress cantilever test structure on a MUMPs 19 die. At a glance the interferometric image qualitatively tells much about the process. Note that the short Poly1, long Poly2, and long gold on

Poly2 cantilevers are stuck to the substrate. The single layer polysilicon cantilevers both show stress gradients, particularly the short Poly2 cantilever. Stacking of the polysilicon layers results in a more curved structure than Poly1 only, but much less curved than Poly2 only. The metal stress is high enough to cause substantial curvature of released polysilicon structures, for example micromirrors. Although simultaneous solution of the multi-layer cantilever equations remains as a mechanical analysis and computer programming problem, the multi-layer cantilever test structure is promising in its simplicity and compactness. For comparison, the multi-layer cantilever test structure is almost the same size as the comb structure included by MCNC on the corner of every MUMPs die. The comb structure provides only a means of monitoring the Poly1 layer whereas the stress cantilevers can conceivably be used to extract the residual stress of all releasable layers.

If the proceeding test structure paragraphs lead the reader to conclude that there are still research opportunities in understanding MUMPs and other surface micromachining processes, this paragraph will certainly reinforce that notion. AFIT researchers and others [12] have noted an uneven thinning of MUMPs polysilicon structures that exhibits a dependence on the amount of gold to which the structure is mechanically and electrically connected. This phenomenon is most easily observed on Poly0 structures which appear an uneven brownish color when viewed with an optical microscope. The author's most dramatic observation of the thinning effect occurred while viewing a partially wirebonded, then released, MUMPs 17 thermal piston micromirror array (Figure 6-7) on the Zygo interferometric microscope. The Poly1 legs of every device which had a gold bond wire attached to it were deformed and the mirror plate stuck to the substrate, while adjacent devices without bond wires were not. Subsequent to this observation, all packaged devices were released before wirebonding. In new MUMPs designs, bond pad size was reduced, and unnecessary gold metallization eliminated. The observed dependence of polysilicon thinning on electrical connection to a gold surface suggests an electrochemical process. The brown-red color of effected Poly0 structures may be indicative of porous silicon formation which is a photoelectrochemical process [13, 14]. An attempt to verify porous silicon formation by stimulation of photoluminescence with

a UV lamp was unsuccessful. Identical MUMPs die were released with an without laboratory lighting to determine if illumination was a contributing factor but results of this experiment were inconclusive.

Because the as-fabricated dimensions of micromechanical structures are critical for extraction of material properties, it is imperative that electrochemical etching be eliminated or quantified for metrology specimens. To support research efforts into the electrochemical etch phenomenon the two test cells shown in Figure 9-6 were developed. One test cell is comprised of four otherwise identical parallel plate actuators that are attached to gold metallized pads of varying area. Resonant frequency measurements will allow extraction of Poly1 flexure cross-sectional area. Similarly, the gold/Poly2 cantilever structures in the other test structure are connected to gold pads of varying area. Cantilever deflection can be measured precisely with an interferometric microscope. Neither of these test structures have yet been measured, so it is unknown if they will be sensitive enough to quantify electrochemical etch rates.
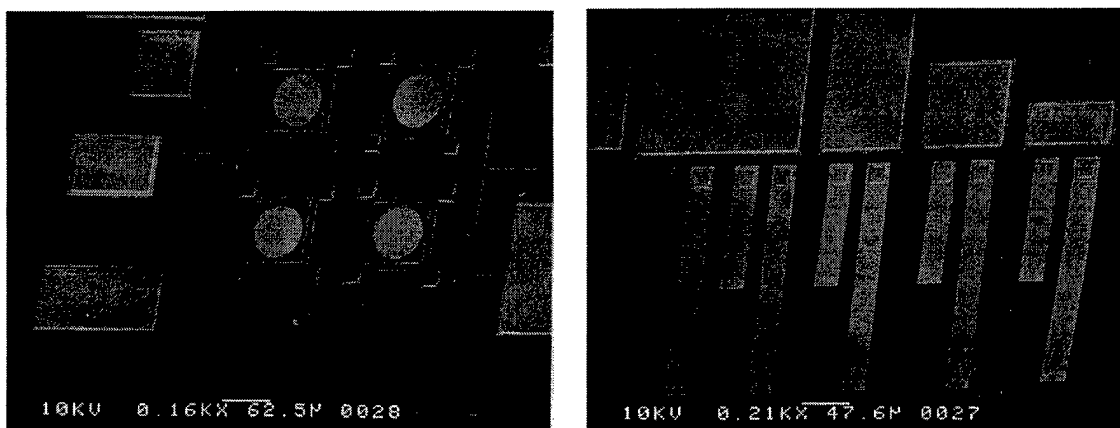
Figure 9-6. MUMPs electrochemical etching test structures.

9.4 Scratch Drive Actuated Rotors

Electrostatic scratch drive actuators (SDAs) provide high force (up to 63 μN) with low drive power [15, 16, 17]. The scratch drive actuator operating principle, and a novel scratch drive actuated rotor structure are illustrated in Figure 9-7. The actuator structure is simply a conductive plate with a protruding bushing

at one end. When sufficient voltage is applied across the plate and ground electrode, electrostatic force pulls the plate down into contact with the dielectric isolation layer. The bushing at the front edge of the plate prevents the whole plate from attaching to the substrate so the plate warps as shown. The warping of the plate causes the bushing to kick forward. As voltage is released and the plate begins to detach from the substrate the elastic strain energy stored in the plate slides the rear of the plate forward. The step size, dx, is a function of peak voltage, plate length, and bushing height [15].
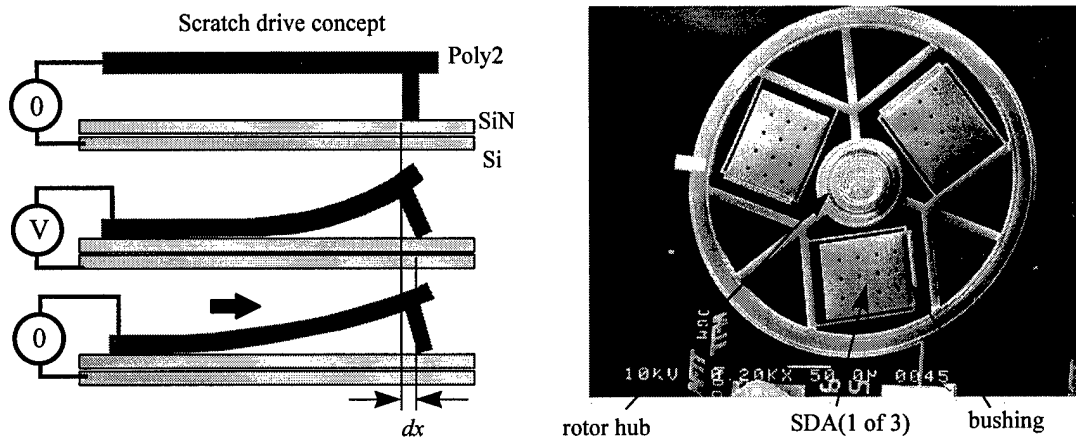
Figure 9-7. Scratch drive actuator operating principle, and scanning electron micrograph of prototype scratch drive actuated rotor on MUMPs 20.

By construction, SDAs exhibit unidirectional lateral motion. Typically, flexures are employed to return SDA structures to a nominal rest position when the drive voltage is released. The innovative SDA rotor structure shown in Figure 9-7 represents the author's attempt to harness the high force and small step size of scratch drive in a structure that can run continuously. Bushing height is maximized by stacking the MUMPs Poly1-Poly2 via etch and Dimple etch. The SDA plates are 125 μm long and 100 μm wide. The overall rotor structure is ~460 μm in diameter. Electrical contact to the SDAs is made through dimples in the outer ring of the rotor to an underlying ring of Poly0, which is wired to a bond pad.

SDA rotors were tested in air on the Zygo interferometric microscope. A single transistor switching circuit was used to apply a square pulse drive signal with a maximum amplitude of ~100 V. Figure 9-8 is an interferometric microscope image captured from video of the SDA rotor in operation. Of

note on this particular device is a substrate defect at least 316 nm high which the SDAs successfully ride over. The SDA rotors tested in air were not long lived. The "best" device lasted for a little over 2 revolutions before stopping. Data for this device was extracted from the video and is listed in Table 9-1. Using a mean value of 13.5 seconds per quarter turn, and the 130 μm distance to the center of the SDAs, the rate of travel for the SDAs is 15.1 μm/second. With the 1 kHz drive signal, the corresponding observed step size is 15.1 nm. The total distance traveled by the center of the actuators is approximately 1.63 mm for 2 revolutions.

fringe lines caused
by substrate protrusion
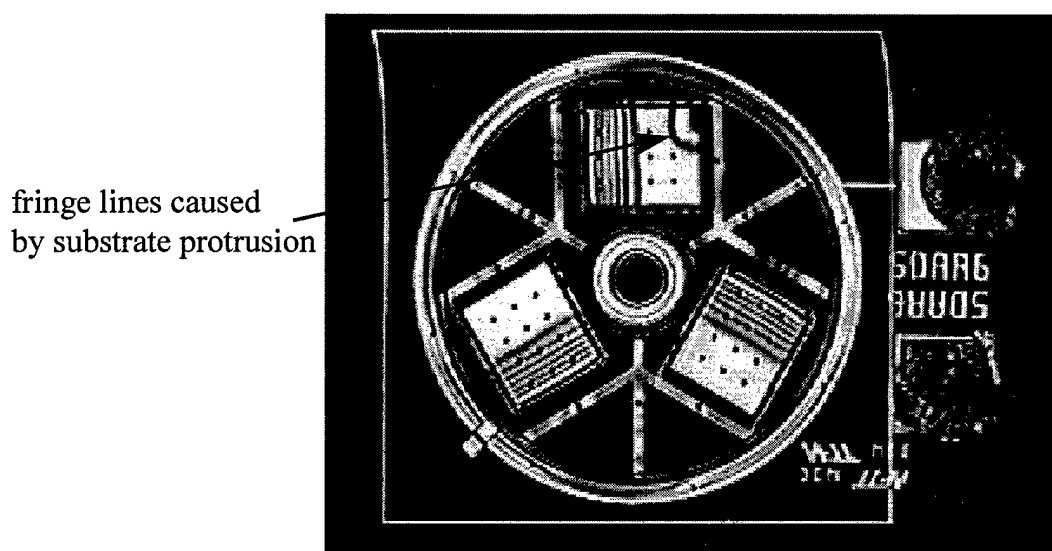
Figure 9-8. Interferometric microscope image of scratch drive actuated rotor in operation.

Table 9-1. Scratch Drive Rotor Data from Videotape

Quarter turns	Time (seconds)	Time per quarter turn (seconds)
0	0	N/A
1	13	13
2	26	13
3	39	13
4	51	12
5	65	14
6	79	14
7	93	14
8	111	18 (sticking observed)

The failure mechanism for SDA rotors remains to be determined. Charge buildup in the silicon nitride layer is contraindicated because the actuators are observed to continue to deform in the same manner as when the device is rotating. SDA rotors that operated, then stopped, were probed to free the rotors. Subsequently the freed SDA rotors operated properly. This suggests that the failure mechanism is friction. The three friction interfaces of the SDA rotor, (rotor hub, rotor dimples, and SDA/substrate), make this structure an interesting candidate for tribology studies.

9.5 Electrostatic Cantilever Motor

As mentioned in Chapter 2, MEMS designs for surface micromachining processes are limited to two primary actuation mechanisms, electrostatic and thermal. While the preceding section demonstrates a novel means of generating rotary motion using electrostatically driven scratch drive actuators, this section presents a new type of electrostatic motor with lateral motion output. Electrostatic and thermal motors in general exhibit complementary characteristics. Electrostatic comb drive motors exhibit relatively low force and small lateral deflection but can operate at high frequency and dissipate little power [18]. Thermally actuated motors exhibit higher force, and larger lateral deflection, but power dissipation is high and the operating frequency is limited by heat dissipation [19]. Force is limited in electrostatic comb drive motors by the overlapping area of the fingers. In surface micromachining processes, where mechanical layer thickness is small (typically 1-3 μm), sufficient overlap area requires large comb structures. Much of the die real estate consumed by a comb drive structure does not contribute to the force generated. Conversely, for parallel-plate or cantilever structures, almost all of the device footprint is consumed by the electrodes, so greater force can be generated in the same device area. Although high electrostatic forces can be generated with surface micromachined parallel plate structures, the deflection range if defined by a sacrificial layer thickness, is vertical and small (1-2 μm). Vertical parallel plate structures can be fabricated in surface micromachining processes but typically require manual assembly [20].

The unique electrostatic cantilever motor structure depicted in Figure 9-9 provides large electrode area (hence large force), and a reciprocating lateral output of 10 μm. A large electrostatically actuated

metal stress cantilever serves as the fundamental drive mechanism. When released the cantilever motor self-assembles. A link arm, attached to the cantilever tip and lateral output slider by floating hinges, converts the vertical deflection of the cantilever tip to lateral motion. The floating hinges are a novel design that exhibit less "slop" than scissors hinges [21]. Not visible in the scanning electron micrograph of the prototype electrostatic cantilever motor in Figure 9-9 is an opening in the Poly0 ground plane beneath the cantilever. The motor is driven by applying voltage between the visible structure and the conductive substrate.
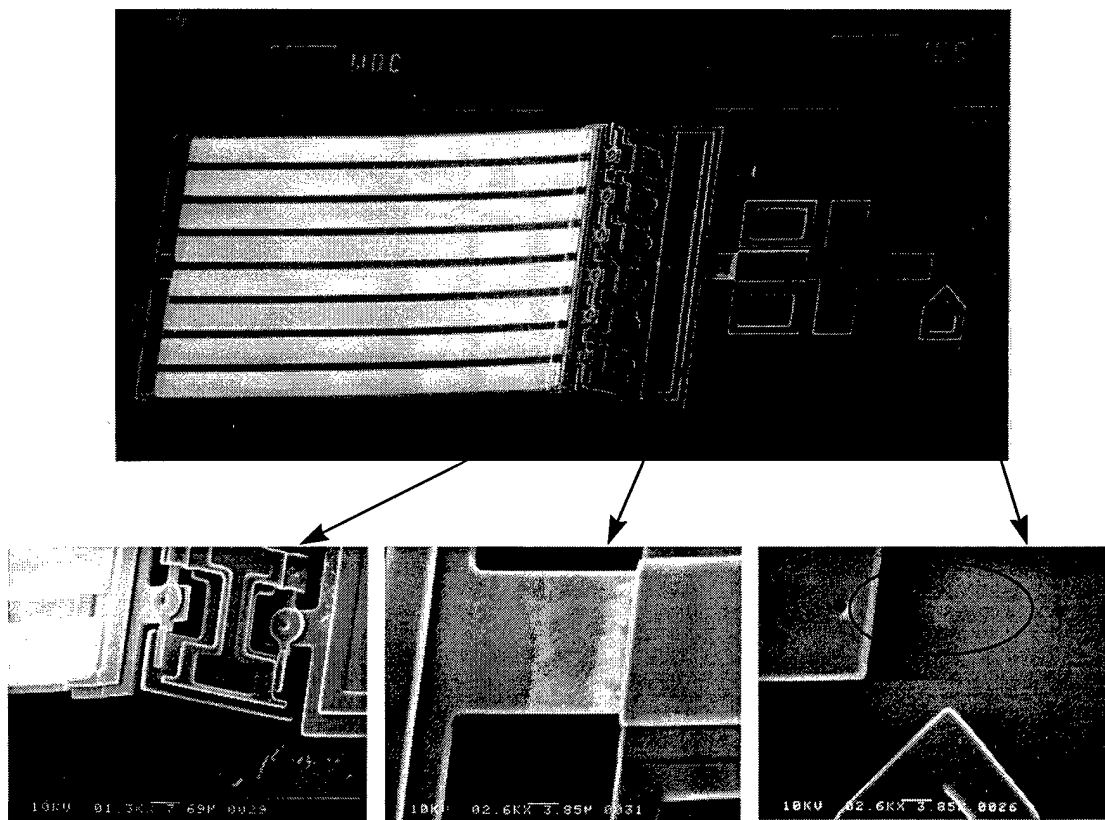
Figure 9-9. MUMPs 21 electrostatic cantilever motor with lateral output after ~500,000 cycles. Whole device is shown on top. From left to right on bottom; link arm attached to cantilever tip by novel floating hinges, worn lateral output slider, and dimple wear at motor tip. The stress cantilever is 350 μm $\times$ 196 μm.

Testing of initial prototype electrostatic cantilever motors was performed in air under the Zygo interferometric microscope. A switching transistor circuit was used to apply a nominal 0-100V square

pulse. Lateral tip motion was measured using the microscope cursor functions and varied for several motors from 9-13 μm. The frequency of the drive signal was varied from DC to over 1 kHz. An image captured from interferometric microscope video of tip motion at 100 Hz is shown in Figure 9-10. Up to 500 Hz, there was no observable change in the lateral output. At frequencies greater than 500 Hz blurring of the video image prevented measurement of the lateral motion, but it is expected that squeeze film damping will limit the operating frequency in air.

As a longevity test, a previously exercised electrostatic cantilever motor was run continuously at 100 Hz for over an hour. The device was still functioning with 10 μm lateral output motion when testing was stopped. The number of total cycles for the device is conservatively estimated at over 500,000. The wear shown in Figure 9-9 makes this device attractive for tribology studies, and suggests several design improvements. The tip deflection of the cantilever can be limited by stops to prevent lifting of the slider assembly. This would prevent the friction and wear observed on the top of the lateral output slider bar. Alternatively the pulse drive waveform can be modified to switch between a nonzero value corresponding to the lateral slider pulled back but not lifted from the substrate, and the cantilever pull down voltage.
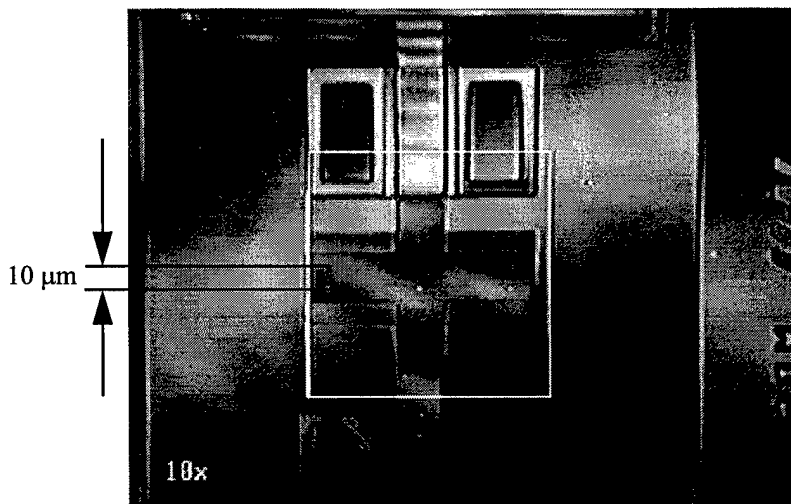
Figure 9-10. Lateral output of electrostatic cantilever motor operating at 100 Hz in air, with ~100 V square pulse drive signal.

9.6 Switches

Arguably, the first reported microfabricated electromechanical switches were implemented as part of a threshold accelerometer in 1972 [22]. In the 25 years since that effort, micro-switches and micro-relays have been, and continue to be the subject of much MEMS research. This is not surprising when one considers the simple mechanical structure of a switch and the innumerable potential applications. Among the desirable characteristics for a "good" micro-relay are high off resistance, low on resistance, low power dissipation, and electrical isolation of the control and signal circuits. These characteristics are straightforward to obtain in specially developed micromachining processes, but can be more difficult in available foundry processes. Design of micro-switches or micro-relays in the MUMPs surface micromachining foundry process is complicated by the lack of a releasable dielectric layer, and by the single metal layer. Without a releasable dielectric layer it is impossible to isolate the signal and control circuits. Previous AFIT switch research has shown that polysilicon to polysilicon contacts exhibit high resistance (10s to 100s of kΩ), most likely due to native oxide on the polysilicon surfaces [23, 24]. Because the MUMPs gold layer can only be deposited on Poly2 surfaces, a flip over structure is required to obtain low contact resistance with metal to metal contacts. The following designs independently address the isolation and contact resistance problems. Combining the concepts will yield a low resistance switch with isolated control and signal circuits.

The micro-relay structure shown in Figure 9-11 employs a MUMPs fabricated structure to which a dielectric layer was added by post-foundry processing. The process developed to add the polyimide (DuPont PI-2721) was intentionally designed to be simple. After stripping the protective shipping photoresist from the MUMPs die, a 10 second hydrofluoric acid etch removes oxide from the polysilicon structures without significant undercutting. The photosensitive polyimide was spun on and patterned to selectively attach the Poly2 contact bars to the Poly1 actuator top plates. After post-baking the polyimide (200 °C for 2 hours), the release etch was completed. The resulting dielectric mechanical attachment is identified in Figure 9-11. Polyimide posts were added to only 2 sample die and no attempt was made to optimize the polyimide process. A large increase in actuation voltage observed for post processed devices

was traced to polyimide residue between the plates [24]. Longer polyimide develop and rinse times would eliminate the residue problem. Most importantly, probing of the devices showed that the polyimide posts provide a strong mechanical connection.
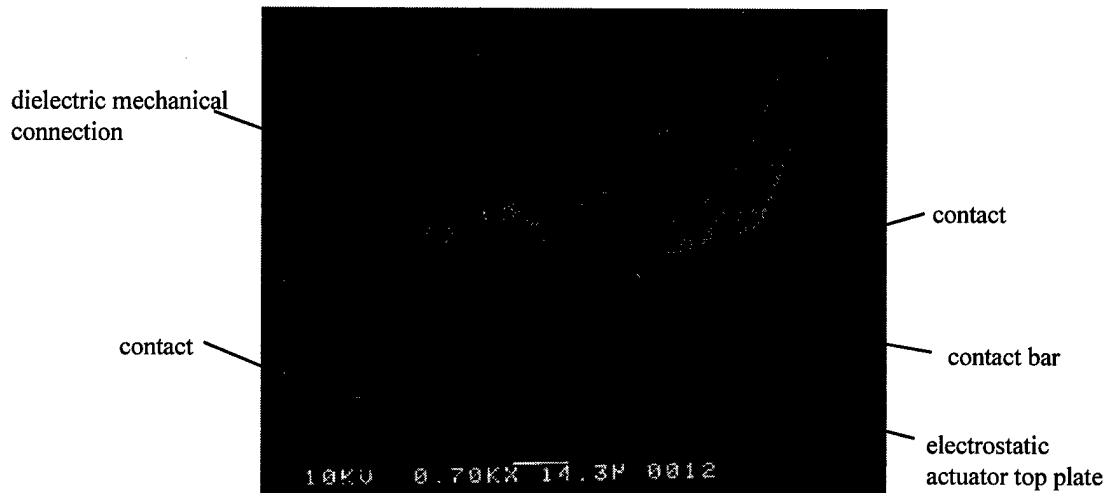
Figure 9-11. Surface micromachined switch with polyimide mechanical connection of contact bar and parallel-plate electrostatic actuator.
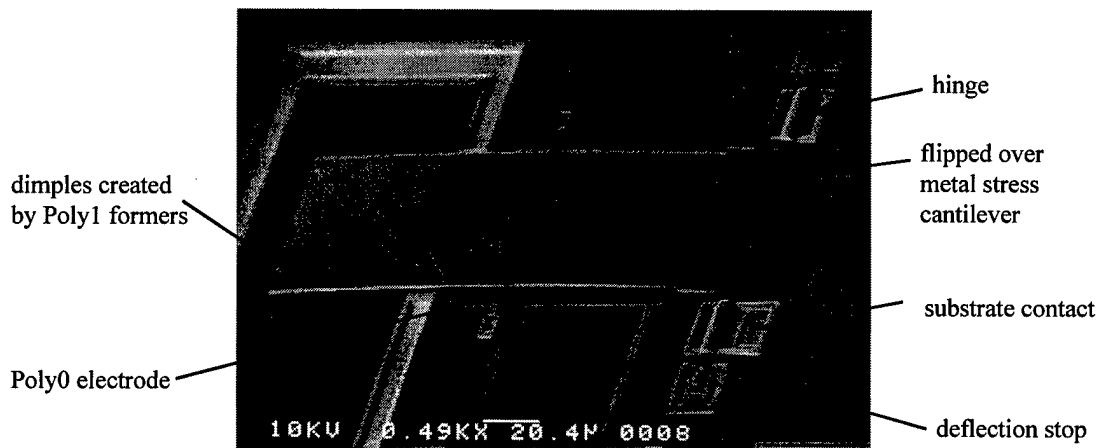
Figure 9-12. Electrostatic micro-relay with metal to metal contacts fabricated in MUMPs.

The electrostatic micro-relay structure shown in Figure 9-12 is yet another structure which exploits the otherwise undesirable residual tensile stress of the MUMPs metal layer. A gold/Poly2 metal

stress cantilever is attached to the substrate by hinges. After release, the cantilever is flipped over to obtain metal to metal contacts for the micro-relay. The curved shape of the cantilever establishes the gap between the contactor and switch contacts. The cantilever is grounded through a substrate contact. Application of a potential to the Poly0 electrode pulls the cantilever down, flattens the curved shape, and closes the switch contacts. Cantilever tip contact with the substrate is limited by dimples created by Poly1 formers which are not visible in the figure. A Poly1 bar over the electrode stops deflection of the cantilever and prevents shorting of the electrostatic electrodes.

In limited testing [24], prototype micro-relays of the type shown in Figure 9-12 exhibit reasonably good switch characteristics. Measurements from four test devices with 270 μm $\times$ 60 μm cantilevers yield a mean contact resistance of 40 Ω, with a mean actuation voltage of 121.5 V. The two raised gold contact surfaces are 14 μm $\times$ 16 μm. Devices were successfully switched at over 100 kHz. After several million switching cycles the contact resistance of a single device was observed to increase by 10 Ω, and the required actuation voltage increased by 8 volts.

9.7 Conclusions and Recommendations

The devices described in this chapter are all deserving of further research effort. The surface micromachined thermal conductivity pressure sensors require further characterization testing. Development and validation of a thermal circuit model would be straightforward and especially useful. The simplicity of the pressure gauge structure developed makes it applicable to other MEMS materials. The only material requirements are means of generating heat and sensing temperature. Detailed study and analysis of the test structures described in Section 9.4 could be a dissertation research effort in itself. Both the scratch drive actuated rotor and electrostatic cantilever motor designs require further study and refinement. The observed friction effects and wear makes both devices interesting test structures for tribology studies. As a first step, both systems should be operated in a controlled low pressure ambient environment to eliminate squeeze film damping. The combined switch developments suggest that good micro-relays can be fabricated using the MUMPs foundry and a post-foundry dielectric mechanical layer.

References

1   B. C. S. Chou, Y-. M. Chen, M. Ou-Yang, and J-. S. Shie, "A sensitive vacuum sensor and the electrothermal SPICE modelling", *Sensors and Actuators*, A53, pp. 273-277, 1996.

2   E. H. Klaassen and G. T. A. Kovacs, "Integrated thermal conductivity vacuum sensor", in *Proceedings of the Solid-State Sensor and Actuator Workshop*, Hilton Head, SC, pp. 249-252, June 1996.

3   G. H. Chapman, N. Sawadsky, and P. P. S. Juneja, "Phase sensitive techniques applied to a micromachined vacuum sensor", *SPIE*, Vol. 2882, pp. 266-277, 1996.

4   H. Guckel, T. Randazzo, and D. W. Burns, "A simple technique for the determination of mechanical strain in thin films with applications to polysilicon", *J. Appl. Phys.*, Vol. 57, No. 5, pp. 1671-1675, March 1985.

5   H. Guckel, D. Burns, C. Rutigliano, E. Lovell, and B. Choi, "Diagnostic microstructures for the measurement of intrinsic strain in thin films", *J. Micromech. Microeng.*, Vol. 2, pp. 86-95, 1992.

6   W. Fang and J. A. Wickert, "Post buckling of micromachined beams", *J. Micromech. Microeng.*, Vol. 4, pp. 116-122, 1994.

7   J. C. Marshall, D. T. Read, and M. Gaitan, "Analysis of fixed-fixed beam test structures", *SPIE*, Vol. 2880, pp. 46-55, October, 1996.

8   W. N. Sharpe, B. Yaun, and R. L. Edwards, "A new technique for measuring the mechanical properties of thin films", *IEEE Journal of Microelectromechanical Systems*, Vol. 3, No. 3, pp. 193-199, September, 1997.

9   B. P. van Drieenhuizen, J. F. L. Goosen, P. J. French, and R. F. Wolffenbuttel, "Comparison of techniques for measuring both compressive and tensile stress in thin films", *Sensors and Actuators*, A 37-38, pp. 756-765, 1993.

10   Y. B. Gianchandani and K. Najafi, "Bent-beam strain sensors", *IEEE Journal of Microelectromechanical Systems*, Vol. 5, No. 1, pp. 52-58, March, 1996.

11   E. Obermier, "Mechanical and thermophysical properties of thin film materials for MEMS: techniques and devices", *Mat. Res. Soc. Symp. Proc.*, Vol. 444, pp. 39-57, 1997.

12   D. A. Koester, Microelectronics Center of North Carolina, Private communication, 1996.

13   M. Madou, *Fundamentals of Microfabrication*, CRC Press, Boca Raton, FL, 1997.

14   P. Langlet, L. Zhang, and J. St. John, "Strategies toward the development of integrated chemical sensors fabricated from light emitting porous silicon", *SPIE*, Vol. 3226, pp. 168-179, September 1997.

15   T. Akiyama, D. Collard, and H. Fujita, "Scratch drive actuator with mechanical links for assembly of three-dimensional MEMS", *IEEE Journal of Microelectromechanical Systems*, Vol. 6, No. 1, March 1997.

16   T. Akiyama and H. Fujita, "A quantitative analysis of scratch drive actuator using buckling motion", in *Proc. IEEE Microelectromechanical Systems*, pp. 310-315, Amsterdam, The Netherlands, February, 1995.

17   P. Langlet, D. Collard, T. Akiyama, and H. Fujita, "A qualitative analysis of scratch drive actuation for integrated X/Y motion system", *Transducers '97, International Conference on Solid-State Sensors and Actuators*, pp. 773-776, June 1997.

18   J. J. Sniegowski, S. L. Miller, G. F. LaVigne, M. Steven Rodgers, and P. J. McWhorter, "Monolithic geared-mechanisms driven by a polysilicon surface-micromachined on-chip electrostatic microengine", *Proceedings of the Solid-State Sensor and Actuator Workshop*, Hilton Head, SC, pp. 178-182, June 1996.

19   J. H. Comtois and V. M. Bright, "Applications for surface-micromachined polysilicon thermal actuators and arrays", *Sensors and Actuators*, A 58, pp. 19-25, 1997.

20   P. B. Chu, P. R. Nelson, M. L. Tachiki, and K. S. J. Pister, "Dynamics of polysilicon parallel plate electrostatic actuators", *Sensors and Actuators*, A 52, pp. 216-220, 1996.

21   D. E. Sene, "Design, fabrication and characterization of micro opto-electro-mechanical systems", *Master's Thesis*, Air Force Institute of Technology, AFIT/ GEO/ENP/95D-03, December 1995.

22   W. D. Frobenius, S. A. Zeitman, M. H. White, D. D. O'Sullivan, and R. G. Hamel, "Microminiature ganged threshold accelerometers compatible with integrated circuit technology", *IEEE Trans. Electron Devices*, Vol. ED-19, pp. 37, 1972.

23   M. Phipps, "Design and development of microswitches for micro-electromechanical relay matrices", *Master's Thesis*, Air Force Institute of Technology, AFIT/GE/ENG/95J-02, June 1995.

24   G. Kading, "Micro-electromechanical switches for micro-satellite power transfer", *Master's Thesis*, Air Force Institute of Technology, AFIT/GCS/ENG/95D-11, December, 1997.

10. Conclusions

10.1 Contribution and Significance

The primary contribution of this research effort is the development and successful demonstration of low cost microfabricated deformable mirrors for adaptive optics. The author's experimental aberration correction and beam steering results show the potential of foundry microfabricated MEM-DMs. The principle benefits of microfabrication are reduced manufacturing cost, and elimination of expensive characterization testing. Additional microfabrication benefits are the reduced size, weight, and power consumption of MEM-DMs. *MEM-DMs are an enabling technology for many new adaptive optics applications.*

The manufactured cost of the 128 element MUMPs prototype mirrors designed by the author is about $200. Packaging and release etching adds another $50, excluding the author's labor. Because the elements are uniform, and fit the analytic deflection model well, characterization testing of a single element is sufficient. Once set up on the interferometric microscope, the author's static fringe characterization test requires only a few minutes. Thus, testing does not significantly increase the "ready to operate" MEM-DM cost. The prototype MEM-DMs at about $2 per element or less, compare very favorably to conventionally manufactured deformable mirrors with a typical cost of $1000 per channel.

The foundry surface micromachining approach employed in this research effort is particularly appropriate for low cost fabrication of prototype deformable mirror systems. Until sufficiently large numbers of MEM-DMs are required, it is difficult to justify the expense of microfabrication process development. Design of practical foundry microfabricated deformable mirrors is straightforward, but must include the constraints of the micromachining process. The author's devices, fabricated primarily in an inexpensive foundry surface micromachining process (MUMPs), exhibit high yield and good deflection uniformity. Without quantitative testing of deflection uniformity, micromirror arrays were characterized using the author's static fringe measurement technique, and then used in a testbed adaptive optics system.

The excellent optical testbed results, and the agreement of those results with theoretical simulations, prove that practical MEM-DMs can be fabricated in foundry processes if properly designed. The lessons learned designing and testing deformable mirrors fabricated in the MUMPs and SUMMiT foundry processes apply directly to any microfabrication approach. Other microfabrication approaches include different foundry processes, extensions to foundry processes, and even processes developed specifically for MEM-DM fabrication.

10.2 Accomplishments

Adaptive optics testbed work concentrated on segmented MEM-DMs primarily because these devices exhibit the greatest potential for low cost adaptive optics systems. Together, the demonstrations of defocus aberration correction, and beam steering suggest the use of segmented MEM-DMs as a single correcting element. Segmented MEM-DMs employing the modulo $\lambda/2$ deflection scheme can simultaneously correct both first order (tip-tilt) aberrations and higher order aberrations. This capability has been demonstrated in the testbed by applying a MEM-DM figure which both corrects a defocus aberration, and shifts the central lobe of the far-field pattern. By eliminating the requirement for a separate tracking sensor and tip-tilt mirror, a compact bare-bones adaptive optics system comprised of a single wavefront sensor, segmented MEM-DM, a few interfacing optics, and PC controller can easily be envisioned. The testbed demonstration of multiple beam steering shows that a segmented MEM-DM can be used to create and steer multiple laser beams. Possible applications include creation of multiple laser beacons for adaptive optics, communication systems, laser radar, and targeting systems.

A lenslet array can be used to improve the fill-factor of a segmented MEMS deformable mirror. A hybrid refractive lenslet/MEM-DM correcting element was experimentally demonstrated in both aberration correction and beam steering applications. The analytical model developed to explain the behavior of the hybrid lenslet/MEM-DM correcting element shows good agreement with the experimental results. Lenslet use simplifies MEM-DM design, but incurs an additional optical design burden. The analysis applied in development of the lenslet/MEM-DM model provides design guidelines for future

systems employing lenslets. The added complexity and cost of lenslets should be avoided whenever possible. Lenslets may be particularly useful for beam projection applications where a non-varying wavefront is incident on the correcting element. A simple thermal circuit model for estimating the optical power handling of the lenslet MEM-DM was developed. Maximum optical power handling estimates from this model are encouraging. The optical power model developed for the lenslet micromirror array is also applicable to micromirror systems which do not employ lenslets.

A new class of piston micromirrors (or actuators) employing direct digital deflection control was devised and tested. This new control scheme further reduces adaptive optics system cost and complexity by eliminating digital-to-analog converters in the deformable mirror control system. A prototype digital deflection system with 21 active elements is currently operating in the laboratory. A wirewrap breadboard logic circuit interfaces the digital deflection micromirror chip to a PC parallel port. The total parts cost for the 21 element breadboard system, including a packaged deformable mirror, is a paltry $152. The simplified control circuitry of the digital deflection scheme paves the way for integration of piston micromirror elements and control circuitry on a single monolithically fabricated chip. Although the number of mirrors, and the number of control bits, of prototype systems to date have been limited by the process and packaging concerns, integrated embodiments will not suffer those same limitations. When one considers the number of wires and transistors in a modern microprocessor, it is easy to envision development of an integrated digital deflection deformable mirror system on a chip with upwards of a thousand individually controlled elements.

The optical quality, or surface figure, of micromirror elements was extensively studied. Prior micromirror characterization work neglected this critically important factor. The degraded optical performance of micromirror arrays with stress-induced mirror curvature and print-through topography was experimentally verified. The optical performance data collected yields two key observations. First, optical power efficiency (or as-drawn fill-factor) is not a good measure of imaging performance. Second, control of mirror surface quality is the most important factor in fabricating piston micromirror arrays. It was shown that commercially available MEMS computer aided design software can be used to model metal

stress induced mirror curvature. Computer aided design tools, and good stress characterization data will be required to optimize micromirror array designs. Post-foundry metallization techniques using a maskless sputtered chromium/gold metallization were shown to preserve and even improve the flatness of micromirror elements. Application of a tailored final reflective surface metallization is a viable manufacturing approach for high quality piston micromirror arrays.

The first two-dimensional thermally actuated piston micromirror arrays were designed and tested. Prior to this work, pure piston motion had not been quantitatively demonstrated with thermal devices. Tilt-free piston travel is insured by preserving thermal symmetry in the device structure. Models were developed to analyze the electro-thermal device behavior. The MEMS computer aided design tools currently being developed model the electrical, thermal, and mechanical behavior of thermal piston micromirror structures. Validation of complete electrical-thermal-mechanical models will facilitate system design and optimization efforts. Future research should focus on reducing device power dissipation which may be a limiting factor for large arrays of thermally actuated devices.

In addition to microfabricated deformable mirrors, a number of other MEMS devices were developed and functionally tested. Tip-tilt mirror systems employing vertical thermal actuators and metal stress cantilevers to increase the maximum steering angles demonstrate the potential of surface micromachined beam steering mirrors. The author's experimental results represent the first quantitative data showing that backbending of surface micromachined polysilicon actuators is predictable and repeatable. Although metal stress cantilevers have been used to some extent by other researchers, the author's employment of these devices for self-assembling microstructures is novel. The proof-of-concept demonstration of the surface micromachined thermal conductivity pressure sensor shows that this simple device can be fabricated in almost any microfabrication process. The author's scratch drive actuated rotor and novel electrostatic cantilever motor designs represent new prime movers for micromechanical systems and are interesting structures for tribology studies.

10.3 Recommendations for Future Research

The accomplishments of this research conclusively demonstrate that MEM-DMs, particularly segmented designs, are ready for application in adaptive optics systems. Consideration of potential near-term applications of MEM-DMs motivates the suggestions for future research efforts. Though each application will impose a unique set of requirements, several questions impact all potential uses and are therefore of more interest for basic research. These issues include device longevity, optical power handling and thermal characteristics, dynamic response, and closed-loop control.

The longevity of the prototype devices used in optical experiments was better than anticipated, but no effort was made to quantify the useful lifetime, or characterize device behavior after a period of time. All testing was conducted in air at room temperature. That the test devices functioned when required over a period of months in this uncontrolled environment is encouraging, but is anecdotal evidence at best. Detailed studies of MEM-DM longevity and performance in different ambient conditions are required.

Temperature excursions can be expected to alter device behavior somewhat by changing the elastic modulus of the flexures. Applications can easily account for temperature induced drift in deflection performance if quantified. Possible methods include modification of the spring constant used to compute drive voltages in the control software, and/or dynamic control of the bias voltage. Both the bias voltage and spring constant values can be changed in "real time" by the controller. Optical power testing and thermal testing are interrelated and should probably be combined research efforts. High incident optical power may induce greater, and more rapid, temperature excursions than ambient temperature variations. Temperature sensing can be performed at the device level by monitoring the resistance through polysilicon flexures. Similarly, measuring the resistance diagonally across the substrate, from one substrate contact to another, should yield an accurate indication of overall MEM-DM temperature.

Closed-loop control of a MEM-DM was not demonstrated in this work and remains as a research opportunity. The principal difficulty in performing a closed loop experiment lies in wavefront sensing of the diffracted optical signal reflected from a segmented MEM-DM. Possible solutions include spatial filtering of the diffracted optical signal prior to wavefront sensing, or use of iterative phase retrieval

algorithms to compute MEM-DM control signals. Phase retrieval approaches will require fewer optical components, and hence will be more desirable for low-cost adaptive optics systems. Continuous facesheet MEM-DMs with good optical surface quality will be better suited to conventional Shack-Hartmann wavefront sensing schemes.

For foundry fabricated continuous facesheet MEM-DMs, such as the author's MUMPs and SUMMiT designs, a logical next research step is post-foundry thinning of the facesheet layer using a timed silicon etch. Thinning the Poly2 layer on MUMPs designs to 0.5 μm would greatly reduce interactuator coupling, and lower the required control voltages. Post-foundry thinning of the MUMPs Poly2 layer would also reduce deformation of the facesheet due to residual stresses. To obtain a foundry-fabricated continuous facesheet MEM-DM with larger strokes, a thermally actuated design in the SUMMiT process, followed by post-foundry thinning of the MMPOLY3 layer is suggested. Designs employing this approach were partially developed, but were abandoned due to insufficient access to the SUMMiT process. Computer aided design tools incorporating electrical-thermal-mechanical models will facilitate design and optimization of thermally actuated MEM-DMs, both continuous and segmented. Thermal actuation of MEM-DMs should be revisited as these software tools become available.

Bonding approaches for post-foundry assembly of continuous facesheet MEM-DMs should still be considered if clean room facilities are available, and a reliable method of alignment and fixturing devised. In addition to eutectic bonding, use of solders and polymers should be explored as bonding options. Use of polymers for planarization prior to post-foundry facesheet fabrication has potential but should only be explored if good dry etching equipment is available.

The most exciting area for future research is segmented digital deflection devices. Though an inherently simple concept, the digital deflection scheme holds tremendous potential for exceptionally low-cost adaptive optics systems. Successful testing of the author's MUMPs digital deflection prototypes suggests exploitation of this concept in other processes as soon as possible. The optical quality of digital deflection designs in a planarized process, such as SUMMiT, will not be degraded by wiring constraints. Thus arrays with larger numbers of elements and better deflection resolution (more control bits) are

possible. Wire bonding to make off-chip electrical connections may limit digital deflection designs in the short term. Advanced wiring approaches such as high density interconnect (HDI) will provide an interim solution, but the full potential of the digital deflection scheme will be realized only in an integrated MEMS/digital process. With integration of some control logic, an electrode word register, resistors, and digital deflection micromirrors on a chip, all wiring constraints are eliminated. In an integrated process, the size of the digital deflection micromirror arrays will be limited only by available chip (or wafer) area. Very large deformable mirror systems with only a few external control wires are feasible. Because the digital deflection scheme requires only logic circuits (switch transistors), not the precision current/voltage sources of D/A converters, requirements for an integrated process are simplified.

Further research is also suggested for some of the author's other MEMS devices. Only functional testing of the author's tilt mirrors was performed. Development of a controller to point beam steering mirrors actuated by three electrostatic cantilevers would be interesting control problem, because the three nonlinear actuators are mechanically coupled. Modeling and characterization testing of the surface micromachined thermal conductivity pressure gauges is required before these devices can be exploited in applications. The test structures developed by the author will support a detailed study of the MUMPs process. In particular, further mechanical analysis of the stress cantilevers, has the potential of yielding a compact metrology test structure. Simultaneous solution of the equations describing single and multi-layer cantilevers is required. The solution algorithm combined with some instrument control and image processing to obtain interferometric microscope deflections, may yield an accurate automated metrology test capability.

In addition to the obvious use of the electrostatic cantilevers motors and scratch drive actuated rotors as MEMS prime movers, interest has been shown in these devices as tribology specimens. The wear shown in the prototype electrostatic motor and the variety of mechanical interfaces make it a fascinating test object. Identification and correction of the failure mechanism for the scratch drive rotors will allow these devices to be exploited in continuously running systems. Two quarter-die test chips with variations of these devices have already been fabricated to support future studies.

Appendix A - MUMPs Deformable Mirror Designs

The primary purpose of this appendix is to facilitate identification of the author's MUMPs designs, particularly the mirror array die. The author intends to make the remaining die available for cooperative research endeavors. For MUMPs runs 11 through 14 only a brief description of each die is provided as there are very few die remaining from these early runs. Beginning with the MUMPs 15 design run, a picture of the whole die, and brief description of the deformable mirror (piston array or continuous facesheet) is provided. The number of die remaining is noted. Other devices on the die, which have at a minimum been checked and found functional, are listed.

   No attempt is made to enumerate details of each design. For design details beyond those described in the text, the reader is referred to the layout files which can be made available. Layouts have been archived in CIF (Caltech Intermediate Format). Each die is labeled using the convention MUMPSxx_AFITyy, where xx is the MUMPs run number, and yy is the die number. The author's CIF files are archived using a similar but shortened naming convention. For example MUMPS24_AFIT5 is archived as "M24A5.cif". The top cell name needed to open the CIF files is listed for each design layout.

MUMPS11_AFIT2: Half die layout with primary emphasis on micromirror devices and thermal actuators. The 100 μm mirror devices used to study stress induced mirror curvature (Chapter 4), and arrays of vertical thermal actuators used to characterize backbending (Chapter 7) are on this die. (none remaining)

MUMPS12_AFIT2: Layout contains four 12×12 row/column addressed arrays, four 12×12 actuator arrays for facesheet bonding experiments, and a variety of test actuators. Sets of test actuators with varied flexure widths proved very useful for resonant frequency testing. (1 remaining)

MUMPS13_AFIT2, MUMPS13_AFIT3, MUMPS13_AFIT5: These MUMPs 13 layouts contain a number of 12×12 actuator arrays with 100 μm spacing and matching nitride membrane designs. (3, 3, 1 remaining respectively)

MUMPS14_AFIT1: Layout contains a 12×12 actuator array (100 μm spacing) with two large Poly1 pullouts to increase deflection range. Although pullouts have been successfully removed, this approach is not recommended. Several variations of large flip mirrors set up and operated with backbent thermal actuators on this layout. (4 remaining)

MUMPS14_AFIT2: Entire layout devoted to switches which must be assembled by flip over eutectic bonding. Enough die left for two attempts at using solder or polymer bonding to assemble switches (5 remaining)
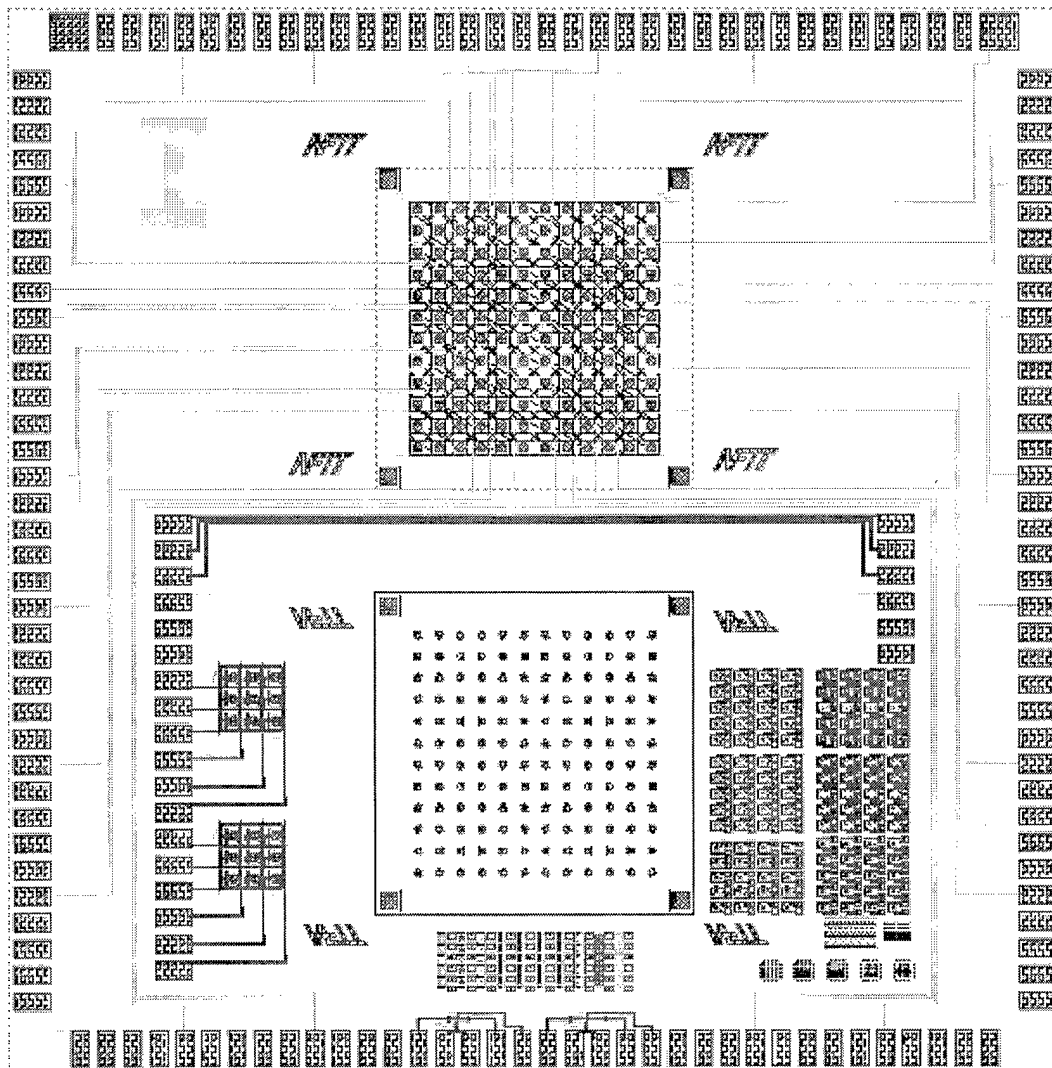
Top cell name:	lensmir_chip1
Actuation:	electrostatic
Active elements:	128
Layout:	12×12 with center-to-center spacing of 203 μm
Mirror Size:	80 μm diameter
Die Remaining:	5
Package:	144 PGA
Other Devices:	3×3 row/column addressed thermal piston micromirrors
	varied thermal piston micromirror structures
Suggested Usage:	facesheet bonding process development, lenslet experiments

Comments: The lower half of the die contains a SiN membrane with poly/Au attachment posts. The goal is to mate two die face-to-face, bond, and then release the membrane via a backside silicon etch. Proposed experiments with MUMPS 15 die should consider the impact of the fabrication irregularities observed (see Chapter 3).

MUMPS15_AFIT2
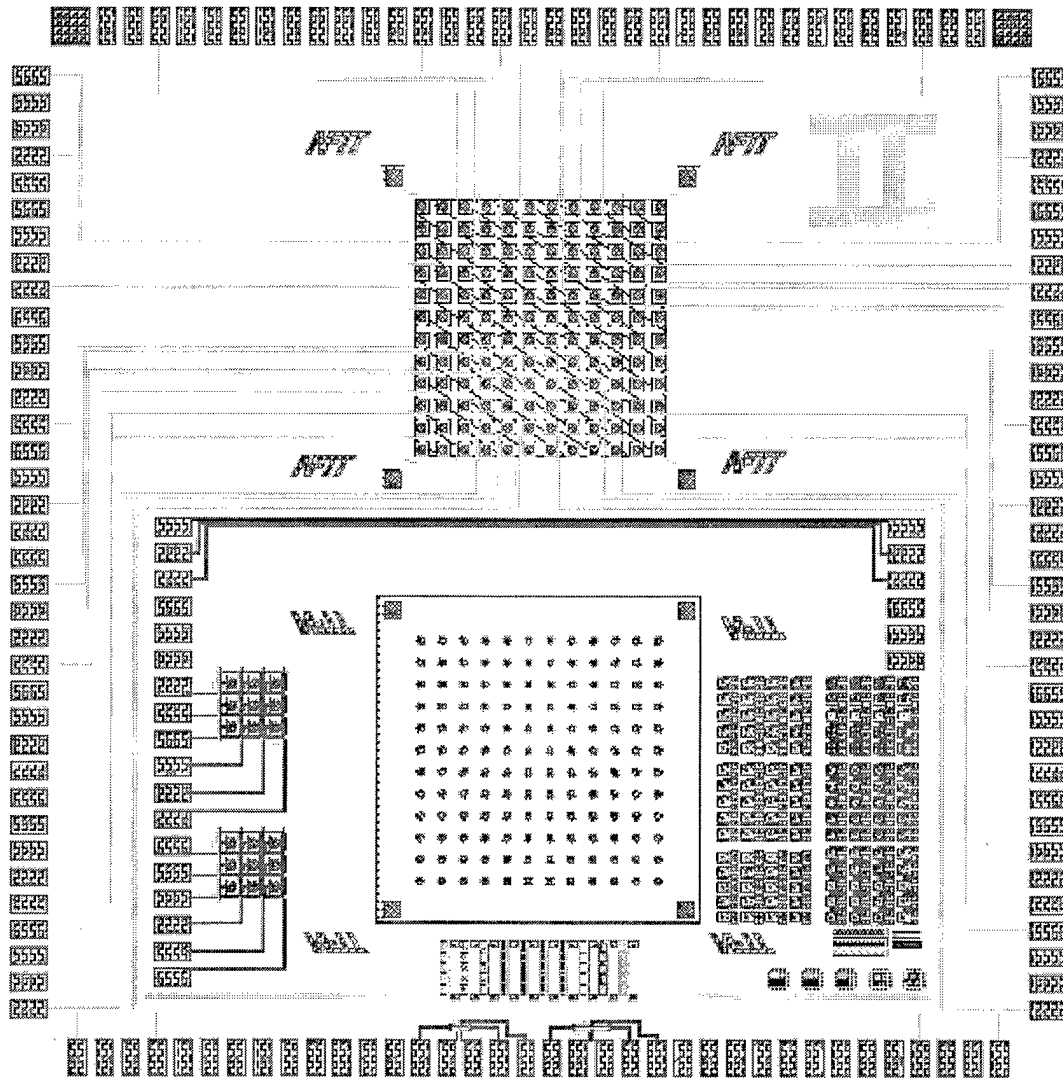
Top cell name:	lensmir_chip2
Actuation:	electrostatic (substrate is common bottom electrode)
Active elements:	128
Layout:	12×12 with center-to-center spacing of 203 μm
Mirror Size:	80 μm diameter
Die Remaining:	2
Package:	144 PGA
Other Devices:	3×3 row/column addressed thermal piston micromirrors
	varied thermal piston micromirror structures
Suggested Usage:	facesheet bonding process development only

Comments: The lower half of the die contains a SiN membrane with poly/Au attachment posts. The goal is to mate two die face-to-face, bond, and then release the membrane via a backside silicon etch. AFIT symbols serve as infrared alignment marks. Proposed experiments with MUMPS 15 die should consider the impact of the fabrication irregularities observed (see Chapter 3).

MUMPS16_AFIT3
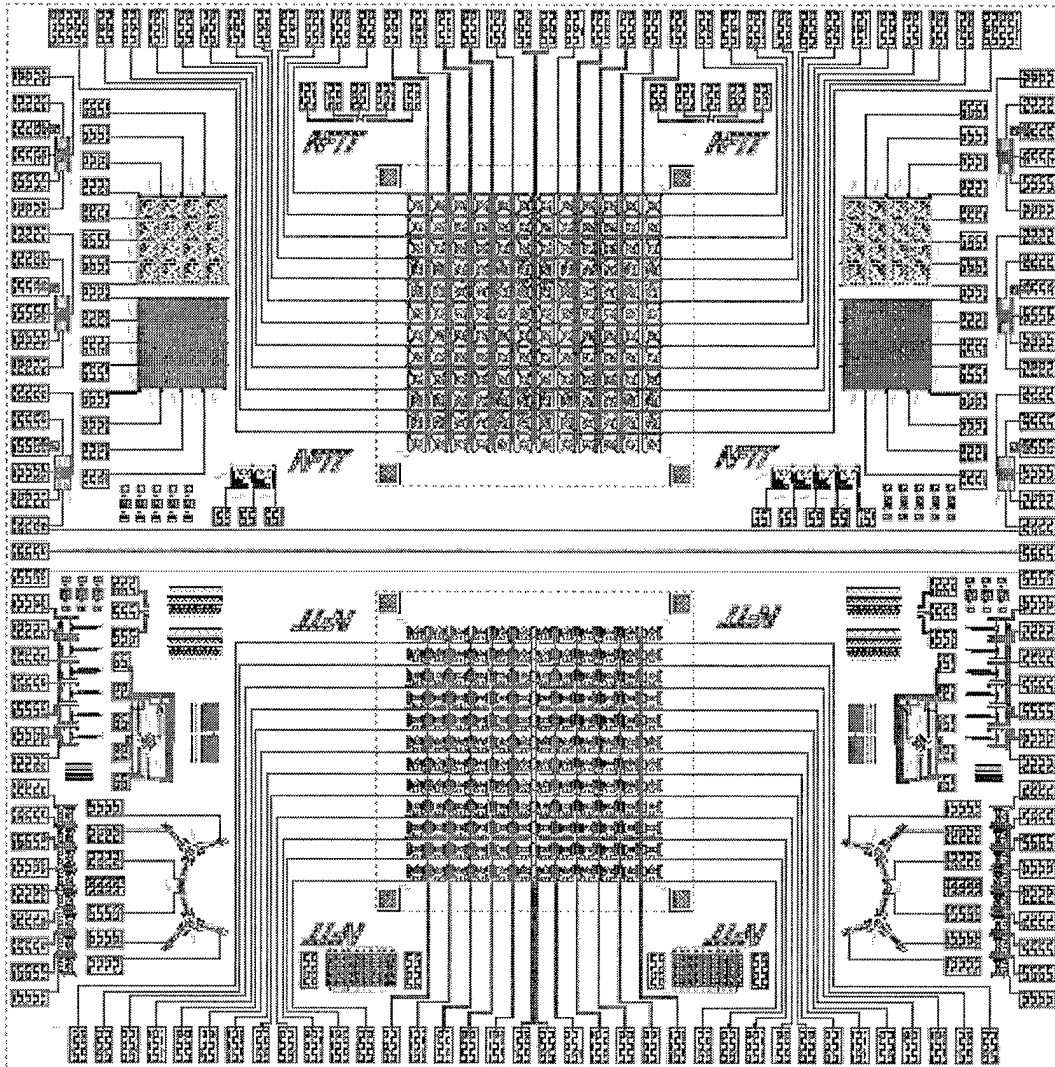
Top cell name:	m16_1
Actuation:	thermal, row/column addressed
Active elements:	144 (two arrays)
Layout:	12×12 with center-to-center spacing of 203 μm
Mirror Size:	80 μm diameter (top), 44 μm diameter (bottom array)
Die Remaining:	4
Package:	144 PGA
Other Devices:	thermally actuated beam steering mirrors, vacuum gauges
	thermal setup/electrostatic beam steering mirrors
Suggested Usage:	development of row/column control for thermal piston devices
	beam steering mirror control development and applications
	facesheet bonding process development

Comments: Use top array for lenslet experiments with suitable control. Mirror size on bottom array is too small. The large Poly2/gold AFIT symbols are alignment marks compatible with the SiN membranes fabricated on MUMPS 15.
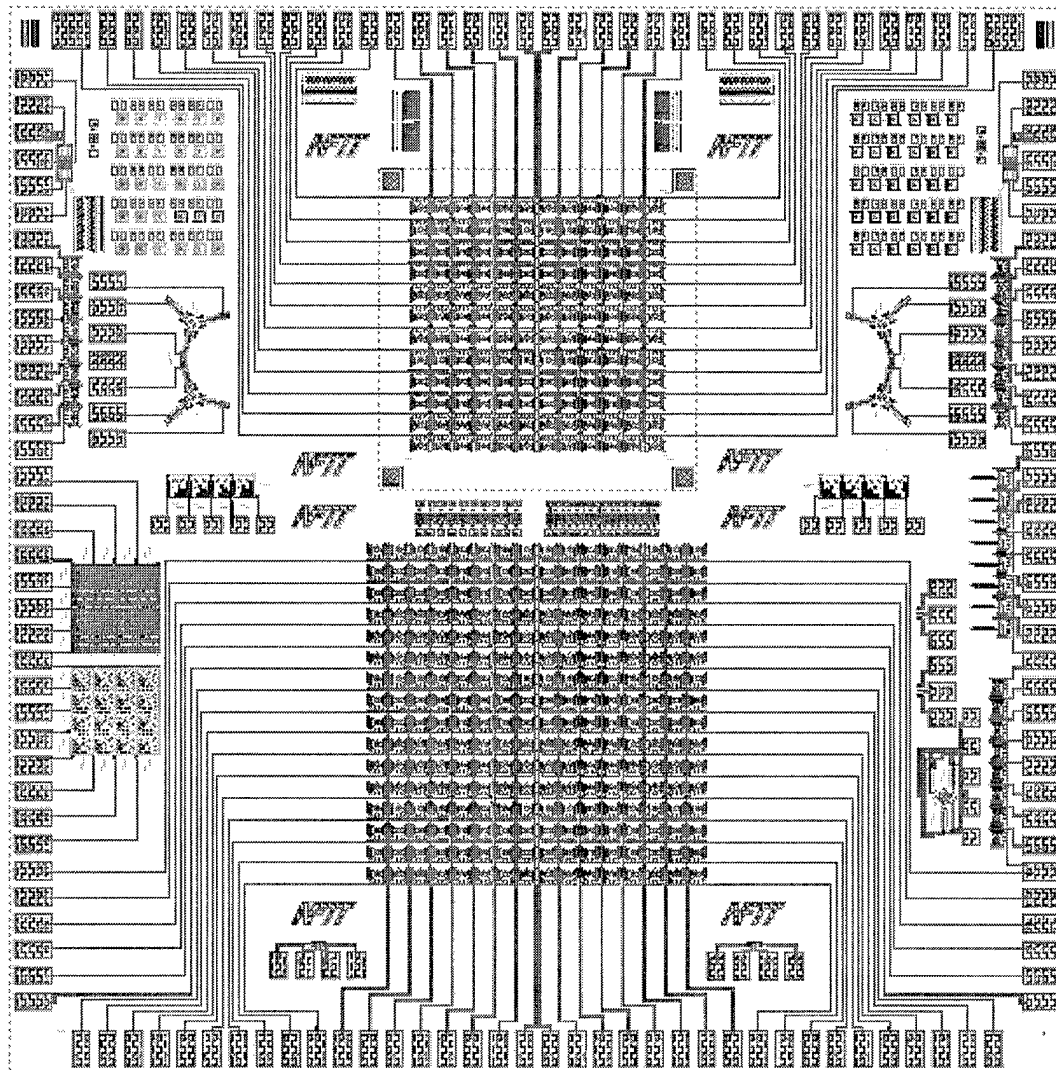
Top cell name:	m16_2
Actuation:	thermal, row/column addressed
Active elements:	144 (top), 256 (bottom)
Layout:	12×12 (top), 16×16 (bottom), with center-to-center spacing of 203 μm
Mirror Size:	44 μm diameter (both array)
Die Remaining:	4
Package:	144 PGA
Other Devices:	thermally actuated beam steering mirrors, vacuum gauges
	thermal setup/electrostatic beam steering mirrors
Suggested Usage:	development of row/column control for thermal piston devices
	beam steering mirror control development and applications
	facesheet bonding process development

Comments: Mirror size too small, use only for facesheet bonding process development. The large Poly2/gold AFIT symbols are alignment marks compatible with the SiN membranes fabricated on MUMPS 15.
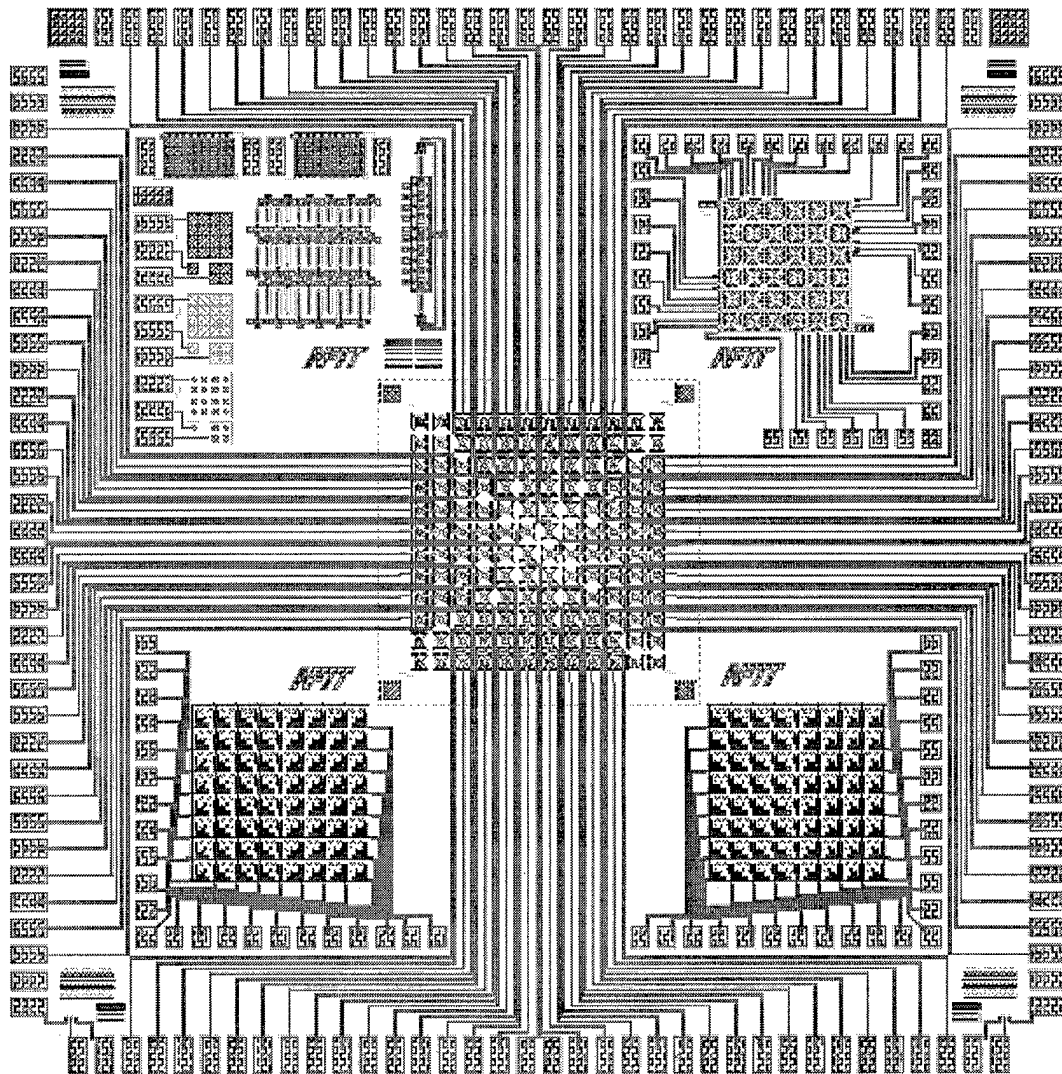
Top cell name:	m17_chip1
Actuation:	thermal
Active elements:	144
Layout:	12×12, with center-to-center spacing of 203 μm
Mirror Size:	50 μm diameter
Die Remaining:	7
Package:	144 PGA
Other Devices:	self-planarized, 36 thermal actuator, continuous facesheet (upper right)
Suggested Usage:	long wavelength aberration control (requires lenslet array)

Comments: Individually addrssed elements with large strokes (>1 μm) make this device attractive for longer wavelength operation. Check lenslet spot size as mirrors may be too small. Can also be used for facesheet bonding process development. The large Poly2/gold AFIT symbols are alignment marks compatible with the SiN membranes fabricated on MUMPS 15.
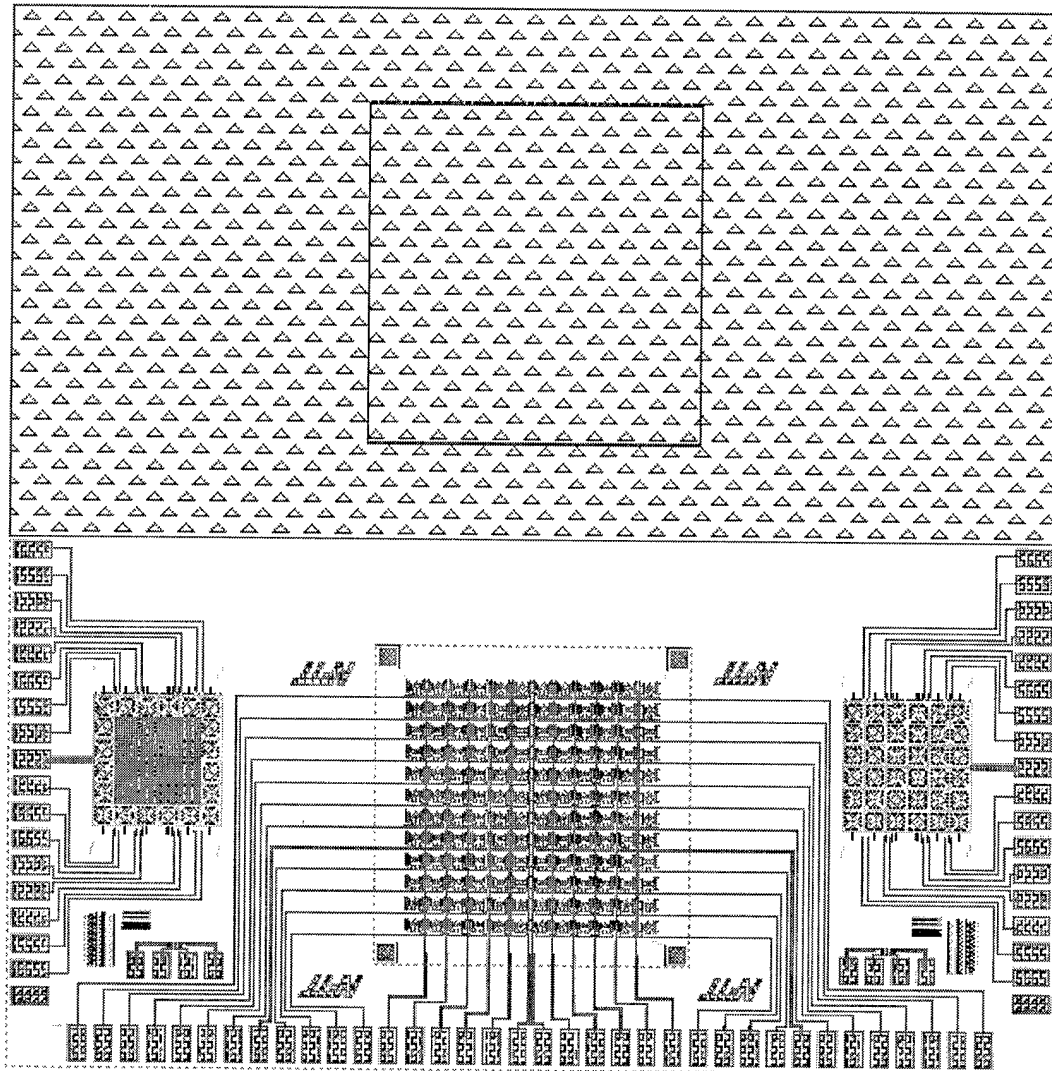
Top cell name:	m17_chip2
Actuation:	thermal, row/column addressed
Active elements:	144
Layout:	12×12 with center-to-center spacing of 203 μm
Mirror Size:	44 μm diameter
Die Remaining:	15
Package:	144 PGA
Other Devices:	self-planarized, thermally actuated, continuous facesheet DMs (only center elements wired) silicon nitride membrane (upper half of die)
Suggested Usage:	development of row/column control for thermal piston devices facesheet bonding process development

Comments: Mirror size on bottom array is too small. The large Poly2/gold AFIT symbols are alignment marks compatible with the SiN membranes fabricated on MUMPS 15.
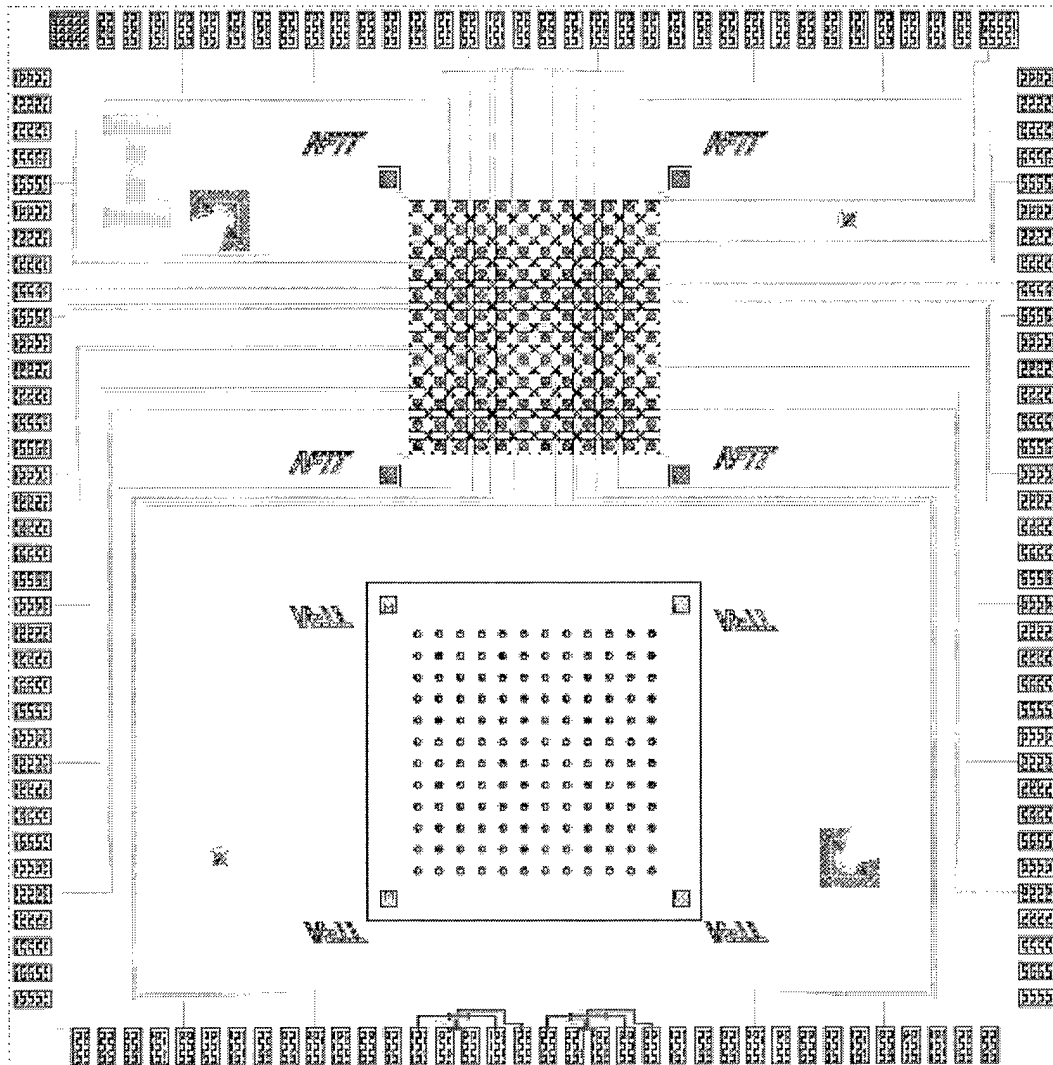
Top cell name:	lensmir_chipIA
Actuation:	electrostatic
Active elements:	128
Layout:	12×12 with center-to-center spacing of 203 μm
Mirror Size:	80 μm diameter
Die Remaining:	12
Package:	144 PGA
Other Devices:	two vacuum gauges
Suggested Usage:	optical aberration control using lenslet array, facesheet bonding

Comments: Redo of MUMPS15_AFIT1 with wider flexures (4 μm), and no fabrication problems. Extraneous stuff was removed, membrane posts converted to Poly2/Au only, and alignment structures added to facilitate flip-over bonding. Larger mirror size could ease lenslet alignment. Were not used in testbed because MUMPS 18 design exhibited lower control voltage. See Chapter 3 for MUMPS 17 lenslet mirror data. High yield and good deflection uniformity observed in testing.

MUMPS18_AFIT7
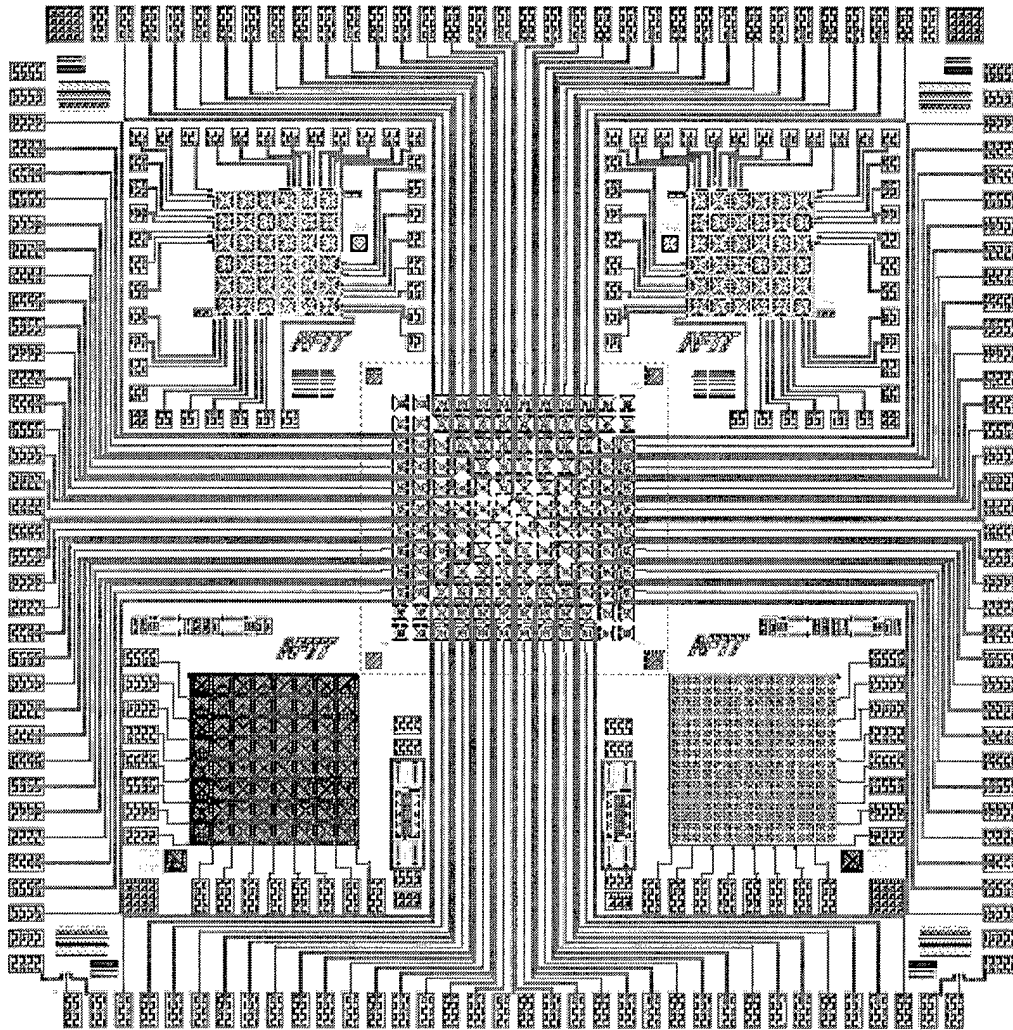
Top cell name:	m18_chip1
Actuation:	thermal
Active elements:	144
Layout:	12×12, with center-to-center spacing of 203 μm
Mirror Size:	50 μm diameter
Die Remaining:	13
Package:	144 PGA
Other Devices:	self-planarized, 36 thermal actuator, continuous facesheet (top)
Suggested Usage:	long wavelength aberration control (requires lenslet array)

Comments: Similar to MUMPS17_AFIT8 but mirror plates do not employ trapped oxide. Lower thermal capacitance should yield faster device response. Testing and comparison of the MUMPS17 and MUMPS18 designs should be very useful for validation of thermal modeling codes as the become available.

MUMPS18_AFIT8

Top cell name:	m18_chip2
Actuation:	electrostatic
Active elements:	128
Layout:	12×12 with center-to-center spacing of 203 μm
Mirror Size:	60 μm diameter
Die Remaining:	3
Package:	144 PGA
Other Devices:	flip mirrors
Suggested Usage:	optical aberration control using lenslet array

Comments: Workhorse array used for lenslet/MEM-DM optical aberration correction experiment (see Chapter 5). The mirrors/actuators employ some self planarization to facilitate facesheet fabrication attempts. Devices feature low control voltage, excellent uniformity, and near 100% yield.
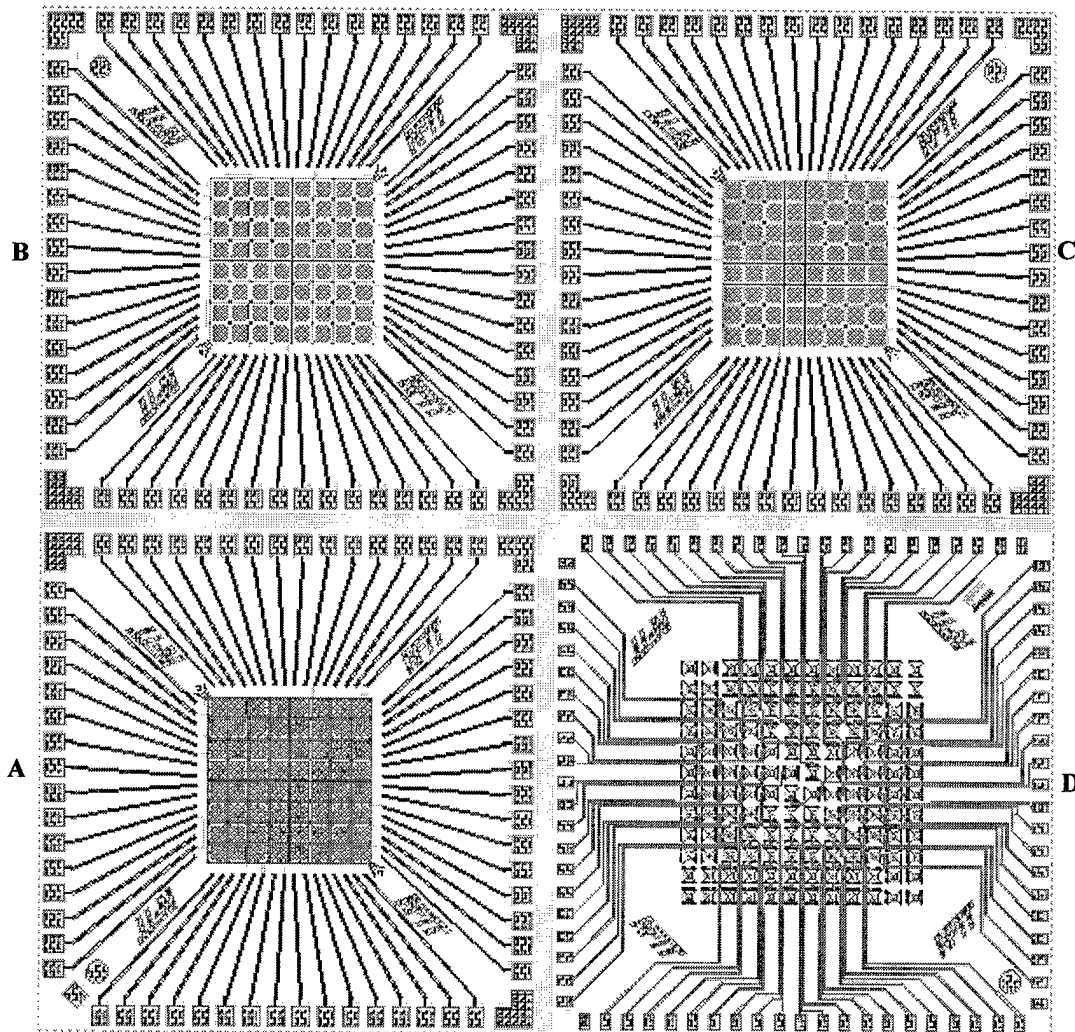
Top cell name: m19_chip1

Quarter Die A
Actuation: electrostatic
Active elements: 64
Layout: 8×8 with center-to-center spacing of 203 μm
Mirror Size: 180 μm × 180 μm
Die Remaining: 3
Package: 68 LCC
Other Devices: none
Suggested Usage: tie tacks and other display applications
Comments: MUMPS metallized device denoted M19_A in micromirror surface figure study of Chapter 4. Stress induced mirror curvature limits optical performance.

MUMPS19_AFIT6 (continued)

<u>Quarter Die B</u> (see picture on previous page)
Actuation:	electrostatic
Active elements:	64
Layout:	8×8 with center-to-center spacing of 203 μm
Mirror Size:	180 μm × 180 μm
Die Remaining:	6
Package:	68 LCC
Other Devices:	none
Suggested Usage:	optical aberration control

Comments: Unmetallized device denoted M19_B in micromirror surface figure study of Chapter 4. Employs a trapped oxide mirror plate for added stiffness. This array yielded the best measured optical performance after metallization. The post-foundry metallization procedure employed is described in Chapter 4.

<u>Quarter Die C</u> (see picture on previous page)
Actuation:	electrostatic
Active elements:	64
Layout:	8×8 with center-to-center spacing of 203 μm
Mirror Size:	180 μm × 180 μm
Die Remaining:	7
Package:	68 LCC
Other Devices:	none
Suggested Usage:	optical aberration control

Comments: Unmetallized device denoted M19_C in micromirror surface figure study of Chapter 4. Reasonably good optical performance can be expected if properly metallized in a post-foundry procedure. Because the Poly2 mirror plate is attached to the underlying Poly1 actuator by vias, these devices do not withstand the rough handling required for the post-foundry release process described in Chapter 4 as well as the M19_B device above.

<u>Quarter Die D</u> (see picture on previous page)
Actuation:	thermal
Active elements:	80
Layout:	12×12 with center-to-center spacing of 203 μm
Mirror Size:	50 μm diameter
Die Remaining:	9
Package:	84 LCC
Other Devices:	none
Suggested Usage:	optical aberration control

Comments: An unmetallized version of the MUMPS 18 thermal piston devices, developed primarily for post foundry facesheet fabrication efforts. Could be used for lenslet experiments with appropriate post-foundry metallization. The central 80 elements are wired to bond pads.
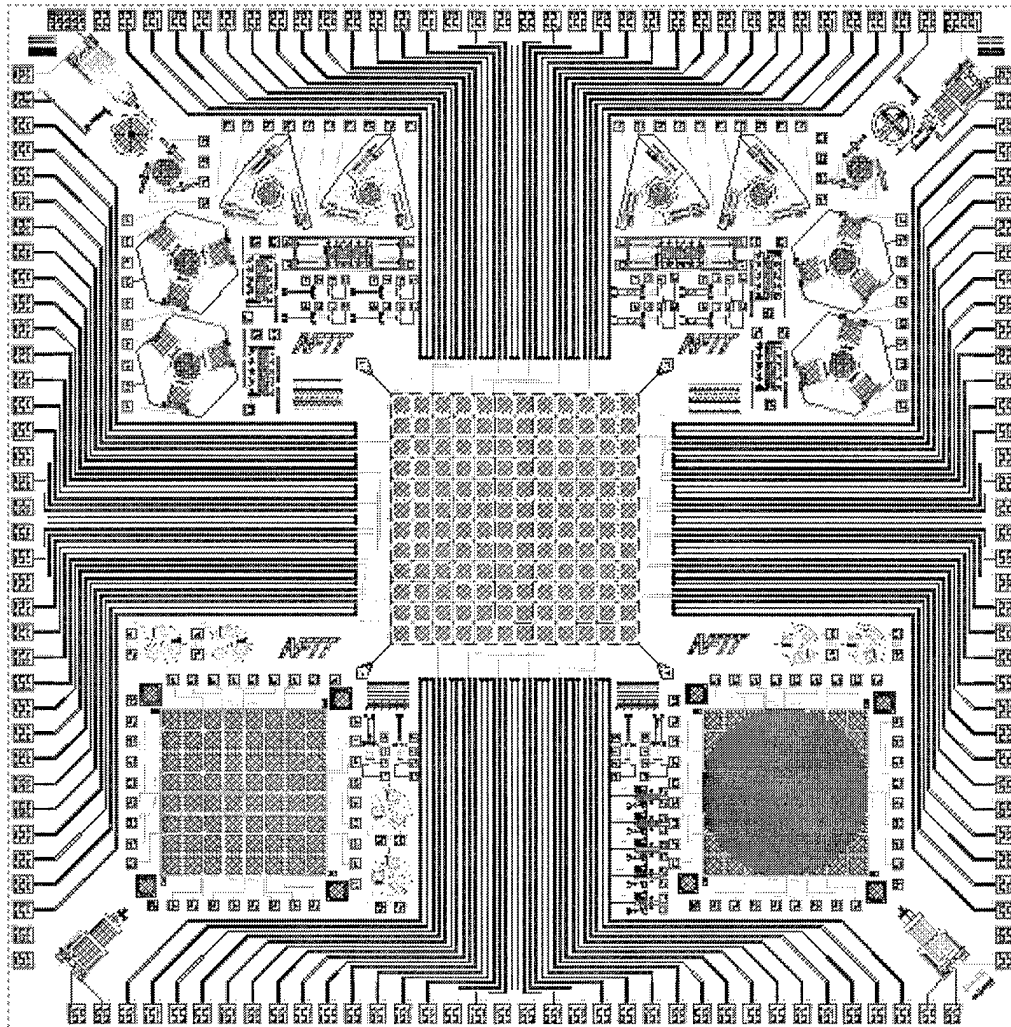
Top cell name:	m19_chp2
Actuation:	electrostatic
Active elements:	128
Layout:	12×12 with center-to-center spacing of 203 μm
Mirror Size:	180 μm × 180 μm
Die Remaining:	6
Package:	144 PGA
Other Devices:	a few flip over switches, electrostatic beam steering mirrors, scratch drive rotors
Suggested Usage:	optical aberration control

Comments: Workhorse array used for bare MEM-DM optical aberration correction experiment (see Chapter 3). Devices feature low control voltage, excellent uniformity, and near 100% yield. Nominal fill-factor over 70%. Post-foundry metallization required to improve reflectivity is addressed in the surface figure study of Chapter 4. Low capacitance Poly1 wiring is used from bondpads to array perimeter.
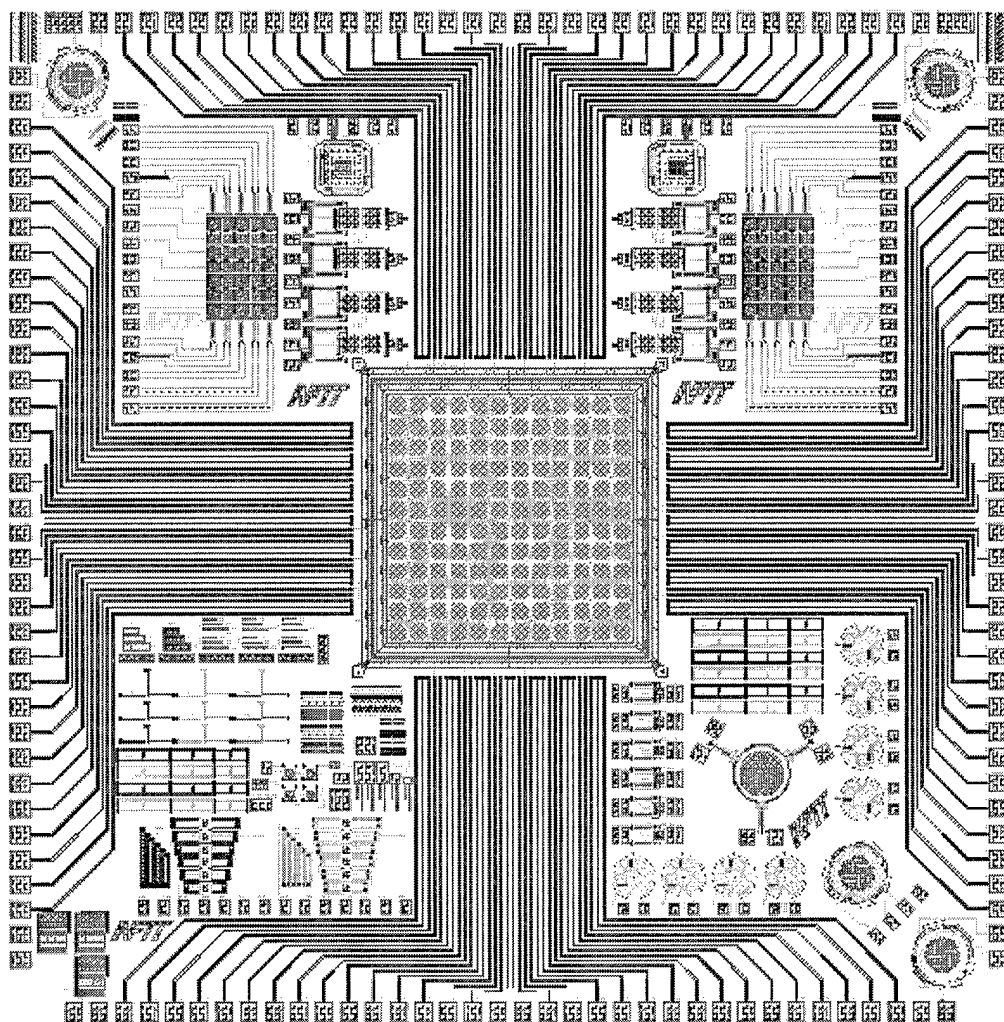
Top cell name:	m20_chp1
Actuation:	electrostatic
Active elements:	128
Layout:	12×12 with center-to-center spacing of 203 μm
Mirror Size:	184 μm × 184 μm
Die Remaining:	8
Package:	144 PGA
Other Devices:	test structures and scratch drive rotors (see Chapter 9)
Suggested Usage:	optical aberration control

Comments: Piston micromirror array employing a self removing metallization mask to facilitate post-foundry metallization (see Chapter 3). The Poly2 metallization mask employs residual stress of the MUMPs metal to assist lift off. Nominal fill-factor of about 80%. Post-foundry metallization steps are; HF etch to expose Poly1 mirrors, sputter metal, package, release, and wire bond. Poly1 only mirror plates bend if devices are fully deflected, but remain flat for small deflections. Low capacitance Poly1 wiring is used from bondpads to array perimeter. Approximately one quarter of the die is devoted to test structures to measure stress and electrochemical etch effects.
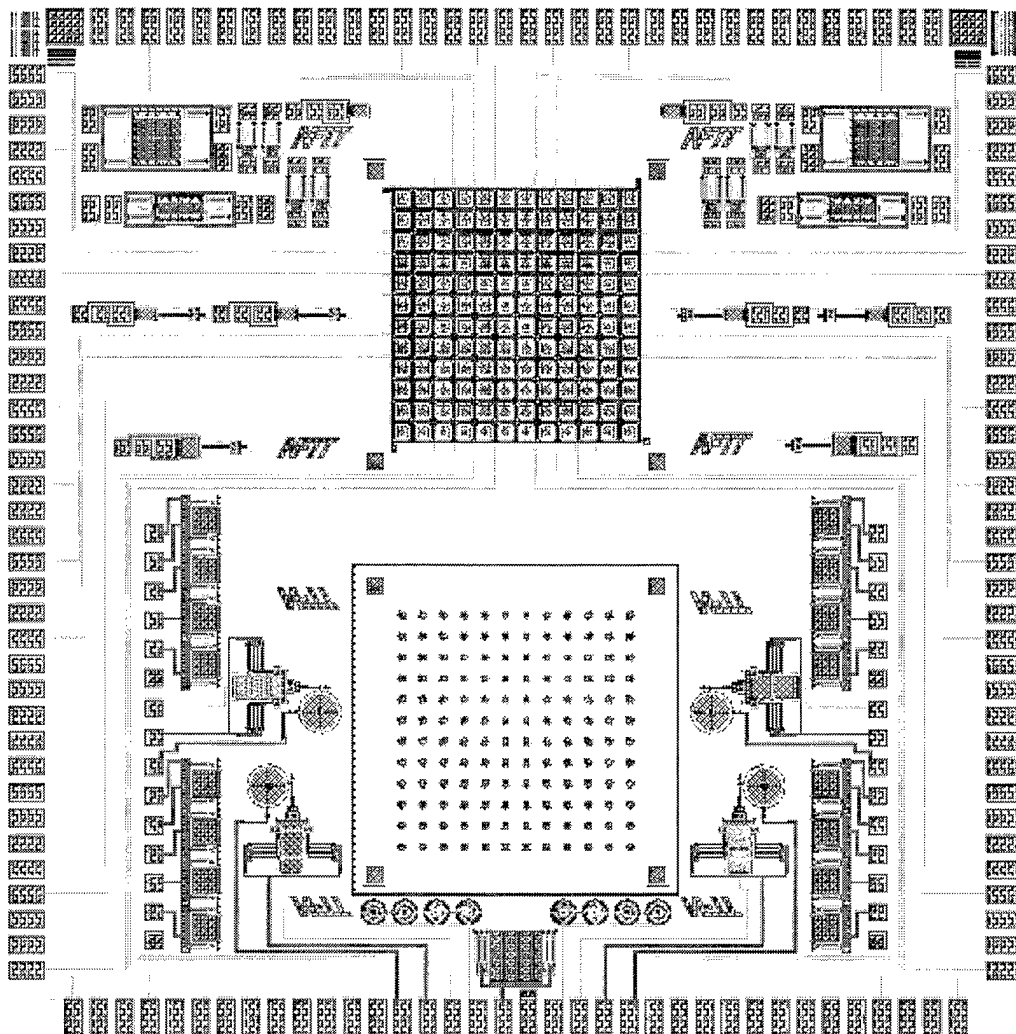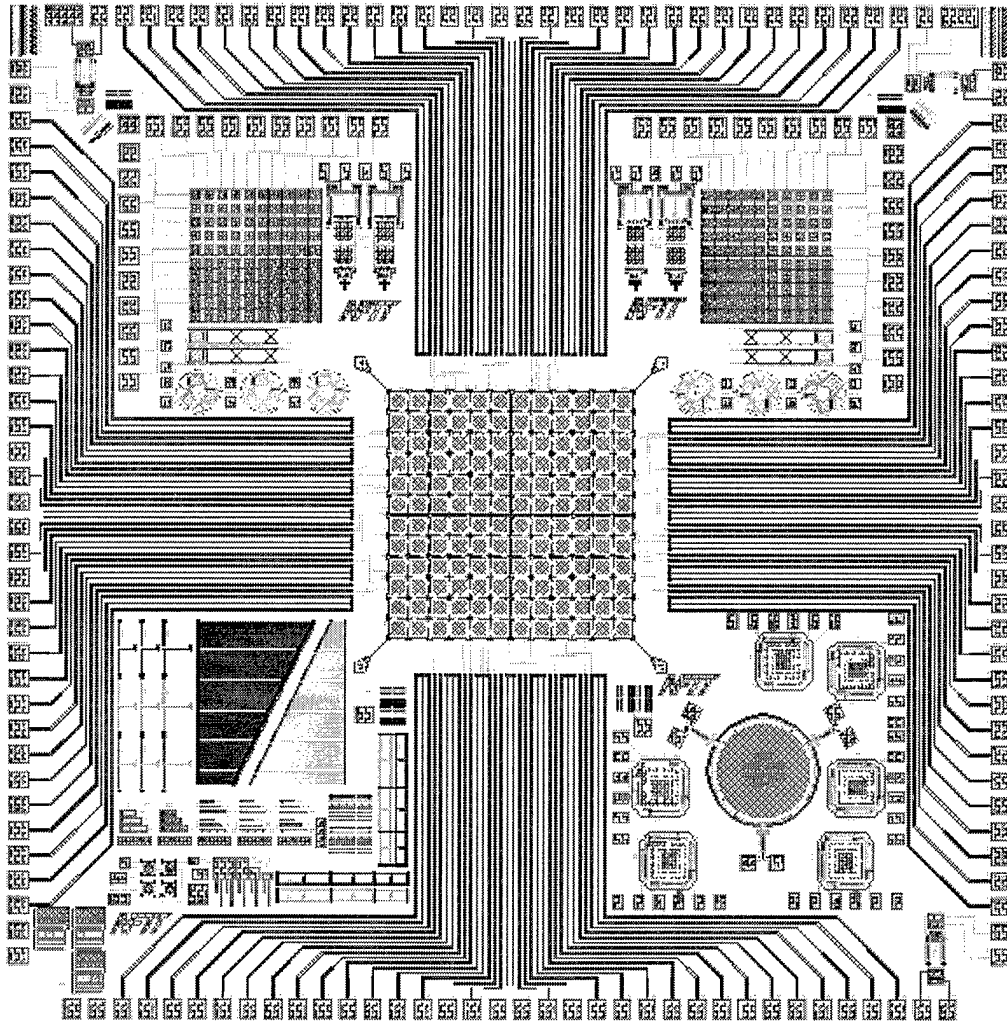
Top cell name: m20_chp2
Actuation: electrostatic
Active elements: 128
Layout: 12×12 with center-to-center spacing of 203 μm
Mirror Size: 162 μm × 162 μm
Die Remaining: 13
Package: 144 PGA
Other Devices: test structures (lower left quadrant), 100 element row/column addressed
                            electrostatic tilting mirrors for display applications, rotary scratch drives
Suggested Usage: optical aberration control with lenslets
Comments: Piston micromirror array is a less aggressive version of MUMP19_AFIT7 designed as a backup. Nominal fill-factor of about 63%. Wiring is identical to MUMPS19 design so these chips can be used for setup and checkout. Post-foundry metallization procedures will also be similar. If metallized and used with a lenslet array, very good results can be expected. Approximately one quarter of the die is devoted to test structures to measure stress and electrochemical etch effects. First functional rotary scratch drives on this chip. Tilt mirror arrays work in bistable mode.
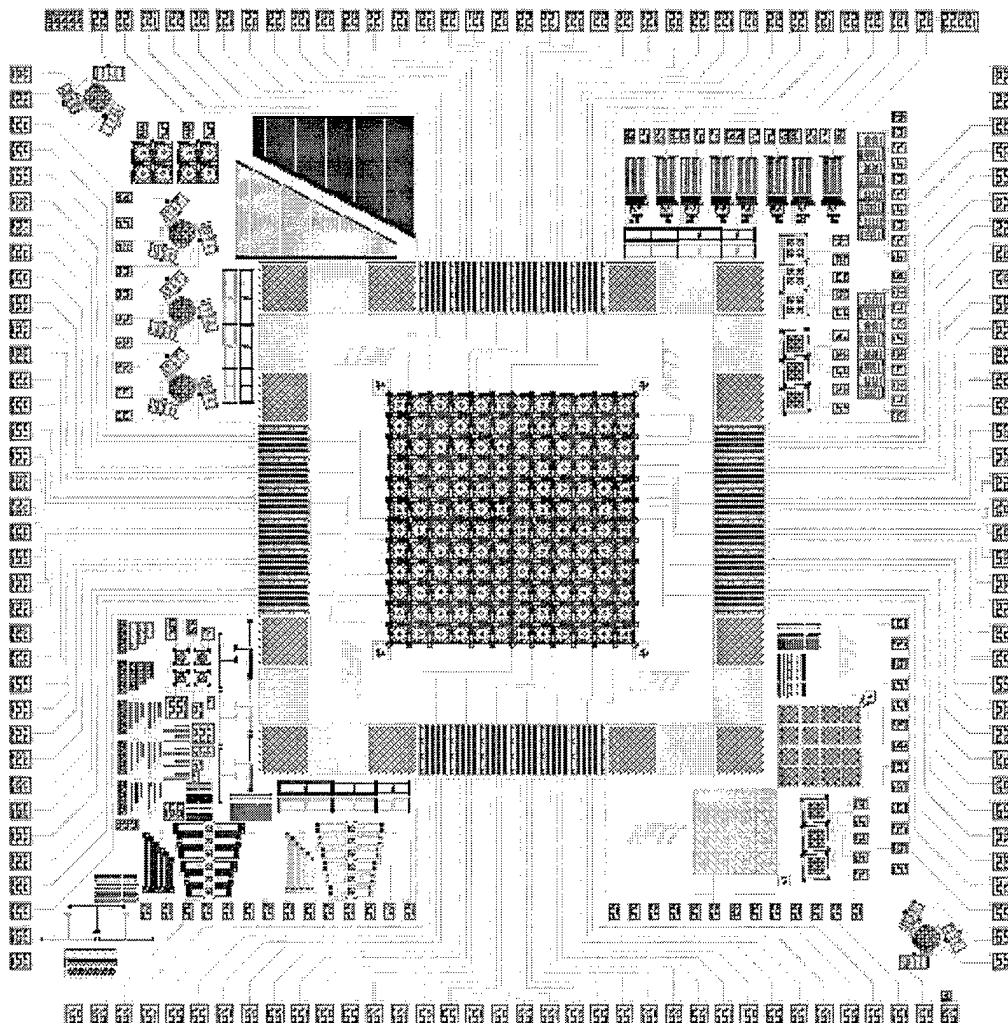
Top cell name:	m21_chp1
Actuation:	electrostatic
Active elements:	128
Layout:	12×12 with center-to-center spacing of 203 μm
Mirror Size:	90 μm diameter
Die Remaining:	12
Package:	144 PGA
Other Devices:	test structures (lower left quadrant), electrostatic cantilever motors, digital deflection micromirrors, electrostatic beam steering mirrors, test structures
Suggested Usage:	facesheet bonding process development

Comments: Piston micromirror/actuator array useful for facesheet bonding experiments, or optical experiments using a lenslet array. First working digital deflection micromirror prototypes and electrostatic cantilever motors on this die. Full repeat of the same test structures fabricated on MUMPs 20 for comparison studies.

MUMPS21_AFIT6
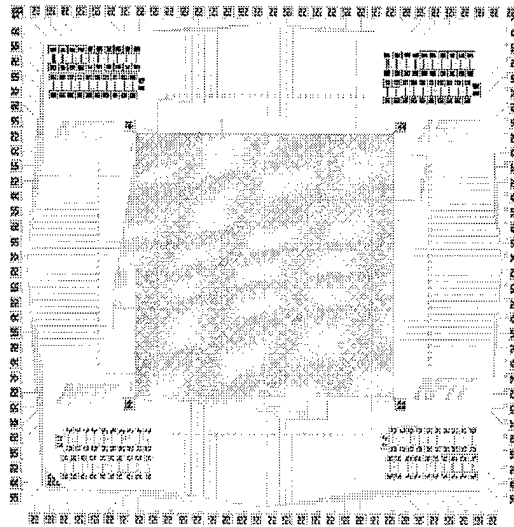
Top cell name:	mumps21_kladitis (sub-diced, upper left corner of layout)
Actuation:	electrostatic
Active elements:	128
Layout:	12×12 with center-to-center spacing of 203 μm
Mirror Size:	2.4 mm self-planarized continuous membrane
Die Remaining:	5
Package:	144 PGA
Other Devices:	polysilicon resistor test bridges
Suggested Usage:	optical aberration correction experiments

Comments: This deformable mirror design represents a hybrid of the axially actuated continuous facesheet and an unsupported membrane. Residual stress and/or stiction in the release process caused stress deformation of the few devices examined. Laser cutting of the four anchor posts at each corner (16 posts total) may alleviate stress problems. Partially supported membrane will require post-foundry metallization for improved reflectivity. No gold was used on this die so that polysilicon resistor test bridges could be baked at high temperature in support of another researcher's experiment. Wirebonding of closely spaced, unmetallized pads can be tricky but several chips have been successfully bonded. For polysilicon pads, bonding should be performed immediately after the release etch.

MUMPS21_AFIT7
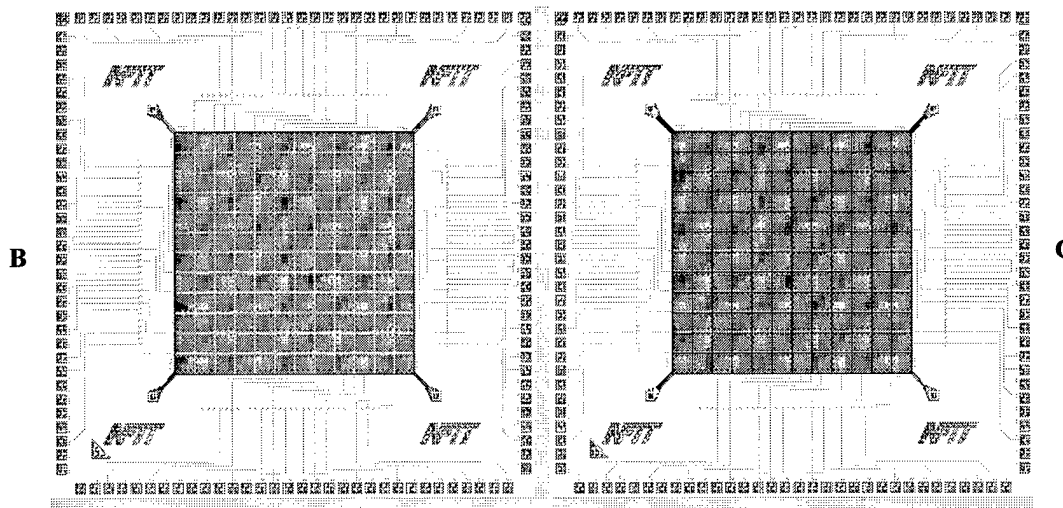
Top cell name: gkading_mumps21 (sub-diced, upper half of layout)

Quarter Die B
Actuation: electrostatic
Active elements: 128
Layout: 12×12 with center-to-center spacing of 203 μm
Mirror Size: 2.4 mm self-planarized continuous facesheet
Die Remaining: 12
Package: 144 PGA
Other Devices: none
Suggested Usage: optical aberration correction experiments
Comments: An axially actuated continuous facesheet deformable mirror design employing a self-planarized Poly2 facesheet. Despite use of only a quarter die, 128 individually addressed actuators are wired to bond pads. Devices can be wirebonded into 144 PGA packages. Stress induced deformation of mirror surface noted during initial testing. Laser cutting of the four anchor posts at each corner (16 posts total) may help alleviate stress problems. Mirror requires post-foundry metallization for improved reflectivity.

Quarter Die C
Actuation: electrostatic
Active elements: 128
Layout: 12×12 with center-to-center spacing of 203 μm
Mirror Size: 200 μm × 200 μm
Die Remaining: 11
Package: 144 PGA
Other Devices: none
Suggested Usage: optical aberration correction experiments
Comments: Segmented version of the continuous facesheet design above. Stress induced curvature of the Poly2 facesheet segments will limit optical performance. A tailored post-foundry metallization required to improve mirror element flatness and reflectivity.
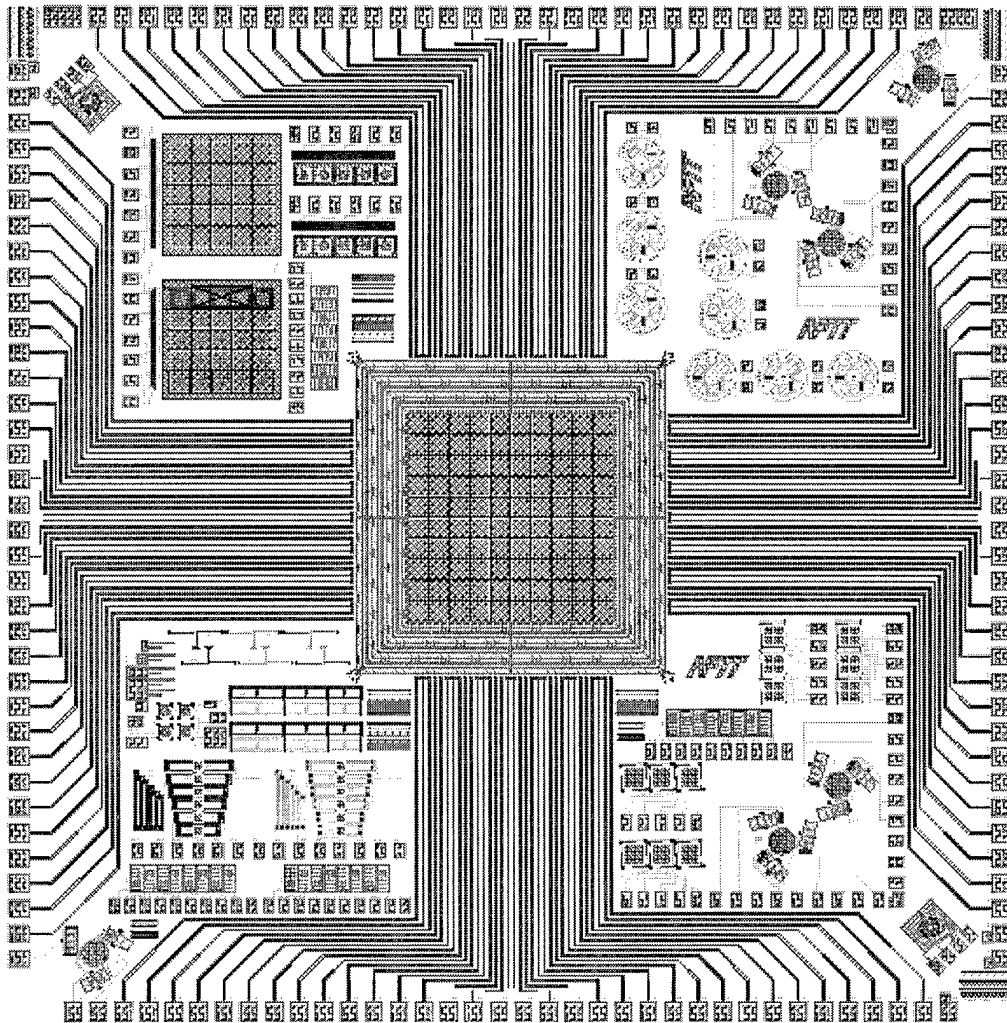
Top cell name:	m22_chp1
Actuation:	electrostatic, digital deflection
Active elements:	44
Layout:	10×10 with center-to-center spacing of 203 μm
Mirror Size:	200 μm × 200 μm, self-planarized
Die Remaining:	13
Package:	144 PGA
Other Devices:	digital beam steering mirrors, test structures, scratch drive rotors, 4 and 5-bit digital deflection prototype mirrors
Suggested Usage:	optical aberration correction experiments

Comments: Digital deflection mirror array with electrodes for 44 active elements wired to bond pads. Active elements roughly fill 8 element diameter circle in center of array. Self-planarization is used to increase fill-factor. Initial testing shows that stress induced curvature of the Poly2 layer limits optical performance. Post-foundry metallization should be tailored to improve mirror flatness and increase reflectivity. A self-removing mask facilitates metallization.
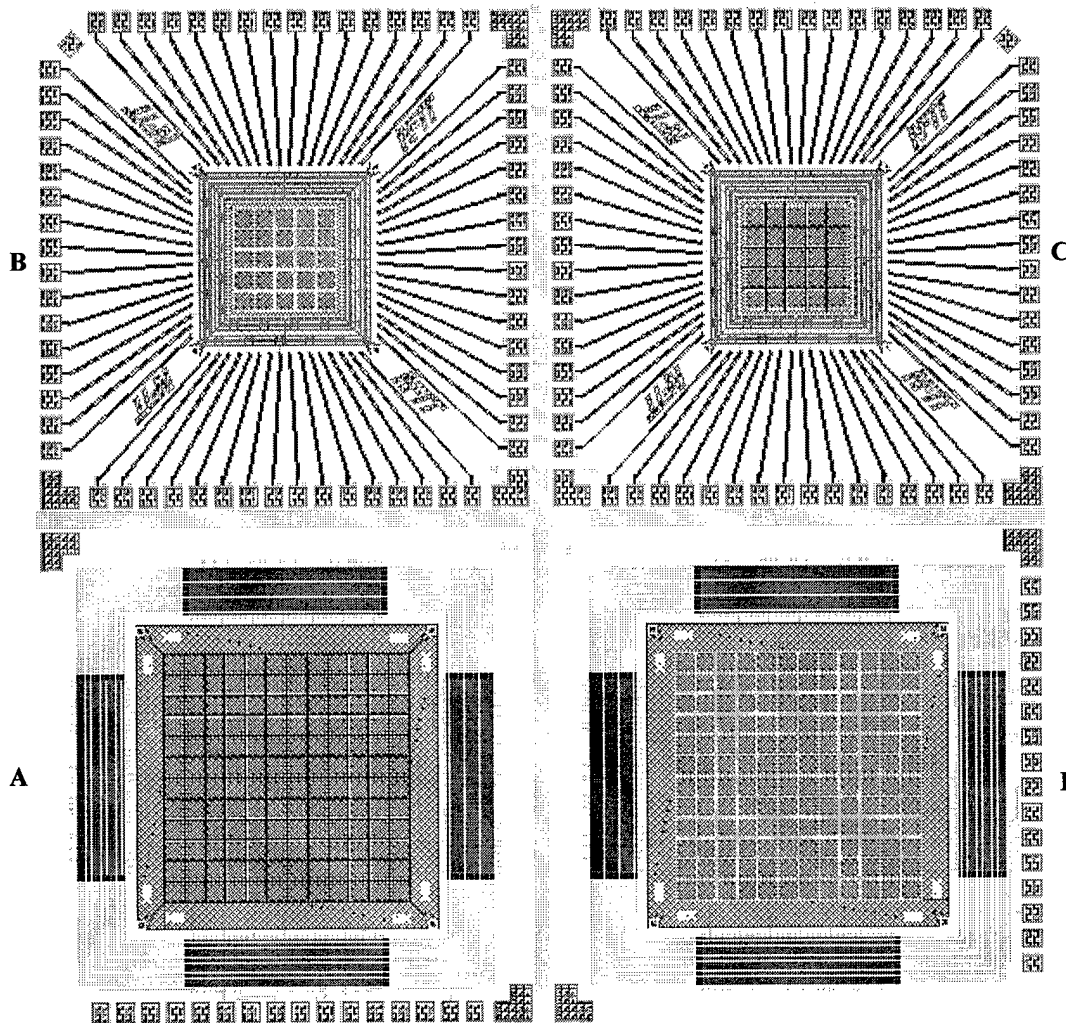
Top cell name: m22_chp2

Quarter Die A

Actuation:	electrostatic
Active elements:	128
Layout:	12×12 with center-to-center spacing of 203 µm
Mirror Size:	200 µm × 200 µm, self-planarized
Die Remaining:	14
Package:	68 LCC (or other, 17 connections required)
Other Devices:	none
Suggested Usage:	optical aberration control (radially symmetric)

Comments: Segmented mirror array with all elements which are equidistant from the mirror center wired together on the die to reduce the number of control signals that must be wired off chip. Self-planarized for improved fill-factor. Stress induced curvature of the Poly2 mirror surfaces limit optical performance. Post foundry metallization may be used to improve optical performance.

MUMPS22_AFIT2(continued)

<u>Quarter Die B</u> (see picture on previous page)
Actuation:	electrostatic, digital deflection
Active elements:	21
Layout:	5×5 with center-to-center spacing of 203 µm
Mirror Size:	1 mm self-planarized continuous facesheet
Die Remaining:	9
Package:	68 LCC
Other Devices:	none
Suggested Usage:	optical aberration correction experiments

Comments: Prototype continuous facesheet mirror with digital deflection actuators. Electrodes for 21 active elements wired to bond pads. Corner elements are not active. Self-planarization is used to improve facesheet flatness. Initial testing confirmed wiring of digital electrodes. Devices are fully functional but optical performance is limited by facesheet quality and small overall size. Post-foundry metallization required to increase facesheet reflectivity. Self-removing mask facilitates metallization.

<u>Quarter Die C</u> (see picture on previous page)
Actuation:	electrostatic, digital deflection
Active elements:	21
Layout:	5×5 with center-to-center spacing of 203 µm
Mirror Size:	200 µm × 200 µm, self-planarized
Die Remaining:	8
Package:	68 LCC
Other Devices:	none
Suggested Usage:	optical aberration correction experiments

Comments: Prototype 21 element segmented digital deflection micromirror array. Corner elements are not active. Self-planarization is used to improve facesheet flatness. Initial testing confirmed wiring of digital electrodes. Devices are fully functional but optical performance is limited by stress-induced curvature of Poly2 facesheet segments. Tailored post-foundry metallization required to improve flatness and increase mirror reflectivity. Self-removing mask facilitates metallization. Small overall size and number of elements will limit applications.

<u>Quarter Die D</u> (see picture on previous page)
Actuation:	electrostatic
Active elements:	128
Layout:	12×12 with center-to-center spacing of 203 µm
Mirror Size:	2.4 mm self-planarized continuous facesheet
Die Remaining:	14
Package:	68 LCC (or other, 17 connections required)
Other Devices:	none
Suggested Usage:	optical aberration control (radially symmetric)

Comments: Continuous facesheet mirror with actuators equidistant from the mirror center wired together on the die to reduce the number of control signals that must be wired off chip. Facesheet is self-planarized. Residual stress in the Poly2 mirror surface causes buckling of the facesheet. Laser cutting of the facesheet fixed point attachments may reduce buckling. Post foundry metallization may be used to improve reflectivity.

MUMPS23_AFIT4
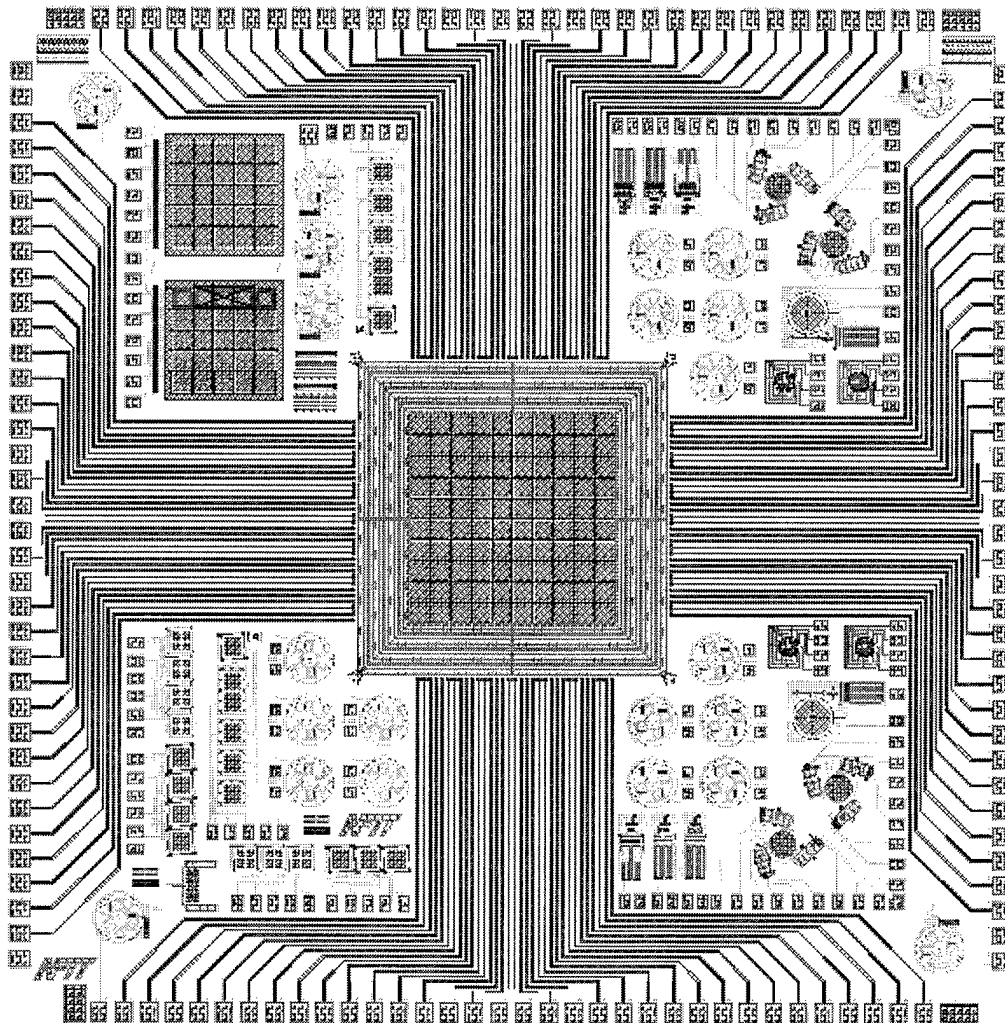
Top cell name:	m23_chp1
Actuation:	electrostatic, digital deflection
Active elements:	44
Layout:	10×10 with center-to-center spacing of 203 μm
Mirror Size:	200 μm × 200 μm, self-planarized
Die Remaining:	9
Package:	144 PGA
Other Devices:	digital beam steering mirrors, scratch drive rotors, 4 and 5-bit digital deflection prototype mirrors, electrostatic cantilever motor variations
Suggested Usage:	optical aberration correction experiments

Comments: Digital deflection mirror array with 44 active elements. Improved version of MUMPS22_AFIT1 with 9 vias attaching facesheet segments to actuators. Initial testing shows that mirror elements are substantially flatter. This design is the best choice for segmented digital deflection experiments. Post-foundry metallization should be tailored to improve mirror flatness and increase reflectivity. A self-removing mask facilitates metallization.
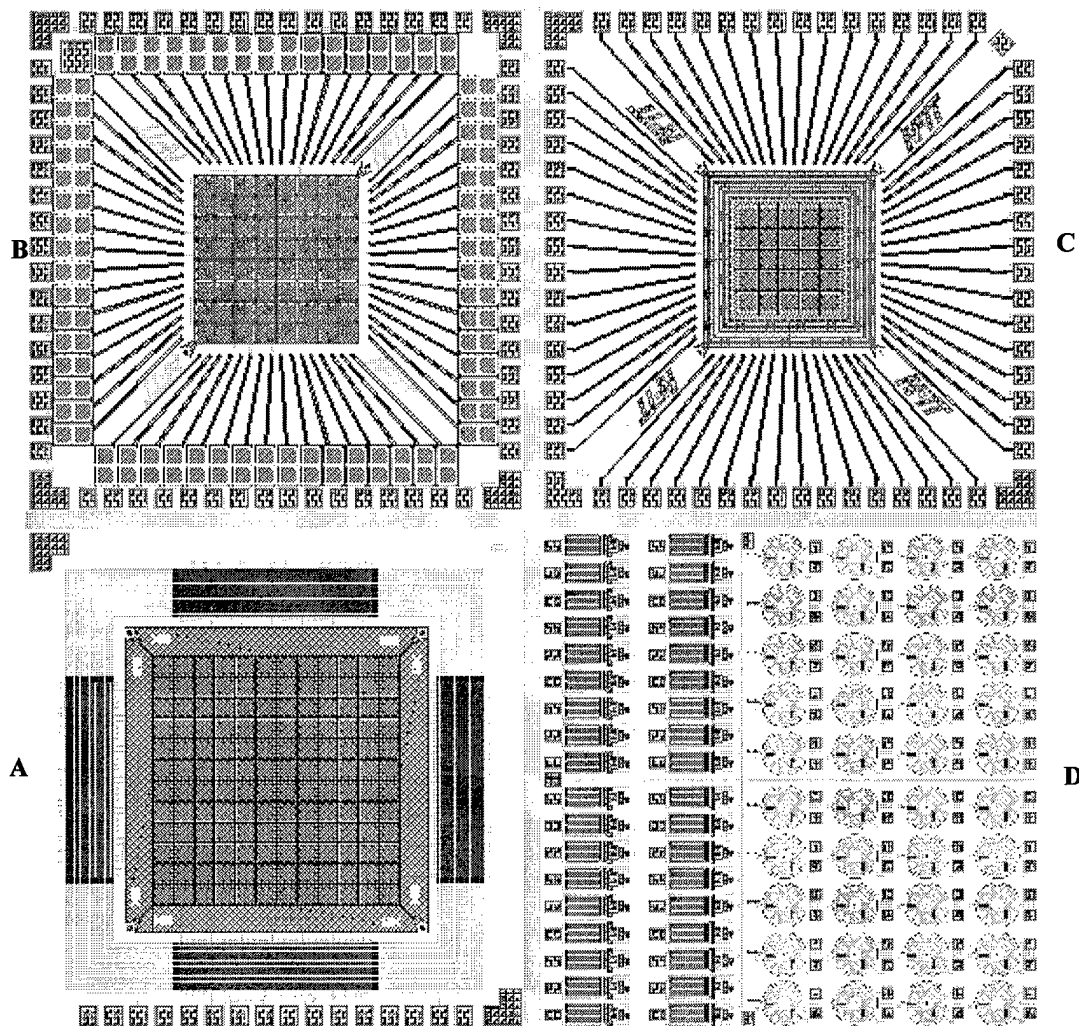
Top cell name: m23_chp2

<u>Quarter Die A</u>
Actuation: electrostatic
Active elements: 128
Layout: 12×12 with center-to-center spacing of 203 μm
Mirror Size: 200 μm × 200 μm, self-planarized
Die Remaining: 14
Package: 68 LCC (or other, 17 connections required)
Other Devices: none
Suggested Usage: optical aberration control (radially symmetric)
Comments: Segmented mirror array with all elements which are equidistant from the mirror center wired together on the die to reduce the number of control signals that must be wired off chip. Improved version of MUMPS22_AFIT2 (Quarter A) with 5 vias attaching Poly2 facesheet to actuator. Post foundry metallization may be used to improve optical performance.

MUMPS23_AFIT5(continued)

Quarter Die B (see picture on previous page)
Actuation: electrostatic, digital deflection
Active elements: 64
Layout: 8×8 with center-to-center spacing of 203 μm
Mirror Size: 180 μm × 180 μm
Die Remaining: 11
Package: 68 LCC
Other Devices: none
Suggested Usage: infrared optical aberration correction experiments
Comments: An electrostatic piston micromirror array employing feedback capacitors (see Chapter 3). Use of MUMPs metal causes curvature of mirror elements, limiting usefulness of this array for visible wavelengths. Initial testing suggests that feedback capacitor scheme does not increase stable deflection range as intended, but shorting of the airgap capacitors has not been ruled out. Quantitative static and dynamic deflection testing required before this array is considered for applications.

Quarter Die C (see picture on previous page)
Actuation: electrostatic, digital deflection
Active elements: 21
Layout: 5×5 with center-to-center spacing of 203 μm
Mirror Size: 200 μm × 200 μm, self-planarized
Die Remaining: 8
Package: 68 LCC
Other Devices: none
Suggested Usage: optical aberration correction experiments
Comments: Improved version of MUMPS22_AFIT2 (Quarter C) with 5 vias attaching Poly2 facesheet segments. Initial testing shows that devices are fully functional and flatness of the mirror surfaces is improved. Tailored post-foundry metallization may improve flatness and increase mirror reflectivity. Self-removing mask facilitates metallization. Small overall size and number of elements will limit applications.

Quarter Die D (see picture on previous page)   **Materials Laboratory Tribology Chip 1**

Actuation: electrostatic
Die Remaining: 12
Package: designed for probe testing
Devices: electrostatic cantilever motors and scratch drive rotors (see Chapter 9)
Suggested Usage: tribology, wear, and failure mechanism studies
Comments: This die contains 36 electrostatic cantilever motors, and 40 scratch drive actuators. Each device is uniquely numbered to facilitate identification. Two variations of electrostatic motors are used; 18 motors have 8 dimples under the cantilever, and 18 motors have 96 dimples under the cantilever. Two variations of scratch drive rotors, denoted SDAR6 and SDAR7 are on the die. Five of each type of scratch drive rotor have force test beams which will engage after the rotor makes 1 full turn. Initial releases of this die show 100% electrostatic cantilever motor yield.

MUMPS24_AFIT3
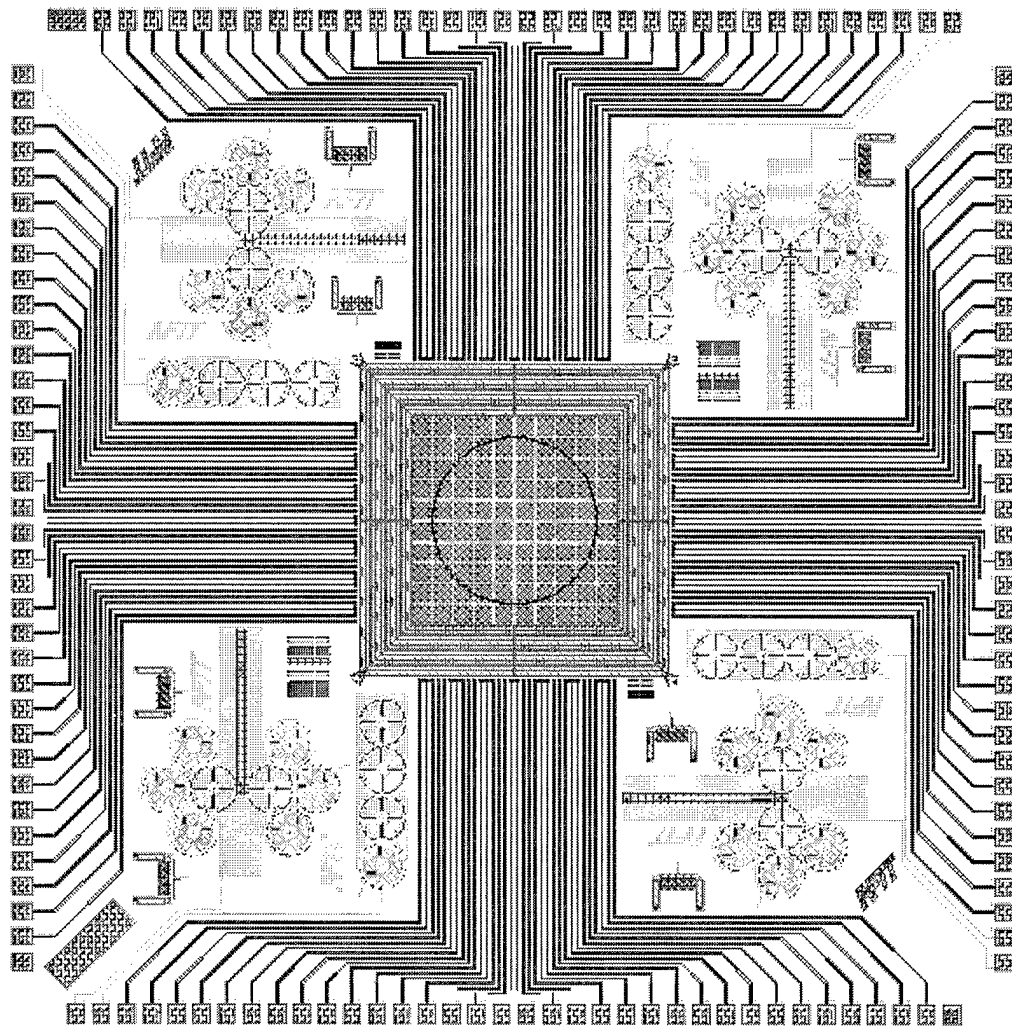
Top cell name:	m24_chp1
Actuation:	electrostatic, digital deflection
Active elements:	44
Layout:	10×10 with center-to-center spacing of 203 μm
Mirror Size:	1.6 mm self-planarized continuous facesheet
Die Remaining:	15
Package:	144 PGA
Other Devices:	scratch drive rotors with gears and force testers
Suggested Usage:	optical aberration correction experiments

Comments: A continuous facesheet mirror 44 digital deflection mirror actuators. Basically an expanded version of the 5×5 prototype. The Poly2 facesheet is cut around the active region to reduce deformation due to residual stress. Post-foundry metallization can be used to increase reflectivity. A self-removing mask facilitates metallization. After mask removal only the circular mirror region will remain.
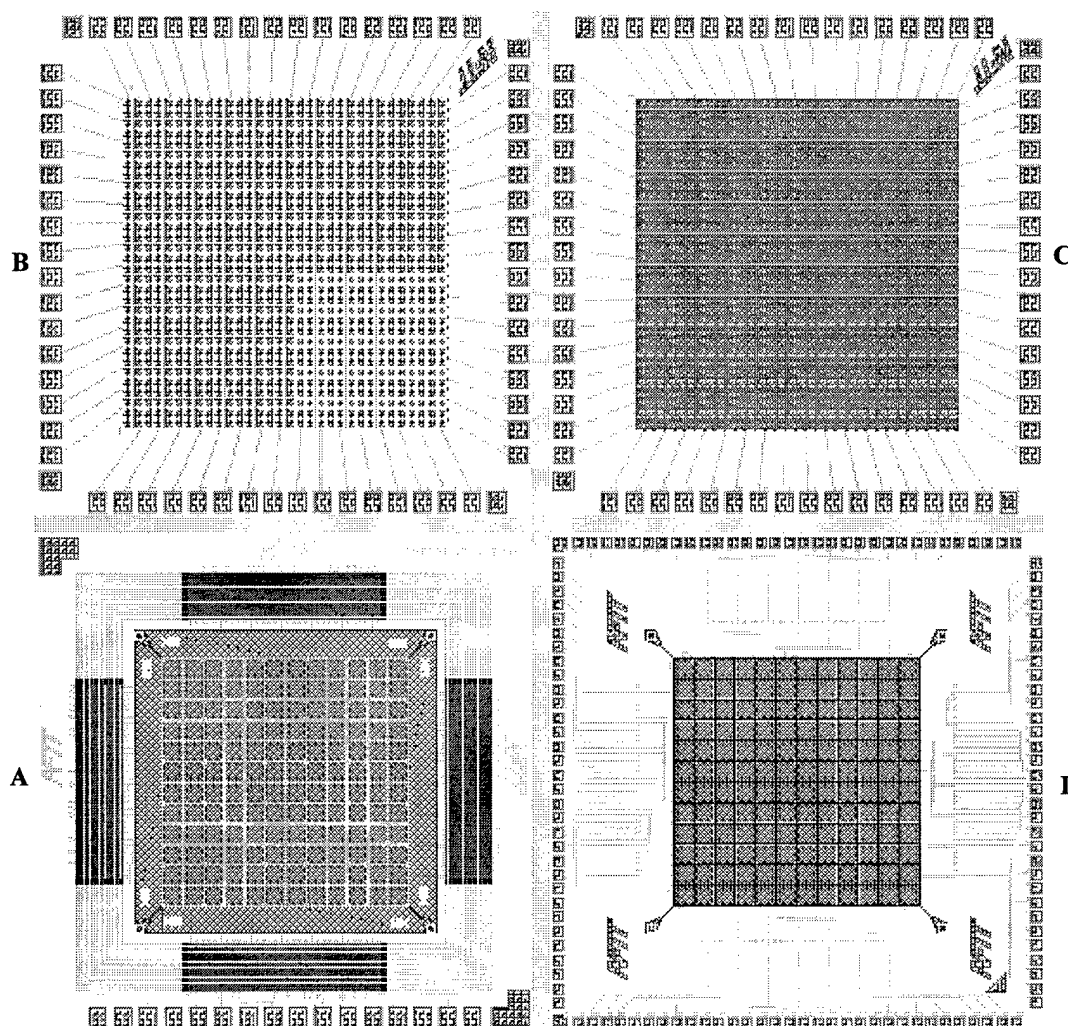
Top cell name: m24_chp2

Quarter Die A
Actuation:	electrostatic
Active elements:	128
Layout:	12×12 with center-to-center spacing of 203 μm
Mirror Size:	2.4 mm self-planarized continuous facesheet
Die Remaining:	15
Package:	68 LCC (or other, 17 connections required)
Other Devices:	none
Suggested Usage:	optical aberration control (radially symmetric)

Comments: Continuous facesheet mirror with actuators equidistant from the mirror center wired together on the die to reduce the number of control signals that must be wired off chip. Improved version of MUMPS22_AFIT2 (Quarter D) continuous facesheet defocus corrector. The fixed point attachments in each corner have been removed in hopes of reducing the stress-induced deformation of the Poly2 facesheet. Post foundry metallization may be used to improve reflectivity.

MUMPS24_AFIT4(continued)

Quarter Die B (see picture on previous page)

Actuation:	electrostatic
Active elements:	1024
Layout:	32×32 with center-to-center spacing of 100 μm
Mirror Size:	81 μm × 92 μm (Poly2)
Die Remaining:	15
Package:	68 LCC
Other Devices:	none
Suggested Usage:	development of row/column address schemes, optical aberration correction experiments

Comments: An aggressive electrostatic piston micromirror array employing row/column address wiring. No metal is used to prevent stress induced mirror curvature. Designed primarily to support development of control schemes to obtain analog or discrete mirror deflections with reduced wiring.

Quarter Die C (see picture on previous page)

Actuation:	electrostatic
Active elements:	1024
Layout:	32×32 with center-to-center spacing of 100 μm
Mirror Size:	78 μm × 89 μm (Metal)
Die Remaining:	15
Package:	68 LCC
Other Devices:	none
Suggested Usage:	development of row/column address schemes, optical aberration correction experiments

Comments: A MUMPs metallized version of MUMPS24_AFIT4 (Quarter B). With the smaller mirror size and trapped oxide mirror plates curvature due to metal stress should be small. With a nominal fill factor of ~70%, these devices should be very useful for optical aberration and beam steering experiments if a viable row/column address control scheme is developed.

Quarter Die D (see picture on previous page)

Actuation:	electrostatic
Active elements:	128
Layout:	12×12 with center-to-center spacing of 203 μm
Mirror Size:	200 μm, self-planarized
Die Remaining:	15
Package:	144 PGA
Other Devices:	none
Suggested Usage:	optical aberration correction experiments

Comments: Redo of the MUMPS21_AFIT7 (Quarter C) segmented mirror array design with 5 facesheet segment to actuator attachment vias. The additional attachment vias have improved the flatness of mirror elements in similarly sized digital deflection devices.
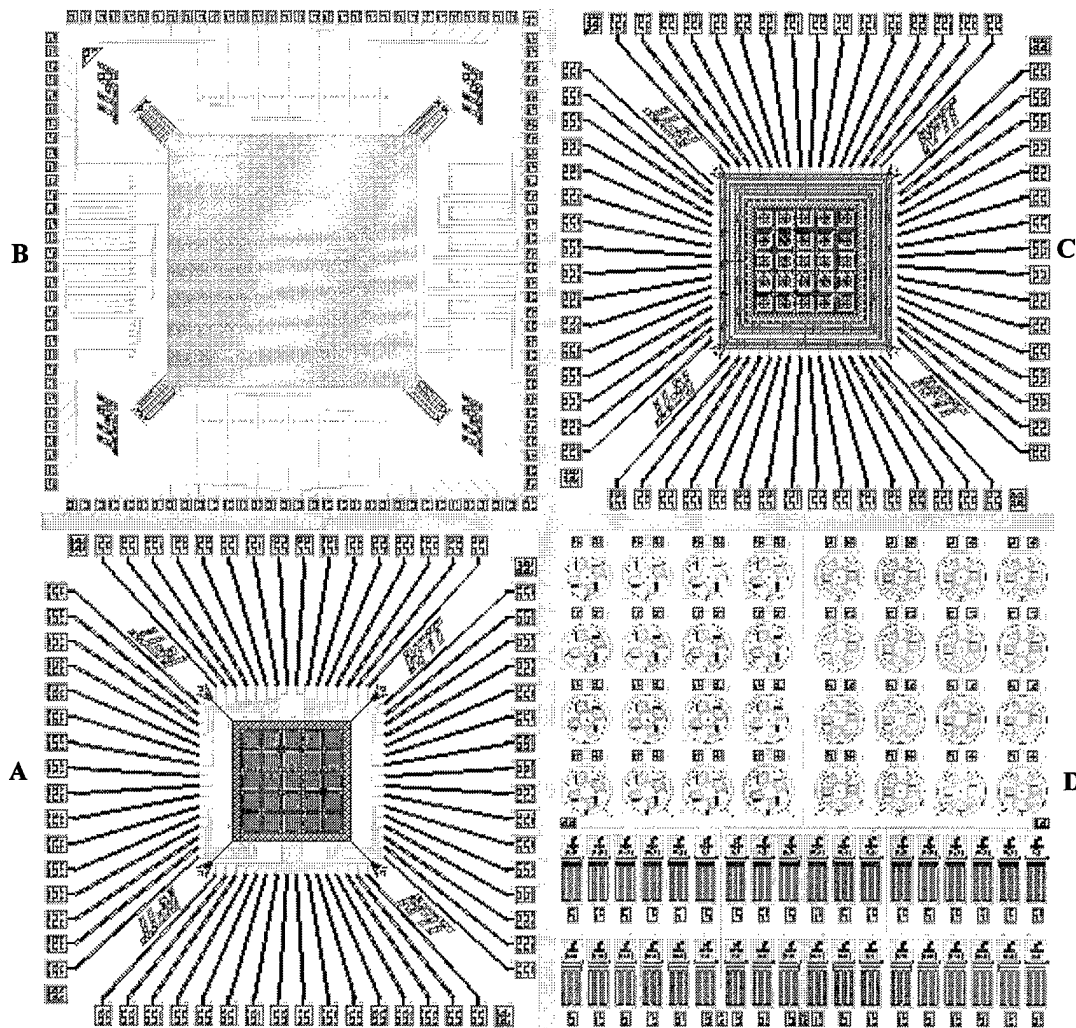
Top cell name: m24_chp3

<u>**Quarter Die A**</u>
Actuation: electrostatic, digital deflection
Active elements: 21
Layout: 5×5 with center-to-center spacing of 203 µm
Mirror Size: 133 µm × 133 µm
Die Remaining: 15
Package: 68 LCC
Other Devices: none
Suggested Usage: optical aberration correction experiments
Comments: Low voltage version of 21 element, segmented digital deflection micromirror array. Self-planarization is not used, hence low fill-factor is low. MUMPs metal is used so curvature can be expected. Small overall size and number of elements will limit applications.

Quarter Die B (see picture on previous page)

Actuation:	electrostatic
Active elements:	128
Layout:	12×12 with center-to-center spacing of 203 μm
Mirror Size:	2.4 mm continuous
Die Remaining:	15
Package:	144 PGA
Other Devices:	none
Suggested Usage:	optical aberration correction experiments

Comments: This design is a modification of the MUMPS21_AFIT6 partially supported membrane mirror. Fixed points in the membrane corners have been removed, and gold/Poly2 cantilevers added in an attempt to stretch the membrane. Flexures supporting the membrane have been stiffened. The membrane will require post-foundry metallization for improved reflectivity. Pads do employ MUMPs metal to make wirebonding the closely spaced pads a little less challenging.

Quarter Die C (see picture on previous page)

Actuation:	electrostatic, digital deflection
Active elements:	21
Layout:	5×5 with center-to-center spacing of 203 μm
Mirror Size:	133 μm × 133 μm
Die Remaining:	15
Package:	68 LCC
Other Devices:	none
Suggested Usage:	optical aberration correction experiments

Comments: Another low voltage version of 21 element, segmented digital deflection micromirror array. This array is an unmetallized version of MUMPS24_AFIT5 (Quarter A). The self-removing metallization mask defines only the array perimeter, not the individual devices. Care must be taken in post foundry metallization to remove metal between elements, otherwise this low fill-factor device will exhibit large interference effects. Small overall size and number of elements will limit applications.

Quarter Die C (see picture on previous page)   **Materials Laboratory Tribology Chip 2**

Actuation:	electrostatic
Die Remaining:	12
Package:	designed for probe testing
Devices:	electrostatic cantilever motors and scratch drive rotors (see Chapter 9)
Suggested Usage:	tribology, wear, and failure mechanism studies

Comments: This die contains 36 electrostatic cantilever motors, and 32 scratch drive rotors. Each device is uniquely numbered to facilitate identification. Three variations of electrostatic motors are used; 12 motors have no dimples under the cantilever, 12 motors have 8 dimples under the cantilever, and 12 motors have 96 dimples under the cantilever. Two variations of scratch drive rotors both differing from the previous tribology chip are included on the die. One type of rotor is powered by four scratch drive (SDAR 10), and the other by six scratch drives (SDAR11). Four of each type of scratch drive rotor have force test beams.

Appendix B - Deformable Mirror Wiring Plans

Numbering for all MUMPs 128 element (12×12) Designs

Column

	1	2	3	4	5	6	7	8	9	10	11	12
1	X	X	1	2	3	4	5	6	7	8	X	X
2	X	X	9	10	11	12	13	14	15	16	X	X
3	17	18	19	20	21	22	23	24	25	26	27	28
4	29	30	31	32	33	34	35	36	37	38	39	40
5	41	42	43	44	45	46	47	48	49	50	51	52
6	53	54	55	56	57	58	59	60	61	62	63	64
7	65	66	67	68	69	70	71	72	73	74	75	76
8	77	78	79	80	81	82	83	84	85	86	87	88
9	89	90	91	92	93	94	95	96	97	98	99	100
10	101	102	103	104	105	106	107	108	109	110	111	112
11	X	X	113	114	115	116	117	118	119	120	X	X
12	X	X	121	122	123	124	125	126	127	128	X	X

Row

Wiring for MUMPS15_AFIT1, MUMPS15_AFIT2, MUMPS17_AFIT10, MUMPS18_AFIT8

Mirror #	Row	Col	Bond	PGA Pin		Mirror #	Row	Col	Bond	PGA Pin
Test	1	1	107	B14		65	7	1	123	A9
Test	1	2	107	B14		66	7	2	124	B8
1	1	3	104	B15		67	7	3	125	A8
2	1	4	100	C15		68	7	4	126	C8
3	1	5	95	F14		69	7	5	127	C7
4	1	6	89	H15		70	7	6	128	A7
5	1	7	88	H14		71	7	7	29	M1
6	1	8	83	L15		72	7	8	50	R6
7	1	9	79	L14		73	7	9	51	R7
8	1	10	76	M14		74	7	10	52	P8
Test	1	11	74	N14		75	7	11	53	R8
Test	1	12	74	N14		76	7	12	54	N8
Test	2	1	107	B14		77	8	1	129	A6
Test	2	2	107	B14		78	8	2	130	B7
9	2	3	105	D13		79	8	3	131	B6
10	2	4	101	D14		80	8	4	132	C6
11	2	5	96	F13		81	8	5	133	A5
12	2	6	90	H13		82	8	6	7	E2
13	2	7	87	J15		83	8	7	26	L2
14	2	8	82	K14		84	8	8	32	P1
15	2	9	78	M15		85	8	9	46	P6
16	2	10	75	P15		86	8	10	47	R5
Test	2	11	74	N14		87	8	11	48	P7
Test	2	12	74	N14		88	8	12	49	N7
17	3	1	110	B13		89	9	1	134	B5
18	3	2	109	C12		90	9	2	135	A4
19	3	3	106	C13		91	9	3	136	A3
20	3	4	102	E13		92	9	4	137	B4
21	3	5	97	E15		93	9	5	3	B1
22	3	6	91	G13		94	9	6	8	D1
23	3	7	86	K15		95	9	7	25	L1
24	3	8	81	K13		96	9	8	31	N2
25	3	9	77	L13		97	9	9	36	R1
26	3	10	72	R15		98	9	10	43	P5
27	3	11	71	P14		99	9	11	44	R4
28	3	12	70	N13		100	9	12	45	N6
29	4	1	113	C11		101	10	1	138	C5
30	4	2	112	B12		102	10	2	139	B3
31	4	3	111	A14		103	10	3	140	A2
32	4	4	103	C14		104	10	4	144	A1
33	4	5	98	E15		105	10	5	4	D2
34	4	6	92	G15		106	10	6	9	F3
35	4	7	85	J13		107	10	7	24	K3
36	4	8	80	M15		108	10	8	30	L3
37	4	9	69	N12		109	10	9	35	P2
38	4	10	68	R14		110	10	10	39	R2
39	4	11	67	P13		111	10	11	41	N5
40	4	12	66	N11		112	10	12	42	R3
41	5	1	117	C10		113	11	1	141	C4
42	5	2	116	A12		114	11	2	141	C4
43	5	3	115	B11		Test	11	3	142	C3
44	5	4	114	A13		Test	11	4	1	D3
45	5	5	99	D15		115	11	5	5	E3
46	5	6	93	F15		116	11	6	10	F2
47	5	7	84	J14		117	11	7	13	G3
48	5	8	65	P12		118	11	8	29	M2
49	5	9	64	R13		119	11	9	34	N3
50	5	10	63	R12		120	11	10	38	P3
51	5	11	62	P11		121	11	11	40	P4
52	5	12	61	R11		122	11	12	40	P4
53	6	1	122	A10		Test	12	1	141	C4
54	6	2	121	C9		Test	12	2	141	C4
55	6	3	120	B9		Test	12	3	143	B2
56	6	4	119	A11		Test	12	4	2	C2
57	6	5	118	B10		123	12	5	6	C1
58	6	6	94	G14		124	12	6	11	E1
59	6	7	60	N10		125	12	7	12	G2
60	6	8	59	P10		126	12	8	28	N1
61	6	9	58	P9		127	12	9	33	M3
62	6	10	57	R10		128	12	10	37	N4
63	6	11	56	R9		Test	12	11	40	P4
64	6	12	55	N9		Test	12	12	40	P4
GND			73	M13		GND			108	A15

Wiring for MUMP19_AFIT7, MUMP20_AFIT6, MUMP20_AFIT7, MUMP21_AFIT5

Mirror #	Row	Col	Bond	PGA Pin		Mirror #	Row	Col	Bond	PGA Pin
1	1	3	98	E14		65	7	1	116	A12
2	1	4	92	G15		66	7	2	115	B11
3	1	5	86	K15		67	7	3	114	A13
4	1	6	80	M15		68	7	4	113	C11
5	1	7	67	P13		69	7	5	112	B12
6	1	8	68	R14		70	7	6	111	A14
7	1	9	69	N12		71	7	7	3	B1
8	1	10	70	N13		72	7	8	9	F3
9	2	3	97	E15		73	7	9	15	G1
10	2	4	91	G13		74	7	10	21	K1
11	2	5	85	J13		75	7	11	27	M1
12	2	6	79	L14		76	7	12	31	N2
13	2	7	63	R12		77	8	1	122	A10
14	2	8	64	R13		78	8	2	121	C9
15	2	9	65	P12		79	8	3	120	B9
16	2	10	66	N11		80	8	4	119	A11
17	3	1	106	C13		81	8	5	118	B10
18	3	2	102	E13		82	8	6	117	C10
19	3	3	96	F13		83	8	7	4	D2
20	3	4	90	H13		84	8	8	10	F2
21	3	5	84	J14		85	8	9	16	H2
22	3	6	78	N15		86	8	10	22	J2
23	3	7	57	R10		87	8	11	28	N1
24	3	8	58	P9		88	8	12	32	P1
25	3	9	59	P10		89	9	1	128	A7
26	3	10	60	N10		90	9	2	127	C7
27	3	11	61	R11		91	9	3	126	C8
28	3	12	62	P11		92	9	4	125	A8
29	4	1	105	D13		93	9	5	124	B8
30	4	2	101	D14		94	9	6	123	A9
31	4	3	95	F14		95	9	7	5	E3
32	4	4	89	H15		96	9	8	11	E1
33	4	5	83	L15		97	9	9	17	H1
34	4	6	77	L13		98	9	10	23	K2
35	4	7	51	R7		99	9	11	29	M2
36	4	8	52	P8		100	9	12	33	M3
37	4	9	53	R8		101	10	1	134	B5
38	4	10	54	N8		102	10	2	133	A5
39	4	11	55	N9		103	10	3	132	C6
40	4	12	56	R9		104	10	4	131	B6
41	5	1	104	B15		105	10	5	130	B7
42	5	2	100	C15		106	10	6	129	A6
43	5	3	94	G14		107	10	7	6	C1
44	5	4	88	H14		108	10	8	12	G2
45	5	5	82	K14		109	10	9	18	H3
46	5	6	76	M14		110	10	10	24	K3
47	5	7	45	N6		111	10	11	30	L3
48	5	8	46	P6		112	10	12	34	N3
49	5	9	47	R5		113	11	3	138	C5
50	5	10	48	P7		114	11	4	137	B4
51	5	11	49	N7		115	11	5	136	A3
52	5	12	50	R6		116	11	6	135	A4
53	6	1	103	C14		117	11	7	7	E2
54	6	2	99	D15		118	11	8	13	G3
55	6	3	93	F15		119	11	9	19	J3
56	6	4	87	J15		120	11	10	25	L1
57	6	5	81	K13		121	12	3	142	C3
58	6	6	75	P15		122	12	4	141	C4
59	6	7	39	R2		123	12	5	140	A2
60	6	8	40	P4		124	12	6	139	B3
61	6	9	41	N5		125	12	7	8	D1
62	6	10	42	R3		126	12	8	14	F1
63	6	11	43	P5		127	12	9	20	J1
64	6	12	44	R4		128	12	10	26	L2
GND			73	M13		GND			108	A15

Element numbering for MUMPS20 through 24 Digital Deflection Designs

Column

	1	2	3	4	5	6	7	8	9	10
1										
2					1	2				
3			3	4	5	6	7	8		
4			9	10	11	12	13	14		
5		15	16	17	18	19	20	21	22	
6		23	24	25	26	27	28	29	30	
7			31	32	33	34	35	36		
8			37	38	39	40	41	42		
9					43	44				
10										

Row

Wiring for 44 Element Digital Deflection Devices
MUMPS22_AFIT1, MUMPS23_AFIT4, MUMPS24_AFIT3

Bit	Bond	PGA Pin		Mirror #	Bit	Bond	PGA Pin		Mirror #	Bit	Bond	PGA Pin
L	78	M15		17	M	93	F15		33	M	129	A6
N	79	L14		17	N	94	G14		33	N	130	B7
M	80	M15		17	L	95	F14		33	L	131	B6
M	69	N12		18	M	84	J14		34	L	3	B1
N	70	N13		18	N	85	J13		34	N	4	D2
L	71	P14		18	L	86	K15		34	M	5	E3
M	99	D15		19	M	48	P7		35	L	15	G1
N	100	C15		19	N	49	N7		35	N	16	H2
L	101	D14		19	L	50	R6		35	M	17	H1
M	90	H13		20	L	39	R2		36	L	24	K3
N	91	G13		20	N	40	P4		36	N	25	L1
L	92	G15		20	M	41	N5		36	M	26	L2
M	81	K13		21	M	45	N6		37	M	135	A4
N	82	K14		21	N	46	P6		37	N	136	A3
L	83	L15		21	L	47	R5		37	L	137	B4
M	66	N11		22	L	42	R3		38	L	132	C6
N	67	P13		22	N	43	P5		38	N	133	A5
L	68	R14		22	M	44	R4		38	M	134	B5
L	60	N10		23	L	114	A13		39	M	138	C5
N	61	R11		23	N	115	B11		39	N	139	B3
M	62	P11		23	M	116	A12		39	L	140	A2
M	63	R12		24	M	117	C10		40	M	9	F3
N	64	R13		24	N	118	B10		40	N	10	F2
L	65	P12		24	L	119	A11		40	L	11	E1
L	96	F13		25	L	111	A14		41	M	18	H3
N	97	E15		25	N	112	B12		41	N	19	J3
M	98	E15		25	M	113	C11		41	L	20	J1
L	87	J15		26	M	120	B9		42	M	27	M1
N	88	H14		26	N	121	C9		42	N	28	N1
M	89	H15		26	L	122	A10		42	L	29	M2
L	75	P15		27	M	12	G2		43	M	141	C4
N	76	M14		27	N	13	G3		43	N	142	C3
M	77	L13		27	L	14	F1		43	L	143	B2
M	57	R10		28	M	21	K1		44	L	6	C1
N	58	P9		28	N	22	J2		44	N	7	E2
L	59	P10		28	L	23	K2		44	M	8	D1
L	51	R7		29	M	30	L3		GND		36	R1
N	52	P8		29	N	31	N2		GND		72	R15
M	53	R8		29	L	32	P1		GND		108	A15
M	54	N8		30	M	33	M3		GND		144	A1
N	55	N9		30	N	34	N3		NC		1	D3
L	56	R9		30	L	35	P2		NC		2	C2
M	105	D13		31	M	126	C8		NC		37	N4
N	106	C13		31	N	127	C7		NC		38	P3
L	107	B14		31	L	128	A7		NC		73	M13
M	102	E13		32	L	123	A9		NC		74	N14
N	103	C14		32	N	124	B8		NC		109	C12
L	104	B15		32	M	125	A8		NC		110	B13

Appendix C - Release and Packaging Procedure

The following release procedure incorporates die mounting as early as possible in the release process. Packaging early improves device yield by eliminating the requirement for repeated tweezers handling of the bare die.

1. Clean all glass and plasticware in deionized water, and dry thoroughly with nitrogen.

2. Beakers required: *First Acetone, Last Acetone, First Methanol, Last Methanol, HF* (hydrofluoric acid)

3. Pour fresh chemicals from bottle into *Last* beakers, then transfer to the appropriate *First* beakers.

4. Soak die in *First Acetone* >5 minutes.   (bulk photoresist removal)

5. Soak die in *Last Acetone* >5 minutes.   (finish photoresist removal)

6. Soak die in *First Methanol* >5 minutes.   (acetone removal)

7. Dry die in clean petri dish on 55 °C hot plate.

8. Add post-foundry mirror metallization if desired.

9. Place clean dry chip carriers on 150 °C hot plate and allow to warm.

10. Apply small dab of CrystalBond 509 hot melt adhesive to carrier (glue flows at 121°C).

11. Place die in chip carrier, position, and remove from heat.

12. Excess glue around edges of die may be removed using a short (2-3 minute) soak in acetone. Use *Last Acetone* if it is not needed for further photoresist removal.

13. Release etch in *HF*. Typical MUMPs deformable mirror etch time is 2.5 minutes.

14. Remove from *HF* and place in *First Methanol*.

15. Soak packaged die in *First Methanol* >5 minutes.

16. Soak packaged die in *Last Methanol* >15 minutes.

17. Dry packaged die on ~55 °C hot plate. For good release yield drying should be characterized by rapid evaporation of methanol without boiling.

18. Probe devices of interest to ensure complete release if etch time is not known. Repeat the release etch (30 seconds per trial), methanol soaks, and drying as required.

19. Wirebond electrical connections.

20. Store devices in a clean, dry area.

Appendix D - Vita

William D. Cowan, Major, USAF

Major William D. Cowan was born 15 October 1960 in Danbury, Connecticut. He graduated from West Virginia Institute of Technology with a Bachelor of Science degree in Electrical Engineering in 1982. He entered the United States Air Force through Officer Training School and was commissioned on 17 May 1983. He was immediately assigned to the Air Force Institute of Technology, to pursue a Master of Science degree in Electrical Engineering, graduating in December 1984. Following graduation, he was assigned to the Electromagnetic Components Branch at Rome Air Development Center in Hanscom AFB, MA. His research at Hanscom included digital compensation of surface acoustic wave oscillators, the first microwave measurements of high temperature superconductors, and an aggressive joint Army/AF program to reduce the size, weight, power consumption, and cost of frequency synthesizers for spread-spectrum communication systems. In 1989, he was transferred to Kirtland AFB, NM where he served in two assignments. His first assignment at Kirtland was to Defense Nuclear Agency's Advanced Research Electromagnetic Pulse Simulator. As Test Program Director, and later Electromagnetic Pulse Branch Chief, he completed more than 10 separate test programs and upgraded the test capabilities of the facility. In 1992, he transferred to the Phillips Laboratory Starfire Optical Range, serving first as Deputy Division Chief of the Ground Based Laser Technology Division, and later as Chief of the Operations & Facilities Branch. At Starfire, Major Cowan supervised engineers and technicians performing critical laser propagation and imaging field experiments in support of the AF Ground Based Laser Antisatellite program, and managed facility support for a remote optical research site with three large telescopes. He participated in several satellite acquisition, tracking, illumination, and imaging field experiments. Major Cowan has over 15 years of experience in Air Force/DoD laboratory and testing facilities, and has technical publications in a variety of diverse fields. In June of 1995 Major Cowan was again assigned to the Air Force Institute of Technology to pursue a Ph.D. in Electrical Engineering. He is a member of SPIE, IEEE, Tau Beta Pi, and Eta Kappa Nu.

Permanent Address: 3285 Shetland Road
                           Beavercreek, Ohio, 45434

E-mail: wcowan@erinet.com

REPORT DOCUMENTATION PAGE

Form Approved
OMB No. 0704-0188

1. AGENCY USE ONLY *(Leave blank)*	2. REPORT DATE	3. REPORT TYPE AND DATES COVERED
	28 April 1998	Dissertation

4. TITLE AND SUBTITLE
Foundry Microfabrication of Deformable Mirrors for Adaptive Optics

5. FUNDING NUMBERS

6. AUTHOR(S)
William D. Cowan

7. PERFORMING ORGANIZATION NAME(S) AND ADDRESS(ES)
Air Force Institute of Technology,
Department of Electrical and Computer Engineering
AFIT/ENG, 2950 P Street, Wright-Patterson AFB, OH 45433-7765

8. PERFORMING ORGANIZATION REPORT NUMBER

AFIT/DS/ENG/98-07

9. SPONSORING/MONITORING AGENCY NAME(S) AND ADDRESS(ES)
Air Force Office of Scientific Research, AFOSR/NE
11 Duncan Avenue, Ste. B115
Bolling AFB, Washington DC 20332-0001

10. SPONSORING/MONITORING AGENCY REPORT NUMBER

11. SUPPLEMENTARY NOTES

12a. DISTRIBUTION AVAILABILITY STATEMENT
Unlimited

12b. DISTRIBUTION CODE

13. ABSTRACT *(Maximum 200 words)*
Microelectromechanical Systems (MEMS) is a rapidly emerging field of research in which batch fabrication processes are used to construct miniature devices. MEMS devices are particularly well suited to optical applications. Foundry microfabrication offers a substantial cost advantage for prototype system development. In this research, foundry MEMS processes are used to fabricate low-cost deformable mirror systems (MEM-DMs) for adaptive optics. The challenges and design trades associated with fabrication of continuous and segmented deformable mirrors in foundry processes are examined in detail. Micromirror surface figure is shown to be critically important. Beam steering and optical aberration correction experiments conclusively demonstrate the potential of low-cost MEM-DMs. The prototype MEM-DM systems are approximately 1/500th the cost of conventionally manufactured deformable mirrors. An innovative direct digital control scheme further reduces adaptive optic system cost by eliminating the digital to analog converter typically required for each controlled element. In addition to the MEM-DMs, other MEMS devices are shown. The thermally actuated piston micromirrors offer greater deflections for operation at longer optical wavelengths. Other MEMS devices examined include a series of tilting mirrors, pressure gauges, test structures, electrostatic scratch drive actuated rotors, and a new type of electrostatic cantilever motor with lateral motion output.

14. SUBJECT TERMS
micro-electro-mechanical (MEMS), micromirrors, adaptive optics, beam steering, deformable mirrors

15. NUMBER OF PAGES
285

16. PRICE CODE

17. SECURITY CLASSIFICATION OF REPORT	18. SECURITY CLASSIFICATION OF THIS PAGE	19. SECURITY CLASSIFICATION OF ABSTRACT	20. LIMITATION OF ABSTRACT
UNCLASSIFIED	UNCLASSIFIED	UNCLASSIFIED	UL